



Fluid circulation and diagenesis of the Lacq Petroleum System : Impact of the geodynamic evolution

Alexy Elias Bahnan

► To cite this version:

Alexy Elias Bahnan. Fluid circulation and diagenesis of the Lacq Petroleum System : Impact of the geodynamic evolution. Earth Sciences. Université de Lorraine, 2019. English. NNT : 2019LORR0221 . tel-02528914

HAL Id: tel-02528914

<https://hal.univ-lorraine.fr/tel-02528914>

Submitted on 2 Apr 2020

HAL is a multi-disciplinary open access archive for the deposit and dissemination of scientific research documents, whether they are published or not. The documents may come from teaching and research institutions in France or abroad, or from public or private research centers.

L'archive ouverte pluridisciplinaire **HAL**, est destinée au dépôt et à la diffusion de documents scientifiques de niveau recherche, publiés ou non, émanant des établissements d'enseignement et de recherche français ou étrangers, des laboratoires publics ou privés.



AVERTISSEMENT

Ce document est le fruit d'un long travail approuvé par le jury de soutenance et mis à disposition de l'ensemble de la communauté universitaire élargie.

Il est soumis à la propriété intellectuelle de l'auteur. Ceci implique une obligation de citation et de référencement lors de l'utilisation de ce document.

D'autre part, toute contrefaçon, plagiat, reproduction illicite encourt une poursuite pénale.

Contact : ddoc-theses-contact@univ-lorraine.fr

LIENS

Code de la Propriété Intellectuelle. articles L 122. 4

Code de la Propriété Intellectuelle. articles L 335.2- L 335.10

http://www.cfcopies.com/V2/leg/leg_droi.php

<http://www.culture.gouv.fr/culture/infos-pratiques/droits/protection.htm>



UNIVERSITÉ
DE LORRAINE

SIReNa



geo
Ressources



TOTAL

Université de Lorraine, Collegium Sciences et Technologies
Ecole Doctorale SIReNa

Thèse

Présentée pour l'obtention du titre de
Docteur de l'Université de Lorraine
Spécialité "Géosciences"

Par **Alexy ELIAS BAHNAN**

Circulation des fluides et diagenèse du système pétrolier de Lacq : Impact de l'évolution géodynamique

Soutenance publique le 10/12/2019

Membres du jury :

Rapporteurs :

Mme Anna TRAVE	Professeur, Université de Barcelone, Espagne
M. Rudy SWENNEN	Professeur, Université Catholique de Louvain, Belgique

Examineurs :

Mme. Mary FORD	Professeur, Université de Lorraine, France
M. Guilhem HOAREAU	Maître de conférences, Université de Pau, France
M. Christophe DURLET	Maître de conférences, Université de Bourgogne, France

Directeurs de thèse :

M. Jacques PIRONON	Directeur de recherche CNRS, Université de Lorraine, France
M. Cédric CARPENTIER	Maître de conférences, Université de Lorraine, France

Invités :

M. Eric C. GAUCHER	Ingénieur Géochimie, TOTAL SA, Pau, France
M. Jean-Pierre GIRARD	Ingénieur Géochimie, TOTAL SA, Pau, France



UNIVERSITÉ
DE LORRAINE

SIReNa



geo
Ressources



TOTAL

Université de Lorraine, Collegium Sciences et Technologies
Ecole Doctorale SIReNa

Thèse

Présentée pour l'obtention du titre de
Docteur de l'Université de Lorraine
Spécialité "Géosciences"

Par **Alexy ELIAS BAHNAN**

Fluid circulation and diagenesis of the Lacq Petroleum System: Impact of the geodynamic evolution

Soutenance publique le 10/12/2019

Membres du jury :

Rapporteurs :

Mme Anna TRAVE	Professeur, Université de Barcelone, Espagne
M. Rudy SWENNEN	Professeur, Université Catholique de Louvain, Belgique

Examineurs :

Mme. Mary FORD	Professeur, Université de Lorraine, France
M. Guilhem HOAREAU	Maître de conférences, Université de Pau, France
M. Christophe DURLET	Maître de conférences, Université de Bourgogne, France

Directeurs de thèse :

M. Jacques PIRONON	Directeur de recherche CNRS, Université de Lorraine, France
M. Cédric CARPENTIER	Maître de conférences, Université de Lorraine, France

Invités :

M. Eric C. GAUCHER	Ingénieur Géochimie, TOTAL SA, Pau, France
M. Jean-Pierre GIRARD	Ingénieur Géochimie, TOTAL SA, Pau, France

*“To raise new questions, new possibilities, to regard old problems from a new angle,
requires creative imagination and marks real advance in science”*

-Albert Einstein

Table of contents

Acknowledgments	9
Résumé étendu	11
Extended abstract	17
General Overview	24
1. Scientific context	24
2. Research objectives	26
3. Thesis organization	26
Chapter 1: State of the art	29
1. Carbonate diagenesis	29
2. Dolomitization	30
3. Regional Geodynamic History	37
4. Stratigraphy and sedimentology of the Lacq petroleum system	41
5. Previous diagenetic models	46
Chapter 2: Methodology	52
1. Sampling campaign	52
2. Thin and thick sections preparation	53
3. Staining	53
4. Petrography	54
4.1. Optical microscope	54
4.2. Cold Cathodoluminescent microscope	54
4.3. Fluorescent microscope	56
4.4. Scanning electron microscope (SEM)	56

5. Geochemistry	56
5.1. Stable carbon and oxygen isotopes	57
5.2. Multiple sulfur isotopes.....	58
5.3. Major and trace element analysis	59
6. Fluid inclusions analyses	60
6.1. Microthermometry	60
6.2. Raman Spectroscopy.....	61
6.3. Infrared microspectroscopy (μ FT-IR)	63
6.4. Confocal Scanning Laser Microscope.....	63
6.5. Aqueous inclusions thermodynamics modeling (AIT)	64
6.6. Petroleum inclusions thermodynamics modeling (PIT).....	65
7. Basin Modeling.....	66
Chapter 3 – Part I: Results: Upper Lacq	69
1. Petrography of diagenetic phases.....	69
1.1. Host Rock.....	69
1.2. Glauconite	69
1.3. Micrite rims	69
1.4. Framboidal pyrites.....	69
1.5. Chert Nodules	69
1.6. Dolomite D1.....	71
1.7. Pyrite 2	71
1.8. Fracture (breccia)	71
1.9. Saddle dolomites D2	71
1.10. Stylolites	72

1.11.	Fracture and dissolution	72
1.12.	Blocky Calcites	72
1.13.	Oil emplacement	72
1.14.	Anhydrites	73
1.15.	Groundwater.....	74
1.16.	Iron Oxides	74
2.	Fluid Inclusion Studies	74
2.1.	Petrography.....	74
2.2.	Fourier Transform – Infrared Spectroscopy (FT-IR)	76
2.3.	Microthermometry	76
2.4.	Raman Spectroscopy	78
3.	Isotope Geochemistry	78
4.	Major and trace element analysis	82
4.1.	Fe-S.....	82
4.2.	REE	82
4.1.	U-Pb LA-ICPMS absolute age dating.....	83
5.	Fluid inclusions thermodynamics modeling	83
6.	Basin modeling.....	85
6.1.	Basal heat flow scenario	85
6.2.	Thermal history reconstruction based on vitrinite reflectance fitting	86
Chapter 3 – Part II: Discussions and interpretations: Upper Lacq.....		88
1.	Paragenesis and fluids involved.....	88
2.	Redox conditions.....	93
3.	Hydrothermal activity.....	93

4. Fluid circulation schemes.....	95
Chapter 3 – Part III: Conclusions: Upper Lacq	99
Chapter 4 – Part I: Deep Lacq: Results	102
1. Petrography of diagenetic phases.....	102
1.1. Micritization	102
1.2. Pyrite	102
1.3. Dolomite 1	102
1.4. Dissolution.....	103
1.5. Calcite 1	103
1.1. Calcite 2	103
1.2. Compaction	103
1.3. Stylolite 1	104
1.4. Fracture A1.....	105
1.5. Dolomite 2	105
1.1. Fracture A2.....	105
1.2. Calcite 3	105
1.3. Fracture B.....	106
1.4. Anhydrite	106
1.5. Stylolite 2.....	108
1.6. Fracture C	108
1.7. Dissolution.....	108
2. Isotope Geochemistry	109
3. Major and trace element analysis	111
3.1. Fe-S.....	111

3.2. U-Pb	112
3.3. REE	112
4. Fluid inclusion studies	113
4.1. Petrography	113
4.2. Microthermometry	116
4.3. Raman Spectroscopy	120
5. AIT-PIT modeling	121
6. Basin modeling	122
Chapter 4 – Part II: Deep Lacq: Discussions	129
1. Basin models	129
2. H ₂ S and its effect on phase diagrams	133
3. Ages of the diagenetic fluids	135
4. Timing and sources of diagenetic fluids	140
5. Redox conditions	148
Chapter 4 – Part III: Deep Lacq: Conclusions	150
Chapter 5: General conclusions and synthesis	153
1. Synthetic model of the Upper and Deeper Lacq reservoirs	153
2. Diagenetic fluids between the NPZ and the Aquitaine foreland	158
3. Guides for prospection	162
Chapter 6: Perspectives	165
List of figures	168
List of tables	176
Appendices	177
Appendix 1: Core logs of the studied wells	178

Appendix 2: Matlab 2 nd derivative algorithms	184
Appendix 3: TVD data used in the Petromod's stratigraphy.....	186
Appendix 4: Porosities added as calibrations in Petromod	187
Appendix 5: Densities added as calibrations in Petromod	189
Appendix 6: Vitrinite and sterane isomerization data added as calibrations in Petromod.....	190
Appendix 7: Photomicrographs of the host rocks in Upper Lacq	191
Appendix 8: $\delta^{18}\text{O}$ and $\delta^{13}\text{C}$ data of Upper Lacq reservoirs	192
Appendix 9: Photomicrographs of the host rocks in Deep Lacq.....	193
Appendix 10: $\delta^{18}\text{O}$ and $\delta^{13}\text{C}$ data of Deep Lacq reservoirs.....	194
Appendix 11: TOTAL's archives isotopic data (Pabian-Goyheneche and Anquelle, 1995)	195
Appendix 12: U/Pb contents in Deep Lacq.....	197
References.....	199

Acknowledgments

The three years spent working on this research project were full of excitement and good memories. I cannot but warmly thank and acknowledge everyone who contributed to the success of this thesis.

Foremost, I am greatly indebted to my directors: Jacques Pironon and Cédric Carpentier for their effort, guidance and advice throughout this project. Their feedback and orientation were paramount to remarkably alleviate my learning curve and provide me with the knowledge and skills to do this research. I sincerely thank them for always being friendly and supportive which made those 3 years successful and enjoyable.

I also thank and acknowledge Eric Gaucher from the Centre Scientifique et Technique Jean Féger (CSTJF) – TOTAL for supervising this project and providing the necessary logistics and access to data archives to conduct this research. Mr. Gaucher always had this friendly and welcoming attitude at CSTJF that made me look forward to the next visit to Pau. I also wish to thank him for his efforts in the conferences, workshops and seminars where we shared many constructive ideas with other colleagues from CSTJF and collaborating universities.

Mme Nathalie Foucal, the director of the Centre de Recherches sur la Géologie des Matières Premières Minérales et Energétiques (CREGU) is warmly thanked for providing the funding and logistic support needed for this research. She was very helpful and made sure that the best conditions were met in the offices and during missions outside the lab.

M. Olivier Fonta, the head of Geosciences Department in GEOPETROL S.A., is thanked and acknowledged for the collaboration in allowing access to the well cores and permission to obtain and work with the samples.

Many people at the GeoRessources Lab helped me in acquiring data and/or learning new skills and techniques. I thank Alexandre Flammang for expertly preparing the thin and thick sections, Delphine Martin for her IT support, Karine Pistre for assisting with some optical microscopes, Vanessa Dyja for teaching me how to operate the confocal scanning microscope and process its data, Chantal Peiffert for operating the LA-ICPMS, Andreï Lacompte for spending time and effort on the SEM, Odille Barres for her help in the

infrared spectrometry and its software and Marie-Camille Caumon for her assistance with the Raman spectroscopy. I also thank Thomas Rigaudier from CRPG for his help in the isotopes analyses. Dr. Mary Ford from CRPG is sincerely thank for her help in explaining the complex geology of the area. Her feedback was crucial to improve the quality of this research. Her master student, Laurine Duvivier is also thanked and acknowledged for her work on the paleowater depth estimations.

Raymond Michels is appreciated for his comments and input on dealing with the vitrinite data.

At CSTJF, Sylvain Calassou, Jean-Pierre Girard, Charlotte Fillon, Emanuel Masini and Aurélien Virgone are warmly thanked for their constructive comments and advice. I also wish to extend my gratitude to M. Jean-Noël Jaubert and Mme Silvia Lasala from the *École Nationale Supérieure des Industries Chimiques* (ENSIC) for their help and assistance in modeling the H₂S effects on the phase diagrams.

On a personal level, this thesis would have been very difficult without my family and friends.

My parents' never-ending sacrifices provided me with the spirit needed to overcome the hardships of leaving home and studying abroad. I am forever in their debt for making me who I am. My brother Elias and my sister Nancy were always there when skies turned cloudy. They have always provided the energy and push I need to complete every new endeavor, and for that, I am eternally grateful. They all kept me going and this thesis would not have been possible without them.

A special person, "*in my mind, in my head*", is warmly appreciated for being there when needed the most. I owe her my deepest gratitude for always putting a smile on my face.

My French and Lebanese friends are also acknowledged for creating an off-work socially active atmosphere to enjoy. Their help in the (arduous) French bureaucracy is also appreciated and acknowledged. In this regard, I warmly thank Héloïse Verron and Joséphine Gigon for their help and guidance during my stay at the GeoRessources Lab. Conferences and workshops spent with Guillaume Barré (the sulfur boy), Camille Tichadou, Maxime Ducoux, Goeffrey Motte and Dimitri Laurent were full of memorable moments and for those friends I am deeply grateful. I warmly thank them for the "serious?" geology-related discussions during conferences, the "~helpful" French vocabulary they taught me and for the most joyful memories we shared together.

Résumé étendu

L'histoire géologique d'un bassin d'avant-pays peut contrôler les types, les sources, les propriétés chimiques et les conditions de pression-température des fluides impliqués dans la diagenèse des réservoirs carbonatés. Dans le bassin Aquitain (sud-ouest de la France), plusieurs gisements d'hydrocarbures sont situés dans les dolomies jurassiques et crétacées. Le système pétrolier de Lacq est un vaste champ pétrolier du sous-bassin de l'Arzacq, dans le bassin Aquitain. Il s'agit d'un anticlinal à cœur de sel dont l'axe est orienté NW-SE. Le système pétrolier comprend deux réservoirs économiquement importants. Le premier est le réservoir supérieur de Lacq, situé à 650 m de profondeur et recouvert par les flyschs paléocènes. Il a produit des huiles lourdes à partir de dolomies fracturées du Crétacé supérieur (Coniacien à Campanien). Le second est le réservoir de Lacq inférieur, situé à une profondeur de 3700 m et recouvert par les marnes de Sainte Suzanne de l'Aptien, et qui produit principalement du gaz sec. Plusieurs modèles ont été proposés pour expliquer la diagenèse et les propriétés pétrophysiques des réservoirs de Lacq. Initialement, la dolomitisation des faciès bioclastiques du réservoir de Lacq supérieur a été expliquée par la diagenèse précoce. Dans ce premier modèle, la circulation des fluides, la diagenèse et les propriétés des réservoirs étaient principalement contrôlées par la distribution des textures sédimentaires primaires. Cependant plusieurs études démontrent que les processus de dolomitisation pervasive peuvent être liés à l'impact des fluides hydrothermaux chauds et profonds circulant le long de fractures. Récemment, les modèles géodynamiques des Pyrénées et du bassin sud aquitain ont été revus et mis à jour pour inclure une phase de rifting au Crétacé inférieur qui a généré un amincissement crustal extrême couplé à une exhumation du manteau. Cet événement a été suivi d'une inversion et de la convergence Pyrénéenne à la fin du Crétacé et au Paléogène. Ce modèle révisé met en évidence l'impact possible des fluides hydrothermaux sur la diagenèse des réservoirs pétroliers dans le sud du Bassin Aquitain. Compte tenu de son histoire géodynamique complexe et de l'abondance des données souterraines, le bassin aquitain sert de laboratoire naturel pour étudier comment l'évolution structurale de l'avant-pays pyrénéen a influencé la circulation des fluides et éventuellement la diagenèse des réservoirs. Dans ce contexte, un réexamen de l'évolution diagénétique de ces réservoirs doit être effectué.

Pour documenter le contrôle possible de cette histoire géologique sur la diagenèse des réservoirs carbonatés, trois forages carottés pénétrant dans les réservoirs du Crétacé supérieur (Lacq supérieur) et du Jurassique supérieur au Crétacé inférieur (Lacq profond) ont été étudiés. Des observations pétrographiques, des études d'inclusion de fluides couplées à la modélisation thermodynamique, à la géochimie isotopique et aux terres rares, ainsi qu'à la modélisation de bassin ont été effectuées pour étudier et décrire les types et les sources de fluides, l'évolution pression-température et le timing de circulation des fluides diagénétiques.

Nos résultats indiquent que dans Lacq supérieur, après le dépôt de carbonate marin et une diagenèse bactérienne précoce au Crétacé supérieur, une dolomitisation de reflux a permis la précipitation d'une phase dolomitique précoce. Les données microthermométriques et les données géochimiques appuient un modèle avec de multiples pulses de fluide commandés par des contraintes structurales régionales. Après le dépôt de la couverture paléocène, la faille de Sainte Suzanne, activée pendant la compression de l'Éocène, aurait pu servir de voie de circulation pour les fluides de formation chauds et profonds vers la zone de pression relativement plus froide et plus basse sur la crête de l'anticlinal de Lacq. Cette faille recoupe les formations riches en argiles Albo-Aptiennes (Marnes de Sainte Suzanne et Marnes d'Assat) qui, en se fracturant et en se contractant, ont pu libérer des fluides riches en magnésium avec une faible salinité. Ces fluides ont été responsables de la dolomitisation hydrothermale, comme l'indiquent les clumped isotopes, qui indiquent une température de cristallisation de la dolomite de 90°C, qui est en déséquilibre thermique (>40°C) par rapport à la température ambiante d'enfouissement de 40-50°C. Après la fin de l'expulsion de magnésium en raison de modifications des contraintes tectonique régionales, les fluides chauds et peu salins ont continué à être expulsés de ce bassin vers Lacq supérieur. Le mélange du fluide pauvre en magnésium, chaud et à faible salinité et du pétrole a précipité des calcites de blocage à inclusions hydrocarbonées et inclusions aqueuses. Ces fluides circulaient à des températures d'environ 90°C. La modélisation de bassin indique également un timing Eocène pour cette circulation de fluide, pendant le climax de la compression pyrénéenne. L'origine du pétrole de Lacq supérieur est discutable compte tenu de la complexité de l'évolution structurale et thermique du système pétrolier. Cependant, le scénario le plus probable est une migration à partir des roches mères de Lacq inférieur traversant les récifs albiens. Après la cimentation de la calcite, les fluides résiduels sont devenus sursaturés par rapport aux

sulfates et une phase mineure d'anhydride a été précipitée. Le moment de la précipitation de l'anhydride est soutenu par les multi-isotopes du soufre qui indiquent origine éocène de l'eau de mer du fluide parent. Enfin, pendant l'exhumation du bassin, des fluides oxydants ont été introduits latéralement sous forme d'eau souterraine. L'entrée verticale est peu probable étant donné l'intégrité du joint paléocène. Cette eau souterraine est légèrement modifiée et enrichie en $\delta^{18}\text{O}$ d'environ +2‰ SMOW par rapport aux valeurs des eaux météoriques. Cet enrichissement pourrait être le résultat d'interactions fluide-roche et d'apports possibles de fluides de formation enrichis en $\delta^{18}\text{O}$.

Dans Lacq inférieur, la diagenèse précoce est marquée par une activité bactérienne à l'origine d'une micritisation locale et de la formation de pyrites framboïdales. Une dolomitisation par "mixing-zone" a permis la précipitation d'une phase précoce de dolomies idiomorphes, enrichies en $\delta^{18}\text{O}$ (jusqu'à +1,8‰ PDB) et en $^{87}\text{Sr}/^{86}\text{Sr}$ par rapport à l'eau de mer jurassique. Dans de rares niveaux stratigraphiques des calcites formées en environnement phréatique ont pu précipiter. La transition vers la mésogénèse est marquée par l'apparition de conditions réductrices associées à une deuxième phase de calcite. Pendant l'hyper-extension aptienne, le pic thermique avec un gradient géothermique proche de 70°C/km a fait entrer les roches mères dans la fenêtre d'huile, tandis que des fractures d'extension reliaient les réservoirs de Lacq inférieur à un réservoir de fluides salés, probablement triasique, qui a permis la précipitation de dolomies baroques avec des salinités d'environ 8,2 et 10,2 éq. wt.% de NaCl. Le Mg^{2+} provenait probablement de minéraux argileux des formations sous-jacentes comme les marnes Liasiques. Pendant le Crétacé supérieur, les changements dans le régime des contraintes liés à l'apparition de la convergence N-S ont créé un nouvel ensemble de fractures qui a permis la circulation de fluides sursaturés par rapport à la calcite. Les fluides présentaient des températures minimales de 100-140°C et des salinités de 9-13,5 éq. wt.% de NaCl. Les valeurs en $\delta^{13}\text{C}$ de ces dolomites baroques et des calcites sont légèrement enrichies par rapport à celles de l'eau de mer, atteignant jusqu'à +5 ‰ PDB, ce qui indique un mélange possible avec du carbone organique précoce, conservé après fermentation organique et méthanogénèse pendant l'enfouissement précoce. L'enrichissement en $^{87}\text{Sr}/^{86}\text{Sr}$ par rapport à l'eau de mer jurassique suggère des interactions avec les marnes. Un troisième événement de fracturation a été associé à la circulation de grands volumes de fluides riches en sulfates, ayant une signature triasique, et qui ont précipité des anhydrites massives immédiatement sous les marnes aptiennes. Les températures d'homogénéisation des

inclusions aqueuses sont comprises entre 90 et 120°C et les salinités entre 4 et 6 éq. wt.% de NaCl. Les signatures en multi-isotopes du soufre obtenus à partir de ces anhydrites suggèrent une connexion possible avec le Trias et un mélange avec des fluides de formation du Barremien,. Ces anhydrites sont recoupées par des stylolites tectoniques formés lors de la compression éocène. L'absence d'inclusions de gaz dans les phases étudiées indique que la charge en gaz dans Lacq inférieur s'est produite après la cimentation et est donc supposée comme étant post-orogénique.

Pour comprendre et synthétiser l'histoire géodynamique et son impact sur la diagenèse du réservoir, les principaux fluides diagénétiques qui ont circulé à des âges similaires dans les Chaînon Béarnais et le champ de Rousse sont comparés à cette étude. Durant le Lias et le Dogger, les fluides oxydants éogénétiques ont précipité une phase précoce de calcites non ferrifères et non luminescentes dans les Chaînon Béarnais tandis qu'à Rousse, les dolomites primaires de la Dolomie de Mano, dont l'origine est encore contestable, se sont formées. Dans Lacq inférieur, l'éogénèse a été marquée par une dolomitisation de "mixing-zone" suivie par des calcites précoces et zonées pendant la transition progressive vers la mésogénèse.

Pendant l'hyper-extension aptienne, dans les Chaînon béarnais, des fluides magmatiques à mantelliques ont permis la précipitation de dolomie et de chlorite dans les fractures des formations jurassiques, avec des températures atteignant 350°C et des salinités >25% NaCl. Dans le même temps, à Rousse, des fluides dolomitiques circulaient à des températures comprises entre 147°C et 167°C avec de faibles salinités. De même, Lacq inférieur a connu des précipitations de dolomie baroques pendant l'entrée dans la fenêtre à huile. Dans les Chaînon Béarnais et Rousse cependant, la proximité des corps mantelliques exhumés et les fortes interactions fluides-manteaux sont la source de Mg pour les fluides chauds dolomitiques. Les fluides circulaient probablement le long de corridors le long du front nord Pyrénéen avec un gradient de température décroissant vers le nord de 350°C à 150°C. Les salinités élevées des fluides dolomitiques des Chaînon béarnais ont été attribuées à la lixiviation des évaporites du Trias lors de la migration ascendante des fluides magmatiques, tandis que les salinités faibles de Rousse s'expliquent par la percolation des fluides météoriques mélangés à des fluides ascendants issus de la serpentinisation et des fluides faiblement salés expulsés par les argiles de bassin. Dans Lacq inférieur, les fluides dolomitiques

atteignaient des températures comprises entre 140-165°C avec des salinités plus élevées (8-10 éq. wt.% de NaCl) que dans le champ de Rousse, mais plus faibles que dans les Chaînons Béarnais. Ces fluides dolomitiques sont ici considérés comme un mélange de fluides provenant du Trias avec un Mg principalement fourni par les formations des Marnes Liasiques et des Marnes à ammonites. La similitude des plages de température des fluides entre Lacq et Rousse renforce la notion de diminution du gradient de température en dehors du domaine d'hyper-extension. Les sources de Mg dans Lacq inférieur diffèrent de celles de Rousse et des Chaînons Béarnais étant donné qu'il n'y a aucune preuve de serpentization ou que des fluides d'origine mantellique ont été identifiés dans Lacq inférieur. De même, les salinités diffèrent d'un endroit à l'autre et dépendent de la géologie locale (présence de discordances et d'apports verticaux de fluides), de la proximité des dômes salins du Trias (absents à Rousse) et des corps mantéliques exhumés (uniquement dans les Chaînons Béarnais).

Les fluides qui ont précipité la calcite post-dolomite dans les Chaînons Béarnais ont circulé à des températures proches de 220°C entre l'Albien tardif et le Cénomanién. La salinité de ces fluides est inférieure à celle de la dolomie baroque (15 éq. wt.% de NaCl) et a été considérée comme le produit d'une source de fluide mixte marine à magmatique. A Rousse, les fluides qui circulaient pendant l'Albien (105 Ma) avaient des températures de 145°C avec des salinités inférieures à celles de l'eau de mer. Le fluide était riche en gaz provenant d'un mélange de fluides résiduels dolomitiques et de fluides d'origine météorique qui ont percolé à travers la discordance cénomaniénne de base. Dans Lacq inférieur, deux populations d'inclusions aqueuses atteignent une température moyenne de 135-140°C, similaire à celle enregistrée dans les calcites de Rousse, mais les salinités sont plus élevées, avec 9 éq. wt.% NaCl. Les fluides ici sont supposés provenir d'une source triasique saline. Pendant le Crétacé supérieur, après la formation du réservoir de Lacq supérieur, la diagenèse a été dominée par la dolomitisation par reflux précoce avec du Mg provenant de l'eau de mer évaporée ainsi que des fluides de formation interstitiels.

Pendant la compression maximale de l'Eocène, des stylolites tectoniques se sont développés dans les Chaînons Béarnais et Lacq tandis que des brèches et des cimentations de calcite ont été enregistrées à Rousse, avec des salinités élevées dues au déplacement vers le haut des saumures de bassin. La chronologie des calcites télogénétiques dans les Chaînons béarnais n'a pas été identifiée de façon

concluante et peut aussi l'être pendant la compression éocène. Cet épisode de compression a été l'événement majeur qui a contrôlé la diagenèse de Lacq supérieur en raison de la dolomitisation hydrothermale due à l'orogénèse, suivie de la céméntation de calcite et d'anhydrite. Les anhydrites finales ont également précipité, peut-être au cours de la même période, dans Lacq inférieur.

Les événements post-orogéniques ont été similaires à Lacq et à Rousse et ont impliqué l'apport d'hydrocarbures en quantités commerciales dans les réservoirs. Dans les Chaînons Béarnais, la proximité des domaines mantéliques exhumés a rendu la région trop chaude pour permettre la maturation de volumes de pétrole économiquement viables.

Par conséquent, il est évident que le contexte géodynamique global, à savoir l'anomalie thermique aptienne, avait un contrôle significatif sur la température des fluides diagénétiques qui circulaient dans la zone étudiée, mais les compositions et les salinités étaient plus influencées par les contextes géologiques locaux dans les sous-bassins compartimentées, plutôt que par les écoulements de fluides à grande échelle du bassin.

Extended abstract

The geologic history of a foreland basin can exert strong control on the types, sources, chemistries and pressure-temperature conditions of fluids involved in the diagenesis of carbonate reservoirs. In the Aquitaine basin (SW France), several hydrocarbon fields are located in Jurassic and Cretaceous dolomites. The Lacq petroleum system is one of the largest petroleum fields in the Arzacq sub-basin, of the Aquitaine basin. It consists of a saltcored anticline whose axis is oriented NW-SE. The petroleum system encompasses two economically important reservoirs. The first is the Upper Lacq reservoir located at 650m depth and sealed by the overlying Paleocene Flysch. It produced heavy oil from Upper Cretaceous (Coniacian to Campanian) fractured dolomites. The second is the Deep Lacq reservoir, which is located at a depth of 3700m and is capped by the overlying Early Aptian Sainte Suzanne marls, and produces mainly dry gas. Several models were proposed to explain the diagenesis and petrophysical properties of the Lacq reservoirs. Initially, dolomitization of the shallow marine carbonates of the Upper Lacq reservoir were considered to be due to early diagenesis, and to impact preferentially the more bioclastic facies. In this initial model, fluid circulation, diagenesis, and reservoir properties were mainly controlled by the distribution of primary sedimentary fabrics. However, several studies demonstrate that processes of pervasive dolomitization can be linked to the impact of deep hot hydrothermal fluids percolating along structural pathways. Recently, geodynamic models of the Pyrenees and the south Aquitaine basin were revisited and updated to include the involvement of an Early Cretaceous rifting phase that evolved to extreme crustal thinning coupled with mantle exhumation. This event was followed by an inversion and the main Pyrenean convergence during the late Cretaceous and the Paleogene. This revised model highlights the possible impact of hydrothermal fluids on the diagenesis of petroleum reservoirs in the southern Aquitaine Basin. Given its complex geodynamic history and the abundance of subsurface data, the Aquitaine Basin serves as a natural laboratory to study how the structural evolution of the Pyrenean foreland domain influenced fluid circulation and eventually reservoir diagenesis. In this context a reexamination of the diagenetic evolution of these reservoirs must be performed.

To document the possible control of this geologic history on the diagenesis of carbonate reservoirs, we study three drill cores penetrating the Upper Cretaceous (Upper Lacq) reservoirs and the Upper Jurassic

to Early Cretaceous (Deep Lacq) reservoirs. Petrographic observations, fluid inclusion studies coupled with thermodynamic modeling, isotopic and rare earth element geochemistry, as well as basin modeling were performed to investigate and describe the fluid types and sources, the pressure-temperature evolution and the timing of diagenetic fluid flow.

Our results indicate that in Upper Lacq, after shallow-marine carbonate deposition and early bacterial diagenesis during the Late Cretaceous, a mixture of marine fluids during reflux evaporation in a lagoonal setting, together with formational fluids allowed the precipitation of an early dolomite phase. Microthermometric and chemical evidence support a model with multiple fluid pulses driven by regional orogenic forces. After the deposition of the Paleocene seal, the Sainte Suzanne Fault, activated during the Eocene compression, could have provided a pathway for the circulation of deep connate hot fluids from the Southern Lacq Basin to the relatively cooler, lower pressure area on the crest of the Lacq anticline. This fault crosscuts the clay-rich Albo-Aptian formations (i.e. Sainte Suzanne and Assat marls), which, upon fracturing and squeezing, may have released Mg-rich fluids with low salinity. These fluids were responsible for hydrothermal dolomitization, as supported by clumped isotope thermometry indicate a dolomite crystallization temperature of 90°C, which is in thermal disequilibrium (>40°C) relative to the ambient burial temperature of 40-50°C. After the end of Mg expulsion from the Albian clays of the Southern Lacq Basin, due to modifications in regional tectonic stress, hot low-saline fluids continued to be squeezed out of this basin and towards Upper Lacq. The combination of the Mg-poor, hot, low salinity fluid from the Southern Lacq Basin and the oil that migrated from the Deep Lacq source rocks precipitated blocky calcites rich in oil and aqueous inclusions. These fluids circulated at temperatures ~90°C with salinities less than that of seawater. Fluid and basin modeling also indicate an Eocene timing for this fluid pulse, during the climax of the Pyrenean compression. The origin of oil in Upper Lacq is debatable given the complexities in the structural and thermal evolution of the petroleum system. However, the most probable scenario is a migration from the Deep Lacq source rocks passing through the Albian reefs. After calcite cementation, the remaining fluids became oversaturated with respect to sulphates and a minor phase of anhydride precipitated. The timing of anhydride precipitation is supported by the multiple sulfur isotopes that indicate an Eocene seawater signature of the parent fluid. Finally, during uplift, oxidizing fluids were laterally introduced as the present-day groundwater. Vertical input is unlikely given the integrity of the Paleocene

seal. This groundwater is slightly modified and enriched with $\delta^{18}\text{O}$, by around +2‰ SMOW relative to the global meteoric water line. This enrichment could be the result of fluid-rock interactions and possible contributions of $\delta^{18}\text{O}$ -enriched formation fluids

In Deep Lacq, diagenesis involved bacterial activity represented by micrite rims and framboidal pyrites. Mixing zone dolomitization in the marine phreatic zone precipitated an early phase of planar dolomites, enriched in $\delta^{18}\text{O}$ (up to +1.8‰PDB) and in $^{87}\text{Sr}/^{86}\text{Sr}$ relative to the Jurassic seawater which indicate precipitation from marine fluids with contribution from a meteoric water source. During the Aptian hyperextension, the climax of the heat flow with a geothermal gradient close to 70°C/km caused the source rocks to enter the oil window, while extensional fractures connected the Deep Lacq reservoirs with a pool of saline fluids, possibly of a Triassic origin, that precipitated the saddle dolomites. With salinities around 8.2 and 10.2 eq. wt.% NaCl. Mg was probably provided from clay minerals in the underlying Ammonite and Liassic Marls formations. During the Upper Cretaceous, changes in the stress regime linked to the onset of the N-S convergence created a new fracture set that changed the intensity of Mg expulsion from depth and allowed the circulation of fluids oversaturated with respect to Ca. The resulting fluids circulated at minimum temperatures of 100-140°C and salinities of 9-13.5 eq. wt.% NaCl. The $\delta^{13}\text{C}$ of these saddle dolomites and calcites are slightly enriched, reaching up to +5‰PDB, which indicate a possible mixing with early organic carbon, preserved after organic fermentation and methanogenesis during early burial. The enrichment of $^{87}\text{Sr}/^{86}\text{Sr}$ relative to the Jurassic seawater is indicative of interactions with marls. A third fracturing event was associated with the circulation of large volumes of sulphate rich fluids, having a Triassic signature, and which precipitated massive anhydrites immediately under the Aptian marls. The homogenization temperatures of the aqueous inclusions are in the range of 90-120°C and salinities of 4-6 eq. wt.% NaCl. Multiple sulfur isotopes obtained from these anhydrites suggest a possible connection to the Triassic and its mixture of the deeply sourced with the Barremian formation fluids. These anhydrites are cross-cut by tectonic stylolite related to the Eocene Pyrenean compression thus placing an upper age constraint on these fluids. The absence of gas inclusions in the studied phases indicate that gas charging in Deep Lacq occurred after cementation and is suggested to be during the post-orogeny.

To understand and synthesize the geodynamic history and its impact on reservoir diagenesis, the main diagenetic fluids that circulated at similar ages in the Chaînons Béarnais and the Rousse field are compared to this study. During the Liassic to Dogger, oxidizing fluids in the eogeneitic realm precipitated an early phase of non-ferroan and non-luminescent calcites in the Chaînons Béarnais while in Rousse, the primary dolomites of Mano, whose origin are still debatable were formed. In Deep Lacq, eogenesis was marked by mixing zone dolomites dolomitization followed by early, zoned calcites during gradual transition towards mesogenesis.

During the Aptian hyperextension, magmatic to mantellic fluids precipitated phases of dolomite and chlorite in fractures within the Jurassic formations, with fluid temperatures reaching up to 350°C and salinities of >25% NaCl at the Chaînons Béarnais. At the same time, in Rousse, dolomitizing fluids circulated at temperatures of 147°C to 167°C with low salinities. Similarly, Deep Lacq experienced saddle dolomite precipitation upon entrance to the oil window. In the Chaînons Béarnais and Rousse however, the proximity of the exhumed mantle bodies in the south and intense fluid-mantle interactions are the source of Mg for the dolomitizing hot fluids. Fluids likely circulated along corridors along the North Pyrenean Frontal Thrust with a temperature gradient decreasing northward from 350 to 150°C. The high salinities of the dolomitizing fluids in the Chaînons Béarnais were attributed to the leaching of the Triassic evaporites during the upward migration of the magmatic fluids, while the low salinities in Rousse were explained by downward migration of meteoric fluids mixed with upward moving serpentinization and clay-released low-salinity fluids. In Deep Lacq, the dolomitizing fluids have a temperature range between 140-165°C with salinities higher (8-10 eq. wt.%) than in the Rousse field, but lower than in the Chaînons Béarnais. These dolomitizing fluids are here considered as a mixture of Triassic-sourced fluids with the Mg mainly supplied by the “Liassic Marls” and the “Ammonite Marls” formation. The similarity in the fluid temperature ranges between Lacq and Rousse reinforce the notion of decreasing temperature gradient away from the hyperextended domain. Mg sources in the Deep Lacq differ than those in Rousse and Chaînons Béarnais given that there is no evidence of serpentinization or mantellic-derived fluids were identified. Similarly, salinities differ from one location to another and depend on the local geology (i.e. presence of unconformity and vertical fluid inputs), proximity to the Triassic salt domes (absent in Rousse) and the exhumed mantle bodies (only in the Chaînons Béarnais).

The fluids that precipitated the post-dolomite calcite in the Chaînons Béarnais circulated at temperatures close to 220°C between the Late Albian to Cenomanian. The salinity of these fluids is lower than the saddle dolomite (15 eq. wt/% NaCl) and were considered as the product of a mixed marine to magmatic fluid source. In Rouse, fluids that circulated during the Albian (105 Ma) had temperatures of 145°C with salinities less than that of seawater. The fluid were gas rich sourced from a mixture of the residual dolomitizing fluids and those of meteoric origin that percolated through the base Cenomanian unconformity. In Deep Lacq, two populations of aqueous inclusions reach an average temperature of 135-140°C, similar to what is recorded in the calcites of Rouse, but the salinities are higher, with 9-14 eq. wt.% NaCl. The fluids here are assumed to be derived from a saline Triassic source. During the Upper Cretaceous, after the Upper Lacq reservoir was formed, diagenesis was dominated by early reflux dolomitization with Mg sourced from evaporated seawater as well as the interstitial formation fluids.

During the Eocene maximum compression, tectonic stylolites developed in the Chaînons Béarnais and Deep Lacq while brecciation and calcite cementation were recorded in Rouse, with high salinities due to upward moving basinal brines. The timing of the telogenetic calcites in the Chaînons Béarnais were not conclusively identified and may also be during the Eocene compression. This compression episode was the major event that controlled the diagenesis of Upper Lacq due to the orogeny-driven hydrothermal dolomitization, followed by calcite and anhydrite cementation. The final anhydrites also precipitated, possibly during the same time, in large volumes in Deep Lacq.

Post-orogenic events were similar in Lacq and Rouse and involved the input of hydrocarbons in commercial quantities in the reservoirs. In the Chaînons Béarnais, the proximity of the exhumed mantle domains made the area too hot to be an economically viable petroleum reservoir.

Therefore, it is evident that the overall geodynamic setting, namely the Aptian thermal anomaly had a significant control on temperature of the diagenetic fluids that circulated in the studied area, but the compositions and salinities were more influenced by local geologic settings in the compartmentalized sub-basins, rather than large scale basinal fluid flows.

INTRODUCTION

General Overview

1. Scientific context

The geodynamic evolution of a foreland basin, behind a hyperextended rift system can influence the types, sources, chemistries and P-T conditions of diagenetic fluids. Such a setting is comparable to the Pyrenees mountain chain and its foreland basins, which, given the accessibility of the basement and the overlying sedimentary cover, provide an excellent case studies to investigate fluid flow and the associated impact of the geodynamic events. Several studies have explained the evolution of the Pyrenees and its foreland basin through a multiphase extension-compression system. The geodynamic models involve Early Cretaceous hyperextension with crustal thinning coupled with mantle exhumation and high temperature – low pressure metamorphism before being inverted and compressed through an orogenic phase during the Paleogene (e.g. Corre et al., 2018; Jammes et al., 2010, 2009; Lagabrielle et al., 2010; Teixell et al., 2016; Vacherat et al., 2016). With this updated view, internal reports in TOTAL (Calasou et al., in prep) highlighted the distribution of unusually high maturities recorded by vitrinite values reaching up to +4% Ro% along major faults zones, while normal burial trend were recoded with depths in the studied wells (Calasou et al., in prep). These anomalous maturities were explained by the possible impact of mantle-related and/or deeply sourced fluids. It is in this framework that two main inter-laboratory/ university projects across France were launched and funded by TOTAL. These are the OROGEN and FLUIDS projects. OROGEN aims to study the behavior and mode and mantle exhumation, age and intensity of the thermal anomalies as well as the source to sink (S2S) investigations. The FLUIDS projects, in which this current PhD project is part of, aims to study fluid-rock interaction and the fluid circulation schemes in the inverted-hyperextended rift system. Recently, certain studies were carried out in the Pyrenean foothills and its foreland basin to investigate how deeply sourced hydrothermal fluids would play an important role in the diagenesis of petroleum reservoirs. For example, in the Chaînons Béarnais, hydrothermal dolomitization in the Jurassic-early cretaceous carbonates was triggered during the extensional phase as a consequence of mantle exhumation (Salardon et al., 2017). Similarly, Renard et al. (2019) revealed two periods of fluids circulations that controlled the diagenesis of the Rousse reservoirs; the first hydrothermal fluid pulse was during the rifting stage, while the second was during the Pyrenean orogenic phase. However, this hydrothermal activity and its impact on the

Lacq petroleum system, once considered the largest and most strategic in France (Biteau et al., 2006) has never been documented so far. The diagenetic models are still poorly understood and do not take into account the recent revisiting and reappraisal of the geology of the Pyrenees and the Aquitaine foreland basin. The objective of this study is the reconciliation of diagenesis and geodynamics in the North-West Pyrenees.

Direct investigation of the fluids involved in diagenesis can be achieved by analyzing the fluids trapped as inclusions inside crystals of diagenetic cements. This technique, known as fluids inclusions microthermometry, is one of the most popular and commonly used non-destructive analytical technique (Shepherd et al., 1985). The concept of this tool relies on careful recognition and observation of phase transitions between liquid, solid and/or gas, which occur during heating and/or cooling of the sample. With reference to simplified multi-component equilibrium phase diagrams of fluid systems, a semi-quantitative assessment of the *PVTX* states of the fluids, at the time of trapping, can be achieved (Shepherd et al., 1985). Isotope geochemistry is necessary in such studies to understand fluid-rock interactions, and the sources and origins of diagenetic fluids. When coupled with basin and structural analysis, the trapping conditions of the fluids can be correlated with the geological history of the studied area. The latter can be used to put these diagenetic events in a timeframe and to justify the types, sources and migration pathways of fluids involved. For example, Travé et al. (2014) studied three regions of the South-Pyrenean fold-and-thrust belt and showed how fluid events and fluid sources evolved according to the activity of the L'Escala thrust in the eastern Catalan basin. Similarly, to explain the low values of porosity and permeability in the middle Jurassic carbonates of the Paris Basin, Brigaud et al., (2009) linked the uplift and exposure events during the Cimmerian and late Aptian to the lateral input of meteoric fluids which have resulted in widespread calcite cementation. They also concluded that the fracture-related dolomites were coupled to hydrothermal fluids circulations in the Late Oligocene extensional phase. Similarly, Carpentier et al. (2014) linked the evolution of different calcite and dolomite phases and their geochemical signatures to the burial and exhumation history of the Jurassic carbonates in the Paris Basin, NE France. Also, Haile et al. (2018) demonstrated how the emplacement of a dolerite sill triggered hydrothermal diagenesis in the Triassic – Jurassic sediments in Svalbard, Norway.

Hence, using a multitude of petrographic, geochemical and modeling tools, diagenetic systems and fluid circulation events can be placed in the structural framework of basins to further assist the geologist in identifying the fluids involved and to better predict their impact on reservoir properties.

2. Research objectives

It is necessary to understand how the diagenesis of the Lacq reservoirs evolved during the geodynamic evolution of the basin. To do so, the following objectives have to be completed:

1. Updating the paragenetic sequence of the Upper Cretaceous and Jurassic-Barremian reservoirs of the Lacq petroleum system.
2. Understand the impact of mantle exhumation and hydrothermal fluids on reservoir diagenesis.
3. Assessing whether the original depositional system controlled reservoir properties or the fluids resulting from hyper-extension and/or compression or the combined contribution of both.
4. Determining the pressure-temperature conditions under which the fluids have circulated and consequently the sources and migration pathways.
5. Put the obtained model in the context of the evolution of the Pyrenees and the foreland basin.
6. Linking the studied fluids to fluids recognized in other parts of the basin, i.e. Chaînons Béarnais and in Rousse reservoirs

This research study is part of the FLUIDS project at TOTAL in collaboration with a multitude of labs and universities.

3. Thesis organization

This thesis manuscript is organized in 6 chapters. Chapter 1 presents the state of the art in the understanding of the geologic setting and evolution of the Aquitaine basin. Then the lithostratigraphy of Lacq is presented as well as the elements of the petroleum systems in the Aquitaine basin. The previous diagenetic models are also presented and will be compared later in the manuscript with results obtained in the present study. Chapter 2 focuses on the methods and techniques utilized to reach the research objectives. The methods involve the sampling strategy, petrography, geochemistry, fluid inclusions analyzes and the different modeling techniques employed. Chapter 3 focuses on the Upper Lacq reservoirs

General Overview - Thesis organization

and is in turn subdivided into 3 parts : results, discussions and conclusions. Similarly, chapter 4 deals with Deep Lacq and has the same subdivisions. The synthesis of both reservoir and an overall view of the Lacq Petroleum System are discussed in chapter 5. The main conclusions are then outlined in chapter 6. In the final chapter, perspectives and future ideas are presented.

Chapter 1: State of the art

Chapter 1: State of the art

1. Carbonate diagenesis

Diagenetic studies and analyses of fluid-rock interactions constitute an important aspect for petroleum geologists to develop conceptual models that help in anticipating reservoir properties (Moore, 2013). These models should take into account the chemical signatures of the fluids, the pressure-temperature conditions of their circulation and the suitable environmental framework under which fluid-rock interactions took place. To this end, a multitude of petrographic, geochemical and modeling tools are available. Petrographic cross-cutting relationships between different phases and events allow the geologist to construct a paragenetic sequence that highlights the relative timing of events. The main diagenetic realms are classified into 3 systems described as follows:

1. *Eogenesis*

Known as near-surface diagenesis, eogenesis encompasses the diagenetic modifications between the deposition of sediments and their burial, in the domain where surface related processes and fluid migrations can still be active. In terms of depth, eogenesis extends to the depth where marine to meteoric waters cease to circulate by gravity or convection (Flügel, 2004).

2. *Mesogenesis*

Also known as burial diagenesis, mesogenesis is characterized by the modifications brought about via formation fluids which could be one or a mixture of connate, marine, meteoric, magmatic and/or basin-derived brines. It is commonly accompanied by porosity reduction due to compaction and burial (Choquette and Pray, 1970). In this domain the fluid chemistry is generally modified by interaction (dissolution vs precipitation) with the host rock.

3. *Telogenesis*

Sometimes labelled as unconformity-related diagenesis, telogenesis refers to the domain when buried carbonates are exhumed, uplifted and affected by surface-related meteoric fluids and/or processes (Flügel, 2004).

Using these categories in diagenetic studies provide a qualitative assessment of the timing and context of fluid flow and fluid-rock interactions

2. Dolomitization

Dolomite is commonly found in almost every diagenetic setting with ages ranging from Precambrian to the recent (Machel, 2004). About 50% of the world's carbonate reservoirs are dolomites and 80% of the oil and gas of North America are produced from dolomitic carbonates (Warren, 2000; Zengler et al., 1980). However, despite extensive and thorough research since 200 years, the origin of dolomites remains controversial given the poor understanding of the chemical and hydrogeological conditions of their formation (Machel, 2004). Since the 1950s, several dolomitization models have been proposed to explain the various types and origins of dolomites. To avoid ambiguities and to clearly differentiate models and interpretations, Machel (2004) determined three specific criteria required for dolomitization. These are:

1. Thermodynamics: dolomitizing fluids need to be supersaturated with respect to dolomite relative to calcite and/or aragonite. Otherwise the product would be calcite or aragonite cementation. Even if the fluids are diluted marine waters, Mg enrichment is necessary.
2. Kinetics: the rate of dolomitization must be higher than the rate of calcium carbonate dissolution, to prevent significant porosity creation and karstification.
3. Hydrology: a suitable fluid delivery mechanism is necessary to transport the required amounts of Mg.

Precipitating dolomite from a Mg-source requires the following reaction to occur (Warren 2000):

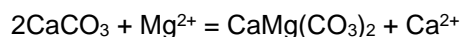


With an equilibrium constant K defined by:

$$K = \frac{[\text{Ca}^{2+}][\text{Mg}^{2+}][\text{CO}_3^{2-}]^2}{[\text{CaMg}(\text{CO}_3)_2]}$$

where the parentheses [] indicate activities of the dissolved and solid species.

Similarly, Hsu (1967) defined an equation for the dolomitization of a limestone precursor by modern seawater with the following reaction:



The most common models used to explain dolomitization are summarized as follows:

(i) Reflux models: the evaporative reflux model involves hypersaline seawater in lagoonal and shallow-marine carbonate platforms enclosed behind a sill. Due to its increased density, the evaporated water would percolate downwards and dolomitize the underlying sediments of the platform down to a depth of 3km (Jones, 2000; Machel 2004). Warren (2000) explains that when CaCO_3 and CaSO_4 precipitated in hypersaline areas, the Mg/Ca ratios and salinities of the remaining brines would increase. These dense brines would then mix with or displace subsurface fluids that were originally marine-derived waters. Drawdown basins have the potential to flush huge volumes of waters through the basin edge as waters in the basin center are lost by evaporation (Warren, 2000). These waters are continuously replaced via the seepage influx of varying proportions of: (a) phreatic seawater seeping in through the basin edge; (b) subsurface waters whose lateral movement to the basin floor is driven by the kilometer-scale drawdown of the water level in the basin; and (c) by much smaller and episodic influxes of meteoric (Warren, 2000). In this way, large volumes of Mg-rich brine pass through previously deposited shelf limestones and precipitate dolomite, both as a pore fill and as a replacement phase. This continuously replenished hydrology of descending evaporitic creates a brine curtain with a subsurface chemistry capable of leaching calcite and precipitating dolomite (Land, 1985; Warren, 2000). Trace elements as Na and Sr tend to decrease away from the source of the refluxing brine (Warren, 2000). Examples of reflux dolomites can be found in the Permian Basin of west Texas and New Mexico (Adams and Rhodes, 1960) and in the Pekelmeer Lagoon, Bonaire island, Netherlands Antilles (Deffeyes et al., 1965).

(ii) The Sabkha model can be coeval with reflux dolomitization but is specific to intertidal-supratidal platforms that are episodically flooded (Machel, 2004). Dolomitization occurs few centimeters below the surface of emerged supratidal flats where meteoric and marine groundwaters are mixing. Sabkha dolomites are syndepositional, thin (1-2 m thick), stratiform, micritic, mimetic and co-precipitating with nodular evaporites (Warren, 2000). To help in discriminating and identifying the products of this model, Warren

(2000) highlights that the top of the dolomite should lie beneath a widespread subaqueous evaporite horizon or a dissolution breccia with a former evaporite horizon. The intensity of dolomitization typically decreases downward or away from the former evaporite layer or the source of the refluxing brine. Positive $\delta^{18}\text{O}$, and elevated Sr and Na are common in sabkha dolomites (Warren, 2000).

(iii) Hyposaline and the mixing zone model: hyposaline environments are those with salinities lower than that of seawater, such as coastal and inland freshwater-seawater mixing zones, marshes, lakes, rivers and caves (Machel, 2004). The diagenetic settings are near-surface to shallow-burial with maximum depths of 1000m. It is worth noting that although the waters in mixing zone or dorag dolomitization models are thermodynamically supersaturated with respect to dolomite, these fluids tend also to be oversaturated with respect to calcite and/or aragonite, thus the window of dolomitization tend to be small (Machel, 2004). This dolomitization window involves calcite undersaturation and dissolution relative to dolomite oversaturation and precipitation. Warren (2000) explain that if saturated meteoric groundwater were diluted by seawater, they would maintain the same Mg/Ca ratio but, because of the lowered ionic strength, the lowered concentrations of sulfate, and the increased proportion of carbonate over bicarbonate in the solution, dolomite would precipitate. The resultant texture should show evidence of calcite dissolution and dolomite precipitation. Mg would be derived mainly from the seawater, but some can also come from the carbonates dissolved in the mixing-zone (Warren, 2000). In regards to the hydrologic setting, the formation of extensive shelf dolomites by diluted waters of a meteoric-seawater mixing zone probably requires a more stable hydrology along a shelf. Unless affected by later diagenesis, the isotopic values tend to parallel the meteoric calcites, with a slight offset to more positive values due to dolomitization, while trace elements like Na and Sr tend to be elevated (Warren, 2000). An example of mixing zone dolomites was described in the Pleistocene Hope Gate Formation, Jamaica (Land, 1973).

(iv) Seawater dolomitization models: these refer to a group of models where the main dolomitizing fluid is seawater. In this sense, seawater dolomitization is not an independent model *sensu stricto* (Machel, 2004). Seawater is the most common natural Mg-rich fluid, which when pumped deeper through carbonates, the kinetic barriers of dolomitization are reduced (Land, 1985). Seawater dolomites are classified as post-depositional, formed during shallow to intermediate burial diagenesis. Fluid flow systems that are involved in seawater dolomitization models can include thermal convection, thermal seawater

convection with reflux of overlying evaporated seawater, fluid flow from an overlying freshwater-seawater mixing zone during platform exposure (Machel, 2004 and references therein). The Devonian dolostones of Alberta Canada (Mountjoy et al., 1999) and the Carboniferous dolomites of Ireland (Gregg et al., 2001) are examples of seawater dolomites with multiple fluid flow schemes involved.

(v) Burial model: during compaction, seawater or its subsurface derivatives are expelled upward through the sediments, triggering limited dolomitization along the channels (funnels) of escaping (dewatering) dolomitization fluids. Mg rich fluids can be provided from chemical reworking and recrystallization of nearby or earlier dolomites, from structural Mg^{2+} expelled during clay dehydration reactions, e.g. montmorillonite-to-illite and smectite-to-illite transformation, and from the deep subsurface dissolution of Mg-rich salts (e.g. canalite $\text{K}_2\text{MgCl}_3 \cdot 6\text{H}_2\text{O}$, polyhalite $\text{K}_2\text{MgCa}_2(\text{SO}_4)_4 \cdot \text{H}_2\text{O}$, and kieserite $\text{MgSO}_4 \cdot \text{H}_2\text{O}$) (Warren, 2000). Compaction, thermo-density convection and tectonically-driven dolomitization models are essentially subtypes of burial models, having similar Mg sources, but differ mainly in the hydrology driving and directing fluid flow (Machel, 2004). Combinations of these flow regimes and fluids are possible under certain circumstances. The potential for moving larger volumes of Mg-rich basinal fluids through a platform margin is greater in a basin undergoing collision compression, especially if the basin also contains thick dissolving salt sequences (Warren, 2000). Resulting dolomites tend to be nonplanar with saddle morphologies, while oxygen isotopes are usually depleted, indicating precipitation at elevated temperatures. Fe and Mn may be elevated due to the reducing conditions that are typical of burial diagenesis, while trace elements such as Sr and Na after successive episodes of dolomitization have reduced the levels of these elements even further (Warren, 2000). The Silurian reefs of Michigan (Jodry, 1968) and the Upper Devonian dolomitized reefs of Alberta (Machel and Anderson, 1989) were partly explained by such a model.

(vi) Thermo-density convection: Changes in temperatures, and consequently in density, of the pore-water result in a thermal convection that influences the effective hydraulic head (Machel, 2004). Lateral temperature variations can be induced by igneous intrusions (Wilson et al., 1990), contact between open and confined water bodies (Kouhout et al., 1977) and thermal conductivity variations of different lithologies (Tucker and Wright, 1990; Moore, 2013). Open convection cells, according to Machel (2004) scheme, are those formed in carbonate platforms that are open to seawater recharge/discharge laterally and vertically.

An important parameter that controls dolomitization in this model is the occurrence of a good and homogeneous permeability of the host rocks (Wilson et al., 2001). Such models can be active at depths of 0.5-2 km with minimum ambient temperatures of 50-60°C (Machel, 2004). Temperatures cooler than 50°C would limit dolomitization, while depths greater than 2 km would reduce permeability and consequently fluid flow. Closed-cell thermal convection can also occur in sedimentary basins over tens to hundreds of meters thickness, on the condition that the sequence is considerably thick, highly permeable, not interbedded with aquitards and the temperature gradient is high enough relative the permeability of the strata (Machel, 2004). Dolomites in such circulatory systems tend to precipitate within permeable aquifers fed from deep foreereef and rise sediments, with a low Mg/Ca ratio and heavy ^{18}O and ^{13}C (Warren, 2000). An example of thermo-density dolomitization model can be found in the core of the Tertiary-Pleistocene carbonates of the Bahamas Platform (Simms, 1984).

(vii) Tectonic (squeegee) model: In this model, deeply buried fluids are expelled from crustal levels affected by tectonics towards the margin of the basins (Machel, 2004). In sedimentary basins, long-range orogeny-driven fluid flow scenarios can be governed either by intrinsic permeability where fluids infiltrate pervasively along grain boundaries and microcracks in a rock, or by hydraulic permeability where fluids flow along major cracks that are sufficiently interconnected to allow a distinct fluid channel to develop (Robb, 2005). At deeper levels in the crust, since the reduction of porosity makes it difficult for fluids to move by intrinsic permeability, channelized flow along deformation-related faults and fractures become more dominant. Such a model is commonly short-lived and episodic but often involves substantial pore-water flow. The difference in temperatures between the deeply buried fluids and their destination results can hydrothermal dolomites (Machel, 2004). This model has been invoked to explain the dolomitization of the Ordovician carbonates in the thrust sheets of the southern Appalachians (Montanez and Read, 1992).

(viii) Hydrothermal dolomitization: This is not an independent model because hydrothermal conditions may occur in different situations across several types of diagenetic settings. Machel (2004) explains that convection cells could supply hot fluids to the overlying cooler strata, thus linking thermal convection to hydrothermal dolomitization. It is important to note that the term “hydrothermal” can be used to describe a mineral only if it formed at temperatures 5-10°C higher than the ambient temperatures (Machel and Lonnee, 2002; White, 1957). Hydrothermal dolomites tend to be fabric-obliterative (Machel, 2004) with ^{18}O isotope

depleted due to thermal fractionation at elevated temperatures (Warren, 2000). Zebra dolomites, a common product of hydrothermal dolomitization, are characterized by a repetition of mm-scale dark grey and light colored dolomite sheets that form from focalized fluid flow of hot saline fluids under an overpressure regime with syn-fracturing dolomitization. Examples of hydrothermal dolomites can be found in the late Variscan of Sardinia (SW, Italy) (Boni et al., 2000), in the Albian carbonates of the Ason valley, Basque Cantabrian Basin, Northern Spain (López-Horgue et al., 2010) and in the Upper Carboniferous carbonates of the southwestern Variscan Cantabrian Zone (Spain) (Gasparrini et al., 2006). Zebra dolomites can be found in the in the Brabant-Wales Massif, Belgium (Nielsen et al., 1998) and in the Middle Cambrian Cathedral Formation: British Columbia, Canada (Swennen et al., 2003).

A summary of the dolomitization models, the sources of Mg, hydrological mechanisms and expected dolomite geobodies is compiled in table 1.

Table 1. Summary of main dolomitization models, sources of Mg and hydrological schemes. Compiled from Warren (2000) and Machel (2004).

Dolomitization model	Model's scale	Source of Mg ²⁺	Delivery Mechanism	Hydrological model	Predicted dolomite pattern
Reflux	Kilometer-scale	Seawater	Storm recharge, evaporative pumping, density-driven flow		
Mixing zone (Dorag)	Kilometer-scale	Seawater	Tidal pumping		
Seawater	Kilometer-scale	Normal seawater	Slope convection ($K_v > K_h$)		
Seawater	Kilometer-scale	Normal seawater	Slope convection ($K_h > K_v$)		
Burial (local scale)	Kilometer-scale	Basinal shales	Compaction-driven flow		
Burial (regional scale)	Basin-scale	Various subsurface fluids	Tectonic expulsion, topography-driven flow		
Burial (regional scale)	Basin-scale	Various subsurface fluids	Thermo-density convection		
Burial (local and regional scale)	Kilometer-scale	Various subsurface fluids	Tectonic reactivation of faults (seismic pumping)		

Extensive revisions with explanations regarding each dolomitization model, its mass balance consideration, thermodynamics, kinetics and hydrological schemes can be found in Sibley and Gregg (1987), Tucker and Wright (1990), Wilson et al. (1990), Amthor et al. (1993), Warren (2000), Swennen et al. (2003), Machel (2004) and Moore (2013).

3. Regional Geodynamic History

The evolution and genesis of the Aquitaine basin is closely linked to the geodynamics of the Pyrenees and the interaction between plate boundaries. Several rifting and collision episodes succeeded each other and resulted in the present-day structural configuration (Fig. 1) (Biteau et al., 2006; Jammes et al., 2010b, 2009; Masini et al., 2014; Teixell et al., 2016).

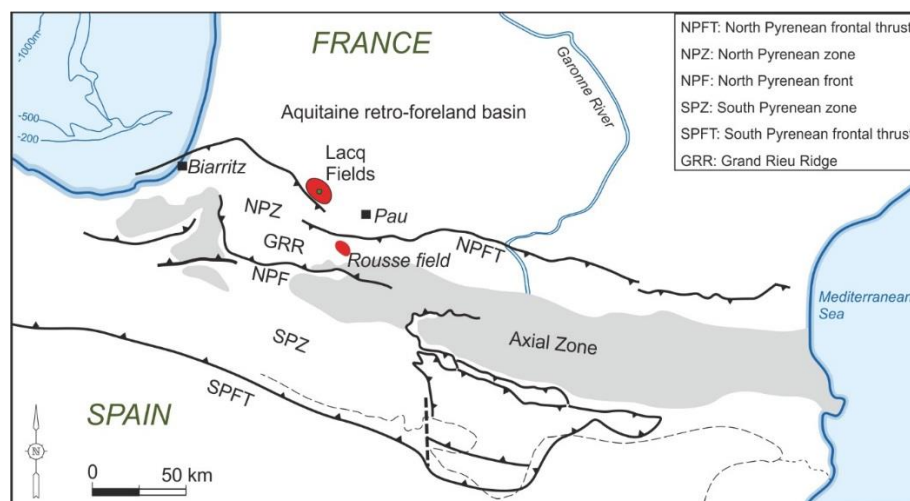


Figure 1. Simplified map of the main structural domains in the Pyrenean domain (Modified after Biteau et al., 2006). The Variscan orogeny since the Ordovician-Silurian till the Permian was due to plate convergence between Gondwana and Laurussia that followed an initial extension during the Cambro-Ordovician (Kroner and Romer, 2013). During the Permian, plate reorganization and extension resulted in the creation of the Northern and Southern Permian basins with massive magmatism and high temperature metamorphism (Schuster and Stüwe, 2008) (Fig. 2). This high-temperature rift-related anomaly affected the lower crust and exhumed the crystalline complexes of the Alps (Delfaud et al., 1980). This event was coupled with an

orogenic collapse and the previously erected relief from the Hercynian orogeny was eroded and flat plain was created (Delfaud and Gautier, 1967; Curnelle and Dubois, 1986).

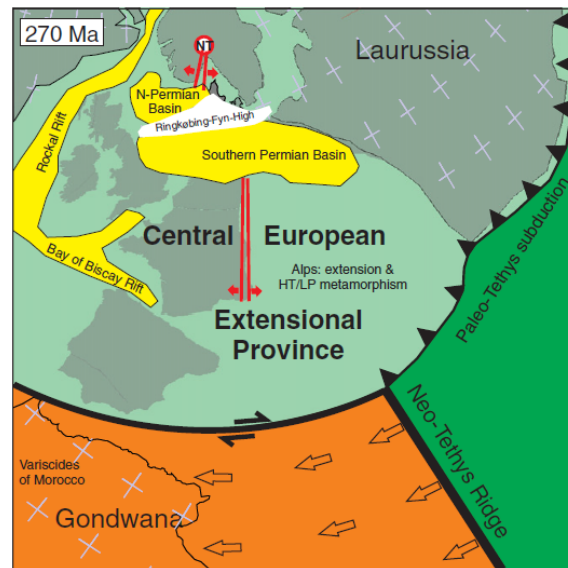


Figure 2. Plate tectonic scenario for the middle Permian (Kroner and Romer, 2013)

Triassic to Jurassic times marked the onset of continental rifting between the European and Iberian plates associated with the breakup of Pangea (Jammes et al., 2010a). Between the Upper Jurassic and Lower Cretaceous, it is generally accepted that 300-500 km of sinistral (left-lateral) motion must have occurred along the Pyrenean domain (Fig. 3a). Deformation between the two plates in the western Pyrenean domain was mostly accommodated by wide transtensional components (Fig. 3b) (Jammes et al., 2010a). At that time, the Aquitaine Basin was a wide intracontinental platform that got tectonically broken up into two subsiding basins: the Arzacq–Tarbes and Parentis subsiding depocentres (Bilotte et al., 2001; Biteau et al., 2006).

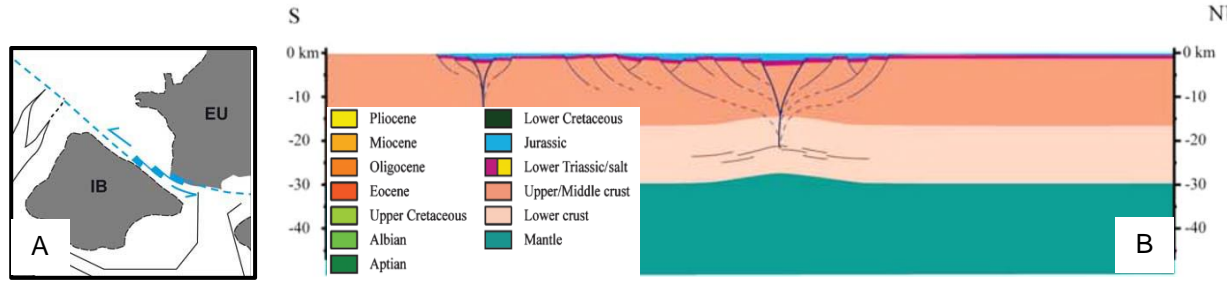


Figure 3. A: plate kinematic scenario showing the wide transtensional corridor with a dominant strike slip-slip component between the Iberian (IB) and European (EU) plates. B: schematic cross-section showing the formation of multiple flower-structure basins (Jammes et al., 2010a).

During the Neocomian, plate reorganization and regional mantle doming coupled, together with a major seawater regression caused an erosional unconformity that produced Bauxites in the axial zones (Masini et al., 2014; Salardon et al., 2017) while a condensed karstic horizon is observed in the Aquitaine area (Bilotte et al., 2001).

Aptian-Albian times were marked by rifting between the European and Iberian plates, as the latter started rotating away from the European plate. Plate motions change from the strike-slip dominated to more orthogonal extension (Fig. 4a) with hyperextension, mantle exhumation and high temperature-low pressure metamorphism (Clerc et al., 2015; Clerc and Lagabriele, 2014; Jammes et al., 2010a; Lagabriele et al., 2010; Vacherat et al., 2016, 2014). The Bay of Biscay began to open and a regional sagging was coupled to tilting of the European basement blocks (Fig. 4b) (Bilotte et al., 2001; Roca et al., 2011). Due to this increased subsidence and sediment overload, Triassic evaporites migrated towards the basin margins (Arzacq and Parentis) and salt ridges were formed (Biteau et al., 2006).

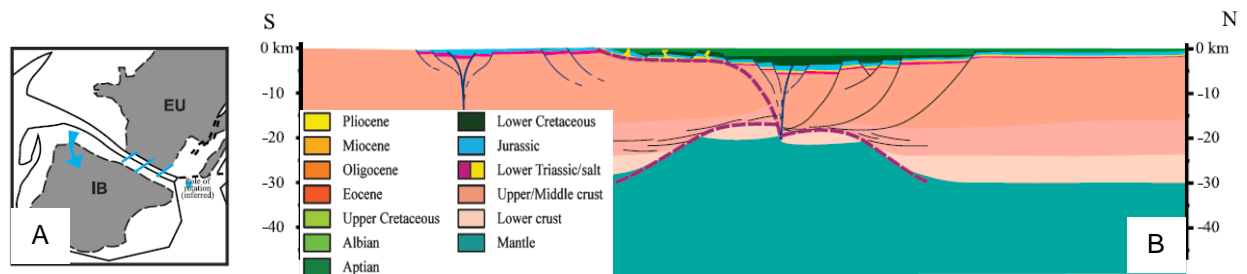


Figure 4. A: plate kinematic scenario showing the counter-clockwise rotation of IB relative to EU causing orthogonal extension in the western Pyrenees B: asymmetric thinning coupled with regional sagging and deepening of the basins coupled with the thick cover of the Sainte Suzanne marls (Jammes et al., 2010a).

Mid-Albian to Cenomanian witnessed post-rift isostatic rebound coupled with alkaline magmatism under the Grand Rieu Ridge (Fig. 1) causing uplift and erosion and resulting in the base Cenomanian unconformity (Biteau et al., 2006; Masini et al., 2014).

Between the Cenomanian and Santonian, post-rift thermal cooling increased the density of the crust which wtriggered a phase of thermal subsidence (Ford et al., 2016).

By the mid-Santonian, the earliest stages of the Pyrenean convergence were recorded and involved the closure of the exhumed mantle domain (Fig. 5) (Clerc et al., 2015; Teixell et al., 2016). Early Cretaceous rift-related faults were inverted with sedimentary covers getting detached and thrust as pop-ups along major thrust faults (Teixell et al., 2016).

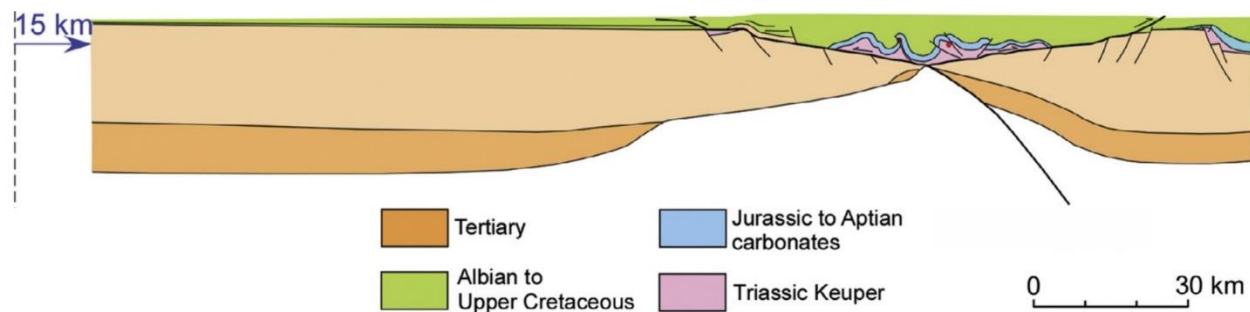


Figure 5. Early stage of Pyrenean convergence (Teixell et al., 2016).

Mid-Eocene times corresponded to the collision climax of the Iberian and European margins (Jammes et al., 2010a; Corre et al., 2016; Teixell et al., 2016). This collision was accommodated by the overriding of the Iberian plate on top of the European margin along the deep ramp of the North Pyrenean Frontal Thrust (NPFT) (Teixell et al., 2016). This juxtaposition of the plates allowed the continental crust to recover its normal thickness which could explain the temperature drop in the northern Pyrenees (Vacherat et al., 2014).

The protocollision stage evolved during the Late Eocene to full-collision deformation in the form of thick-skinned thrust accretion of the Iberian shelf basement (Jammes et al., 2010c; Teixell et al., 2016). Anticlinal structures of the axial zone (Figs. 1 and 6) were uplifted by the piggy-back sequence of thrust propagation in the Iberian plate. This basement thrust sequence is the cause of the strong structural relief and the root of the present-day topography (Teixell et al., 2016).

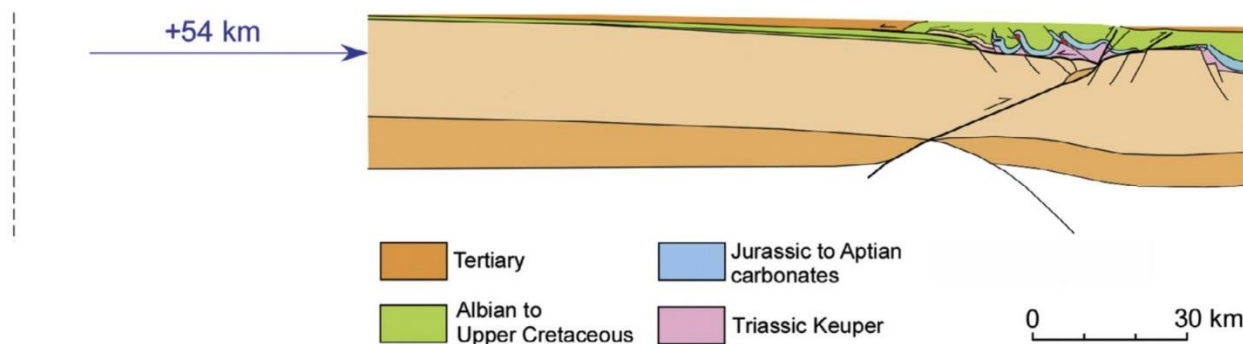


Figure 6. Protocollision stage expressed by overriding of the Iberian Plate on top of the European plate along the NPFT (Teixell et al., 2016).

Presently, the Arzacq basin extends over the European plate and shows a progressive crustal thinning from 25 km in the north to less than 20 km in the south (Masini et al., 2014). This thinning is the result of the increase in the Cretaceous extension southwards (Daignières et al., 1994). It is bounded to the south by a basement block called the Grand Rieu Ridge (Fig. 1). It serves as a topographic barrier between the Arzacq and the hyperextended Cretaceous Mauléon basin, formed over the Iberian plate to the south (Masini et al., 2014).

The axial zone further to the south (Fig. 1) corresponds to the southern border of the Mauléon basin which was affected by south-verging, thick skinned tectonic thrusting during the Eocene compression (Jammes et al., 2009; Masini et al., 2014).

In summary, several rifting phases since the Cambrian-Ordovician till the Albo-Aptian have left inherited structures that controlled and shaped the deformation during the rifting episodes. The culmination of these rift systems, followed by the Paleogene orogeny have resulted in the present-day Pyrenees elevated structures and the Aquitaine foreland basin.

4. Stratigraphy and sedimentology of the Lacq petroleum system

The Lacq petroleum system is one of the largest petroleum fields in the Arzacq sub-basin, within the Aquitaine (Fig. 7).

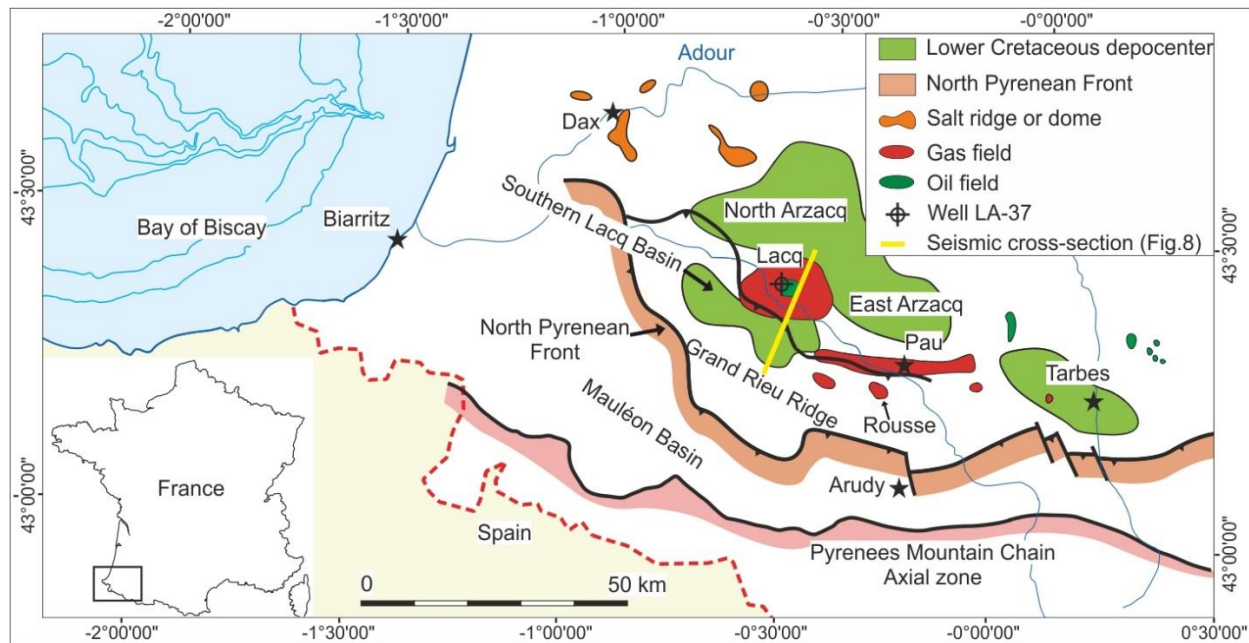


Figure 7. Simplified geologic map of the SW part of the Aquitaine basin, showing the structural elements and Cretaceous basins surrounding Lacq (modified after Biteau et al., 2006).

It is a salt-core anticlinal structure whose hinge line strike NW-SE (Fig. 8). It encompasses two economically important reservoirs. These are the 650m-deep Upper Cretaceous (Coniacian to Campanian) fractured dolomite reservoir (Upper Lacq, Fig. 8), which produces heavy oil and is sealed by the overlying Ypresian Flysch, and the 3700m-deep Jurassic to Barremian (Deep Lacq) carbonate reservoirs producing mainly dry gas capped by the overlying early Aptian Sainte Suzanne marls (Fig. 8) (Le Marrec et al., 1995).

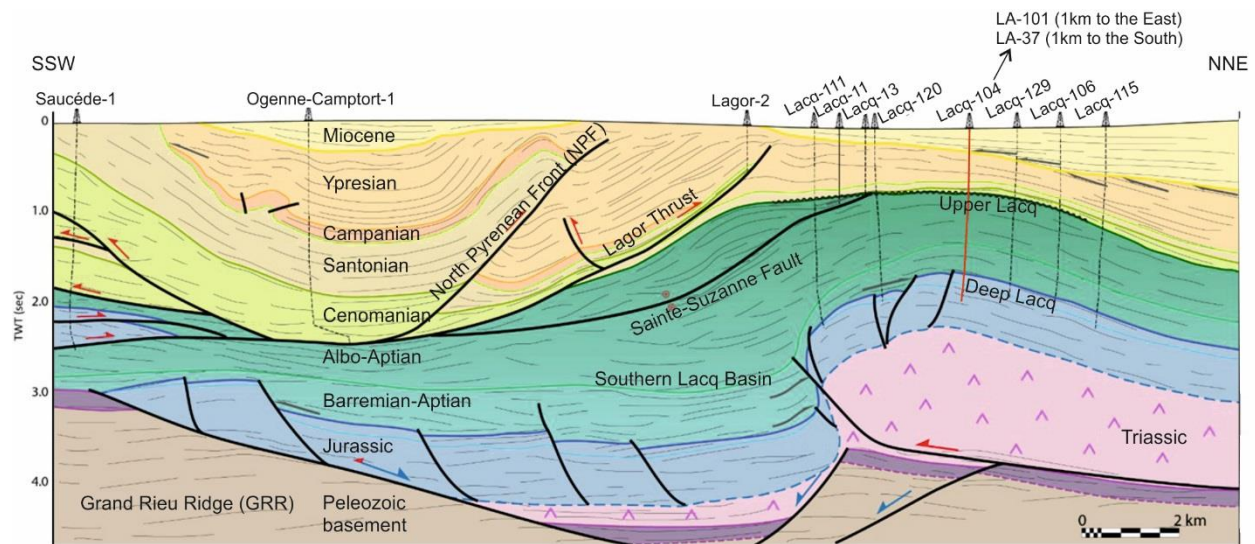


Figure 8. Interpreted NNE-SSW seismic cross-section through the Lacq structure in the Arzacq basin (See Figure 7 for location). Due to the lack of a reliable velocity model the vertical scale is in two-way time (TWT). For equivalent depth estimations, well LA-104 (red line), reaches a true vertical depth (TVD) of 4346 m.

The structural and sedimentary history of the Lacq area is closely linked to the evolution of the Aquitaine basin, whose architecture was partly inherited from the Variscan orogeny and later modified by the motion between Iberian and European plates (Bilotte et al., 2001). A lithostratigraphic summary with the main geologic events is compiled in figure 9.

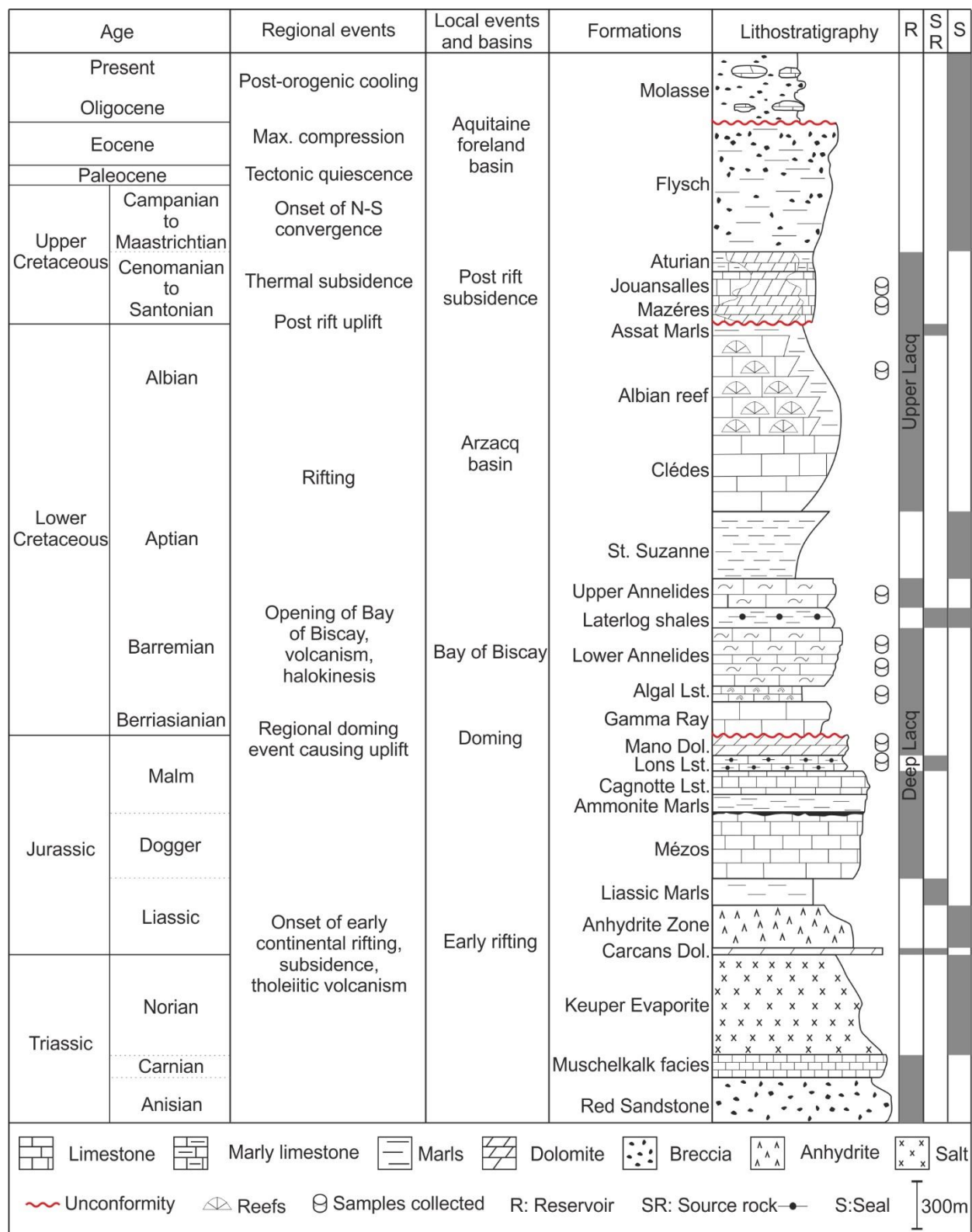


Figure 9. Lithostratigraphic column of the Arzacq and SW Aquitaine Basins including elements of the Lacq petroleum system and a summary of main geodynamic events, which impacted the area since the Triassic.

Basement strata consists of Cambrian to Devonian shales, silts, sandstone and minor limestone that are capped by Permian redbeds, andesites and volcano-clastic deposits (Beziat and Joron, 1986; Biteau et al., 2006). The core of the Lacq anticline consists of an evaporitic sequence divided into 3 members: (1) Keuper evaporites, (2) Muschelkalk carbonates and red shales and (3) Bunter red beds and sandstones (Curnelle et al., 1980). Early Liassic (Rhaetian-Hettangian) Carcans dolomite form a minor petroleum system sealed by the surrounding anhydrites (Canerot et al., 1990). During the Jurassic (Hettangian-Callovian) extensional regimes led to westward deepening of the carbonate shelf with Liassic limestones, shales, and marls and Dogger limestones and dolomites (Biteau et al., 2006). Oxfordian to Early Kimmeridgian extensional tectonics differentiated the platform into an inner shelf with Meillon dolomites and a more open marine setting with Ammonite marls towards the Adour sub-basin (Delfaud and Gautier, 1967). Middle to Upper Kimmeridgian times were characterized by a stable shelf environment along with local sediment condensation and syn-sedimentary halokinesis along basement faults (Curnelle et al., 1982). A basin-wide regression during the Late Portlandian triggers the precipitation of Mano dolomites in a restricted lagoon setting. This regression exposed the inner shelf to karstification and erosion giving rise to Garlin Breccia (Delfaud and Gautier, 1967). The Neocomian was a period of sea level lowstand followed by transgression, such that during the Berriasian, Ger Limestones were deposited in a lacustrine environment. Shaly to sandy deposits characterize the Gamma Ray formation to the west (Biteau et al., 2006). The opening of the Bay of Biscay during the Early Cretaceous resulted in (1) strong differentiation of the paleogeography, (2) shallow-marine transgression, (3) sea-level fluctuations and (4) halokinesis along basin edges (Choukroune et al., 1973; Deregnaucourt, 1981). Algal limestones with outer to inner shelf facies characterize the Hauterivian before emergence, karstification and salt movements during the Barremian (Canerot et al., 1992; Debroas and Souquet, 1976). This regression also resulted in a lacustrine and restricted evaporitic domains where Laterlog shales are deposited. By the end of the Barremian – Early Aptian, a general flooding of the shelf resulted in the Annelides Limestones formation (Canerot et al., 1992).

Major changes in the Lower Aptian correspond to coeval salt movement along the northern and southern edges of the basin. The basin also experienced accelerated subsidence, reactivation of basement-inherited faults, extrusion of salt diapirs and their replacement by surrounding sediments (Canerot et al., 1990, 2005; Biteau et al., 2006). Transgression during the Upper Aptian displaces Urgonian-type shelves towards the

south with increased growth of patch reefs along the shelf-basin transition (Masini et al., 2014). The growth of patch reefs persisted during the Albian along with minor clastic turbidites sourced from the east. By the end of the Albian, the tectonic regime changed to compression. This resulted in major changes in paleogeography, increased halokinesis, southern migration of subsiding areas, transgression in the north, uplift of the Lacq and Meillon domains and deposition of thick syn-tectonic sediments (Jammes et al., 2009; Puigdefabregas and Souquet, 1986). Cenomanian to Maastrichtian times are marked by a general transgression that covers the entire Aquitaine basin with shelf carbonates (Biteau et al., 2006). The carbonate section from the Aptian to the Cenomanian forms the Upper Lacq carbonate petroleum system. Heavy oil producing reservoirs include Aptian – Albian reefs and Senian-Cenomanian carbonates which are sealed by the Assat marls and Aturian sediments. Source rocks are still debatable but are suspected to be of Upper Kimmeridgian – Barremian origin with possible migration routes towards the Upper Cretaceous reservoirs of the anticline. The structural configuration of the anticline provides suitable trapping conditions.

During the Paleocene to Eocene, carbonates were deposited in a bathyal to inner neritic environment (Cerepi et al., 2003). These are covered by flysch deposits filled with debris flows, turbiditic conglomerates and marls (Puigdefabregas and Souquet, 1986). With the maximum compression episode during the Late Eocene, the entire Pyrenean chain emerged and supplied continental detrital sediments, shales, conglomerates, lacustrine limestones and gypsum-rich clays to the foreland Aquitaine basin (Jammes et al., 2009; Masini et al., 2014). Outer neritic shaly deposits are recognized in the Oligocene as the subsiding areas moved northwest. Uplift persisted since the Miocene with more conglomeratic molasses supplied to the basin (Bilotte et al., 2001).

5. Previous diagenetic models

Studies on the Aquitaine basin and the Lacq reservoirs date back to the 1950s with the initial drilling of the Lacq -1 well by Elf Aquitaine in January 1950. Since then, several models were suggested to explain diagenesis and reservoir properties. It was initially observed by Bouroullec et al. (1986), that fractures are well-developed in siliceous facies and are often open with abundant oil impregnation. It was also observed that around 680m depth, strata typical of external to deep platform with pelagic fauna with frequent early

Chapter 1: State of the art - Previous diagenetic models

silicifications lie stratigraphically on top of deeper layers with bioclastic facies deposited in an internal platform, rich in benthic debris, with rare silicifications, but with more pervasive dolomitization (Fig. 10). Bouroullec et al. (1986) then conclude that the good reservoir properties of Upper Lacq are governed by the distribution of fractures in the upper strata, which in turn are the product of the brittle behavior from silicification, whereas the dolomite facies in the lower strata further enhance the reservoir properties through intercrystalline and vuggy porosities.

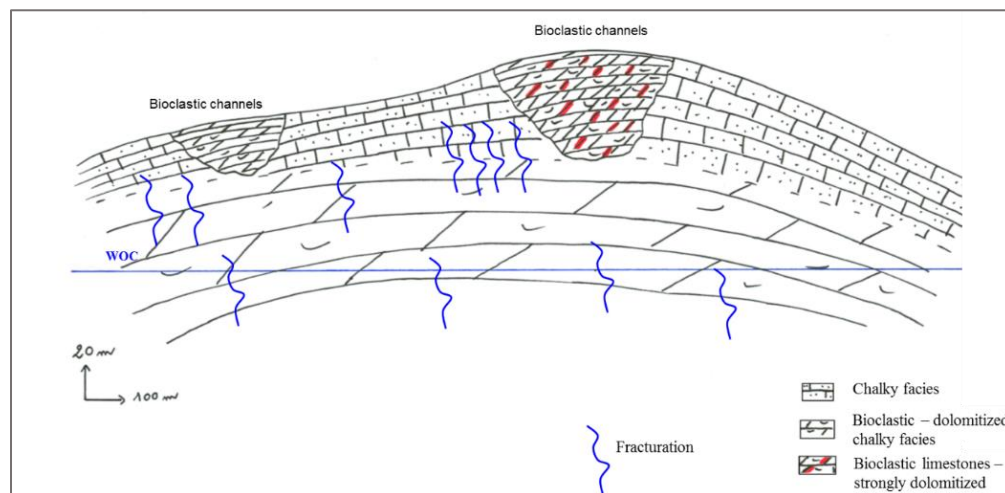


Figure 10. Schematic illustration explaining the distribution of fractures and dolomite bodies in the Upper Lacq's reservoirs (modified after Bouroullec et al., 1986).

The origin of silica was explained by the development of silicified beds in the deeper and external depositional settings while dolomites were also considered to be of sedimentary origin, developed preferably in the more bioclastic and energetic levels (Fig. 11) (Bouroullec et al., 1986).

Chapter 1: State of the art - Previous diagenetic models

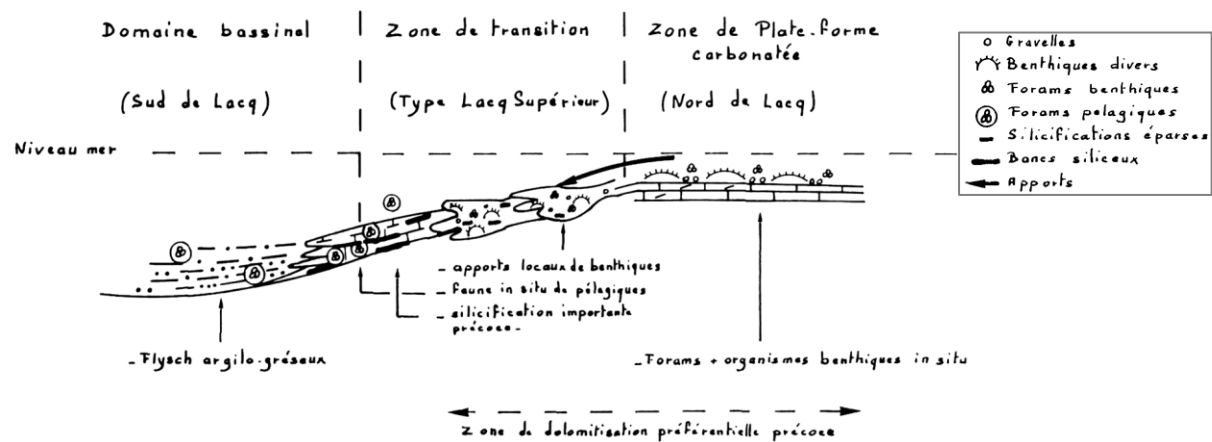


Figure 11. Sedimentary model to explain distribution of reservoir properties in Upper Lacq modified after Bouroullec et al., 1986).

However, since 2004, with the drilling of the horizontal well LA-415 well, the understanding of Lacq's diagenesis started to change. This well penetrated through the productive reservoirs of Upper Lacq for nearly 550m in a NNE-SSW direction (Fig. 12a).

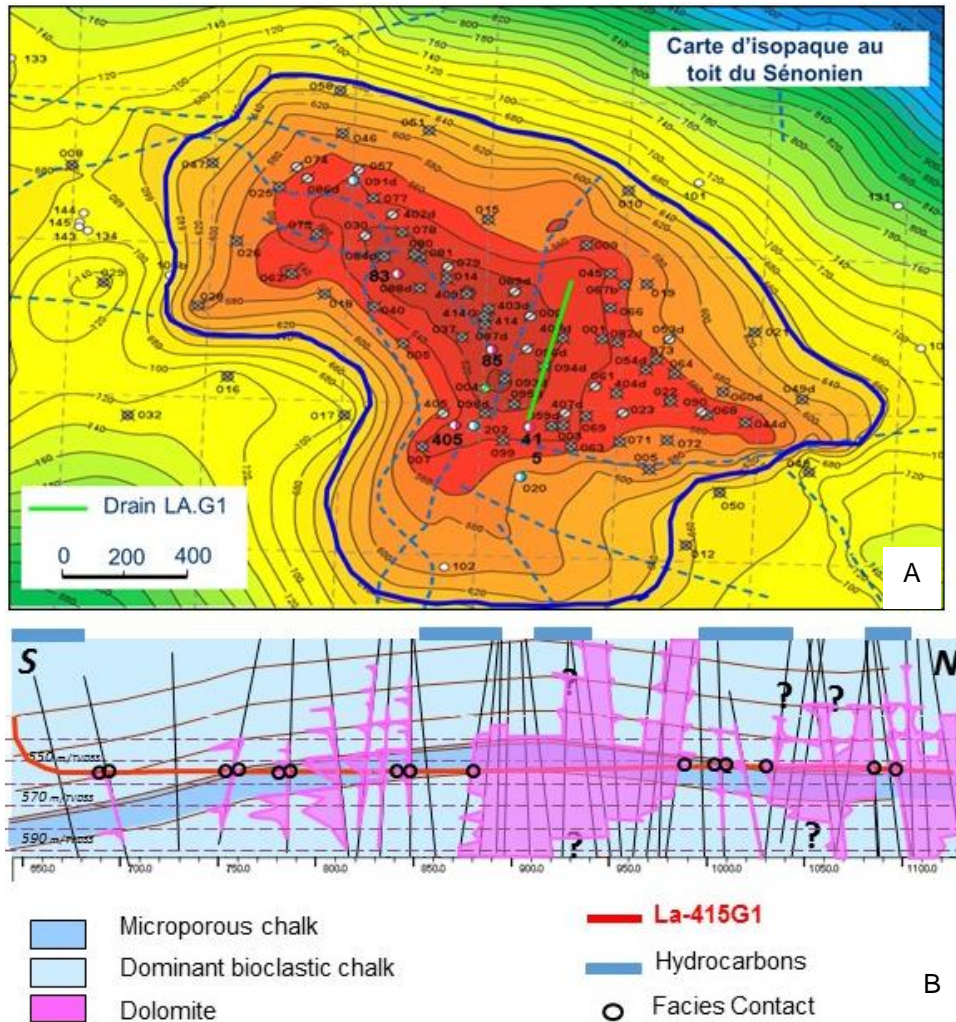


Figure 12. A: Senonian isopach map of Lacq reservoir and the location of the LA-415 G1 horizontal well. B: schematic model of the distribution of dolomite bodies based on the observations of LA-415 G1. Modified after (Lambert et al., 2006).

After coupling observations of the fracture orientation with the dolomite bodies, the proposed schematic model in figure 12-B was constructed and suggest a hydrothermal dolomitization controlled by the fracture network in the Upper Lacq reservoir. This interpretation differs drastically from what Bouroullec et al. (1986) suggested for the origin and distribution of dolomites and highlighted the possible involvement of larger-scale geodynamic events affecting diagenesis and reservoir properties.

In this context, the outcropping analogues of the Upper Jurassic to Barremian reservoirs of deep Lacq in the Chaînons Béarnais were investigated by Salardon et al. (2017) to document the impact of Cretaceous hyperextension and Paleogene compression on fluid circulations and diagenetic modifications. Their study

concluded that oxidizing fluids circulated during the Jurassic rifting phase, and were proceeded by hot mantle-derived fluids, possibly mixed with marine waters, during the Cretaceous hyperextension. Finally with uplift and exposure during the Paleogene Pyrenean compression, meteoric oxidizing fluids were reintroduced (Salardon et al., 2017).

More recently, a quantitative study was conducted on the Rousse field, nearly 40 km southeast of Lacq (fig. 7). The purpose was to understand diagenesis and fluid rock interactions in the Jurassic Mano dolomites to be able to predict reservoir properties since Rousse is selected as a pilot site for CO₂ capture and sequestration (Renard et al., 2019). By integration AIT-PIT modeling and 1D basin modeling, it was concluded that two episodes of fluid migrations affected the quality of the reservoirs. The first fluid circulated at temperatures of 150-170°C during the Late Jurassic to Early Cretaceous, while the second fluid circulated at 170°C during the late Eocene corresponding to the Pyrenean compression period.

These abovementioned works indicate multiple fluid circulation episodes under different temperature conditions. The evolution of ideas and the multi-scale approaches utilized in such works (i.e correlating μm -scale fluid inclusion data to km-scale basin modeling) provide a suitable background for this PhD project and facilitates the interpretation and correlation of data to the overall geological context.

Chapter 2: Methodology

Chapter 2: Methodology

1. Sampling campaign

Samples from the Upper Lacq carbonate reservoir were retrieved mainly from well LA. 37 (location on figure 8). LA.37, was initially drilled as a quality-control well in the center of a square delimited by four oil-producing wells, thus making it a suitable target to study reservoir properties. For Deep Lacq, wells with enough stratigraphic coverage and abundant diagenetic cements were selected after scanning nearly 460 thin sections from the storage site at TOTAL CSTJF (Fig. 13).



Figure 13. Thin sections from various wells of Lacq kept in the storage facility at CSTJF - Pau

In total, four wells were selected for both Upper and Deep Lacq reservoirs. These are LA37-80-101 and 104, logged and sampled at Boussens' storage site (Fig. 14). The log sheets of these wells as well as their exact GPS coordinates are listed in appendix 1.



Figure 14. Photo of core LA-104 observed and sampled at the storage facility in Boussens.

Sampling strategy focused on selecting facies with coarse cement phases, fractures, veins, stylolites and observable cross-cutting relationships and distributed enough to stratigraphically cover the reservoirs. 64 hand samples were then retrieved for further petrographic and geochemical work.

2. Thin and thick sections preparation

Retrieved samples were then cut perpendicular to the coarsest veins and vugs for maximum exposure. In total, 88 new thin sections and 32 thick sections from both reservoirs were prepared at the lithopreparation lab of GeoRessources (Nancy). Thin sections without glass cover have a thickness of 30 μm and are used under optical, cathodoluminescent and fluorescent microscopes. For major and trace element analysis, these thin sections were also analyzed under the scanning electron microscope and the LA-ICPMS technique. Thick sections have a thickness of 120 μm and were used to conduct the fluid inclusions study.

3. Staining

Staining is a rapid technique to distinguish four types of carbonates (calcite, ferroan calcite, dolomite and ferroan dolomite). Preparation of the solution and the dipping technique are performed following the outline of Dickson (1965). The procedure consists of preparing 2 solutions; one by dissolving 0.2g of alizarin red in 100cc of 1.5% HCl and the other by dissolving 2g of potassium ferricyanide in 100cc of 1.5% HCl. The staining liquid is then composed of 3/5 of alizarin red solution and 2/5 of potassium ferricyanide. Thin sections are then soaked for nearly 1 minute to allow the reaction on the carbonate surface to take place. After the test, the sample is gently rinsed with distilled water and left to dry.

4. Petrography

Optical, cathodoluminescent and fluorescent microscopy techniques allow the observation of different facies, phases and crosscutting relationships. Limestone rock classification was carried out using the Folk (1962) and Dunham (1962) schemes. Porosity description is based on Choquette & Pray (1970). Calcite textures and growth habits are described following the criteria of Flügel (2004), whereas dolomite textures are described with reference to Sibley and Gregg (1987).

4.1. Optical microscope

Optical microscopes are used to examine rock facies, textures, crystal sizes, porosity types, cement growth habits and cross-cutting relationships among veins or other phases. For these purposes, Olympus BX51 microscopes fitted with transmitted and reflected light sources are used to observe thin sections under plane (PPL) and crossed polarized light (CPL). Vision under transmitted light allows observation of carbonate and silicate minerals, while reflected light is used to detect mineral phases that appear as black or opaque under transmitted light.

4.2. Cold Cathodoluminescent microscope

Cold cathodoluminescence (CCL) microscopy is a widely used technique in sedimentary geology. It allows the user to rapidly visualize mineral distributions, recognize complex mineral intergrowths and differentiate between cement phases. It also provides fundamental diagenetic data on recrystallization, cementation, veining episodes and cross cutting relationships. The technique relies on observing the intensity of luminescence of the studied phase upon bombardment by high-energy electrons (Boggs and Krinsley, 2006). In carbonate mineral assemblages, luminescence is influenced mainly by the relative abundance on Mn, Fe, and REE (Flügel, 2004). Mn^{2+} and trivalent REE cations are the most important activators of luminescence where Fe^{2+} is the main quencher (Boggs and Krinsley, 2006; Machel, 1985; Price, 1989; Richter et al., 2003). The luminescence of calcites and dolomites can be often interpreted in terms of pH and E_h to have a qualitative assessment of the redox conditions (Barnaby and Rimstidt, 1989; Machel, 1985).

Barnaby and Rimstidt (1989) explain how a mineral with zonations evolving from point A to B (fig. 15) be interpreted in terms of redox conditions. With oxidizing conditions defined by point A, MnO and $\text{Fe}(\text{OH})_3$ are relatively stable; hence low concentrations of Mn and Fe are incorporated into calcites forming under these conditions. Under the moderately reducing conditions defined by the bright field, MnO_2 is progressively dissolved to release Mn^{2+} to the fluid but $\text{Fe}(\text{OH})_3$ remains relatively stable. This results in precipitation of calcite enriched in Mn but poor in Fe. Since Mn is an activator, the precipitated calcites are brightly luminescent. Under the reducing conditions defined by the dull luminescent field (point B), $\text{Fe}(\text{OH})_3$ is progressively dissolved to yield Fe^{2+} to the pore water, which is reflected by the elevated Fe contents of these late calcites.

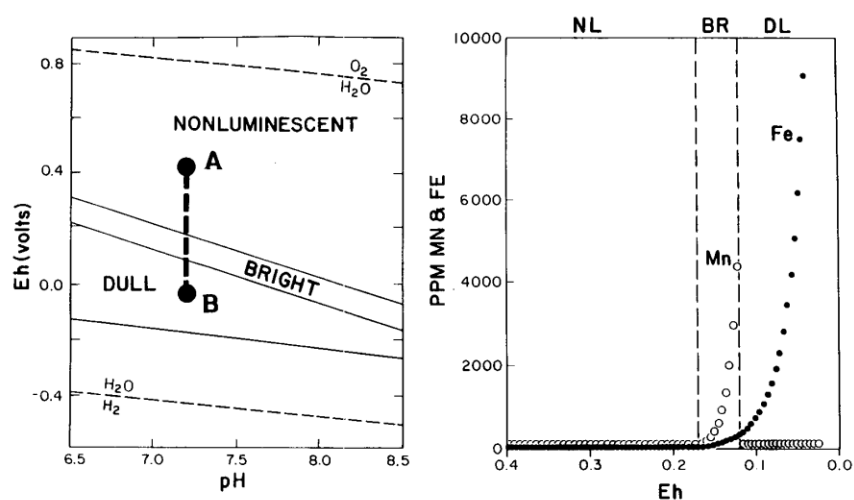


Figure 15. Mass-balance model of equilibrium for Mn and Fe uptake in calcite cement. A: pore space in CaCO_3 sediment incrementally cemented by calcite under successively lower Eh conditions towards point B (Barnaby and Rimstidt, 1989).

However, caution is advised when interpreting CL responses of carbonate minerals as there is a tendency to neglect the influence of REEs contribution to the luminescent colors such that the petrographer focuses only on relative Mn^{2+} and Fe^{2+} to interpret diagenetic environments (e.g. Koepnick, 1976; Amierux, 1982; Grover and Read, 1983). For this reason, it is advisable to check if there are ions, other than Fe and Mn, involved before relying on CL colors to interpret redox conditions (Meyers, 1974 and Machel, 1985).

Observations were carried out at the GeoRessources laboratory in Nancy on an Olympus microscope coupled to a CITL cold cathode instrument CL8200 Mk4 fitted with a Technosyn Cold Model 8200 Mk2 electron gun. The electron beam operating conditions were set at 13-15 kV and 350 μA -400 μA .

4.3. Fluorescent microscope

Fluorescent (UV) microscopy is utilized to observed organic matter and differentiate oil from aqueous inclusions. The technique relies on the visible fluorescence of petroleum oils when excited by an ultraviolet light source. The absorption of electron energy during excitation triggers a transition from ground state energy levels to an excited state which when deactivated to return back to ground state triggers releases energy in the form of fluorescence (Bourdet and Eadington, 2012). The color and intensity of fluorescence depends mainly on aromatics, conjugated polyenes and polar compounds (Bourdet and Eadington, 2012). U.V. microfluorescence observations were made using a Zeiss® AX10 optical microscope equipped with an HBO-100 epi-fluorescence source filtered at 365 ± 5 nm and an LP400 nm emission filter.

4.4. Scanning electron microscope (SEM)

This microscope was used to compliment the observations made with the previous classical microscopes (except UV) and provide geochemical constrains on the identity of ambiguous mineral phases (eg. pyrite vs. pyrrhotite) as well as checking for major elemental compositional variations across different cements and growth zones. Thin sections studied by SEM are subjected to a focused high-energy electron beam to trigger some interactions between the electron beam and the atoms in the sample. X-rays are common products of such interactions and are the target for analysis by the energy dispersive spectrometer (EDS). These emitted X-rays and the spectra generated by the EDS are specific for each chemical element thus allowing qualification and quantification of major elements (Girão et al., 2017). The measurements were done using a PHILIPS XL30 Scanning Electron Microscope (SEM), equipped with an energy dispersive spectrometer (EDS) using a Si-(Li) semi-conductor detector, coupled with a HITACHI S-4800 scanning electron microscope (SEM) at SCMEM-GeoRessources Nancy. Operating conditions were set at a voltage of 15kV, current of 12μA and a signal-to-noise(s) time of 10/5. Studied thin sections were first carbon-coated under vacuum conditions to avoid electron charging. Hematite, albite, SrSO₄, wollastonite and hematite were used as internal standards for O, Na, S, Ca and Fe respectively.

5. Geochemistry

5.1. Stable carbon and oxygen isotopes

Oxygen and carbon stable isotope geochemistry is being increasingly used in the interpretation of carbonates. When combined with petrography and other proxies, isotopes can greatly elucidate the origin of the studied samples (Tucker and Wright, 1990). Possible investigations include fluids and fluid-rock interactions, fingerprinting sources of fluids, estimating paleotemperatures and getting an overview on the diffusion and reaction mechanisms. Oxygen isotopic composition $\delta^{18}\text{O}$ of carbonates provide information on the temperature of precipitation and/or the isotopic composition of the ambient fluids whereas $\delta^{13}\text{C}$ isotopic signatures give information on the source of carbon (Tucker, 1995; Flügel, 2004; Moore, 2013). Processes that can be determined by both $\delta^{13}\text{C}$ and $\delta^{18}\text{O}$ include burial and meteoric diagenesis, methane influence, bacterial or thermal sulfate reduction, recrystallization, soil weathering and similar processes that are influenced by change of temperature, depth and/or carbon source (Hoefs, 1996; Horita, 2014; Jorgensen, 1987; Moore, 2013; O'Neil et al., 1969; Tucker and Wright, 1990). Large veins were selected to avoid risks of a mixing of several generations of cement during the micro-drilling. A Thermo Scientific MAT253 isotope ratio mass spectrometer at CRPG laboratory, Nancy France, was used to perform the analysis. Measurements were calibrated using international standards IAEA CO-1, IAEA CO-8 and NBS 19. Values are reported in per mil (‰) relative to V-PDB (Vienna Pee Dee Belemnite). Reproducibility was checked by replicate analysis of laboratory standards and was $\pm 0.07\text{‰}$ (1 σ) for oxygen isotopes and $\pm 0.01\text{‰}$ (1 σ) for carbon isotopes.

Representative samples were later selected for clumped isotope thermometry investigation. Δ_{47} measurements have been performed at California Institute of Technology (USA) with an automated acid digestion and gas purification device coupled to a dual inlet Thermo MAT253 as described in Passey et al. (2010). Samples weighed into silver capsules (~ 8 mg) were reacted in a common phosphoric acid bath (~103 %) for 20 minutes at 90°C under static vacuum (evacuated to <0.5 Torr at the beginning of the reaction). The evolved CO_2 was passed through an ethanol/dry ice U-trap (~ -80°C) before being collected on a liquid nitrogen temperature (-196°C) U-trap. Following the 20 minutes reaction period, the CO_2 was carried through a Porapak Q 120/80 mesh gas column held at -20°C using He as the carrier gas. The purified CO_2 was analyzed using a Thermo Scientific MAT 253 Mass Spectrometer configured to collect masses 44–49. Mass 48 was monitored to detect any hydrocarbon contamination. Measurements of each

gas were done at 16 V and consisted of 8 acquisitions, each of which involved 7 cycles of sample-standard comparison with an ion integration time of 26 s per cycle (i.e., total integration time of 1456 seconds for each CO₂ sample).

$\delta^{18}\text{O}$ and $\delta^{13}\text{C}$ data were also acquired as part of each Δ_{47} analysis and were calculated using the “Brand” parameters reported in Brand et al. (2010). In order to account for the temperature dependence of oxygen isotope fractionation between CO₂ gas and carbonate resulting from the reaction with phosphoric acid at 90°C, fractionation factors of 1.00811 and 1.009218 were respectively used for calcite and dolomite following Rosenbaum and Sheppard (1986) and Swart et al. (1991). The Δ_{47} raw data were corrected for instrument nonlinearity and scale compression (Huntington et al., 2009; Passey et al., 2010). Several heated (at 1000°C) and equilibrated gases (at 25°C) of various bulk isotopic compositions were run during each session. These gases were used to convert measurements into the interlaboratory absolute reference frame (Dennis et al., 2011). $\delta^{18}\text{O}$ and $\delta^{13}\text{C}$ values are expressed in per mil with respect to the VPDB standard. To guarantee accuracy of the Δ_{47} data, we routinely analyzed two carbonate reference materials (Carrara marble and TV04, also reported by Dennis et al., 2011 and many other studies). One of these two carbonate standards was analyzed typically every five analyses and distributed along the diagenetic cement samples in order to check for analytical stability/accuracy of the whole procedure, as well as long-term external reproducibility of our measurements. The Δ_{47} values obtained are: $\Delta_{47}\text{-CDES25} = 0.409 \pm 0.019\text{‰}$ (1SD, n = 19) for Carrara; $\Delta_{47}\text{-CDES25} = 0.670 \pm 0.014\text{‰}$ (1SD, n = 16) for TV04.

Finally, the corrected Δ_{47} values were converted into temperatures using the composite $\Delta_{47}\text{-T}$ calibration determined for all carbonate minerals for the 0–300°C temperature range (i.e. Bonifacie et al. (2017); $\Delta_{47}\text{-CDES90} = 0.0422 \times 10^6 / T^2 + 0.1262$). The oxygen isotopic compositions of the water ($\delta^{18}\text{O}_{\text{water}}$) from which the carbonates precipitated were calculated for each estimated $T\Delta_{47}$ using the $\delta^{18}\text{O}_{\text{carb}}$ values measured for the carbonate as well as the oxygen isotope fractionation between the carbonate and water from O'Neil et al. (1969) for calcite and Horita (2014) for dolomite.

5.2. Multiple sulfur isotopes

Multiple sulfur isotope analysis is a relatively new technique that involves the measurements of $\delta^{33}\text{S}$, $\delta^{34}\text{S}$, $\delta^{36}\text{S}$, $\Delta^{33}\text{S}$ and $\Delta^{36}\text{S}$ and focuses on the deviations from ideal mass-dependent equilibrium isotopic

fractionations. These anomalies are the consequences of mass-dependent biological or abiotic processes such as photosynthesis, photochemical reactions, volcanic eruptions, hydrothermal fluid circulations, bacterial or thermochemical sulphate reductions (Johnston et al., 2005; Farquhar et al., 2010), and for the determination of the sources and mixing pools of sulfur (Ono et al., 2006; Peters et al., 2010; McDermott et al., 2015). Multiple sulfur isotopes analysis ($\delta^{34}\text{S}$, $\delta^{33}\text{S}$, $\delta^{36}\text{S}$) was performed on carbonate-associated sulphate (CAS) on samples from the LA-37 well. The extraction technique of Sansjofre et al. (2016) was used to analyze CAS isotopic signature. This technique involves leaching the soluble sulfates fraction with saline water several times before dissolving the carbonates in 4N HCl solution over 12 hours. Then, a solution of BaCl_2 was added to the acidified sample to precipitate sulfates as barium sulfates.

The recovered barium sulfates were then reacted with the STRongly Reducing Hydriodic Hypophosphorous acid solution (STRIP) (Kitayama et al., 2017) to produce Ag_2S upon reacting with AgNO_3 solution. This Ag_2S is then reacted with F_2 during a whole night in nickel containers at 350°C to produce SF_6 . After cryogenic and gas chromatography separation steps, the resulting SF_6 was analyzed in a ThermoFinnigan MAT 253 dual-inlet gas-source mass spectrometer. All the different steps of the multiple sulfur isotopes analysis were carried out at Institut de Physique du Globe de Paris (IPGP, France). Values are given with respect to Vienna Cañon Diablo Troilite (V-CDT) related to the classical delta notation.

5.3. Major and trace element analysis

Major elements were analyzed to check for possible chemical differences between dolomite and calcite phase and to identify ambiguous minerals whose petrography was obscure or with low confidence. The elements analyzed were Si, Al, Fe, Mn, Mg, Ca, Na, Cl, K, Ti, P, S, Sr and F. The measurements were done using a PHILIPS XL30 Scanning Electron Microscope (SEM), equipped with an energy dispersive spectrometer using a Si-(Li) semi-conductor detector, coupled with a HITACHI S-4800 scanning electron microscope (SEM) at Service Commun de Microscopie Électronique - SCMEM-GeoRessources Nancy. Operating conditions were set at a voltage of 15kV, current of 12 μA and a signal-to-noise(s) time of 10/5. Studied thin sections were first carbon-coated under vacuum conditions to avoid electron charging. Hematite, albite, SrSO_4 , wollastonite, olivine and hematite were used as internal standards for O, Na, S, Ca, Mg and Fe respectively. Laser Ablation-Inductively Coupled Mass Spectrometry (LA-ICPMS) was used

to study Rare Earth Elements (REEs) and U and Pb contents in dolomite and calcite cements. The analyses were carried out at the GeoRessources laboratory in Nancy. Laser sampling was performed with a 193 nm GeoLas Pro ArF Excimer laser (Microlas®, Göttingen, Germany) equipped with beam homogenization optics. Ablation was performed by focusing the beam at the sample surface with a constant fluency of 10 J/cm² and constant repetition rate of 5 Hz. Helium was used as a carrier gas to transport the laser generated aerosols from the ablation cell to the ICP-MS. Ablated material was analyzed by an Agilent 7500c Quadrupole ICP-MS (Agilent®, Santa Clara, California) equipped with an Octopole Reaction System with enhanced sensitivity optional lenses (Cs type, Agilent). The certified glass standards NIST610, NIST612 and NIST614 SRM were used as reference materials for the calibration of the LA-ICP-MS. The protocol for routine analysis of REE in carbonate was checked using GSR6 reference carbonate standard. Absolute concentrations and limit of detection were obtained from the equations developed by Norman et al. (1996). Detection limit range from a few ppm for Ce to down to 0.5 ppm for heavy rare earth elements. For consistent representation, obtained REE concentrations were normalized to the Post-Archean Australian Shale (PAAS). The redox states of parent fluids can be estimated with the Ce anomaly by using the method of Bau and Dulski (1996), which compares $(\text{Ce}/\text{Ce}^*)_{\text{PAAS}}$ calculated as $\text{Ce}_{\text{PAAS}} / (0.5\text{La}_{\text{PAAS}} + 0.5\text{Pr}_{\text{PAAS}})$ to $(\text{Pr}/\text{Pr}^*)_{\text{PAAS}}$ calculated as $\text{Pr}_{\text{PAAS}} / (0.5\text{Ce}_{\text{PAAS}} + 0.5\text{Nd}_{\text{PAAS}})$.

6. Fluid inclusions analyses

6.1. Microthermometry

Microthermometric measurements were performed on a Linkam THMS600 heating - cooling stage connected to an Olympus BX51 microscope (GeoRessources, Nancy, France). The stage was calibrated using synthetic H₂O pure fluid inclusion standard that has a final ice melting temperature ($T_{\text{m ice}}$) at 0.0°C, a natural aqueous fluid inclusion standard (T_{a} 33.2) that homogenizes into the liquid phase at T_{h} of 164.0°C and synthetic pure CO₂ inclusion with an eutectic temperature (T_{e}) of -56.9°C. The acquired temperatures of phase transition (i.e. homogenization into the liquid phase) have an accuracy of about $\pm 0.2^\circ\text{C}$, and the obtained data was calibrated accordingly. In the case of fluid inclusion trapped in dolomites, the glass cover of the stage was removed to allow clearer observations of the very small inclusions. Without the glass cover, the error range increased to $\pm 1.6^\circ\text{C}$.

6.2. Raman Spectroscopy

Raman spectroscopy was used to validate very low salinities and determine the composition of gas phases in aqueous fluid inclusions following the procedure outline in Caumon et al. (2015). Raman spectra of water are influenced by the decrease of hydrogen bond of water by chloride (Perera et al., 2009; Walrafen, 1962). Salinity can be determined by the analysis of the Raman spectrum of water based on the decrease of the strength of the hydrogen bond of water by chloride (Walrafen, 1971; Perera et al., 2009). An increase salinity (chlorinity) results in a decrease of the intensity of the lower part of the OH stretching vibration band of water around 3200cm^{-1} . The OH band is the combination of two main bands at 3250 and 3420 cm^{-1} corresponding to OH (hydrogen bond) and OH (covalent bond) of water respectively (Caumon et al., 2014). The ratio of intensities at 3250cm^{-1} and 3420cm^{-1} is then calculated and plotted as a function of mass% NaCl (Caumon et al., 2014 and references therein). Analyses were performed with a LabRAM HR spectrometer (Horiba Jobin Yvon) equipped with a 600g.mm^{-1} grating and an Edge filter. The confocal hole aperture was $400\mu\text{m}$ and the slit aperture was of $200\mu\text{m}$. The excitation beam was provided by a Stabilite 2017 Arp laser at 457.9nm or 514.5nm and a power of 200mW . The acquisition time was set to 10s and the number of accumulations was 10 in order to optimize the signal-to-noise ratio. In cases where the signal was not clear or noisy, the acquisition time was increased to 20s with the diaphragm aperture closed from 1000 to $500\mu\text{m}$. This step reduces the noise from the host rocks but requires more acquisition time of 20s for a clearer signal. For quantification purposes, spectral acquisition was done first on each liquid or gas phase then followed by another spectral acquisition of the host mineral phase. The second spectrum is used as for baseline correction. The uncertainty of salinity quantification using this method is ± 0.4 eq.wt. % NaCl (Caumon et al., 2014).

6.2.1. CH_4 quantification

To quantify the gases present in the fluid inclusions, Raman spectra were acquired at homogenization temperatures (i.e. disappearance of the gas phase into the liquid) by fitting a Linkam CAP500 heating–cooling stage on the spectrometer. Measurements were obtained in the liquid phase and in the calcite host mineral which was used to adjust the baseline. Quantification of the CH_4 was done following the best fit, second-order polynomial curve obtained from the calibrations of Caumon et al. (2014b), outlined as follows:

$$m\text{CH}_4 = 0.008 + [50.2 \times A(\text{CH}_4)/A(\text{H}_2\text{O})] - 660 \times [A(\text{CH}_4)/A(\text{H}_2\text{O})]^2 \quad (1)$$

such that $m\text{CH}_4$ is the molality in mol/kg of water and $A(\text{CH}_4)/A(\text{H}_2\text{O})$ the methane-to-water peak area ratio. The adjusted R^2 of the fit is 0.996. The uncertainty on the calculated CH_4 molality value resulting from the calibration function ($\pm 1\sigma$) is less than $\pm 2\%$ (Caumon et al., 2014). The area ratios were calculated using the integral tool in LabSpec. The area of the stretching vibration band of water was measured between 2700 and 3950 cm^{-1} , including the stretching vibration peak of dissolved CH_4 at around 2905 cm^{-1} , then the peak area of methane was measured separately and subtracted from the total area of methane and water. This best-fit curve, which links the peak area ratios to a molality scale, follows the thermodynamic model of Duan and Mao (2006).

6.2.2. H_2S and HS^- ratios for pH assessment

To have insight into the pH conditions of the circulating fluids, spectra with peaks between 2550 and 2600 cm^{-1} were analyzed to quantify the concentration of HS^- (2570 cm^{-1}) and H_2S (2590 cm^{-1}) (Schmidt and Seward, 2017). At high pH, H_2S in water is dissociated into HS^- that becomes the dominant species while at low pH conditions, dissolved H_2S species are dominant (Peltzer et al., 2016). To quantify the ratios of these species, the Raman spectra were treated using the *Opus (Bruker)* software. After baseline correction, the spectra were decomposed using the Levenberg-Marquadt algorithm to differentiate the HS^- and H_2S species. The area (A) ratio of these two species is correlated with pH using the following interlaboratory equation:

$$\text{pH} = 0.43 \ln[A(\text{HS}^-)/A(\text{H}_2\text{S})] + 7 \quad (2)$$

The linear regression coefficient was reported to be $R^2=1$. But the margin of error should be within the area quantification of the area of HS^- and H_2S , which is a function of the signal-to-noise ratio. Concentration of H_2S can also be calculated from the Raman spectra using the following equation:

$$m\text{H}_2\text{S} = [A(\text{H}_2\text{S})/A(\text{H}_2\text{O})] \times [71.2 - (1.19 \times m\text{NaCl})] \quad (3)$$

$m\text{H}_2\text{S}$ is the molality, $A(\text{H}_2\text{S})$ is the integrated area of the H_2S peak, $A(\text{HS}^-)$ integrated area of the HS^- peak and $m\text{NaCl}$ is the molality of sodium chloride. Similarly, the molality of HS^- can be obtained as follows:

$$mHS^- = [A(HS^-)/A(H_2O)] \times [71.2 - (1.19 \times mNaCl)] \quad (4)$$

equations (3) and (4) have a linear regression coefficient $R^2=0.993$ to 0.998 , implying an error range of less than 1%.

6.3. Infrared microspectroscopy (μ FT-IR)

FT-IR was used to qualitatively assess compositional differences between the different types of oil inclusions studied. Infrared spectra were recorded with a Bruker Fourier Transform Infrared (FTIR) spectrometer Equinox 55, coupled with a Bruker A590 microscope. The microscope is equipped with a narrow-band mercury-cadmium-telluride (MCT) detector with a $100\mu\text{m}$ diameter window, cooled to 77K. The spectra were obtained in transmission mode in the mid infrared range ($4000\text{--}400\text{ cm}^{-1}$) with a 4 cm^{-1} spectral resolution. A series of circular diaphragms allows the diameter of the analyzed section to vary from 100 to $20\mu\text{m}$ with the objective magnification of $\times 15$. μ FTIR spectra were obtained in less than two minutes by the accumulation of 200 scans. The contributions of atmospheric CO_2 and H_2O were removed from their independently recorded spectra.

6.4. Confocal Scanning Laser Microscope

For P-T modeling of oil inclusions, it is necessary to consider the composition of the oil trapped in inclusions. Pironon et al. (1998) lists the limitation and difficulties in accurately determining the composition of oil inclusions using conventional gas chromatography, Nuclear Magnetic Resonance (NMR) spectroscopy, Raman and Fourier-Transform Infrared microspectroscopy and UV spectroscopy. However, 3-D volumetric reconstruction of oil inclusions allows the determination of bubble points curves and eventually the stability phase diagrams. These 3-D images are obtained by compiling stacks of images captured using a Confocal Scanning Laser Microscope (CSLM) fitted with a Biorad Rainbow system adapted to a Nikon inverted microscope at the GeoRessources Lab (Nancy, France). Emission source was an Argon laser at 488 nm and a diode laser at 405 nm. Observations were done through an oil-immersed 60x objective lens. This method allows volume estimation of the cavity of a petroleum inclusion with an accuracy greater than 95%. The x–y resolution is $0.2\mu\text{m}$ and the resolution along the z-axis is approximately $0.5\mu\text{m}$. The studied chips are glued on a glass plate using paraffin to avoid any movement during acquisition. For better accuracy, the radii of the gas phases in oil inclusions were measured prior to CSLM measurements using optical light

microscopes. This method, using CSLM, is able to estimate the volume of the gas phase in an oil inclusion with a margin of error of less than 5% (Pironon et al., 1998). Image processing is carried out with ImageJ, color histograms are plotted with Excel and the second derivative of the color histogram to objectively and consistently remove the noise is calculated with Matlab (appendix 2).

6.5. Aqueous inclusions thermodynamics modeling (AIT)

After trapping, it is assumed that no changes in mass or volume of the fluid inclusion take place during uplift (Goldstein and Reynolds, 1994). This means that the fluid inclusions follow a path of constant density. Lines of constant density on a P-T diagram are known as "isochores" (Roedder, 1984). To draw these isochores, Zhang and Frantz (1987) constructed a P-T equation given by:

$$P = A_1 + A_2(T) \quad (5)$$

Where P is the pressure, T is the temperature and

$$A_1 = 6.1 \times 10^{-3} + (2.385 \times 10^{-1} - a_1)T_h - (2.855 \times 10^{-3} + a_2)T_h^2 - (a_3T_h + a_4T_h^2)m \quad (6)$$

$$A_2 = a_1 + a_2T_h + 9.888 \times 10^{-6}T_h^2 + (a_3 + a_4T_h)m \quad (7)$$

a_1 , a_2 , a_3 , a_4 , are constants fit to the data sets extracted from plots of homogenization temperatures as a function of experimental temperature and pressure and are listed in table 2.

Table 2. Constant coefficients for the H₂O-NaCl system obtained by Zhang and Frantz (1987).

Constants	Values
a_1	18,6102
a_2	-9,53E-03
a_3	1,34907
a_4	-7,67E-03

m is the molality in mol/kg. It is calculated from the salinity reported as equivalent weight %NaCl following the revised equation of Bodnar (1993):

$$Wt. \% NaCl = (1.76088 \times T_{mice}) - (0.409223 \times T_{mice}^2) \times (0.00046162 \times T_{mice}^3) \quad (8)$$

Then

$$m = \frac{Wt.\% NaCl}{(100 - Wt.\% NaCl)} \times \frac{58.5}{1000} \quad (9)$$

58.5 is the molar mass of NaCl

Fitting equations (6), (7), (8), and (9) into (5) would give an isochore of an aqueous inclusions in the single-phase domain. Equation (8) identifies the salinity of the fluids with an accuracy better than ± 0.05 wt% NaCl at all T_{mice} between 0 to -21.2°C (Bodnar, 1993). The overall errors in the computation of the isochores are less than $\pm 3^\circ\text{C}$ and 1% of the total pressure (Zhang and Frantz, 1987).

6.6. Petroleum inclusions thermodynamics modeling (PIT)

PIT modeling focuses on constructing the P-T phase diagram of a constant composition petroleum inclusion, and have a direct compositional assessment of the chemistry of the oils. The P-T evolution of an oil inclusion follows an isochoric (constant density) line first in the two-phase liquid-gas domain then in the one-phase domain (fig. 16) (Bourdet et al., 2008).

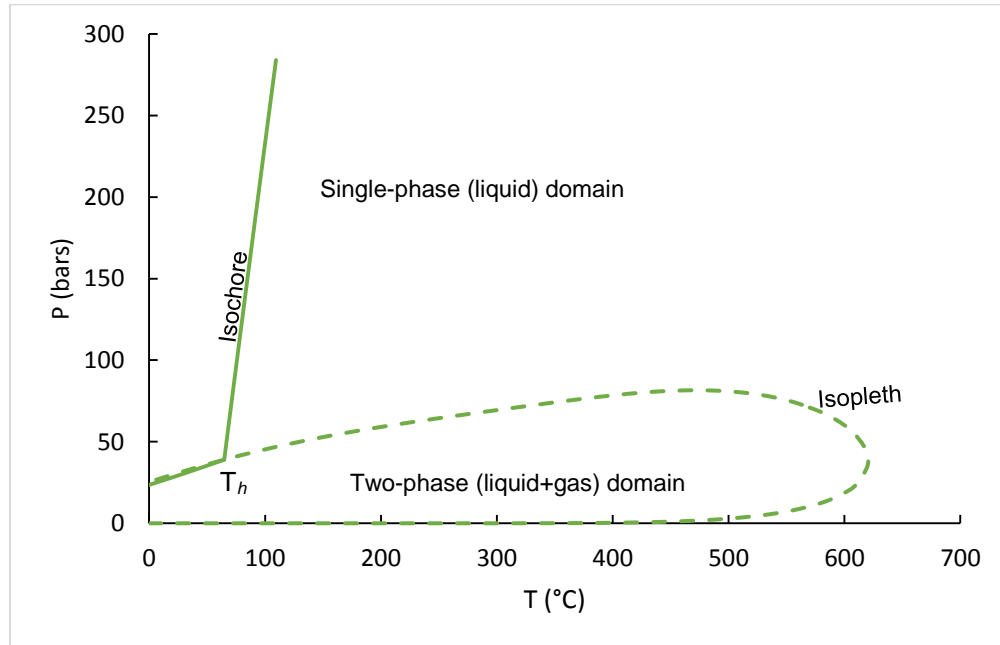


Figure 16. P-T phase diagram of an oil inclusion. Filled line is the isochore moving from the two-phase domain to the single-phase domain at the T_h . Dashed line is the isopleth that separates the two domains.

To construct such a phase diagram, the PIT modeling software developed by Thiéry et al. (2002) was used. The software relies on the database of natural oil PVT properties with estimations of the gas-oil immiscibility P-T fields designed by Montel (1993). The software relies on the equation of state of Peng and Robinson, (1976) given as:

$$P = \frac{RT}{v-b} - \frac{a(T)}{v(v+b)+b(v-b)} \quad (9)$$

where P is the pressure, T is absolute temperature and R is the ideal gas constant. v is the molar volume and b is a constant related to the size of the hard spheres. a is a measure of the intermolecular attraction force. The software of Thiéry et al. (2002) simplifies the composition of oils into mixtures of 12 simple hydrocarbons (C_1 , C_2 , C_3 , iC_4 , nC_4 , iC_5 , nC_5 , nC_6 , nC_7 , nC_8 , nC_9 , nC_{10}) and two heavier components, noted here C_{n1} and C_{n2} . Empirical correlations in the software consider that the mole fractions of molecules of more than six carbon atoms obey a geometric law of exponent α , while the lighter components of C_1 - C_6 are described by a second parameter, denoted β (Thiéry et al., 2002). Input parameters involved the vapor volume fraction obtained by image processing of CSLM images and the homogenization temperatures T_h . Phase diagrams are then derived from a cross-plot of α and β parameters, with a pressure uncertainty of less than 50 bars.

7. Basin Modeling

The Petromod 1D software was used to model the evolution of lithostatic and hydrostatic P-T conditions over time. Stratigraphic and thermal maturity data were inserted into the software to better constrain the basin model. Ages were determined following the stratigraphic chart of Biteau et al. (2006), while duration of unconformities were deduced from works like Le Marrec et al. (1995), Bilotte et al. (2001) and Huyghe et al. (2012). Subsidence evolution was obtained by using the backstripping method. Backstripping and decompaction of a layer from present day thickness to depositional thickness is calculated with the assumption of the conservation of the solid matrix volume (Hantschel and Kaureauf, 2009). This conservation of the volume is based on the Terzaghi type models that simplifies the lithostatic pressure by taking into account only the vertical component of the stress tensor as the maximum principal stress, while pore pressure formation is caused mainly by the overburden load and porosity reduction is

controlled by the Terzaghi's effective stress value, which is equal to the difference of the lithostatic and the pore pressure (Hantschel and Kaureauf, 2009). The amount of eroded material during unconformities was estimated on the basis of the best-fit scenario between the measured and simulated vitrinite maturities. True vertical depths (TVD) from well logs were used as compacted stratigraphic thicknesses of the drilled formations. A synthetic stratigraphic well (summarized in appendix 3) is eventually prepared after compilation of data from drilling reports during the operations of wells LA-101-104-37-80. A correlation plate between the 4 wells was not possible to construct because not all formations are recovered upon drilling and the penetrated depths are different from one well to the other (appendix 1). These reports also provided data about porosity and density, which were added as calibrations and are listed in appendix 4 and 5 respectively. Source-rock typing by Connan and Lacrampe-Couloume (1993) provide suitable biomarker data (sterane isomerization: $29\alpha\alpha\text{S}/29\alpha\alpha\text{R}$) to calibrate source rock maturity. Also, measured vitrinite maturities and equivalent vitrinites calculated from RockEval Tmax data, using the equation of Jarvie et al. 2018, were collected from unpublished internal TOTAL reports and added as thermal calibrations (see appendix 6).

Chapter 3: Upper Lacq

Chapter 3 – Part I: Results: Upper Lacq

1. Petrography of diagenetic phases

1.1. Host Rock

Host rocks in Upper Lacq consists of limestones and partially dolomitized limestones having intramicrite to biomicrite facies (Folk, 1962) with a wackestone to packestone texture (Dunham, 1962) (Fig. 17a). Skeletal fragments of foraminifera, echinoderms, and gastropods are abundant and can reach up to 700 μm in length. The red color after staining indicates a non-ferroan composition of the matrix. CCL microscopy reveals a brown to dull-orange luminescence of the matrix. Appendix 7 shows the main lithologies of the host rocks recognized in Upper Lacq.

1.2. Glauconite

Pellets of glauconite have simple, rounded morphologies, with generally smooth surfaces (Fig. 17a). Sizes range between 20 μm up to 200 μm . Rarely, some pellets are amalgamated into larger aggregates. Local concentrations of glauconite are observed associated with stylolite residues.

1.3. Micrite rims

A few μm -thick rims of micrite penetrating some skeletal fragments were observed (Fig. 17c). These have a dark grey color in plane polarized light (PPL) and a bright yellow luminescence under CCL.

1.4. Framboidal pyrites

This phase of pyrite occurs as framboidal aggregates adjacent to shells and skeletal fragments. Under reflected light, pyrites appear as golden to bright yellow (Fig. 17d). Crystal sizes can reach up to 55 μm with rounded to sub-rounded geometries.

1.5. Chert Nodules

This scarce phase was observed only in a few samples. Individual nodules can reach up to 4 cm in length with circular to oblate morphologies. In thin sections, a few silica microfractures, with thicknesses of 2-4 μm

can be seen cross-cutting or terminating at the chert nodules (Fig. 17e). Silica crystals have a white to yellowish grey color with sweeping extinction under cross-polarized light.

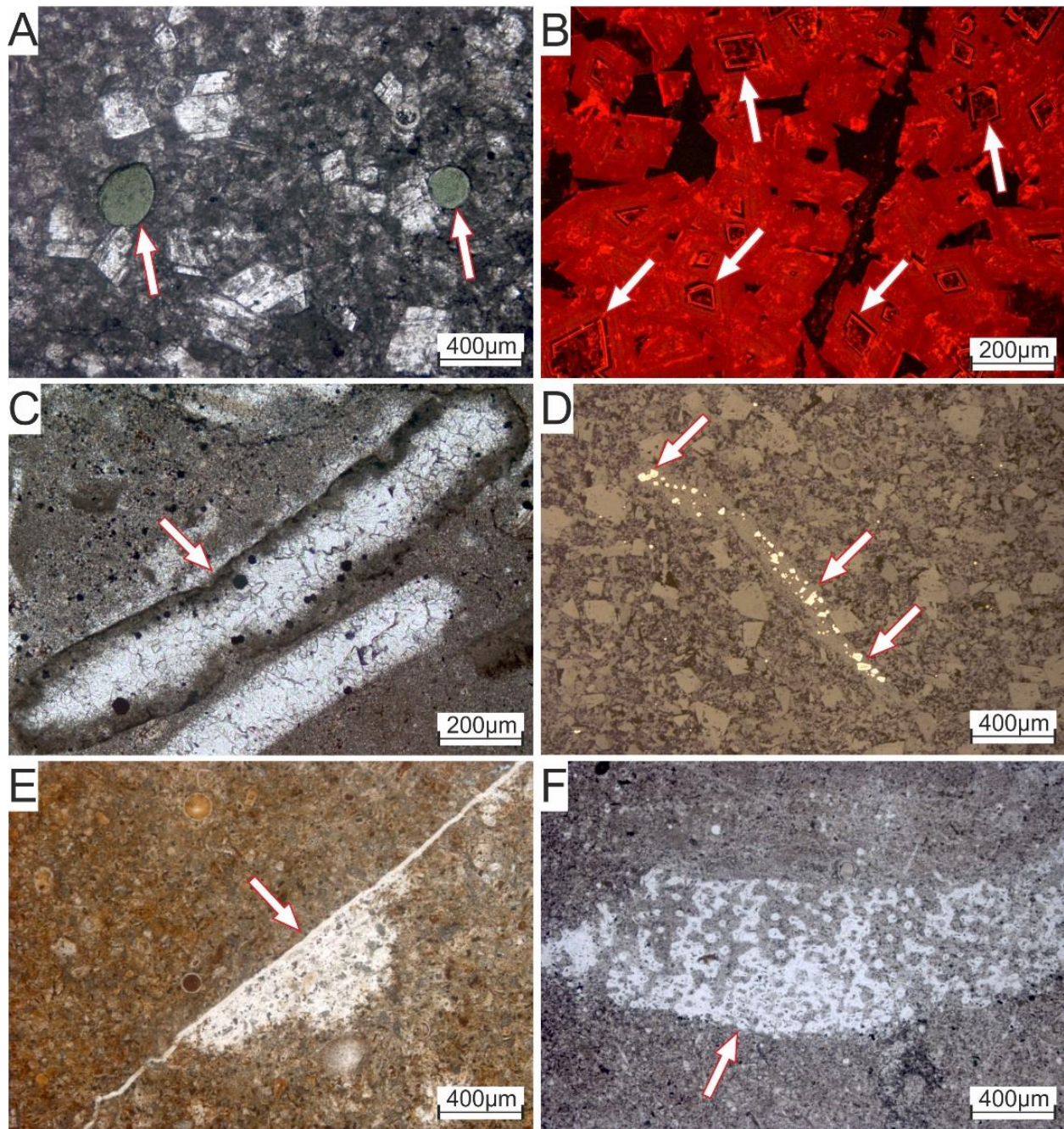


Figure 17. A: Limestone matrix with micrite and dolomite in PPL. Arrows point to the rounded greenish detrital glauconite pellets. B: CCL photomicrograph showing the dark zoned core of the D1 dolomite (arrows). The red-luminescent overgrowth corresponds to the D2 dolomite. C: Micrite rim (arrow) penetrating a shell fragment in PPL. D: Aggregates of bright yellow framboidal pyrite (arrows) inside in a bivalve shell in PPL. E: Microfracture (arrow) filled by silica in contact with a displaced chert nodule (in PPL). F: Clast of siliceous sponge (in PPL).

1.6. Dolomite D1

This phase consists of euhedral dolomite rhombs. They constitute the cores of dolomite crystals present in the matrix (Fig. 17b). Rhombs have average sizes between 30 and 200µm. Under PPL, D1 appears as turbid and rich in impurities. Fluid inclusions are too small to allow measurements (<3 µm) . Under CCL, D1 is mostly non-luminescent with a single brightly luminescent rim. This phase is colorless after staining indicating a non-ferroan composition.

1.7. Pyrite 2

The second phase of pyrites appear as cubes larger than the early framboidal aggregates. Individual crystal sizes can reach up to 2.5 mm in length (Fig. 18a). In some cases, relics of dolomite rhombs were observed inside the engulfing pyrite crystals. No cross-cutting relationships with the later dolomite/calcite phases were observed and thus its timing cannot be robustly determined.

1.8. Fracture (breccia)

Brecciated fragments of D1 were observed under PPL. Under CCL, edges of brecciated crystals show an irregular non-planar shape and a bright yellow external rim probably due to a dissolution event (Figs. 18b and c).

1.9. Saddle dolomites D2

This phase has two morphologies. The first engulfs D1 cores and appears as creamy white overgrowth cement under PPL and labeled D2. When viewed under CCL, a uniform bright red luminescence was observed (Figs. 17b and 18b). Overgrowths can reach up to 150 µm in thickness and contain some aqueous fluid inclusions that were investigated in this study. The non-ferroan composition of D2 is attested by its white color after staining. In fractures (Fig. 18b) or in mm-scale vuggy porosity, coarse dolomite crystals were observed. The latter morphology is that of the saddle dolomite crystals. Under cross-polarized light, crystals show typical sweeping extinction. CCL observations revealed a uniform bright red luminescence. Crystal sizes can reach up to 2 mm in length. Similarly, colorless results after staining indicate a non-ferroan composition. This dolomite phase was not affected by brecciation (Fig. 18b), but was impacted by stylolites (Fig. 18c).

1.10. Stylolites

Stylolites affect the brecciated D1 and the saddle dolomites (Fig. 18c). The oblique direction of stylolite peaks in vertical wells indicates that they are tectonic in origin and formed during Pyrenean shortening. Concentrations of glauconite along stylolites have also locally been observed. In a few thin sections, the amplitude of stylolites can reach few mm.

1.11. Fracture and dissolution

Fractures with open pore spaces cross-cut the host rocks. The width of open fractures can reach 4-6 mm. Blocky calcites are often observed on the edges of fractures (Fig. 18e and f). Dissolution is mostly expressed through the partial dissolution of stylolites (Fig. 18d) and the partially eroded fracture walls (Fig. 18e and f).

1.12. Blocky Calcites

This cement phase is creamy white to transparent in PPL with typical cleavage planes at 74° and 55°. Growth habits include equant to blocky forms with larger crystal sizes towards the center of pores and fractures (Fig. 18e). Individual crystal sizes can reach up to 3 mm. CCL microscopy revealed a dark brown to dull orange luminescence (Fig. 18e). These calcites are the main pore-reducing cements and occlude most of the inter-dolomite and fracture porosity. The pink color after staining indicates a non-ferroan composition (Fig. 18d).

1.13. Oil emplacement

Oil inclusions exist inside the blocky calcite and oil coatings occur on calcite and dolomite crystals. Oil inclusions have a brown to orange color under ultraviolet (UV) light, while the coatings on calcites show a darker brown color (Fig. 18f).

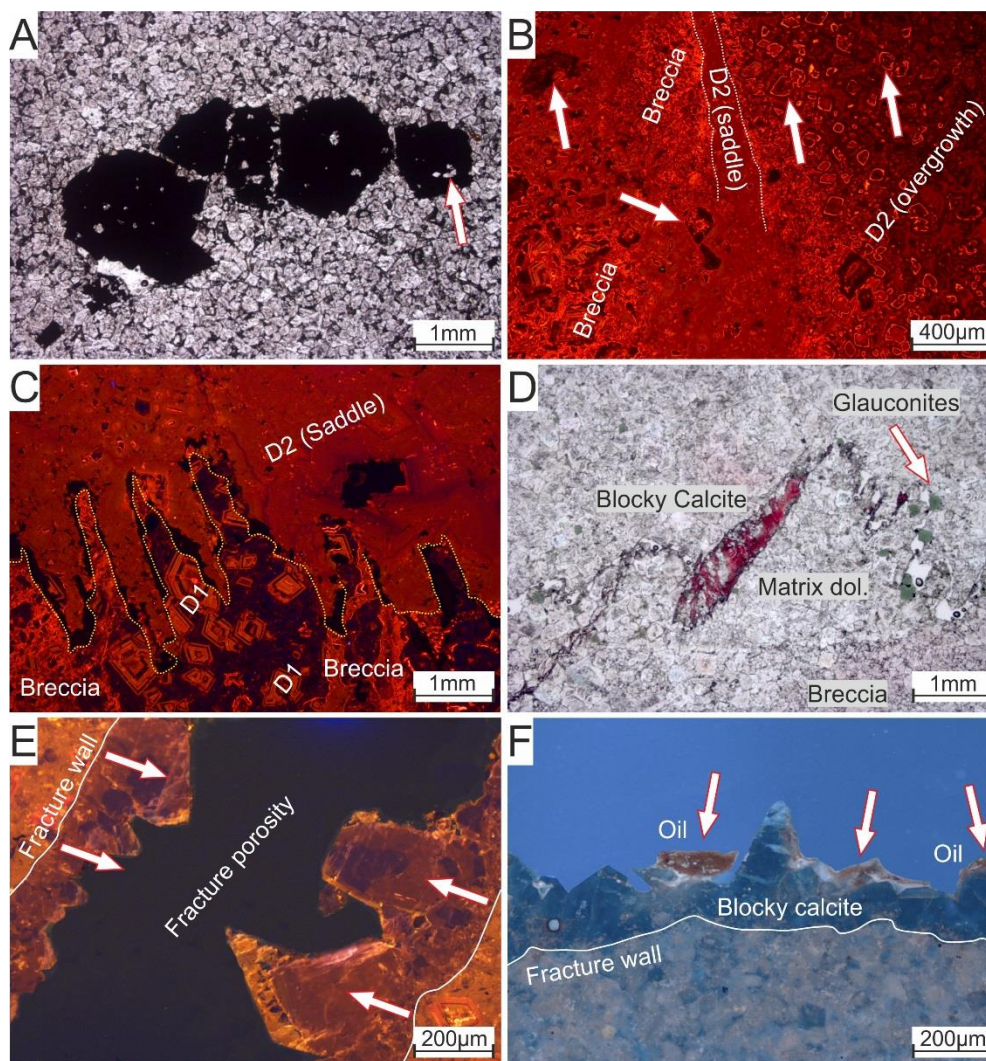


Figure 18. A: Pyrite 2 crystals engulfing some relics of dolomites (arrow; in PPL). B: CCL Cross-cutting relationships between fractures (between dashed line), partially dissolved and brecciated D1 rhombs (arrows) engulfed by the D2 overgrowths. C: CCL image of a stylolite (yellow line) impacting both brecciated D1 dolomites and saddle dolomites D2. D: Partially dissolved stylolite, in dolomite matrix, filled with pink-stained, blocky calcite (in PPL). Glauconites (arrow) are also displaced and concentrated along the stylolite surface. E: CCL image of fracture walls lined with dull orange to brown blocky calcites. The crystal size increases towards the center of the fracture as indicated by the arrows. F: Same fracture under UV light with oil coatings (arrows) on top of the blocky calcites.

1.14. Anhydrites

A few creamy white to colorless tabular crystals of anhydrite constitute the last diagenetic phase in the sequence. Cleavage plans are parallel to the main growth axis. These anhydrites post-date calcite cements and dolomites and contain no aqueous or oil inclusions. Figure 19a shows a milky white to beige anhydrite crystal occluding dolomite intercrystalline porosity. Notice the brown oil-coatings over the dolomite rims.

1.15. Groundwater

Present-day operators of the Lacq field report the existence of the watertable at a depth of nearly 723 m. Ground water is thus added to the paragenesis as a separate phase.

1.16. Iron Oxides

This scarce phase is represented by brown to orange coatings surrounding a few pyrite crystals (Fig. 19b). Under reflected light, the coatings appear dark brown to black. The pyrites engulfed by the iron oxides show non-planar and altered crystal edges.

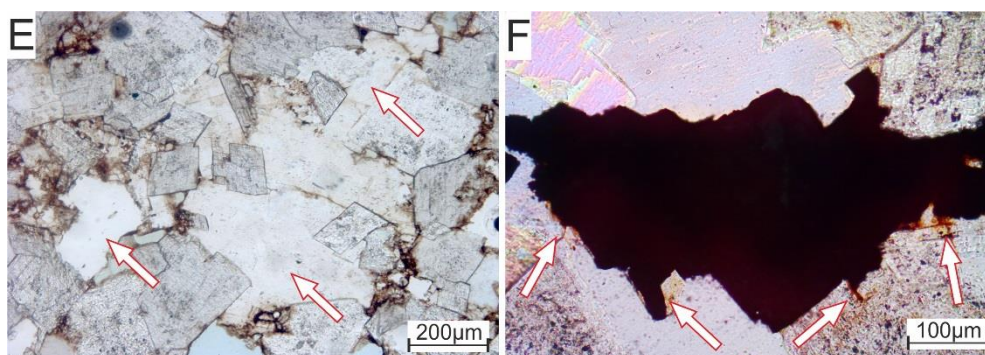


Figure 19. A: Tabular anhydrite crystals under plane-polarized light filling inter-dolomite porosity. Brown oil coatings are found on the rims of the dolomite crystals. B: Iron oxides (arrows) on the edges of a pyrite crystal. The colored crystal on the left corner is a tabular anhydrite.

2. Fluid Inclusion Studies

2.1. Petrography

Phases of interest with abundant aqueous inclusions are the D2 overgrowths, saddle dolomites and blocky calcites (Fig. 20). Fluid inclusions in the D2 dolomites (Fig. 20a) have two phases (liquid and gas) with rectangular to oval shapes and average sizes around 5-8 μm (Fig. 20b). Similarly, in the saddle dolomites, two phases of aqueous inclusions were identified in growth zones (Fig. 20c) and have rectangular to elongated shapes with sizes between 5 and 10 μm (Fig. 20d). The two-phase aqueous inclusions in blocky calcites (Fig. 20e) are larger, reaching up to 20 μm in size and with shapes ranging from geometric (rectangular, cubic and triangular) to lozenge and oblate (Fig. 20f).

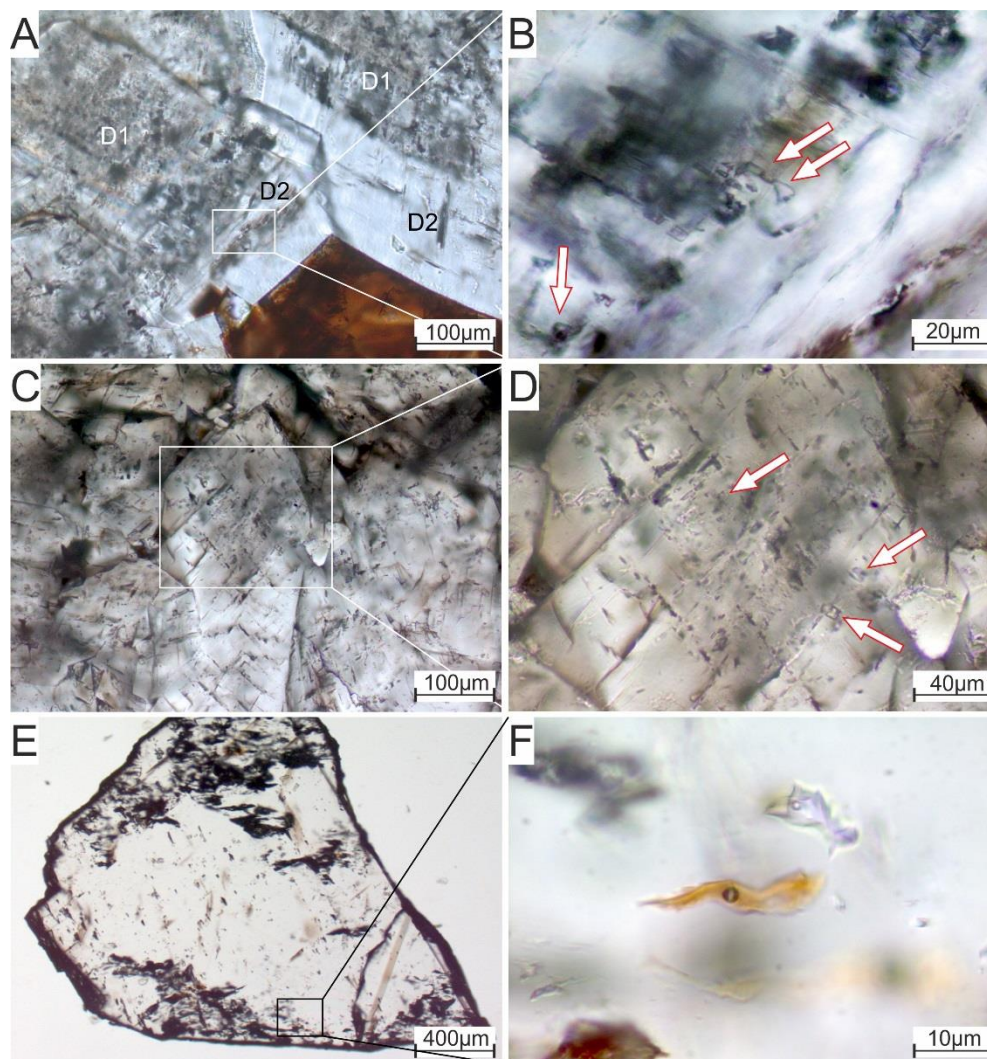


Figure 20. A: D2 overgrowth around D1 cores. B: Zoom of the image A showing two-phase aqueous inclusions (arrows) in D2. C: Large crystals of saddle dolomite with their typically curved edges. D: Zoom of the image C with rectangular two-phase aqueous inclusions (arrows). E: Crystal of blocky calcite containing patches of oil and aqueous inclusions. F: Zoom of the image E showing two-phase oil (orange) and aqueous (clear) inclusions.

Two types of oil inclusions occur in the blocky calcite of Upper Lacq. Under UV, the first type has a brown fluorescence, while the second type shows a strong white fluorescence. Both types of oil inclusions were observed very close to aqueous inclusions in the blocky calcite (Fig. 20f) and are absent from the D2 or saddle dolomite phases. This co-genetic association of oil and aqueous inclusions, and their absence in older diagenetic cements indicate that oil inclusions are primary. White fluorescent oil inclusions are rarely observed and possible the product of a late pulse of oil inclusions. Multiple pulses of oil migrations at the time of calcite cementation can explain the concomitant association of two populations of orange

and white-fluorescent oil inclusions co-genetically with the same population of the primary aqueous inclusions.

2.2. Fourier Transform – Infrared Spectroscopy (FT-IR)

Hydrocarbons with a brown fluorescence are characterized by a spectrum suggesting the occurrence of water and aromatics (Fig. 21), which are absent in the inclusions with strong white fluorescence. Both types of hydrocarbons have very low CH_4 content.

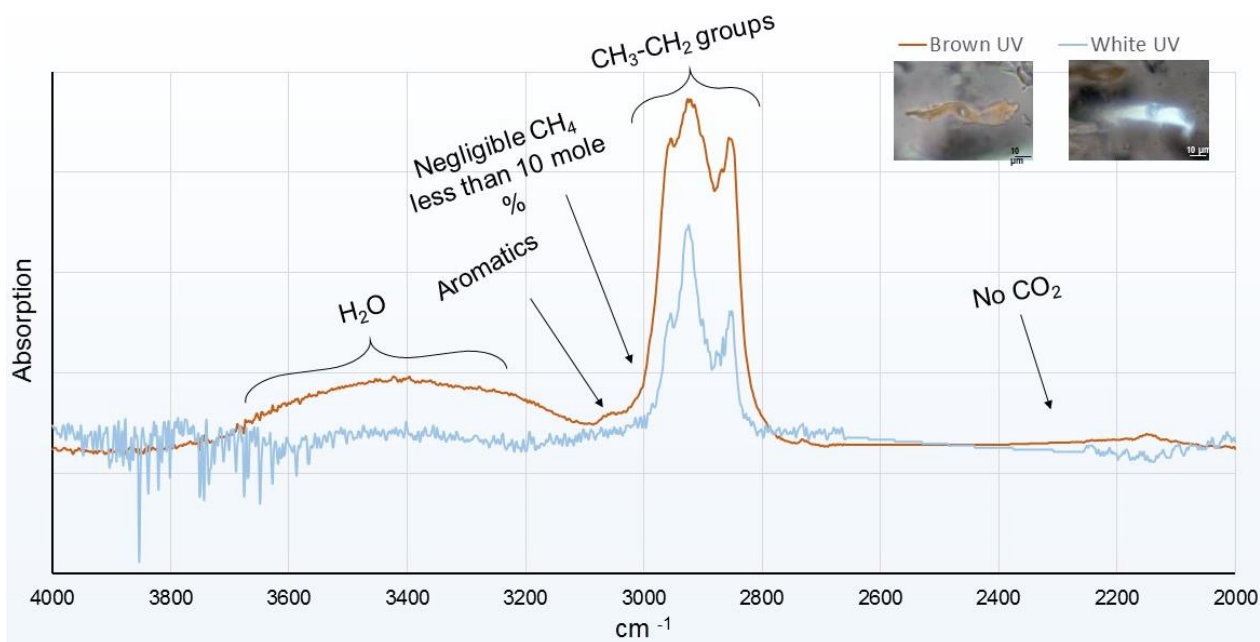


Figure 21. FT-IR spectra of the two types of oil inclusions

2.3. Microthermometry

Microthermometry data were obtained from fluid inclusions (FIs) in D2 overgrowths, saddle dolomites (Fig. 22a) and calcite phases (Fig. 22b). Because D2 and saddle dolomites are considered as different morphologies of the same phase, their FI data are joined together. All FIs in all the studied phases homogenized into the liquid phase, i.e. disappearance of the gas phase at T_h . FIs in D2 and saddle dolomites homogenized at a T_h mode ranging between 77 and 80°C. (Fig. 22a). T_h values for blocky calcites show a more restricted mode around 76 and 80°C (Fig. 22b). Oil inclusions with brown fluorescence in blocky calcites have T_h values between 56°C and 68°C with a T_h mode around 66-68°C. Oil inclusions with white fluorescence are rare and homogenize at around 70°C (Fig. 22b).

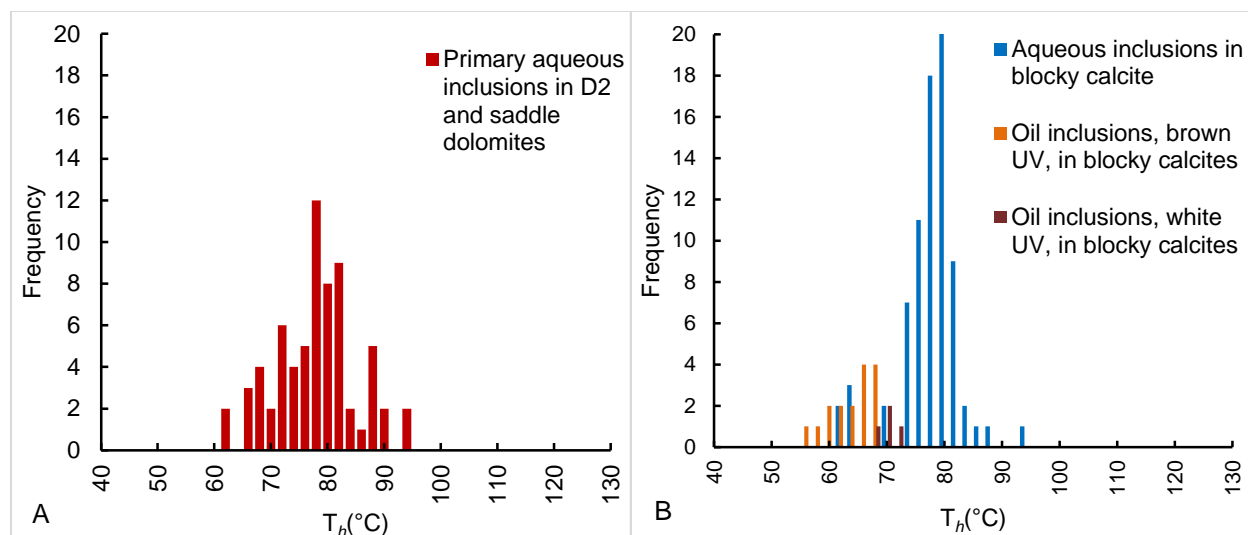


Figure 22: Frequency histograms of the homogenization temperatures of aqueous and oil inclusions in (A) dolomite and (B) calcite phases.

In the Albian reefs (Clansayesian Reef Formation) at depths of 1400-1403 m, the main inclusion type trapped in the blocky calcite phase is a brown-fluorescent oil homogenizing at around 76-80°C (Fig. 23a). Aqueous inclusions are very rare but homogenize in the same temperature range as the oil inclusions. After freezing down to -100°C, phase changes were observed, and final ice melting temperatures were recorded. Eutectic (T_e) or first-melting temperatures were difficult to record in most FIs, but in a few inclusions, first melting of ice with coexistence of solid (ice), liquid, and gas phases occurred between T_e of -21 to -22°C. Final ice melting temperatures were measured between -4 and -0.2°C. These values correspond to very low salinities, equal or lower than values of seawater (Fig. 23b)

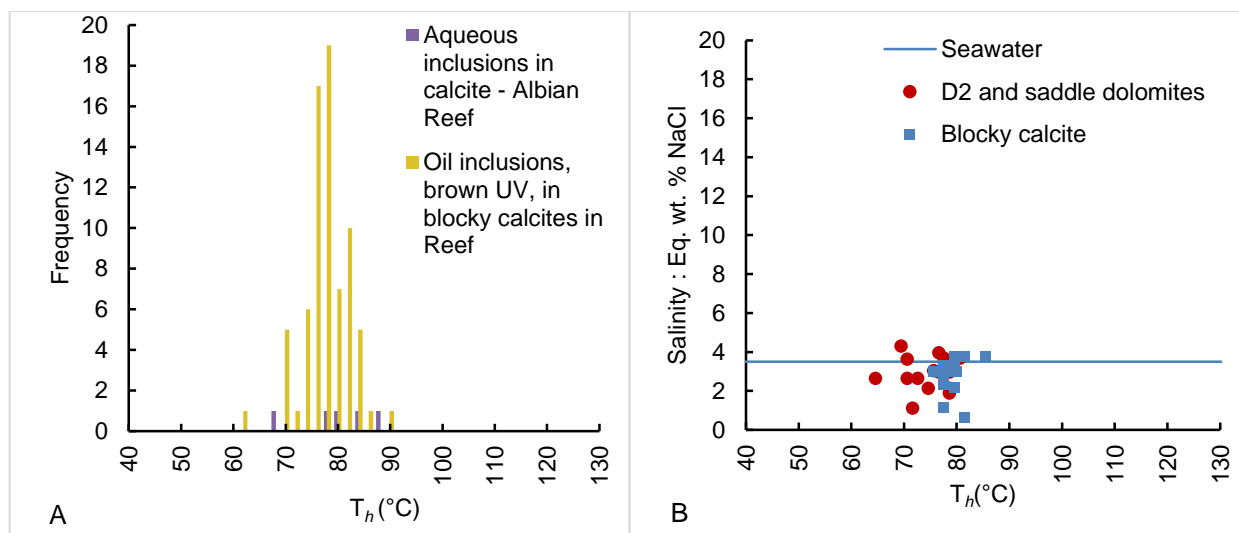


Figure 23. A: Frequency histogram of homogenization temperatures of aqueous and oil inclusions in the blocky calcite of the Albian Reef Formation B: T_h vs. salinity cross-plot of the studied phases.

2.4. Raman Spectroscopy

The very low salinities measured with microthermometry were confirmed by Raman spectroscopy. Analysis of the liquid phase in fluid inclusions of the blocky calcite reveal salinities ranging between 1.2-2.4 % eq. wt. NaCl. These values are in the same range that those obtained through microthermometry. Raman measurements made on the gas phases showed no CO_2 , CH_4 , H_2S or any other gas component except H_2O vapor. Unfortunately, high fluorescence in dolomites prevented the acquisition of reliable data.

3. Isotope Geochemistry

$\delta^{18}\text{O}$ and $\delta^{13}\text{C}$ composition were measured in four different carbonate phases (appendix 8): (1) the host rocks ($n=3$), (2) the dolomitized matrix constituted by a mixture of D1 and D2 dolomites ($n=28$), (3) saddle dolomites ($n=6$) and (4) the final blocky calcite ($n=6$; Fig. 24). The host rock powders were obtained from micritic lithologies to insure the absence of any contamination from diagenetic phases. A few sub-samples from each carbonate phase were further investigated by carbonate clumped isotope thermometry (Δ_{47}). Figure 24 and Table 3 report the average $\delta^{18}\text{O}_{\text{carb}}$, $\delta^{13}\text{C}_{\text{carb}}$, Δ_{47} , $T(\Delta_{47})$ and $\delta^{18}\text{O}_{\text{water}}$ results. The investigated carbonate rock has a “bulk” $\delta^{13}\text{C}$ values ranging from -1.5‰ to 3.6‰ (VPDB) and $\delta^{18}\text{O}$ ranging from -2.3‰ to -12.4‰ (VPDB). However, the genetically distinct phases show more homogeneous and clustered $\delta^{18}\text{O}/\delta^{13}\text{C}$ values, with respective $\delta^{18}\text{O}$ composition of -3.4 ± 0.8 ‰ for the host rock, -5.3 ± 1.2 ‰ for the

dolomitized matrix, $-8.7 \pm 0.4\text{‰}$ for the saddle dolomite and $-10.6 \pm 1.0\text{‰}$ for the last blocky calcite. Average $\delta^{13}\text{C}$ values are of $2.2 \pm 0.9\text{‰}$ for the host rock, $3.0 \pm 0.3\text{‰}$ for the dolomitized matrix, $2.0 \pm 0.8\text{‰}$ for the saddle dolomite, and $0.3 \pm 1.1\text{‰}$ for the blocky calcite. The $\delta^{18}\text{O}$ and $\delta^{13}\text{C}$ composition of the host rock fall within the range of expected values for biogenic calcites precipitated in equilibrium with Late Cretaceous seawater (Steuber, 1999). In contrast, the younger carbonate phases show a gradual depletion in $\delta^{18}\text{O}$ and $\delta^{13}\text{C}$.

Similarly, each carbonate phase displayed distinctive Δ_{47} compositions convertible into precipitation temperature estimations. Values obtained are of (1) $19 \pm 5^\circ\text{C}$ and $18 \pm 15^\circ\text{C}$ for the host rock, (2) $58 \pm 7^\circ\text{C}$, $63 \pm 2^\circ\text{C}$ and $56 \pm 7^\circ\text{C}$ for the dolomitized matrix samples, (3) 92°C (error unknown as only one measurement) for the saddle dolomite and (4) $76 \pm 5^\circ\text{C}$, $81 \pm 6^\circ\text{C}$ for the blocky calcite. As illustrated in figure 24b, the decrease in $\delta^{18}\text{O}$ values is correlated with an increase in Δ_{47} temperatures.

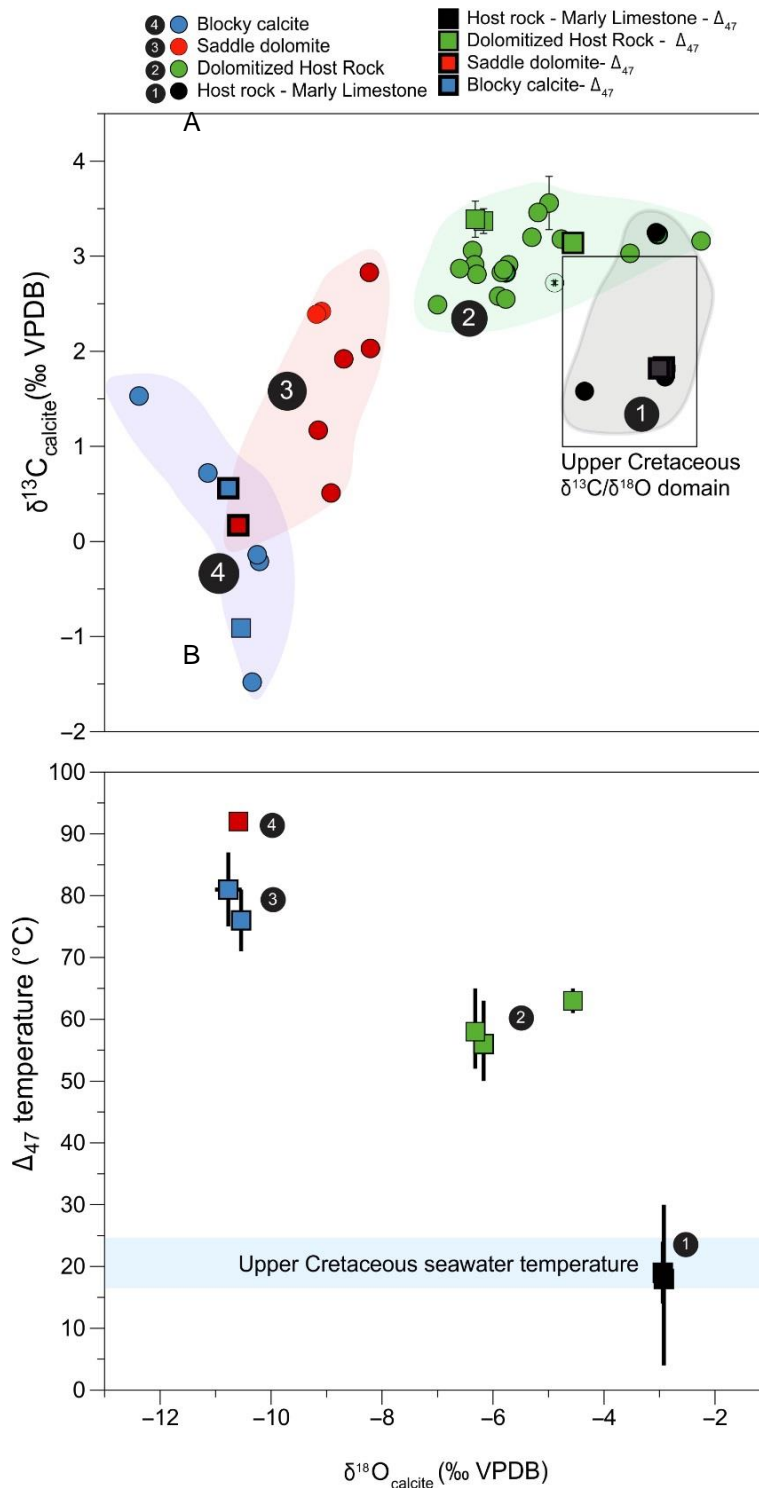


Figure 24. A: $\delta^{18}\text{O}/\delta^{13}\text{C}$ cross plot. Symbol colors refer to specific carbonate phases numbered from '1' to '4'. The colored areas highlight the dispersion of $\delta^{18}\text{O}$ and $\delta^{13}\text{C}$ values recorded for each carbonate phase. Square symbol represents the sample selected for clumped isotope measurements. When not shown, uncertainties are included in the symbol size. The black rectangle represents the expected $\delta^{18}\text{O}$ and $\delta^{13}\text{C}$ values of marine carbonate precipitated in equilibrium with Upper Cretaceous seawater (Steuber, 1999). B: Cross-plot of $\delta^{18}\text{O}$ versus $T(\Delta_{47})$. Uncertainties are reported as 1SD of the mean out of one to three replicates. Expected Upper Cretaceous seawater temperature is reported in the blue shaded area (Steuber, 1999).

Chapter 3 – Part I: Results: Upper Lacq - Isotope Geochemistry

Table 3. Stable isotope results ($\delta^{18}\text{O}$, $\delta^{13}\text{C}$ and Δ_{47}) of the samples set investigated.

Phase	n	$\delta^{18}\text{O}$		$\delta^{13}\text{C}$		Δ_{47}	Δ_{47} errors (‰)		$T(\Delta_{47})_{\text{error}} (1\text{SD}) (^{\circ}\text{C})$		
		‰VPDB	±STD	‰VPDB	±STD	CDES90 ⁽¹⁾	STD	SE	Mean ⁽²⁾	Min	Max
Blocky cal.	3	-10,77	0,03	0,56	0,24	0,463	0,011	0,006	81	87	75
Blocky cal.	3	-10,54	0,08	-0,91	0,09	0,473	0,010	0,006	76	81	71
Matrix dol.	3	-6,17	0,14	3,37	0,13	0,515	0,016	0,009	56	63	50
Matrix dol.	3	-4,56	0,04	3,14	0,1	0,500	0,004	0,002	63	65	61
Matrix dol.	3	-6,32	0,07	3,39	0,19	0,511	0,015	0,009	58	65	52
Saddle dol.	1	-10,59		0,17		0,442			92	-	-
Host rock	2	-2,92	0,05	1,83	0,04	0,624	0,043	0,030	18	32	6
Host rock	2	-2,94	0,22	1,82	0,05	0,621	0,017	0,012	19	24	14

"Note. Errors on average $\delta^{18}\text{O}$ and $\delta^{13}\text{C}$ are given as 1 S.D. Errors on samples Δ_{47} and $T\Delta_{47}$ are 1 SD of the mean values calculated out of replicate Δ_{47} measurements of the same powder.
(n) is the number of replicate measurements of the same carbonate powder
⁽¹⁾ Δ_{47} CDES90 are values relative to the 'carbon dioxide equilibrium scale' CDES, without acid fractionation correction.
⁽²⁾ Paleotemperatures calculated using the composite Δ_{47} -T calibration (Eq. 3 from Bonifacie et al. 2017)

The calculated oxygen isotopic compositions of the parent fluids ($\delta^{18}\text{O}_{\text{water}}$) are of -1.9 to -1.7‰ SMOW for the host-rock, -0 to -6.0‰ SMOW for the dolomitized matrix, +1.5 to +2.0‰ SMOW for the saddle dolomite and 0 to +3.5‰ SMOW for the blocky calcite (Fig. 25).

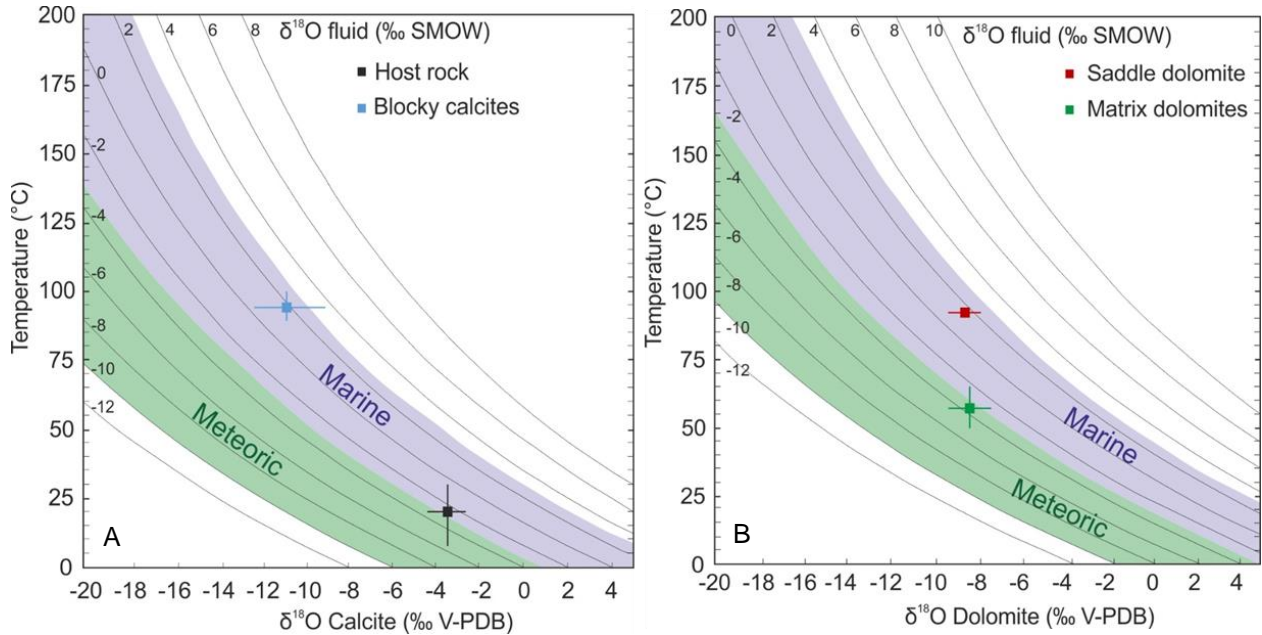


Figure 25. A: Fractionation curves of O'Neil et al., (1969) to investigate the parent fluids of calcite phases. B; Fractionation curves of Horita et al., (2014) for the parent fluids of dolomite phases. The average signatures of the parent fluids derived from marine and meteoric sources are represented with the blue and green shaded areas respectively.

Multiple sulfur isotopes analysis on CAS resulted in $\delta^{34}\text{S}$ of $20.00\text{‰ V-CDT} \pm 0.013\text{‰}$, $\delta^{33}\text{S}$ of $10.28\text{‰ V-CDT} \pm 0.016\text{‰}$ and $\delta^{36}\text{S}$ of $37.85\text{‰ V-CDT} \pm 0.091\text{‰}$. From these values, $\Delta^{33}\text{S}$ and $\Delta^{36}\text{S}$ were calculated and yielded values of $-0.487\text{‰} \pm 0.016\text{‰}$ and $-0.487\text{‰} \pm 0.091\text{‰}$, respectively.

4. Major and trace element analysis

4.1. Fe-S

The breakdown of pyrite (FeS_2) to pyrrhotite (FeS) releases free sulfur which can be absorbed by metals to allow mineral deposition, or can be used as a pre-requisite for TSR reactions (Zhabin and Kremenetskiy, 1993). After normalizing the atomic percentage of Fe and S in each spectral location on the sulphide crystals (Fig. 26), the data indicate a nearly uniform ratio of $\text{Fe/S} = 0.5$, typical of pyrite and not pyrrhotite.

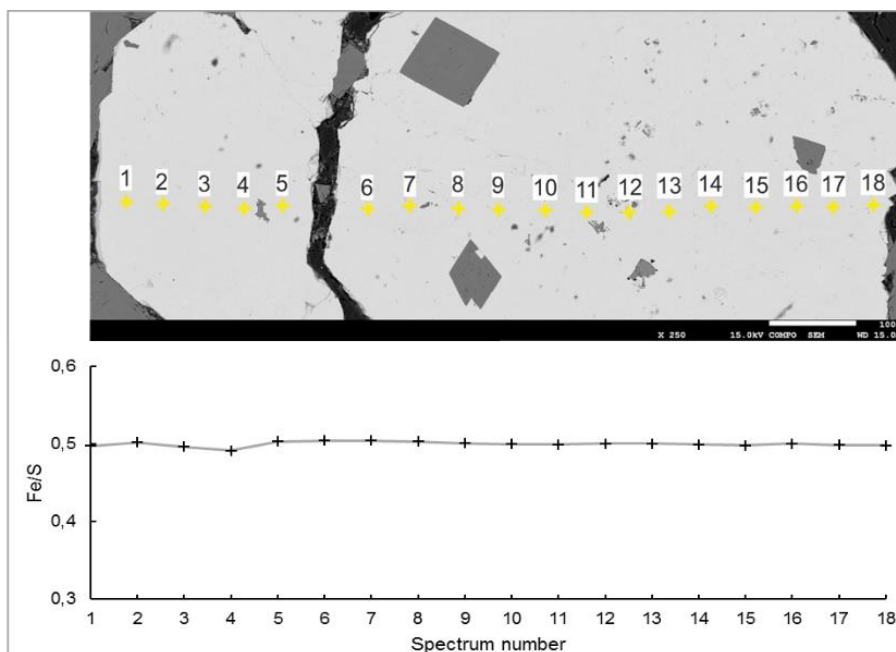


Figure 26. SEM-EDS photomicrograph of a sulphide crystals with the location of spectral measurements and the resulting ratio of Fe and S.

4.2. REE

REE concentrations were obtained from micritic limestones, matrix and saddle dolomites, and the calcite cements. Figure 27 presents the PAAS-normalized REE patterns plotted on a logarithmic scale. Micrites are more enriched in REE than the dolomite and calcite phases. Also, the middle REE elements show a bulge pattern with slightly higher concentrations than the light and heavy elements. In the case of the matrix

dolomites, Tm concentration was lower than the detection limit of the spectrometer and a valid measurement was therefore not possible.

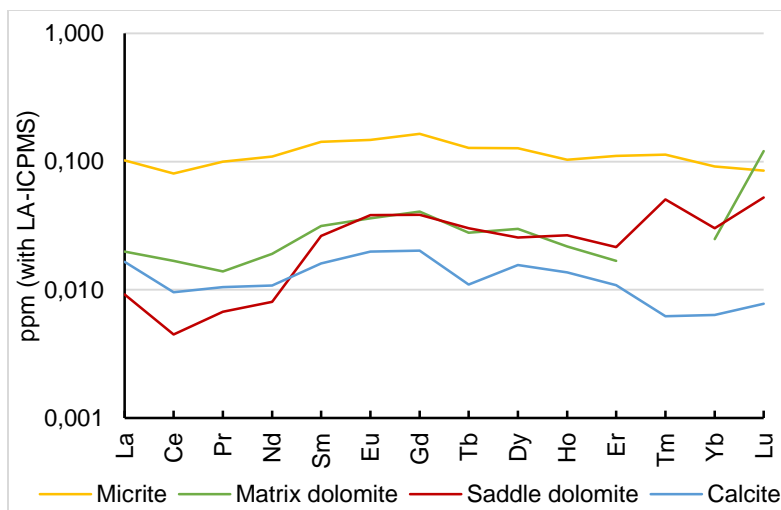


Figure 27. PAAS-normalized REE pattern of the micritic host rock, matrix dolomites, saddle dolomite and calcite. Patterns of dolomite and calcite phases show a bulge (relative enrichment) in the middle REE.

4.1. U-Pb LA-ICPMS absolute age dating

In order to obtain absolute dating with the U/Pb method on calcite and dolomite phases 15 measurements were performed with LA-ICPMS to estimate the U and Pb elemental concentration. Obtained concentrations are in the range of 0.001 to 0.005 ppm for U and Pb and were thus too low to meet the minimum requirement for absolute age dating (table 4).

Table 4. U-Pb data acquired through LA-ICPMS on selected phases from Upper Lacq. The obtained results are too low to allow absolute age dating.

Sample	Mineral Phase	Pb (ppm)	U (ppm)	Error
LA37_691-693	Blocky Calcite	0,256	0,0058	0,0021
	Matrix Dolomite	0,508	Below detection limit	0,035
	Saddle Dolomite	0,409	Below detection limit	0,011
	Saddle Dolomite	0,275	Below detection limit	0,02
LA37_708-709	Blocky Calcite	0,596	0,0074	0,0023
	Saddle Dolomite	0,939	Below detection limit	0,0085
	Matrix Dolomite	1,022	Below detection limit	0,019

5. Fluid inclusions thermodynamics modeling

Petroleum inclusion thermodynamic (PIT) and aqueous inclusion thermodynamic (AIT) modeling were applied to the oil and aqueous inclusions of the blocky calcite. The orange-fluorescent oil inclusions were selected for this technique as they are larger, clearer and cause less fluorescent noise than the rare white-fluorescent oil population. This step allowed the construction of isochores for the two inclusion types and allowed to estimate P-T conditions of trapping indicated by their intersection domain. The inclusions used are coeval primary inclusions selected during petrographic analysis (Chapter 3 – Part I – section 2.1). Initial attempts to construct the phase diagrams of oil inclusions via PIT software were made using the radii measured from the CSLM fluorescent photomicrographs and with manual selection of the threshold values without any mathematical processing of the pixels. These effects have resulted in exaggerated liquid/vapor ratio that led to erroneous phase diagrams as the one displayed in figure 28a. With such a diagram, the trapping pressures would be around 240-360 bars.

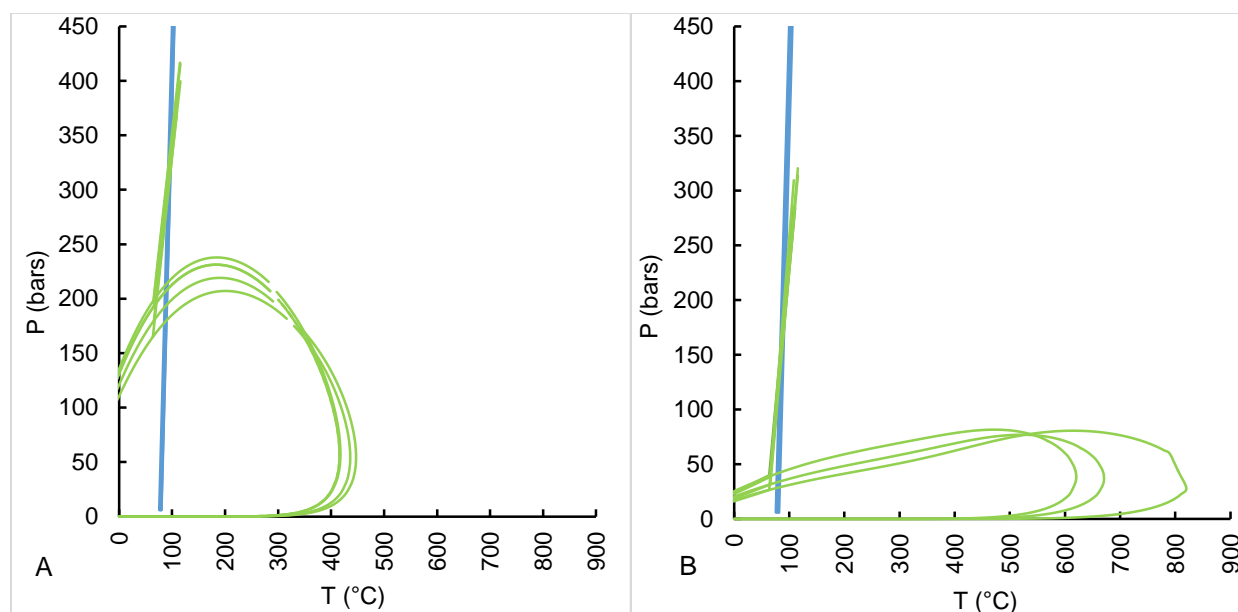


Figure 28. A: Erroneous phase diagram of oil inclusions in blocky calcites of Upper Lacq using the radii measured from the CSLM fluorescent photomicrographs and with manual selection of the threshold values without any mathematical processing of the pixels. B: Corrected phase diagram constructed following the protocol described in chapter 2 section 4.5.

Corrected results indicate a trapping temperature between 82 and 92°C at pressures of 136-210 bars respectively (Fig. 28b). For the Albian reef located at a depth of 1400m, the double-isochore technique was not possible due to the scarcity of aqueous inclusions and the difficulty in accurately determining their co-genetic relationships with the oil FIs.

By using the confocal scanning microscopy and associated image processing, the volume of gas can be used to obtain a qualitative assessment of the type of trapped oil. Figure 29 displays the evolution of 8 different types of reference oils (Bourdet et al., 2008) with the results for Upper Lacq and Albian reef oils. The close association of the plotted Lacq oil to the North American Black Oil indicates that the Lacq oil is heavy.

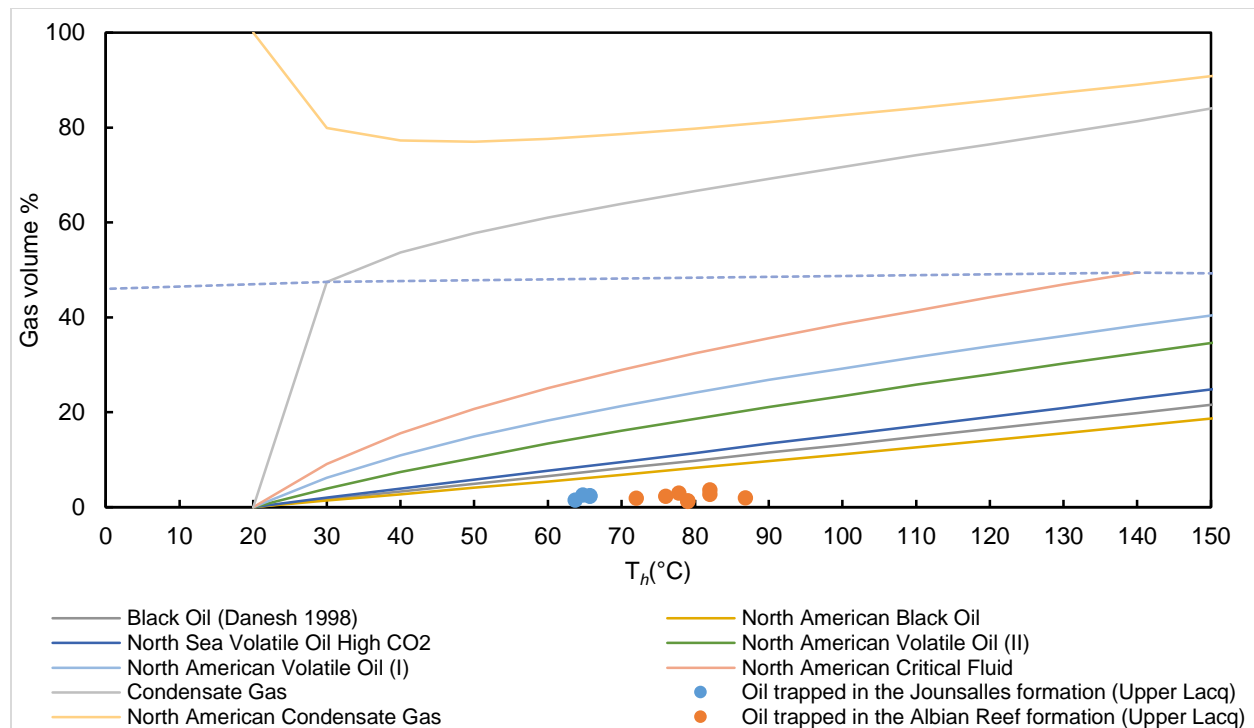


Figure 29. Gas volume % vs. T_h trends for 8 different reference oils with plotted results for Upper Lacq and Albian reef oils. L-V line separates the homogenization to the liquid domain below from the gas domain above. Modified after Bourdet et al., (2008).

6. Basin modeling

6.1. Basal heat flow scenario

Modeling the syn-rift to post-rift basal heat flow requires taking into account the thermal maturity of organic material using vitrinite reflectance data as well as the geodynamic history of Lacq since the late Aptian. This history includes (i) the Albo-Aptian rifting, followed by (ii) an erosion phase during the Late Albian - Early Cenomanian, (iii) a phase of post-rift cooling during the Cenomanian - end Santonian, and (iv) the principal inversion and shortening episode during the Eocene. These input data constrain a best-fit model where the heat flow reaches a peak of about 130 mW/m² during the Aptian extension before a decrease to

nearly 45 mW/m² at the onset of N-S convergence. These values were modeled to obtain an acceptable present-day geothermal gradient of 30°C/km. Such a geothermal gradient is reasonable since the foreland basin was superimposed directly on a still-hot rift with ongoing thermal subsidence that is driven by the post-rift thermal cooling (Angrand et al., 2018).

6.2. Thermal history reconstruction based on vitrinite reflectance fitting

Vitrinite reflectance measurements are plotted according to their stratigraphic location in figure 30. Basin modeling results in an acceptable fit between the modeled thermal gradient (black line in figure 30) and the measured vitrinite reflectance values. The thermal maturity of Upper Cretaceous formations follows a normal burial trend, interrupted by a minor erosional event on the base Oligocene boundary. Our modeling assumes 200 meters of eroded material at the base Cenomanian unconformity, and 400 meters during the maximum exposure at the base Oligocene unconformity. These values take into account the shape of the onlaps and toplaps of reflectors on both sides of the unconformities (Fig. 8).

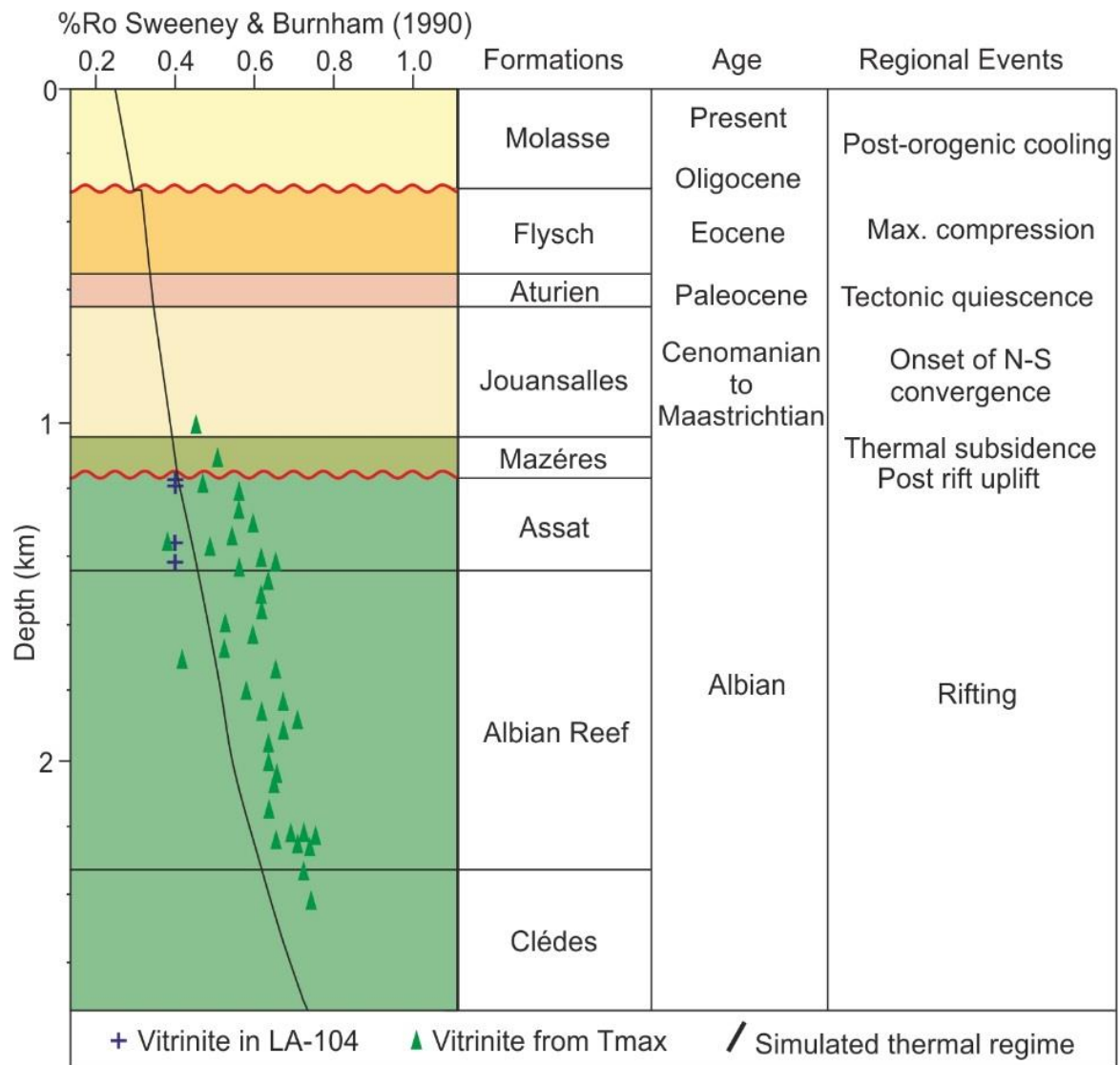


Figure 30. Simulated thermal regime in Petromod constrained by vitrinite reflectance measurements.

Chapter 3 – Part II: Discussions and interpretations: Upper Lacq

1. Paragenesis and fluids involved

The chronological sequence of diagenetic phases deduced from petrographic observations is represented in figure 31.

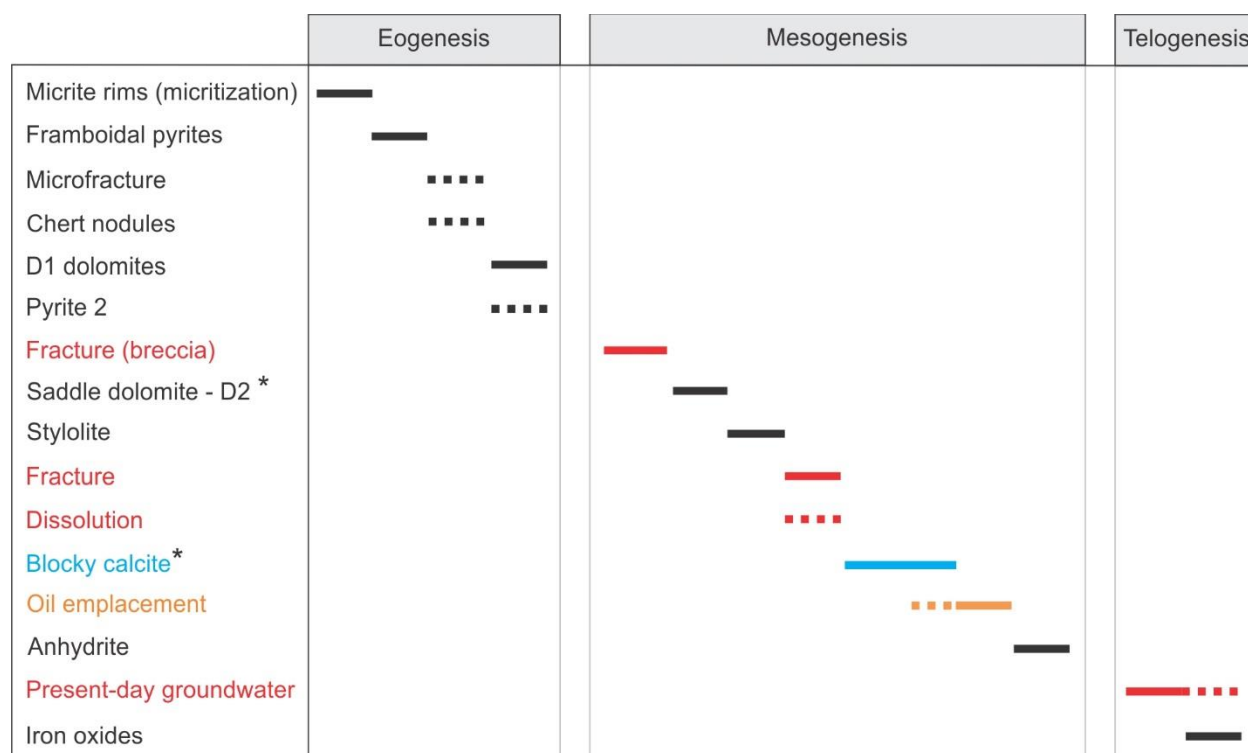


Figure 31. Chronology of diagenetic phases and fracturing events observed in Upper Lacq from oldest at the top to youngest at the base. Dashed lines correspond to phases whose exact paragenetic timing cannot be precisely constrained. Asterisks* indicate the phases investigated here in thermometric studies (FI and Δ_{47}).

The wackestone/packstone facies precipitating in a shallow marine depositional environment has been characterized by Δ_{47} thermometry. Carbonate clumped isotopes show surface temperatures around 20°C and $\delta^{18}\text{O}$ of parent fluids around -1.9 ‰SMOW (Table 3). These values (1) point towards precipitation conditions in a shallow marine depositional environment, by marine fluids with a potential meteoric water influx and (2) demonstrate the absence of significant recrystallization of the host-rock during burial.

During eogenesis, microborers and bacterial activity resulted in destructive micritization of carbonate clasts with the micrite envelope developing from the edges to the center of the grain (Bathurst, 2007). Framboidal pyrites precipitated as a result of bacterial sulphate reduction (BSR) of organic matter just below the surface of the sediment (Machel, 2001). Such an interpretation is supported by the distribution of framboidal pyrites that are mainly associated with skeletal grains and micritized rims. The relative timing of silicification is difficult to constrain as chert nodules were observed only in micritic, non-dolomitized samples. However, given the occurrence of siliceous sponges (Fig. 17f), the timing was relatively early as diagenesis of amorphous organic silica is favored by pH variations due to the degradation of organic matter at low temperature during early burial (Hinman, 1990). Silica was likely provided by siliceous sponges after the death of organisms and locally reprecipitated by replacement of the micritic matrix. Early diagenesis ends with the D1 dolomites. Their non-luminescence and $\delta^{18}\text{O}$ of parent fluids of -1.6 to +1.2‰SMOW (Fig. 25) suggest a mixing between oxidizing meteoric fluids and trapped formation fluids, of a marine origin, that can provide Mg needed for this volumetrically-limited dolomite phase. Since the bulk powders extracted from the matrix dolomites are a mixture of D1 and D2 dolomite phases, the Δ_{47} temperature of around 60°C could reflect an average between these two end-members. Pyrite 2 post-dates D1 rhombs since relics of D1 were observed inside pyrites. Merino and Canals (2011) argue that if the dolomitizing fluids contain some metals, and if enough organic matter is present in the host carbonates, pyrites should precipitate during and after the dolomitization phase by the reduction of aqueous sulphates released from organic carbon. The non-ferroan composition of all dolomite phases in Upper Lacq, as well as contacts between some pyrite 2 and the D1 dolomite are in accordance with such a mechanism. Any Fe^{2+} in the dolomitizing fluids was likely consumed by the precipitation of reduced sulfur species, and the dolomitizing fluid was then depleted in iron. The scarce distribution and limited quantity of pyrites observed suggest that initially the quantity of Fe^{2+} in the dolomitizing fluids was actually low. A similar mechanism has been demonstrated in the Neogene Monterey and Sisquoc Formations in Santa Maria Basin, California (Compton, 1988).

During mesogenesis, the Upper Lacq reservoir experienced its main diagenetic modifications. Here we consider that mesogenesis is the burial domain isolated from surface-related processes while telogenesis occurs during the late stage of exhumation when oxidizing surficial fluid enter in the diagenetic system. Mesogenesis started with an episode of fracturing and brecciation that generated new pathways for

dolomitizing fluids. Some breccias are cross-cut and cemented by D2 and saddle dolomite, suggesting that these dolomites formed during or just after fracture opening. Therefore, after the early D1 phase, new dolomitizing fluids circulated along fractures and precipitated D2 as overgrowth cements in intercrystalline pores or as pore-filling saddle dolomite crystals in the open fractures. This dolomitization possibly occurred under high pressures given the occurrence of breccia and fractures in these dolomitized facies. Differences in dolomite sizes and extinction behavior can be attributed to the crystallization space available (Machel, 2004). Using Δ_{47} temperatures, more depleted values of -0.6 ‰SMOW were obtained for D2. These isotopic signatures point toward a marine source. Post-dolomitization diagenesis involved fracturing, calcite cementation, and oil migration. A second fracturing phase preceded the precipitation of the blocky calcite. FIs in calcite have a T_h range of 70-90°C with highest modes at 80°C, with salinities being equal to or lower than that of seawater (Fig. 23b). The $\delta^{18}\text{O}$ of the parent-fluids precipitating the calcite is in the range of +0.4 to +0.8 ‰SMOW (table 3), typical of a marine source. The opening of new fractures and circulation pathways for the parent-fluids of the blocky calcite may have connected the Upper Lacq reservoir with new reservoirs of trapped connate fluids depleted in Mg. This fluid pulse is distinct from that responsible for dolomite precipitation especially in that it is associated with oil migration. Several pulses of oil migration can explain the coexistence of two types of oil inclusions in the same calcite cement. Scarce inclusions with a strong white fluorescence, and containing water, as indicated by FT-IR spectra, are probably more mature than inclusions with brown fluorescence. They are therefore associated with a second pulse of oil migration. A third pulse is assumed to be responsible for the oil coatings on top of calcite. This last pulse was important enough to allow an economically valuable infill of the Upper Lacq reservoir. PIT modeling also demonstrates that the oil trapped as inclusions in the blocky calcite phase is heavy. This is in agreement with Connan and Lacrampe-Couloume (1993) who propose that the oil in Upper Lacq originally migrated as heavy oil and was not a consequence of post-migration modifications.

After calcite cementation and oil emplacement, anhydrites precipitated. The multiple sulfur isotopes signatures of CAS are listed in table 5 and are compared with the Eocene marine fluids signatures (Crockford et al., 2019 and references therein). The overlap in the results indicates a marine seawater origin for the parent fluids.

Table 5. Multiple sulfur isotope signature of CAS from anhydrite-rich samples (this study) and those of the reference Eocene seawater of Crockford et al. (2019) and references therein.

	This study		Eocene marine water	
	Value (‰ V-CDT)	Error (‰ V-CDT)	Value (‰ V-CDT)	Error (‰ V-CDT)
$\delta^{34}\text{S}$	20.00	± 0.013	22.87	± 7.86
$\Delta^{33}\text{S}$	0.036‰	± 0.016	-0.001	± 0.042
$\Delta^{36}\text{S}$	-0.487‰	± 0.091	0.713	± 0.508

The presence of calcium sulphates provided a source for this anhydrite phase, which can precipitate after Mg depletion, as previously documented in the dolomitized Devonian reservoirs of Alberta, Canada (Butler, 1970; Mountjoy et al., 1999; Machel, 2004).

During telogenesis, meteoric fluids were laterally re-introduced in the diagenetic system. Vertical input is unlikely given the integrity of the Paleocene seal. Late input of meteoric fluids is supported by the occurrence of present-day groundwater in the Upper Lacq reservoir at a depth of -723 m. Groundwater samples, collected from Upper Lacq, were analyzed for their δD and $\delta^{18}\text{O}$ isotopes by Esquevin et al. (1987) and are plotted against the Global Meteoric Water Line (GMWL) in figure 32. The results show that the groundwater in Upper Lacq is slightly modified and enriched with $\delta^{18}\text{O}$ relative to the GMWL. This enrichment indicates that the groundwater in Upper lacq were modified since entering the subsurface domain and could be the result of fluid-rock interactions and possible contributions of $\delta^{18}\text{O}$ -enriched formation fluids.

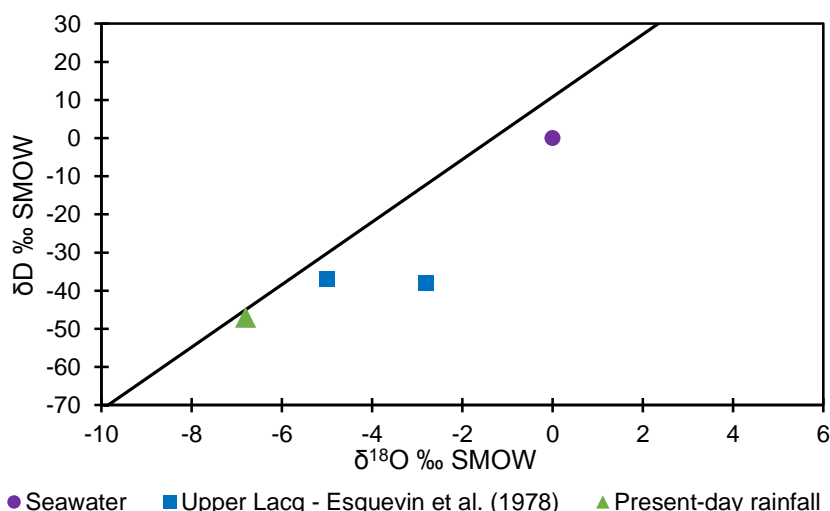


Figure 32. δD vs. $\delta^{18}\text{O}$ in ‰ SMOW for the groundwater collected from Upper Lacq plotted against the Global Meteoric Water Line (GMWL). Isotopic values of the present-day rainfall are also added, sourced from IAEA (2018). The slight

enrichment of the groundwater in Upper Lacq compared to the GMWL and the present-day rainfall could be the result of mixing with $\delta^{18}\text{O}$ – enriched formation fluids or contamination by the host rock.

The mixing of this groundwater with H_2S , possibly of a deep TSR origin, currently present in and commercially extracted from the Lacq reservoirs may contribute to sulfuric acid speleogenesis (SAS) that can explain the karstic cavity at a depth of nearly 2200 m reported in the drilling reports of LA – 101. Similar cases of SAS have been recently documented in Jurassic and Cretaceous carbonates of the north Pyrenean foothills and the southern Aquitaine foreland basin (Laurent et al., 2019).

In summary, three different origins of fluids contributing to diagenesis can be documented; these are: (1) a mixture of meteoric and marine fluids precipitating D1 dolomites, (2) another mixture of marine and clay-released fluids for saddle dolomite, calcite and anhydrite cements, and then a (3) modified meteoric source for the present day groundwater in the reservoir. A clay source of fluids is supported by the ultrafiltration effect and the dilution of the salinities as detected by the fluid inclusions studies.

An important criterion to consider here is the amount of magnesium required for dolomitization and its possible sources. Several sources can be involved such as: (a) Mg derived from the Triassic evaporites of the core of the Lacq anticline, (b) serpentization reactions close to the exhumed mantle domain, which could have released Mg into the fluids, (c) Mg-rich fluids released from the compaction and dewatering processes of the Albo-Aptian Ste-Suzanne and Assat marls. Mg sourced from the salt diapir in the core of the anticline is ruled out because of the very low salinities measured in the aqueous fluids inclusions of the D2 and saddle dolomite phases.

Serpentization- or mantle-derived Mg from the exhumed mantle domain is plausible given the geodynamic setting and the proximity to the exhumed mantle bodies, e.g. Sarrance anticline and Arbailles Massifs (Salardon et al., 2017). However, such a deep source would provide higher values of $\delta^{18}\text{O}$ ‰ SMOW and inclusions should contain evidence of mantle-derived CO_2 or H_2 . The lack of supporting evidence in the studied samples makes it difficult to support this hypothesis.

Clay dewatering is a very likely candidate to provide the amount of Mg required for dolomitization. The Apto-Albian Sainte Suzanne and Assat Marl Formations reach considerable thicknesses of more than 5 km in the southern Lacq basin (Fig. 8; Biteau et al., 2006). Such a thickness would contain enough Mg, trapped

in formational fluids that were expelled along faults and fractures and dolomitized the Upper Lacq reservoirs. Fluids generated by dewatering are characterized by low salinities because of the reduction of the total dissolved salts (TDS) through clay ultrafiltration (Tremosa et al., 2019), an increase in the $\delta^{18}\text{O}$ signature upon clay dehydration (Minami et al., 2018), and an enrichment in Mg due to the diagenetic smectite-illite transformations (Schrijver et al., 1996).

As supported by the isotope geochemistry, the parent fluids of saddle dolomites and calcites were marine in origin. These marine fluids, trapped as connate waters in deep part of the basin, were expelled during the first fracturing phase that opened new circulation pathways. During their migration, it is possible that the fluids were modified by mixing with low salinity Mg-rich fluids generated by clay dewatering.

2. Redox conditions

The nonluminescence of D1 dolomites and the contribution of meteoric fluids, at very shallow depths suggest that the first dolomitizing fluids were oxidizing. Later fluids involved in saddle dolomitization and calcite cementation were relatively enriched in middle REE (MREE). Such a REE pattern can be interpreted as the signature of fluids circulating in a reducing environment (Haley et al., 2004). Further indications of this reducing state are provided by the dull red and dull orange luminescence of the saddle dolomite and calcite respectively (Barnaby and Rimstidt, 1989). In addition, such a reducing system is also in agreement with the presence of not biodegraded and unoxidized oil inclusions in calcites. During telogenesis, oxidizing conditions were recovered with the present-day groundwater at the origin of the oxidization of the pyrite 2.

3. Hydrothermal activity

To better constrain the evolution of P-T conditions during the burial history of the Upper Lacq reservoir, fluid pressure gradients need to be estimated. Figure 33 illustrates the evolution of hydrostatic and lithostatic pressure gradients (through Petromod 1D) experienced by the Upper Lacq reservoirs assuming a geothermal gradient decreasing from 110°C/km during the peak Aptian rifting to 50°C/km in the present day (Angrand et al., 2018; Renard et al., 2019). Cooling between 88.6 and 83.5 Ma is a continuation of the isostatic rebound after the Aptian rifting. The loop in the gradients (between 40 and 33.9 Ma) is caused by the base Oligocene unconformity. The intersection of the oil and aqueous inclusions isochores indicate

the range of trapped P-T conditions obtained with PIT-AIT modeling. These conditions are not in equilibrium with the thermal evolution of the reservoir. The good match observed between temperature estimates based on two independent geothermometers (fluid inclusions with the double isochore technique and carbonate clumped isotope thermometry, figure 33) strongly support the reliability and accuracy of each thermometer (c.f. see Mangenot et al., 2017). The two techniques reveal a thermal disequilibrium between the mineralizing fluid and the host-rock. Indeed, a gap of at least 30-40°C, between the maximum burial temperatures and the minimum trapping conditions, is observed. This suggests that the parent fluids of calcites and similarly of dolomites were hotter than the burial temperatures and hence imply the involvement of hot hydrothermal fluids.

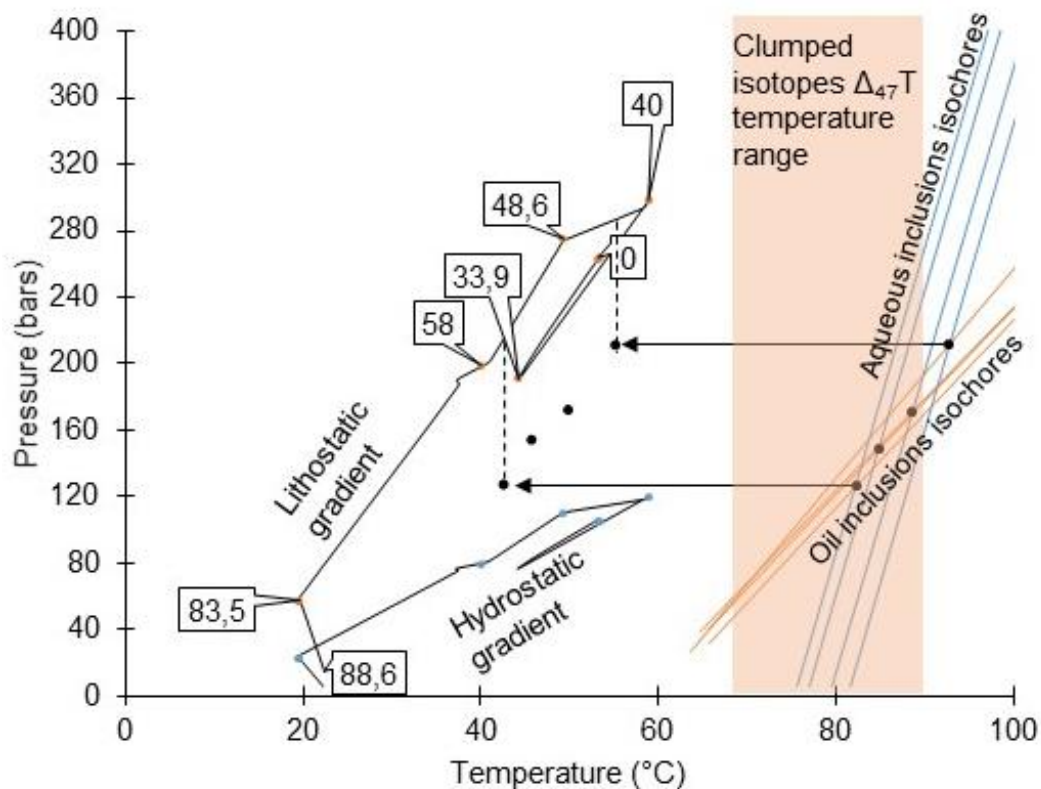


Figure 33. P-T trapping conditions and evolution of fluid pressure gradients simulated with Petromod-1D and PIT-AIT respectively. Numbers in tags are ages in Ma. The pink area represents the calcite temperature estimation deduced from Δ_{47} thermometry (i.e. an isotopic thermometer independent of any pressure effect). The intersection of both isochore types indicates the trapping conditions of inclusions in blocky calcites. The loop in the hydrostatic and lithostatic gradients represent the base Oligocene unconformity at 40-34 Ma. The arrows correspond to the extrapolation of the P-T conditions to the domain between the hydrostatic and lithostatic fluid pressure.

However, by extrapolating the pressure range of the fluids to the domain between hydrostatic and lithostatic gradients (arrows in figure 33), a timing between 60 and 40 Ma can be estimated. This age corresponds to

the Selandian-Bartonian (Paleocene to mid-Eocene), during the Pyrenean compression. In the Rousse reservoir, 30 km southeast of Lacq (Fig. 7), Renard et al. (2019) concluded that one of the two fluid pulses experienced by the Rousse system was due to Eocene Pyrenean tectonic compression. By measuring the difference between the trapped FI pressure and the hydrostatic pressure gradient, a minimum estimate of the overpressure of nearly 80 bars can be estimated. Such an overpressure is very common in oil-producing anticlines.

Further evidence that supports the hydrothermal activity are data provided by the well LA-415 (400m east of LA-37, Figs. 7 and 8). This horizontal NNE-SSW-oriented well on the crest of the Lacq anticline penetrated the productive reservoirs of Upper Lacq and cross-cut N100° and N60° trending vertical fractures (Fig. 34). The close association of fractures and dolomite bodies was interpreted as evidence of fracture-controlled hydrothermal dolomitization (Lambert et al., 2006).

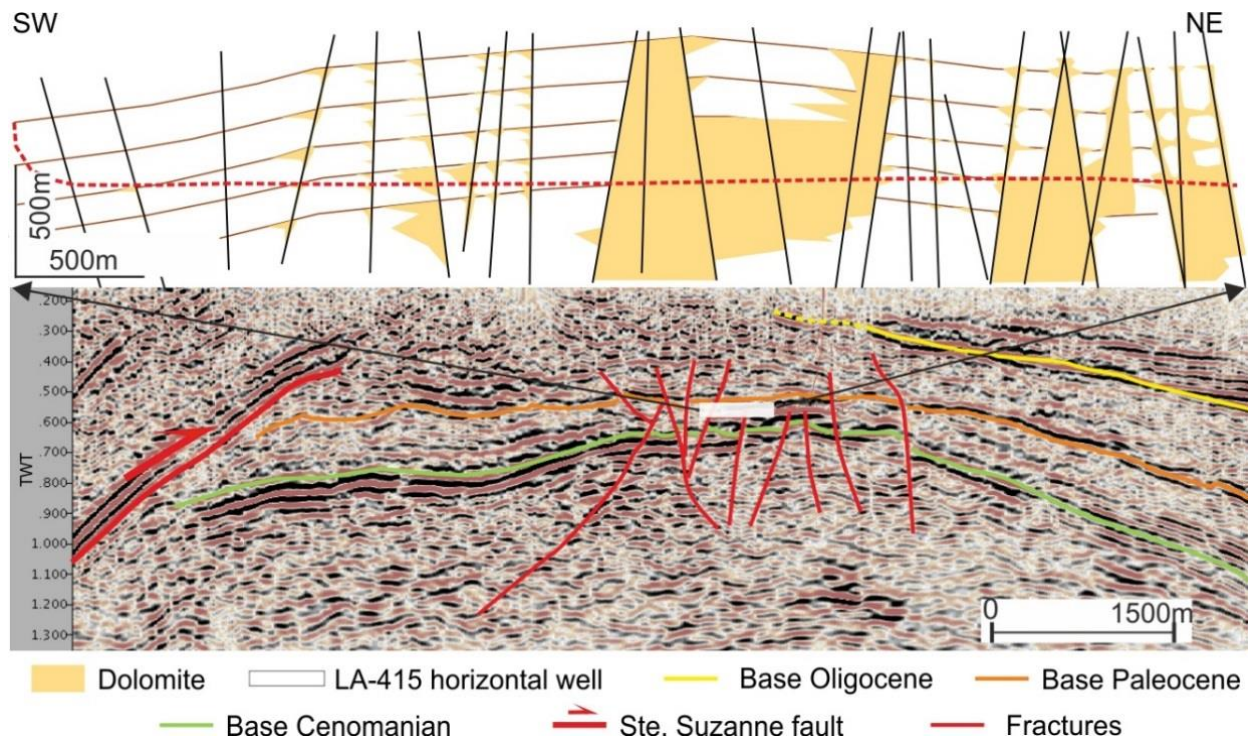
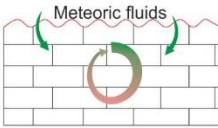

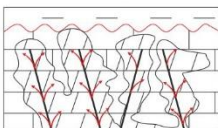
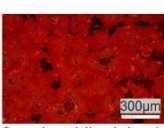
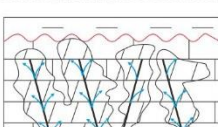
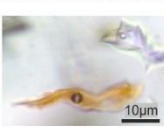
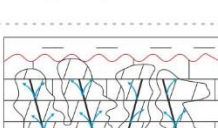

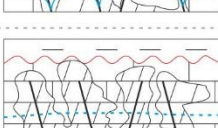



Figure 34. Schematic model of the distribution of dolomite bodies based on the observations of the well LA-415 (trajectory shown in dashed red line). The fractures drawn in the scheme were identified on the larger scale NE-SW seismic cross section (Based on Lambert et al., 2006).


4. Fluid circulation schemes


A synthesis diagram of all fluids involved in the diagenetic evolution of the Upper Cretaceous Upper Lacq reservoir, their circulation pathways and resulting products are summarized in figure 35. The early oxidizing meteoric to marine fluids involved in the precipitation of the D1 dolomite rhombs are relatively early since the Paleocene seal was not in place to prevent the vertical circulation of fluids to the reservoir. Mixing zone dolomitization models can explain this process in a lagoonal and shallow marine setting on the carbonate platform behind the Albian reef barrier. The seawater percolating downwards and the interstitial formation fluids provided the Mg required for this minor dolomitization phase. When the Paleocene flysch was deposited, the vertical supply of meteoric fluids was interrupted. The clay-released fluids from the thick Albo-Aptian formations in the Southern Lacq basin (Fig. 8) became the dominant fluids involved in hydrothermal dolomitization (Fig. 35). The thermal disequilibrium and the heat source can be provided by the burial gradient as the fluid pool is likely to be in the deeper parts (>3 km depth) of the South Lacq Basin. The Sainte Suzanne Fault, activated during the Eocene compression, could have provided a pathway for the circulation of deep connate hot fluids from the Southern Lacq Basin to the relatively cooler, lower pressure area on the crest of the Lacq anticline. This fault crosscuts the clay-rich Albo-Aptian formations (i.e. Sainte Suzanne and Assat marls), which, upon fracturing and squeezing, may have released Mg-rich fluids with low salinity. Additional Mg could have been provided by the precursor D1 dolomites, which were partially dissolved upon fracturing and brecciation. Evidence of partial dissolution of precursor dolomites can be found in the partially corroded rims and dissolved cores as seen in figure 18B.


The mixing zone dolomitization model agrees with previous interpretations that considered the dolomites of Upper Lacq as being early products that precipitated in a shallow marine platform (Bouroullec et al., 1986; Le Marrec et al., 1995). However, the overpressured hydrothermal activity, with fluid circulation at around 80 bars higher than the hydrostatic pressure gradients (Fig. 33), that formed the bulk of the dolomite bodies of Upper Lacq was not previously considered.

Age	Fluid types and sources	Main events	Schematic illustration (not to scale)	Main product	Supporting evidence
Upper Cretaceous ?	Meteoric and formational fluids	Mg from formation fluids and evaporated seawater Meteoric fluids contribute to oxidizing conditions Mixing zone dolomitization		 D1 dolomites	Early diagenesis, oxidizing conditions, low-temperature end-member that resulted in Δ_{47} temperature ~ 60°C
Eocene	Hot, deeply buried marine and clay-released Mg-rich fluids	Fracturing and faulting during compression. Change in hydrological system. Orogeny-driven fluid flow. Hydrothermal dolomitization		 D2 and saddle dolomites	Reducing conditions, salinities lower than seawater, $\delta^{18}\text{O}$ of parent fluids in the marine domain, Δ_{47} temperature ~ 90°C
Eocene	hot, deeply buried Mg-poor fluids and oil-rich fluids	Mg already expelled from the clays. Oil starts migrating from Deep Lacq. Orogeny-driven fluid-flow continues. Hydrothermal fluid circulation		 Blocky calcites with oil and aq. FIs	Reducing conditions, salinities lower than seawater, $\delta^{18}\text{O}$ of parent fluids in the marine domain, fluid trapping temperature ~ 90°C
Eocene	hot, deeply buried marine fluids ?	Same Eocene seawater became oversaturated with respect to sulphates after calcite cementation. Oil already in Upper Lacq.		 Anhydrites	Multiple sulfur isotopes indicate an Eocene seawater origin of the parent fluid of anhydrite
Present-day	Modified groundwater	Lateral supply of groundwater.		Groundwater table at -723m	Drilling reports of present-day operators

 Limestone

 Dolomite

 Paleocene Flysch

 Paleocene unconformity


 Groundwater table

Figure 35. Summary diagram of fluid circulation schemes with their main products.

Stress variations in and around a seismically active fault system would affect local fluid pressures and allow the mobilization of considerable volumes of fluids (Sibson et al., 1975). This orogeny-driven style of fluid migration was involved in the dolomitization of the Albian carbonates of the Asón valley in the Basque Cantabrian Basin of northern Spain (López-Horgue et al., 2010), the middle Jurassic oil reservoirs of the Paris Basin (e.g. Carpentier et al., 2014; Mangenot et al., 2018b) and the dolomitized carbonates in the St. George Group of western Newfoundland, Canada (Conliffe et al., 2010). The new fracturing event that preceded calcite cementation probably connected the Upper Lacq reservoir with another reservoir of fluids. This is supported by the fact that the new fluids are depleted with respect to Mg and the precipitation of dolomite have stopped. Also, these new fluids are associated with oil inclusions which were absent in previous dolomite phases. The new fracturing stage was probably linked to modifications in regional tectonic stress that have possibly affected the intensity of clay dewatering and consequently the amount of

Mg expelled. Fluid and basin modeling suggest that also during the Eocene compression, these circulating fluids were not in thermal equilibrium with the host rocks (Fig. 35). These Ca-rich fluids have possibly mixed with oil-rich fluids expelled from the Deep Lacq source rocks as new fluid pathways opened and the connection with new fluid reservoirs started during this second fracturing stage. The origin of oil in Upper Lacq is debated given complexities in the structural and thermal evolution of the petroleum system (Connan and Lacrampe-Couloume, 1993; Le Marrec et al., 1995; Serjouni, 1995; Houzay et al., 2008). However, the most probable scenario is a dysmigration from the Deep Lacq source rocks passing through the Albian reefs. This circulation scheme was documented by the correlation of sterane distribution patterns between the Deep Lacq source rocks, Albian reefs and oils of the Upper Lacq reservoir. Connan and Lacrampe-Couloume (1993) concluded that oils found in Upper Lacq migrated from the Jurassic-Barremian sources rocks laterally through the reef to accumulate in Upper Lacq. The abundance in oil inclusions observed in the Albian reef samples is also in agreement for this scenario of oil migration. Therefore, lateral flow of connate (marine) fluids mixed with the migrating oil and precipitated blocky calcites rich in oil and aqueous inclusions.

Multiple sulfur isotopes indicate an Eocene marine origin for the parent fluids of anhydrites. Thermodynamically, the solubility of calcite is reduced in sulphate rich solutions and CaCO_3 would be the first mineral that precipitates (Li and Duan, 2011). Since the timing of calcite cementation is also mid-Eocene in age, we suggest that the marine parent-fluid of anhydrite was the same as the parent-fluid of calcites. Because of the precipitation of blocky calcite, the fluid became gradually depleted in CO_3^{2-} and permitted the precipitation of anhydrite (Fig. 35). The precipitation of this sulphate phase is typical for solutions originating from marine to modified marine fluids as documented in the Devonian reservoirs of Alberta, Canada (Butler, 1970; Mountjoy et al., 1999; Machel, 2004).

Finally, during uplift and telogenesis, differences in hydraulic heads from nearby elevated areas would provide a suitable driving mechanism for the lateral supply of the crest of the anticline with the present-day groundwater (Fig. 35).

Chapter 3 – Part III: Conclusions: Upper Lacq

A revised paragenesis for the Upper Cretaceous Upper Lacq oil reservoir is presented where the evolution of the Pyrenean domain and the Aquitaine foreland basin have played a major role in controlling the timing of carbonate reservoir diagenesis. We argue that at least three fluid sources were involved in the diagenetic modifications of the Upper Lacq reservoir.

After shallow-marine carbonate deposition and early bacterial diagenesis during the Late Cretaceous, a mixture of marine fluids in a lagoonal setting, together with formational fluids in the mixing zone allowed the precipitation of the early D1 dolomite phase. Microthermometric and chemical evidence support a model with multiple fluid pulses driven by regional orogenic forces. After the deposition of the Paleocene seal and during the Major orogenic compressive phase, Mg-rich, low salinity, hot, relatively deep fluids from the Southern Lacq Basin migrated along the Saint Suzanne fault, under a state of thermal disequilibrium being at least 30-40°C hotter than the ambient host rocks. These hot fluids are due to higher burial temperatures sourced from the deeper sections in the South Lacq basin. These fluids dolomitized the Upper Lacq reservoir. After the end of Mg expulsion from Albian clays of the Southern Lacq Basin, due to modifications in regional tectonic stress, hot low-saline fluids continued to be squeezed out of this basin and towards Upper Lacq. The combination of the Mg-poor, hot, low salinity fluid from the Southern Lacq Basin and the oil that migrated from the Deep Lacq source rocks precipitated blocky calcites rich in oil and aqueous inclusions. AIT-PIT and basin modeling also suggest an Eocene timing for this fluid pulse. After calcite cementation, the remaining fluids became oversaturated with respect to sulphates and a minor phase of anhydrite precipitated. The timing of anhydrite precipitation is supported by the multiple sulfur isotopes that indicate an Eocene seawater signature of the parent fluid. Finally, during telogenesis, oxidizing fluids were reintroduced possibly by lateral input because the overlying Paleocene flysch seal would inhibit downward percolation of fluids.

In conclusion, by using a multidisciplinary petrographic, geochemical and modeling approach we provide evidence that the main diagenetic events in the southern Aquitaine basin were mainly linked to the Pyrenean convergence during the Eocene. Even if a minor early dolomitization event cannot be totally ruled

out, orogeny-driven hydrothermal dolomitization is the principal mechanism that affected the Upper Cretaceous carbonate reservoirs in the Lacq area.

Chapter 4: Deep Lacq

Chapter 4 – Part I: Deep Lacq: Results

1. Petrography of diagenetic phases

Precursor limestones consist of chalky mudstones, wackestones to bioclastic packstones (Fig. 36 a and b). Bioclastic material range from microforaminifera, to shells of mollusks, sponges, echinoderms and annelids, with sizes reaching up to 2 mm in size. Appendix 9 shows the main lithologies recognized in the Deep Lacq reservoirs.

1.1. Micritization

Coatings and microborings filled by micrite growing from the walls of the bioclasts inwards are observed (Fig. 36a). This phenomenon, in some cases, is important enough to engulf the entire bioclast and hence obscuring the original structure of the grain. Under CCL, a heterogeneous and disturbed orange to dull brown luminescence is revealed.

1.2. Pyrite

Clusters and agglomerates of rounded, to sub-rounded framboidal pyrite crystals are observed on shells and bioclastic fragments and inside bioclastic micropores (Fig. 36b). Individual crystal sizes range between few μm up to a maximum of nearly 40 μm . With reflected light microscopy, a yellowish golden color, typical of pyrites, is observed. These small crystals are abundant on the shells and bioclasts and also in the micrite matrix (arrows in Fig. 36b)

1.3. Dolomite 1

This dolomite phase is represented by planar porphyrotopic rhombohedral dolomite crystals floating in host matrix (Fig. 36c). Average crystal sizes are in the range of 30-80 μm . CCL microscopy reveal a bright yellow triangular core surrounded by a uniform, brick red cement rim before a final, dark red, outer rim (Fig. 36c). In the case of Mano Dolomite Formation, the lithology is dominated by planar S morphologies, with partial preservation of the original oolites.

1.4. Dissolution

Moldic porosity, later infilled by other cements (Fig. 36d), provide indirect evidence that dissolution may have occurred before later cementation.

1.5. Calcite 1

This is a local phase limited to the Annelids Limestone Formations. It appears as zoned dog-tooth to columnar calcite cements lining the walls of moldic pores (Fig. 36d and e). Under CCL microscopy, zonation evolve from a dull-orange/brown core to progressively brighter orange to yellow colors (Fig. 36e). Crystal sizes range between 5-30 μm . Zonations are well developed and show no evidence of recrystallizations. No aqueous or oil inclusions are observed in this phase. Upon staining, red colors are obtained.

1.1. Calcite 2

This second calcite phase appears as a yellow-orange overgrowth engulfing the dog-tooth calcites of the Annelids Limestone Formation. The crystals are coarse ($\sim 300\mu\text{m}$), equidimensional and have sub-rounded terminations which helps to distinguish them from other calcite phases. Under CCL, no zoning is observed but rather uniform shades of yellow to dull orange colors with no evidence of recrystallization (Fig. 36e). When this phase develops in open vuggy pores, sizes can reach up to 650 μm . No aqueous or oil inclusions were observed in this phase. Upon staining, Calcite 2 shows pink to red colors.

1.2. Compaction

This episode is represented by mechanical compaction and breakage of the rounded bioclasts and shell fragments. Figure 36f shows an example of annelid stem that has undergone mechanical compaction as supported by the partial breakage of its walls.

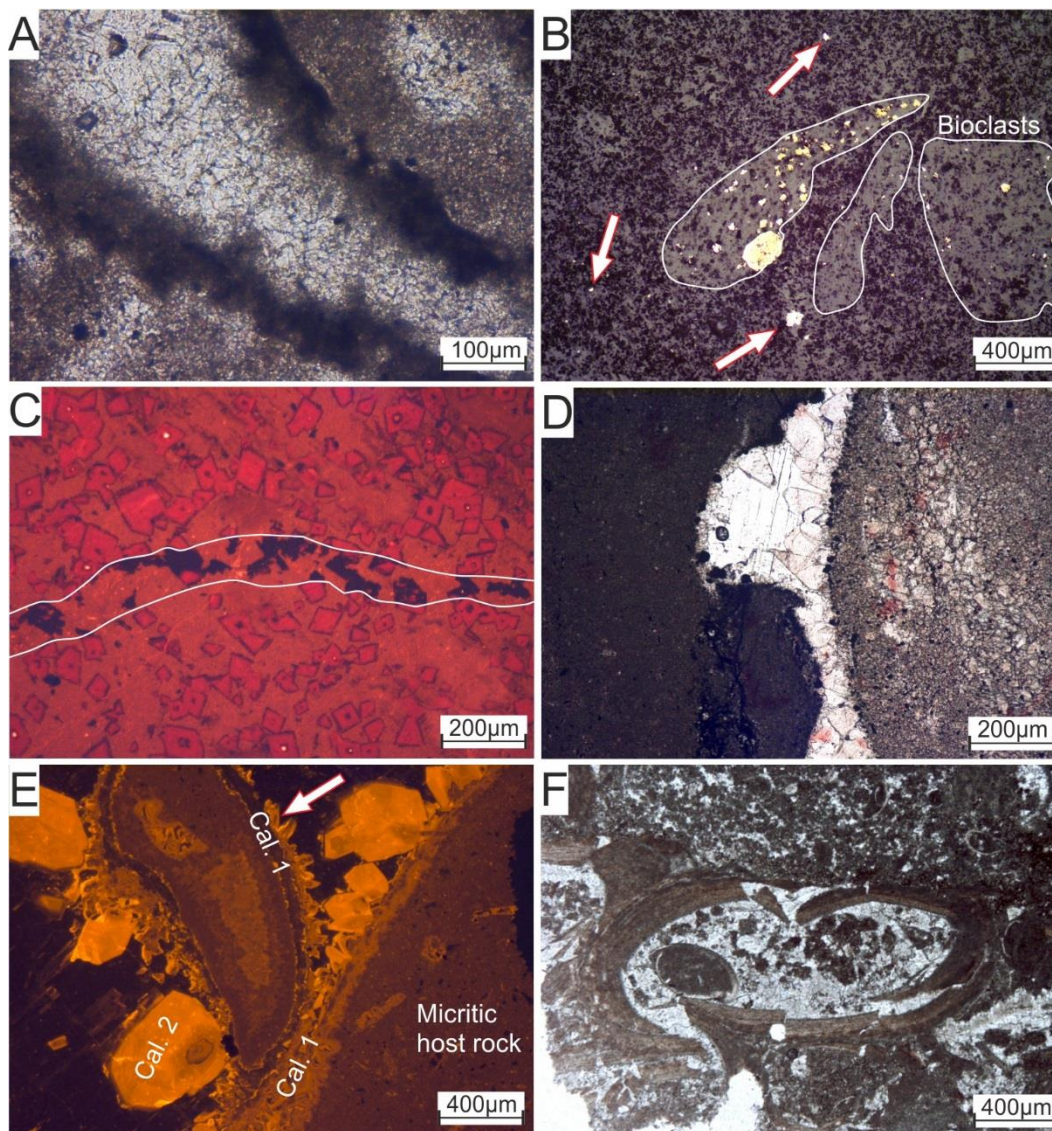


Figure 36. A: PPL image of a shell fragment affected by destructive micritization. The shell is later replaced by other calcite phases. B: reflected light image showing ghosts of bioclasts with local concentrations of rounded to sub-rounded pyrites. Arrows point to pyrites disseminated into the micritic matrix. C: CCL image of planar rhombic dolomite crystals floating in a micritic matrix and cross-cut by a calcite and anhydrite vein. D: shell mold cemented by calcite and anhydrite cements. This shell was initially dissolved and moldic porosity was filled by younger cement phases. E: CCL image of the zoned “dog-tooth” calcite 1 phase precipitated at the contact with the host rock and covered by the yellow-luminescent calcite 2 phase. F: Broken annelid tubes as evidence of mechanical compaction.

1.3. Stylolite 1

This is a minor compaction phase represented by low-amplitude stylolites. Despite the fact that the wells were not oriented, the stylolite planes have a horizontal orientation parallel to the stratigraphy. These stylolites are cross-cut by calcite/dolomite-infilled fracture A (Fig. 37a).

1.4. Fracture A1

Fractures A1 cross-cut the host rocks and stylolites 1 (Fig. 37a) and are characterized by straight walls with width between 5µm up to 3cm. Infilling cements are composed of saddle dolomite and calcite.

1.5. Dolomite 2

In the fracture set A, very coarse dolomite crystals, reaching up to 3mm in size, with curved faces were observed (Fig. 37c). They have turbid cores and growth zones full of fluid inclusions that are too small for analyses. Oil inclusions were also identified in the growth zones. CCL microscopy reveal a zoned core with luminescence alternating between different shades of bright colors. In some cases, the original saddle dolomite growth zone were replaced by a calcite phase (Fig. 37b). This places the timing of saddle dolomitization before the calcite 3. Upon staining, no coloration was observed.

1.1. Fracture A2

The observation of host rocks fragments inside fractures A (Fig. 37b) sealed by the calcite 3 cements suggest a crack-and seal fracturing mechanism during or prior to the cementation of the calcite 3.

1.2. Calcite 3

This dominant cement phase occludes most of the fracture and vuggy porosity (Fig. 37c) and significantly reduces reservoir quality. Calcites are blocky with sizes increasing towards the open spaces and can reach up to 8mm in size (Fig. 37d). Lack of uniform CCL zonations and the heterogeneous brown to dull orange colors suggest possible recrystallization. Relics of Dolomite 2 are frequently observed in Calcite 3 (arrows in Fig. 37d). This phase is rich in oil and aqueous inclusions.

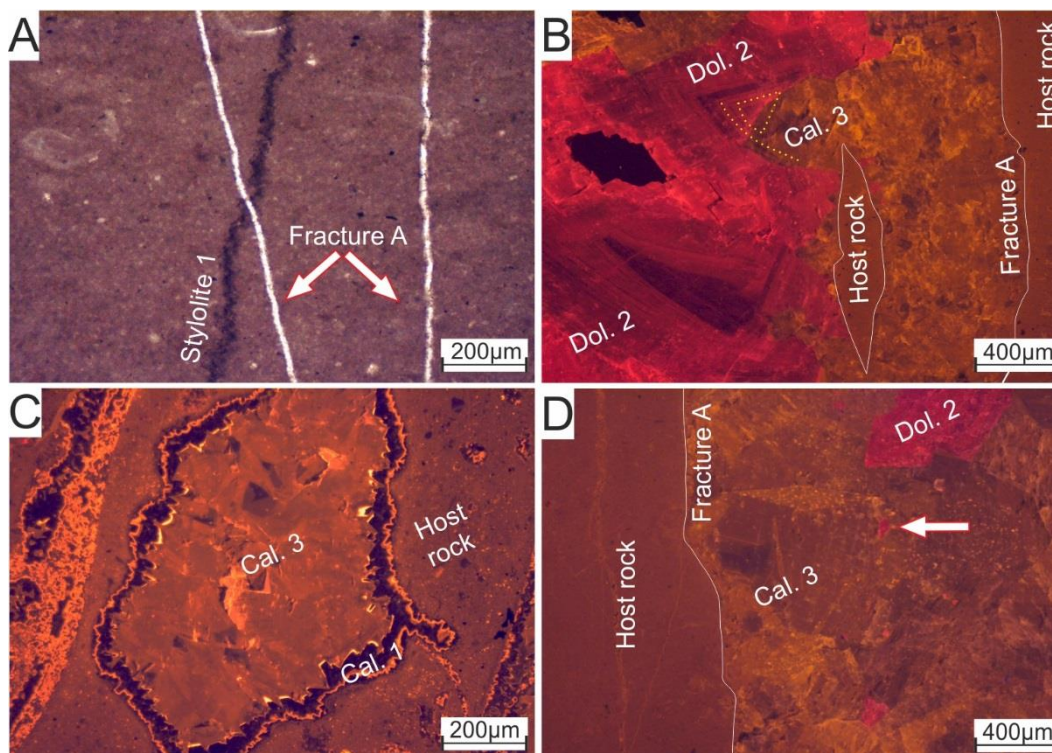


Figure 37. A: PPL photomicrograph of stylolite 1 crosscut by fracture set A. B: CCL image of the cross-cutting relationships between fracture A, dolomite 2 and calcite 3 phases. Fragments of host rocks in the fracture are indicators of fracture reopening mechanism. Dolomite 2 is partially replaced by calcite 3 (see the yellow dotted line between Dol. 2 and Cal. 3). C: CCL image of a vuggy pore now filled by Cal. 1 and Cal. 3 calcites. D: CCL image of coarse calcite 3 crystals. Arrows indicate remnants (relics) of Dol. 2 after replacement. Cal. 3 shows heterogeneous shades of yellow to dull orange luminescence.

1.3. Fracture B

Fracture set B postdates calcite 3 and is coupled with anhydrite cementation. The width of fractures can reach up to 1cm (Fig. 38a and b) and appear mostly as vertical fractures when viewed macroscopically. No cross-cutting relationship is seen between fracture A and fracture B but chronological evidences between calcite 3 and anhydrite (Fig. 38c) places this event after calcite.

1.4. Anhydrite

Anhydrite was observed along the vertically oriented fracture set B in wells LA-101 and LA-104 (Fig. 38a) and tend to form massive nodules and concretions that replace the precursor fabrics of the Upper Annelids Formation. The vertical thickness of anhydrite layers, observed in the studied cores (Fig. 38a) can reach up to 50 cm. Stratigraphically, the massive anhydrites lie immediately under the Sainte-Suzanne marls, partially replace the Upper Annelids Limestone Formation, and reach around 15 to 20 meters in total

thickness. This is the last diagenetic cement that replaces younger calcite and dolomite phases. Under plane polarized light, anhydrites appear clear white to creamy, while under cross-polarized light, an array of bright second order colors were observed (Fig. 38b, c and d). No luminescence with CCL microscopy was detected. Similarly, under PPL, CPL and CCL, no evidence of gypsum precursor were observed. Several morphologies of anhydrites have been identified.

1. Coarse and tabular crystals with size reaching up to 2mm (Fig. 38b and d). These often show evidence of calcite and dolomite replacement (Fig. 38c) and are rich in oil and aqueous inclusions.
2. Fine fibrous crystals filling nodules with a chicken-wire texture inside the host rocks. Fracture set B is often observed connected to these nodules (Fig. 38b). Individual crystal size is no more than 50 μm (Fig. 38b). These are too small to observe aqueous or oil inclusions.

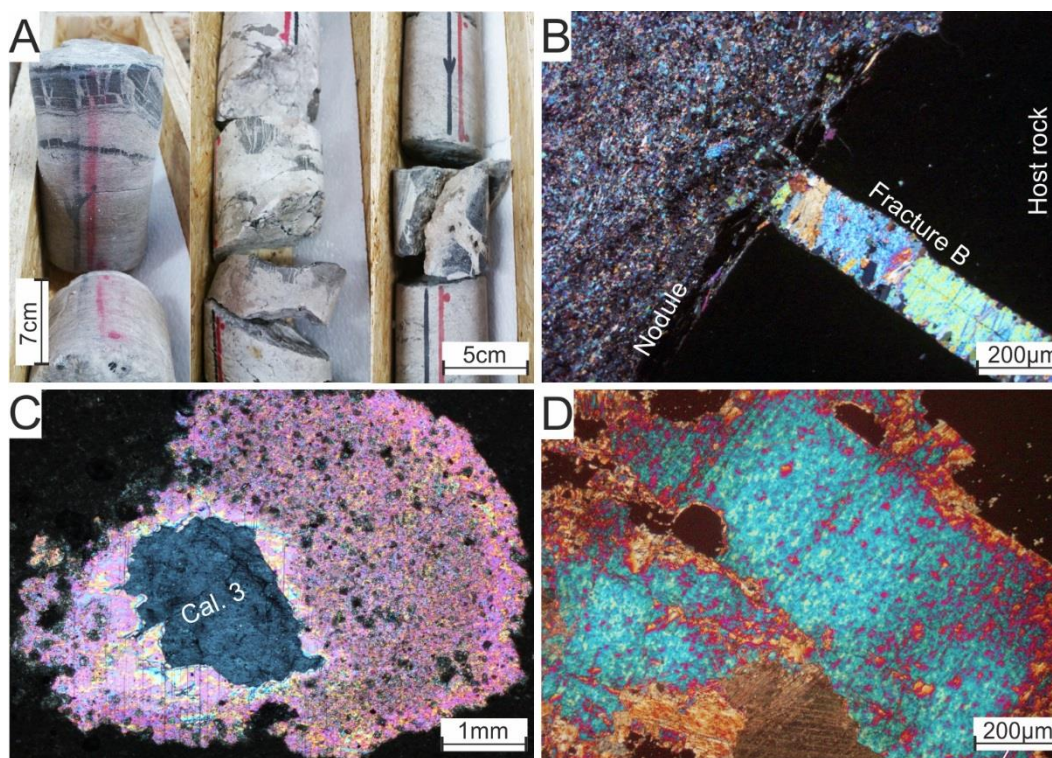


Figure 38. A: Photographs of well LA-101 and LA-104 with massive anhydrites few meters below the Sainte Suzanne Formation. B: CPL image of an anhydrite-filled fracture C in a host micrite matrix in contact with an anhydrite nodule. C: CPL image of an anhydrite with partial replacement of a calcite 3 crystal. D: CPL image of coarse anhydrite crystals with bright 2nd order birefringence.

1.5. Stylolite 2

Another compaction phase is represented by stylolite 2. These stylolites have amplitudes in the range of 200 to 600µm (Fig. 39a) and are mostly oblique relative to the vertical wells. These stylolites crosscut anhydrites.

1.6. Fracture C

This last fracturing phase affected all previous phases and generated fracture porosity in the reservoir of Deep Lacq. The fracture set C cross-cuts calcite-filled fracture A (Fig. 39b) and anhydrite-filled fracture B (Fig. 39c).

1.7. Dissolution

A final phase of dissolution is represented by solution-enhanced fractures (Fig. 39c) and vuggy porosities (Fig. 39d).

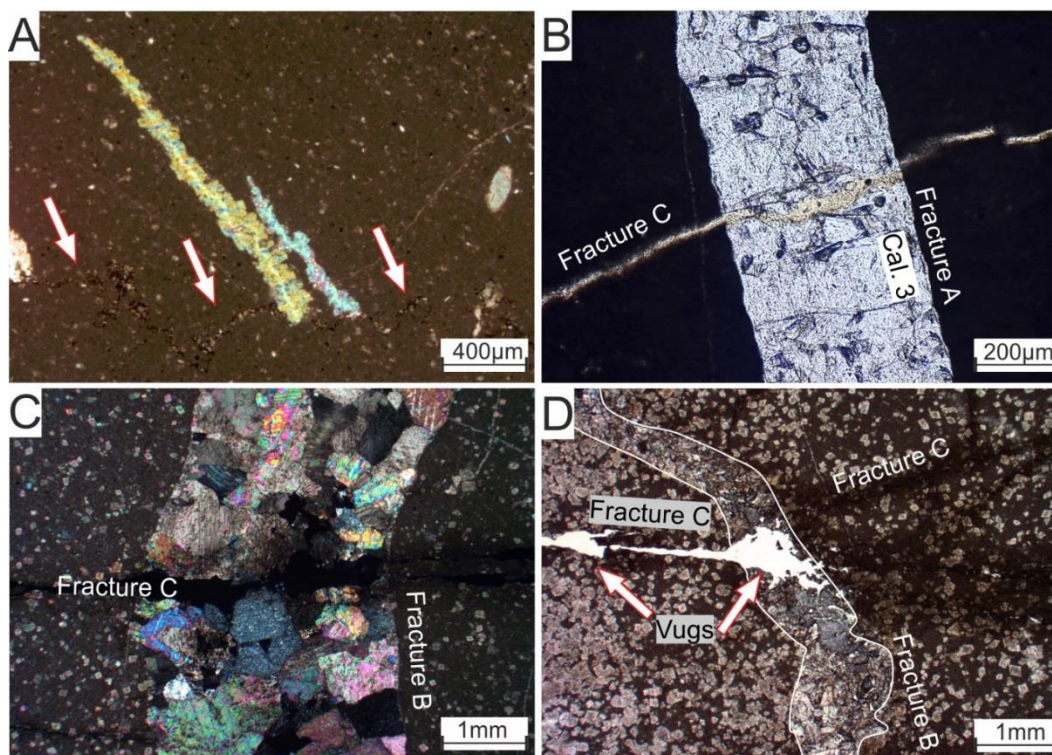


Figure 39. A: CPL photomicrograph of anhydrite affected by stylolite 2 (arrows). B: PPL image of a fracture A filled by calcite (Cal. 3) crosscut by an open fracture C. C: Anhydrite-infilled fracture B crosscut by fracture C. D: Fracture B crosscut by a fracture C with a solution-enhanced vuggy-porosity.

2. Isotope Geochemistry

$\delta^{18}\text{O}$ and $\delta^{13}\text{C}$ isotopes were obtained from the micritic host rocks ($n=10$), Dol. 2 ($n=4$) and Cal.3 ($n=10$) cements (Fig. 40 and appendix 10). $\delta^{13}\text{C}$ of the host black mudstones are in the range of -2.4‰ to $+2.5\text{‰}$ PDB and $\delta^{18}\text{O}$ between -3.7‰ to -2.6‰ PDB. Isotopic data ($n=14$) for Dol 1 shown in figure 40 were not obtained during the present study because of difficulties in obtaining pure Dol. 1 powders not contaminated by the host micrite. They were provided from internal TOTAL archives (Pabian-Goyheneche and Anquelle, 1995) and were sampled from the matrix dolomites of an oolitic limestone that constitute the bulk host rocks of the Mano Dolomite Formation. Dol.1 has a $\delta^{18}\text{O}$ ranging between -0.2 and $+1.8 \text{‰}$ PDB and a $\delta^{13}\text{C}$ between -1.4 to $+2.1 \text{‰}$ PDB. Dol. 2 have $\delta^{13}\text{C}$ values between $+5.5$ and -5.6‰ PDB and a depleted $\delta^{18}\text{O}$ between -6 and -8‰ PDB. $\delta^{13}\text{C}$ of calcite 3 is between $+1.6$ and $+4.3 \text{‰}$ PDB while $\delta^{18}\text{O}$ varies between -2.8 and -5.6‰ PDB. An additional isotopic values of Dol. 2 was retrieved from internal TOTAL archives (Pabian-Goyheneche and Anquelle, 1995) and have a $\delta^{18}\text{O}$ value of -8‰ PDB and a $\delta^{13}\text{C}$ of -5.6‰ PDB. Isotopic values provided by TOTAL for calcite ($n=49$) have $\delta^{13}\text{C}$ ranging between -5.2 to $+2.5 \text{‰}$ PDB and $\delta^{18}\text{O}$ between -1.7 to -6.2‰ PDB (appendix 11). These measurements were likely conducted on bulk powders and not specifically from pure phases. Late Jurassic seawater represented by the dashed box in figure 40, has a $\delta^{13}\text{C}$ range between 0.1 to $+3.2 \text{‰}$ PDB and a $\delta^{18}\text{O}$ range of -1.8 to $+0.2 \text{‰}$ PDB (considering the 1σ range of Veizer et al., 1999). Error ranges for individual data points are within the symbols plotted in figure 40 with a range of ± 0.01 - 0.03 (1σ) from the reported values.

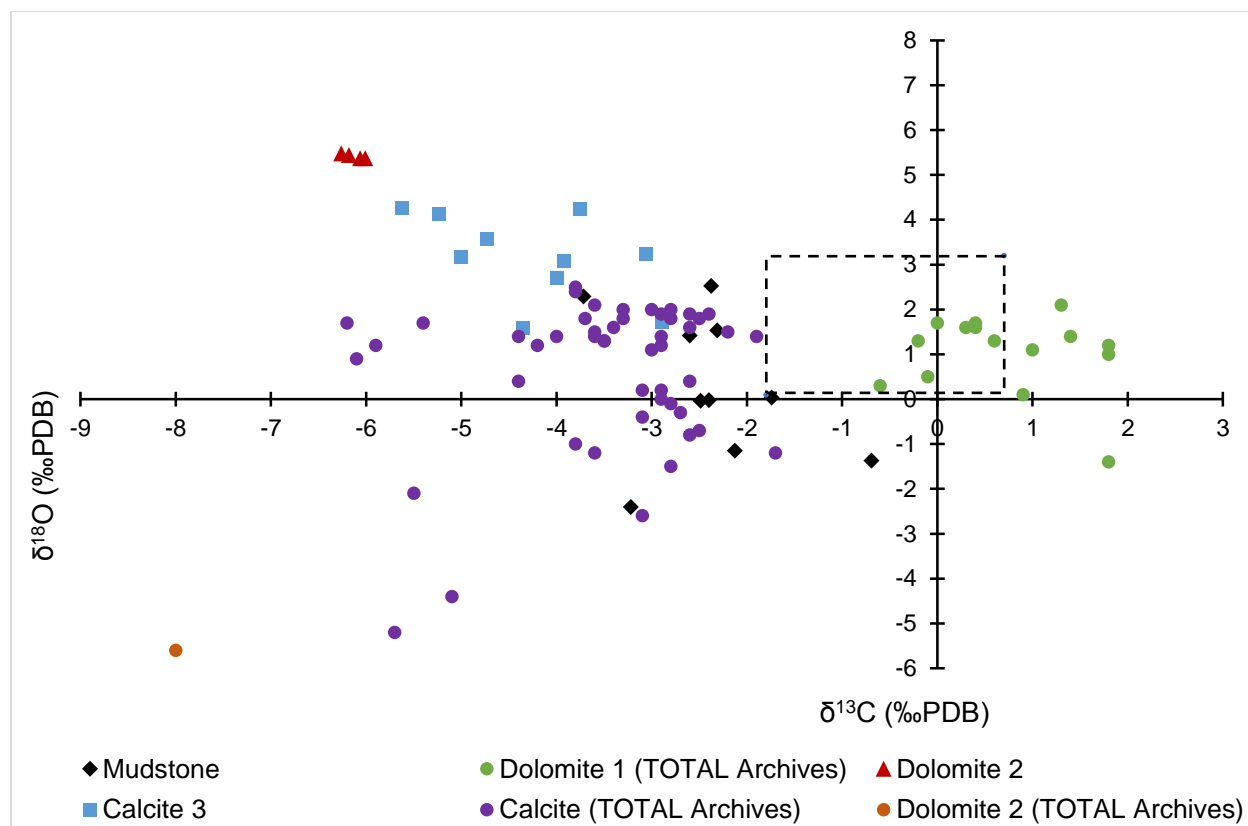


Figure 40. Cross-plot of $\delta^{18}\text{O}$ and $\delta^{13}\text{C}$ isotopes for Deep Lacq. Dashed box represents the Late Jurassic seawater signature (Veizer et al., 1999). Data from TOTAL archives (Pabian-Goyheneche and Anquelle, 1995) are presented as colored circles.

The dataset presented in figure 39 show two trends in the studied Dol. 2 and Cal. 3 cements. The samples collected in this work show a trend of increasing $\delta^{13}\text{C}$ with decreasing $\delta^{18}\text{O}$, while the data provided by TOTAL show a trend that is in the range of the host rocks and the reference Jurassic seawater. The depleted $\delta^{13}\text{C}$ values are not statistically enough to make solid arguments.

$^{87}\text{Sr}/^{86}\text{Sr}$ isotopic ratios from the Dol.1 (n=4), Dol. 2 (n=1) and Cal. 3 (n=15) phases were provided by TOTAL's archives (Pabian-Goyheneche and Anquelle, 1995) (appendix 11) and were plotted relative to the Late Jurassic seawater signature (Veizer et al., 1999) in figure 41. The $^{87}\text{Sr}/^{86}\text{Sr}$ ratio of the Dol.1 (n=4) are in the range of 0.70705 to 0.7078 while that of Dol. 2 (n=1) at 0.70714. Calcite 3 (n=15) have $^{87}\text{Sr}/^{86}\text{Sr}$ ratios between 0.707235 and 0.707549. All of these ratios are more enriched than the signature of the Late Jurassic seawater which range from 0.706791 to 0.707066.

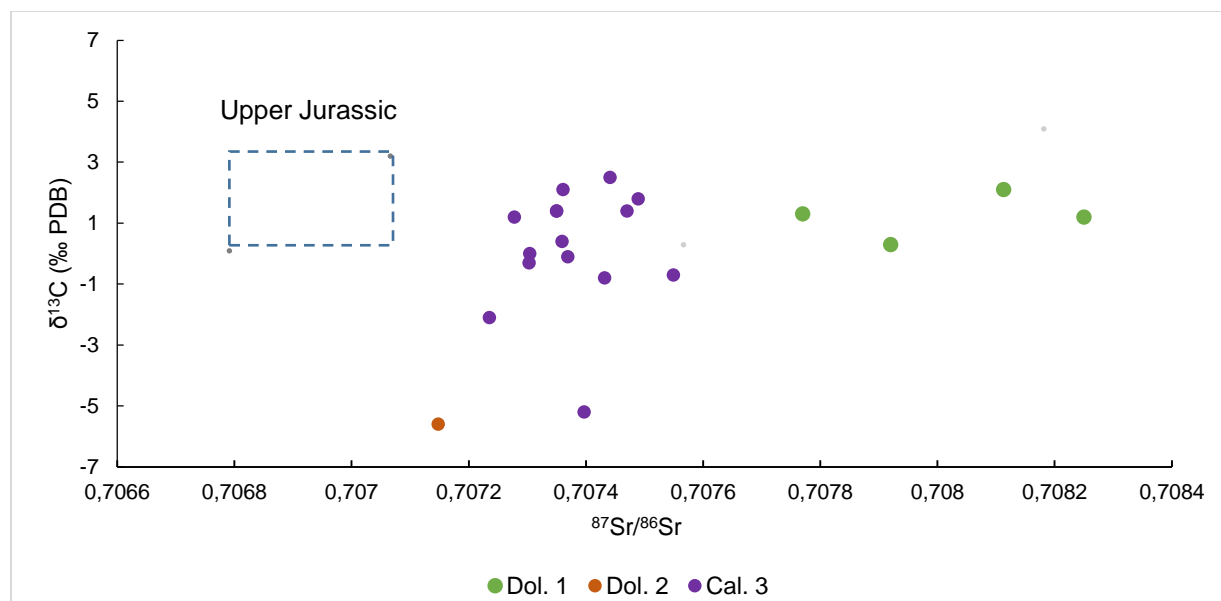


Figure 41. Cross plot of $^{87}\text{Sr}/^{86}\text{Sr}$ ratio versus $\delta^{13}\text{C}$ values of Dolomite 1, Dolomite 2 and Calcite 3 cement relative to the signature of the Upper Jurassic seawater (Veizer et al., 1999).

Multiple sulfur isotopes measured in the anhydrites of Deep Lacq are presented in table 6. Since no reference data for $\delta^{33}\text{S}$ or $\delta^{36}\text{S}$ of the Triassic evaporites were available in Crockford et al. (2019), only the $\delta^{34}\text{S}$ values of this study were compared to the Triassic $\delta^{34}\text{S}$ being around 12.61 ± 4.65 ‰ V-CDT. The $\delta^{34}\text{S}$ in Deep Lacq are more enriched with values between 18.97 and 19.12 ‰ V-CDT.

Table 6. Multiple sulfur isotope results of Deep Lacq

	$\delta^{33}\text{S}$ (‰ V-CDT)	Error	$\delta^{34}\text{S}$ (‰ V-CDT)	Error	$\delta^{36}\text{S}$ (‰ V-CDT)	Error
Sample 1	9.82	± 0.009	19.12	± 0.006	36.23	± 0.078
Sample 2	9.74	± 0.011	18.97	± 0.005	35.92	± 0.062

3. Major and trace element analysis

3.1. Fe-S

For the same purpose as in Upper Lacq an attempt was made to check the Fe and S ratios of sulphides. The ratios measured on anhedral sulphides from deep Lacq are indicated on the SEM photomicrograph in figure 42. After normalizing the Fe and S atomic percent to 100, the relative ratios are 0.51 and 0.52, typical of pyrite and not pyrrhotite.

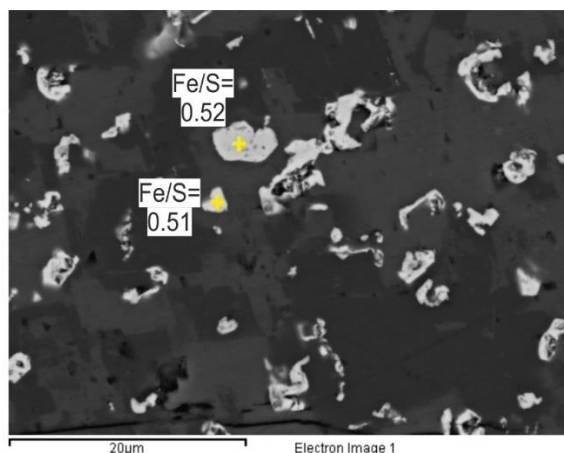


Figure 42. SEM-EDS photomicrograph of sulphide crystals with the location of spectral measurements and the resulting ratio of Fe and S.

3.2. U-Pb

Host rocks, Dol 1 and 2, Calcite 1, 2 and 3 were investigated with LA-ICPMS to determine if enough U and Pb were available to proceed with absolute age dating. The list of U and Pb contents is tabulated in appendix 12. As with the case in Upper Lacq, host rocks and cement phases in Deep Lacq are depleted in U and Pb with quantities being several orders of magnitude lower than the minimum requirement to do the analysis.

3.3. REE

REE concentrations have been measured in micritic limestones and matrix dolomites of the Mano Formation, planar P dolomites (Dol 1), calcite phases 1, 2 and 3 and in saddle dolomite crystals. Figure 43a shows the PAAS-normalized REE patterns plotted on a logarithmic scale. The REE concentrations are very low, all being less than 1 ppm. REE concentrations of the micritic host rocks are very low, around 0.01 ppm. The matrix dolomite, which constitutes the bulk matrix of the Mano Dolomite Formation have REE concentrations between 0.2 and 0.5 ppm. Dol 1 phase, mostly from rhombic dolomite crystals floating in a micritic matrix, have average REE concentrations of 0.6-0.8 ppm. Cal. 1 is relatively depleted with concentrations around 0.02 to 0.03 ppm and drops to an average range of 0.02 ppm. Cal 2 contains an average concentration in REEs of 0.8 to 1 ppm. The REE pattern for the Dol 2 cement shows a bulge in the middle REE (MREEs). Cal 3 have average concentrations of nearly 0.08-0.1 ppm.

The plot of Pr vs. Ce anomalies in figure 43b shows that the micritic limestone has a mixed signal between the positive La and negative Ce anomalies. Oolitic dolomites, Cal 1 and Cal 2 have a Ce and La anomaly ratios of 1, are at the borderlines between positive La and negative Ce anomalies. Dol 2 cements are mostly in the domain of negative La anomalies while Cal 3 shows a mixed signal between the 2 domains. Samples of the Mano Formation are mostly in the positive La anomaly domain. Dol 1 is similar to the host limestones in that they have a mixed signal. Saddle dolomites and calcites show a mixed signature between negative Ce and positive La anomalies.

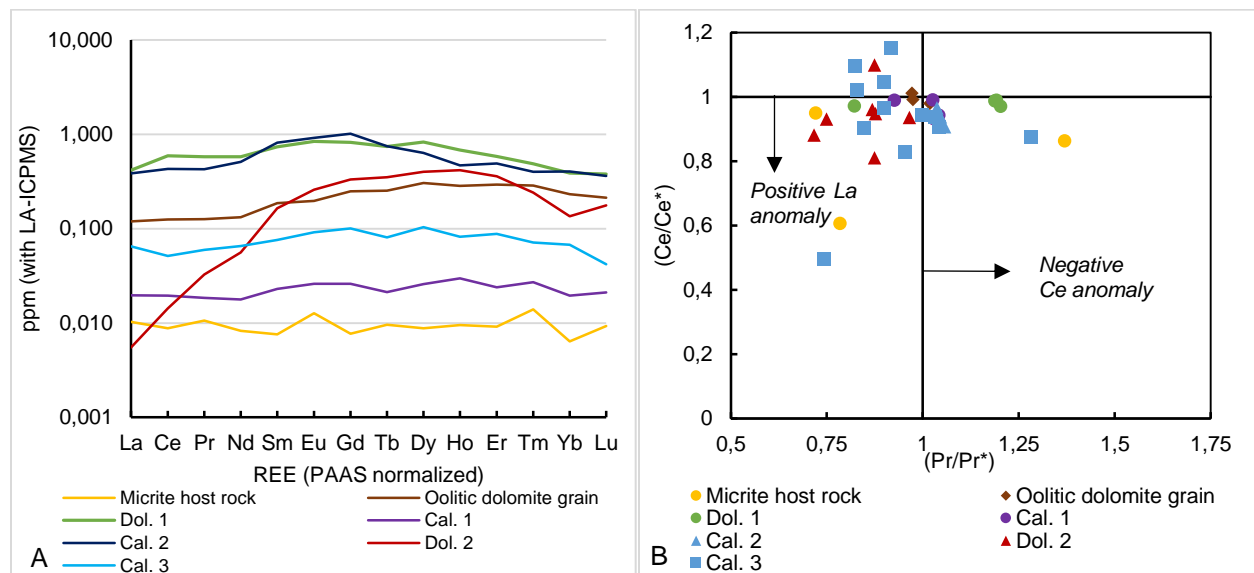


Figure 43. PAAS-normalized REE pattern for the studied phase in Deep Lacq. B: Cross-plot of Pr vs. Ce anomalies.

4. Fluid inclusion studies

4.1. Petrography

Dolomite 2, Calcite 3 and Anhydrite are the coarsest cement phases in Deep Lacq with fluid inclusions of suitable sizes allowing proper observations and analyses.

4.1.1. Fluid inclusions in dolomite 2

In dolomite 2 crystals, two-phase aqueous inclusions and two-phase oil inclusions were observed along growth zones (Fig. 44). The aqueous inclusions have mostly irregular to oval shapes with very small sizes ranging between 3 to 8 μm . These aqueous inclusions are close to two-phase light brown oil inclusions which, when viewed under UV light, display a strongly fluorescent blue to white color (Fig. 44b)

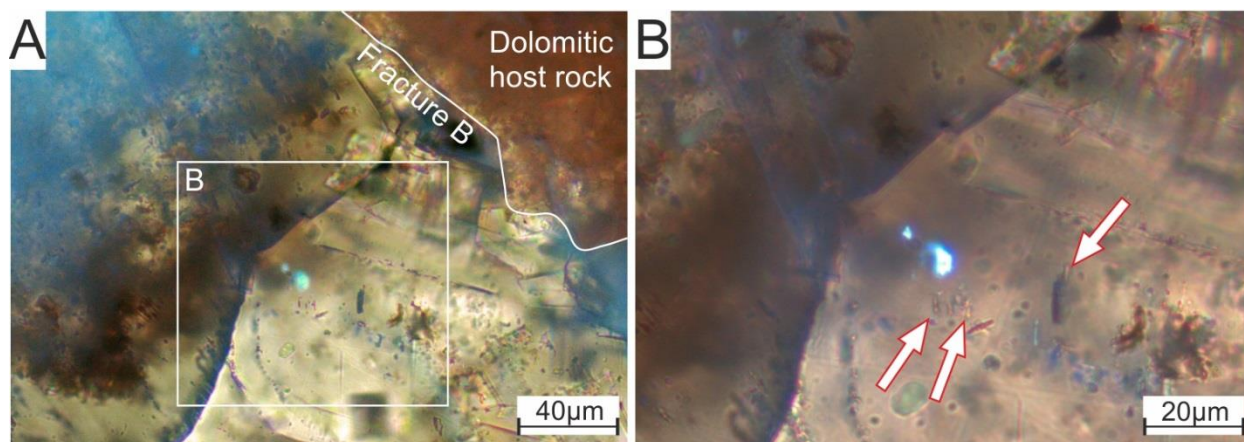


Figure 44. Coarse dolomite 2 crystal with oil and aqueous inclusions. B: The oil inclusion show a strongly fluorescent blue to white color. Arrows point to small aqueous inclusions in the same growth zone as the oil inclusion.

4.1.2. Fluid inclusions in calcite 3

In the calcite 3 coarse blocky calcite phase, two types of two-phase aqueous inclusions were identified along growth zones or in clusters between the growth zones and are hence considered primary (Fig. 45a). Type 1 aqueous inclusions are observed adjacent to two-phase oil inclusions (Fig 45b and c). These aqueous inclusions have inverted geometries, rectangular, oval and irregular shapes with sizes ranging from 5 up to 70 μm . The oil inclusions are very similar to those in the saddle dolomite in that they have a light-brown color under plane light and a strongly fluorescent blue to white colors under UV light. Their sizes can reach up to 120-130 μm . Type 2 aqueous inclusions were also found in the same crystals, either in clearly defined growth zones or in clusters. They have similar sizes as those of type 1 with similar planar to irregular shapes (Fig. 45d). The main distinguishing criteria is that they are not associated to any oil inclusions.

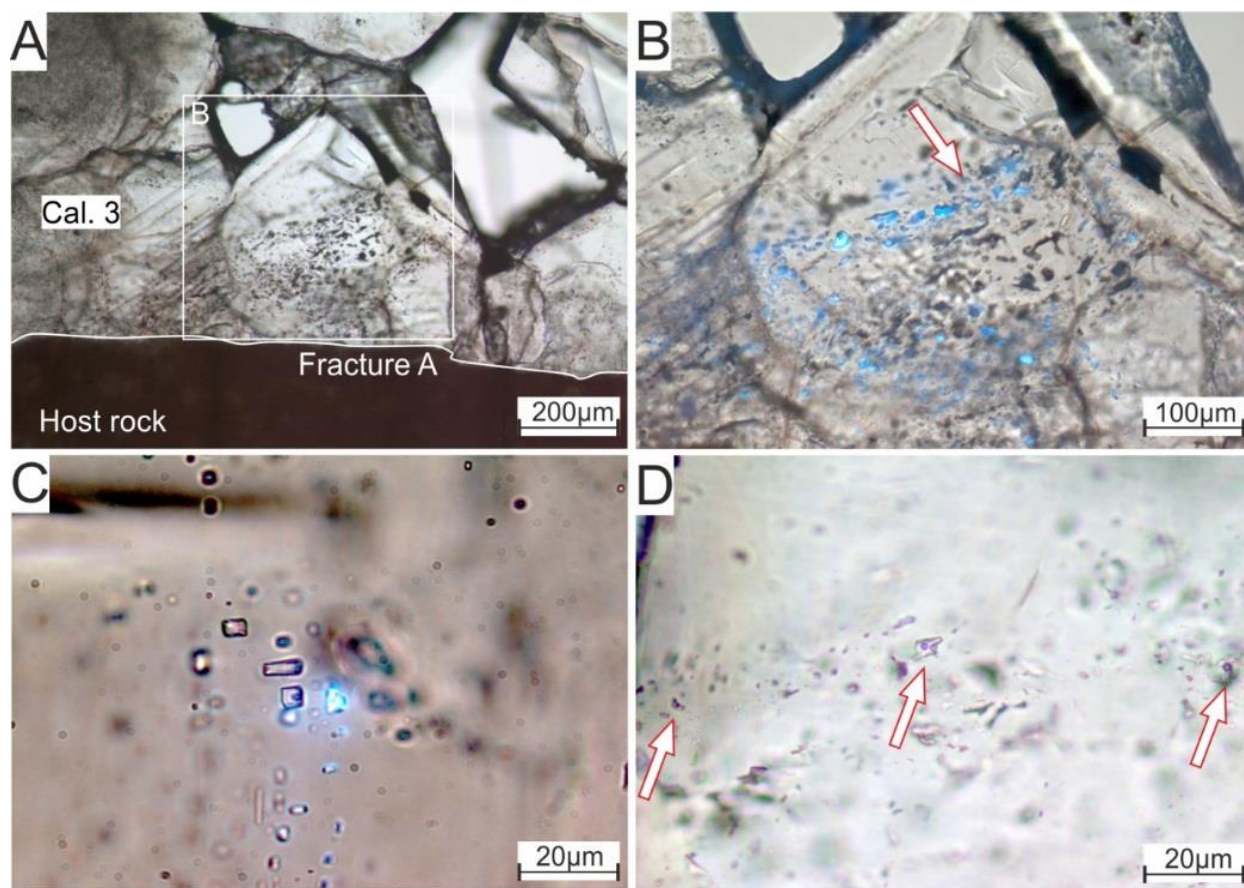


Figure 45. Fluid inclusion in Cal 3. A: inclusion-rich calcite 3 filling fracture A. B: Oil and aqueous inclusions along growth zones in a coarse calcite 3 crystal. Arrow points to type 1 aqueous inclusion that are slightly deeper in the crystal. A zoomed image is shown in C, which shows co-occurrence of blue fluorescent oil inclusions and type 1 aqueous inclusions. D: Type 2 aqueous inclusions not associated with oil inclusions in the same calcite 3 crystal.

4.1.3. Fluid inclusions in anhydrites

Two-phase primary aqueous and oil inclusions are observed in coarse anhydrite crystals. The aqueous inclusions have cubic to rectangular shapes with relatively small sizes in the order of 5-15 μm (Fig. 46a). Oil inclusions in anhydrites are two-phased, with brown to orange color under PPL and strong blue fluorescence under UV (Fig. 46b). They have elongated rectangular to inverted geometric shapes and are coeval to the two-phase aqueous inclusions.

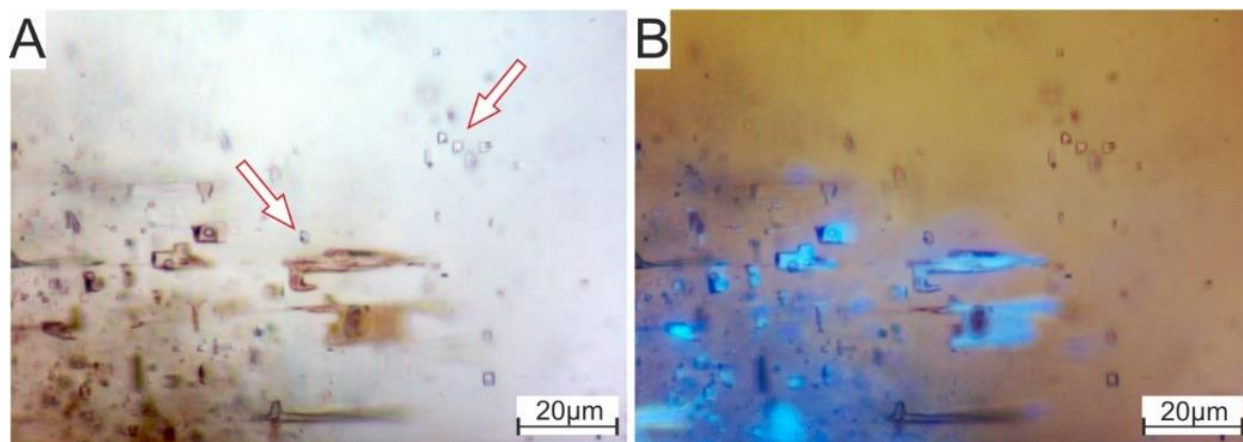


Figure 46. Fluid inclusions in anhydrites. A: Photomicrograph under PPL showing brown two-phase oil inclusions surrounded by aqueous two-phase inclusions (arrows). B: UV light showing the strong blue color of oil inclusions.

4.2. Microthermometry

4.2.1. Fluid inclusions in dolomite 2

The studied sample of dolomite was retrieved from the Mano Dolomite Formation at a depth of 3707-3715 m. The aqueous inclusions in dolomite 2 phase homogenized into the liquid phase at a T_h range of 132-148°C with a mode T_h at 144°C (Fig. 47a). The oil inclusions also homogenized into the liquid phase at a T_h range of 80-98°C with a mode T_h at 88°C (Fig. 47a). After freezing down to -100°C, phase changes were observed and the final melting ice temperatures were recorded. Eutectic (T_e) or first-melting temperatures was not possible to observe given the very small sizes of the aqueous inclusions. Only two reliable T_m ice were recorded between -6.8 and -5.2°C that correspond to salinities of 8.2 and 10.2 eq. wt.% NaCl respectively (Fig. 47b).

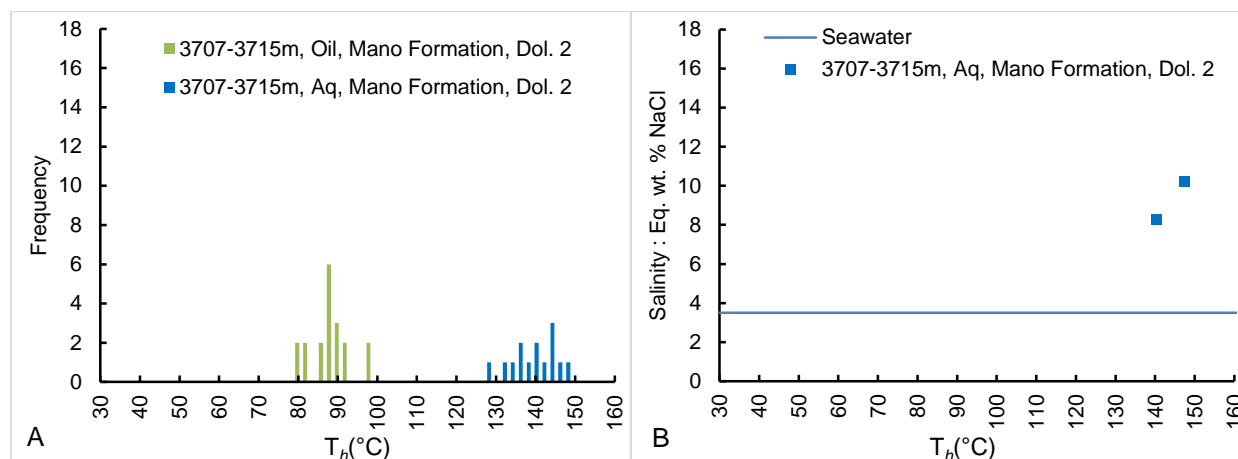


Figure 47. A: Histogram showing homogenization temperatures of aqueous and oil inclusions in the dolomite 2 at a depth of 3707-3715 m in the Mano Dolomite Formation. B: T_h vs. salinity cross-plot of the studied aqueous FIs in Mano Formation.

4.2.2. Fluid inclusions in calcite 3

Microthermometry results in calcite 3 are listed according to the depth of the studied sample, then joined all together in a summary histogram and a salinity cross-plot.

The first studied sample belongs to the Lower Annelids Formation, collected from a depth of 3488-3494m. The two-phase aqueous inclusions homogenized into the liquid phase at a T_h range of 118-148°C with a mode T_h at 134°C (Fig. 48a). T_m ice was recorded between -7 and -10°C that correspond to a range of salinities of 10.8 to 14.3 eq. wt.% NaCl (Fig. 48b)

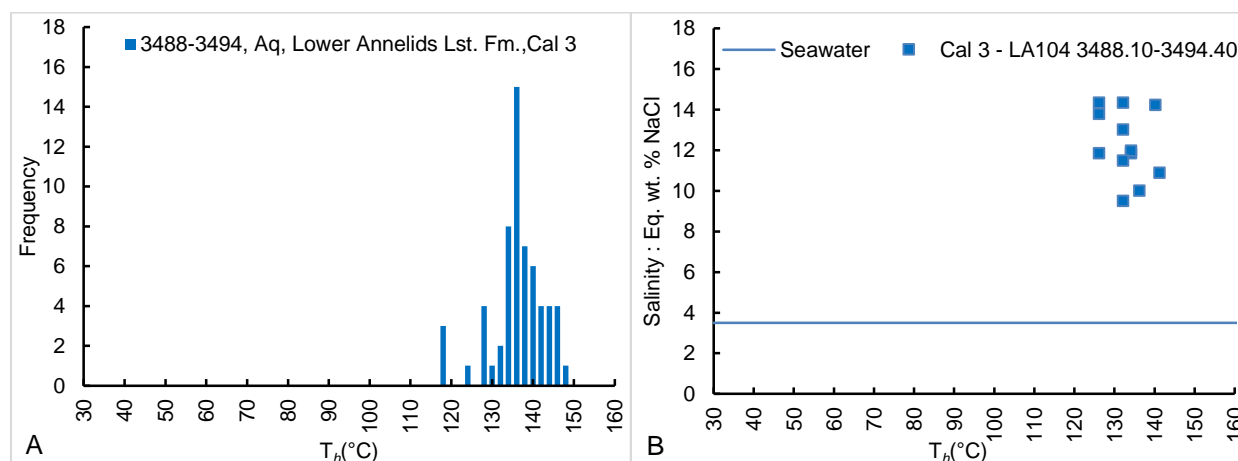


Figure 48. A: Histogram showing homogenization temperatures of aqueous inclusions in the calcite 3 phase at a depth of 3488-3494m in the Lower Annelids formation. B: T_h vs. salinity cross-plot of the studied aqueous FIs.

The second studied sample belongs to the Algal Limestone Formation, collected from a depth of 3584-3589 m. Two populations of two-phase aqueous inclusions are present. The first was observed along growth zones and homogenized into the liquid phase at a T_h range of 95-105°C with a T_h mode at 102°C (Fig. 49a). The second population was observed along clusters or groupings whose association to growth zones could not be robustly established. This second population also homogenized into the liquid phase but at a higher T_h range of 118-142°C with a mode at 126°C. Two-phase oil inclusions are petrographically associated with the first FI population. The oil inclusions homogenized into the liquid phase at a T_h range of 30-40°C. Both populations of aqueous inclusions have similar salinities measured from both the final ice melting temperatures and the Raman spectra. T_{mice} was recorded between -5.6 and -9°C that correspond to a range of salinities of 9-13.5 eq. wt.% NaCl respectively (Fig. 49b).

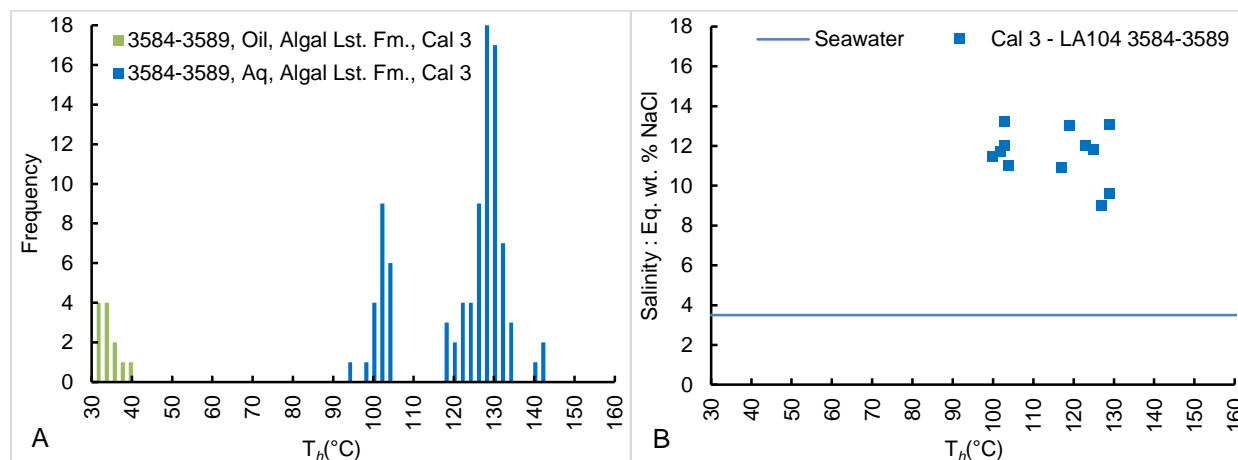


Figure 49. A: Summary histogram showing homogenization temperatures of 2 population of primary aqueous and one population of oil inclusions in the calcite 3 phase at a depth of 3584-3589m in the Algal limestone formation. B: T_h vs. salinity cross-plot of the studied aqueous FIs.

The third studied samples is the deepest and belongs to the Lons Limestone Formation, retrieved from a depth of 4116-4117m. One population of two-phase aqueous inclusions is identified. It homogenized at a T_h range of 106-110°C with the mode at 108°C (Fig. 50a). T_{mice} was recorded between -8.3 and -9.3°C that correspond to salinities of 12 and 13.2 eq. wt.% NaCl respectively (Fig. 50b). The oil inclusions homogenized into the liquid phase at a T_h range of 50-66°C with a mode T_h at 56°C (Fig. 50a).

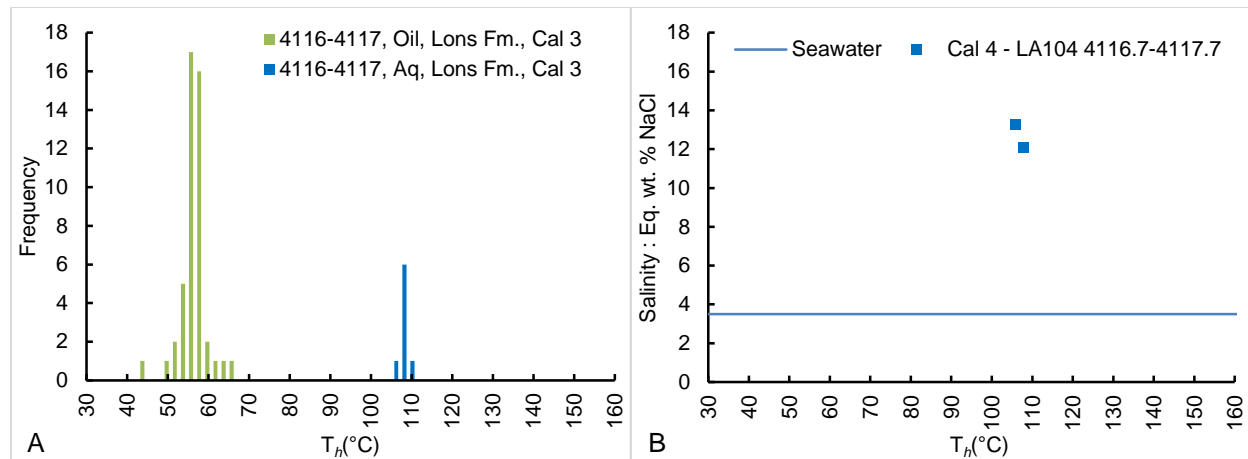


Figure 50. A: Histogram showing homogenization temperatures of aqueous and oil inclusions in the calcite 3 phase at a depth of 4116-4117m in the Lons Limestone Formation. B: T_h vs. salinity cross-plot of the studied aqueous FIs.

A summary of homogenization temperatures of the aqueous and oil inclusions studied in the Cal. 3 phase is presented in the histogram of figure 51a. The two populations of oil inclusions, studied from different depths, with a difference of nearly 500m between the samples, coexist with the population of the aqueous inclusions that homogenize between 95 and 110°C (Fig. 51a). The higher temperature aqueous population is oil-poor. All the studied aqueous inclusions from both populations have similar salinities between 9 and 14.3 eq. wt.% NaCl (Fig. 51b).

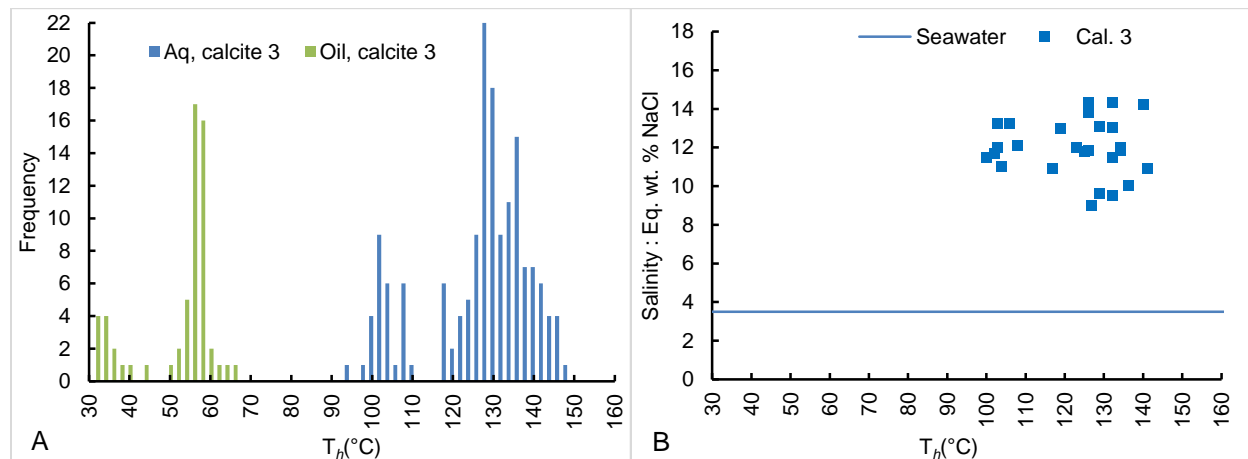


Figure 51. A: Summary histogram of the homogenization temperatures recorded in all studied aqueous and oil inclusions in the calcite 3 phase. B: T_h vs. salinity cross-plot of the studied aqueous FIs in Cal. 3 phase.

4.2.3. Fluid inclusions in anhydrite

The studied anhydrite sample was retrieved from the Algal limestone at a depth of 3672-3673m. The primary two-phase aqueous inclusions homogenized at a T_h range of 90-128°C with the mode at 94°C (Fig. 52a). The oil inclusions homogenized into the liquid phase at a T_h range of 32-78°C with a mode T_h at 56°C. T_{mice} could not be recorded with confidence due to repetitive decrepitation and/or darkening of the fluid inclusions. Instead, salinities were obtained from the Raman spectra of the liquid phase which indicated 4 to 6 eq. wt.% NaCl (Fig. 52b).

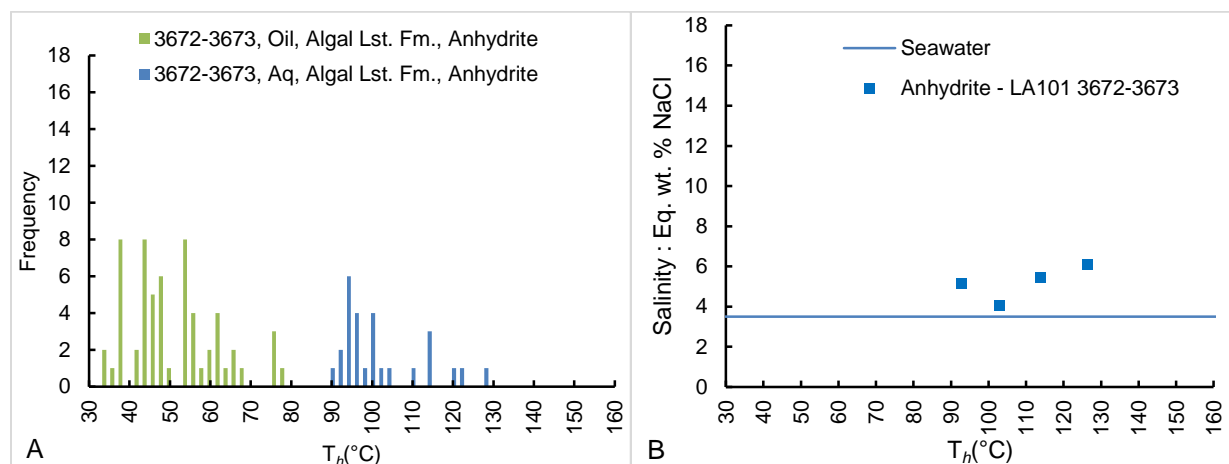


Figure 52. A: Histogram showing homogenization temperatures of aqueous and oil inclusions in the anhydrite phase at a depth of 3672-3673m in the Lons limestone formation. B: T_h vs. salinity cross-plot of the studied aqueous FIs.

4.3. Raman Spectroscopy

Raman spectra on the liquid and gas phases of the aqueous FIs in dolomite 2, calcite 3 and anhydrite were analyzed to qualify and quantify any gases present. Measurements were made in the liquid phase at both the homogenization and the room temperatures while in the gas phase only at room temperatures. The detected species include CH_4 , H_2S and HS^- and are listed in table 7. The pH of the fluids can then be obtained, using equation (2) described in chapter 2 – section 6.2, which yielded a pH range of 5.0 to 5.5. At room temperature, the composition of the gas phase is also measured and ratio of CH_4/H_2S is calculated.

Table 7. Summary of the CH₄, H₂S and HS⁻ and pH compositions detected with Raman spectra.

Host mineral	T _h (°C)	Aqueous phase at homogenization temperatures							Gas phase at room temperature	
		H ₂ O	H ₂ S	CH ₄	NaCl	HS ⁻	Average CH ₄	Average H ₂ S	Average pH	Average CH ₄ /H ₂ S
Dol. 2	139	91,35%	4,73%	0,30%	0,33%	3,30%	0,27%	4,93%	5.5	4.86
Dol. 2	140	90,86%	5,14%	0,25%	0,37%	3,39%				
Cal.3	106	91,71%	2,28%	0,38%	4,11%	1,52%	0,30%	2,08%	5.1	2.64
Cal.3	107	92,44%	2,15%	0,33%	4,25%	0,82%				
Cal.3	108	92,96%	1,27%	0,33%	3,90%	1,53%				
Cal.3	110	92,50%	2,45%	0,32%	4,07%	0,66%				
Cal.3	134,2	91,53%	2,57%	0,36%	3,63%	1,90%				
Cal.3	126	91,20%	1,59%	0,21%	3,83%	3,17%				
Cal.3	129	92,46%	2,23%	0,18%	3,56%	1,56%				
Anhydrite	94	93,91%	0,93%	0,25%	3,70%	1,21%	0,29%	0,87%	5.0	2.03
Anhydrite	96	93,93%	0,81%	0,32%	3,70%	1,24%				

5. AIT-PIT modeling

As previously done with the oil inclusions in Upper Lacq, the same steps are followed using the confocal scanning microscope and the image processing software to determine the volume of gas in the inclusions. This parameter can be used to obtain a qualitative assessment of the type of trapped oil. Figure 53 shows oils trapped in dolomites, calcite 3 and anhydrite cements of Deep Lacq plotted against 8 different types of reference oils (Bourdet et al., 2008). The close association of the plotted oil to the Black Oil (Danesh, 1998) and North American Black Oil allows to characterize all studied oils in the studied phases are all the same heavy oils.

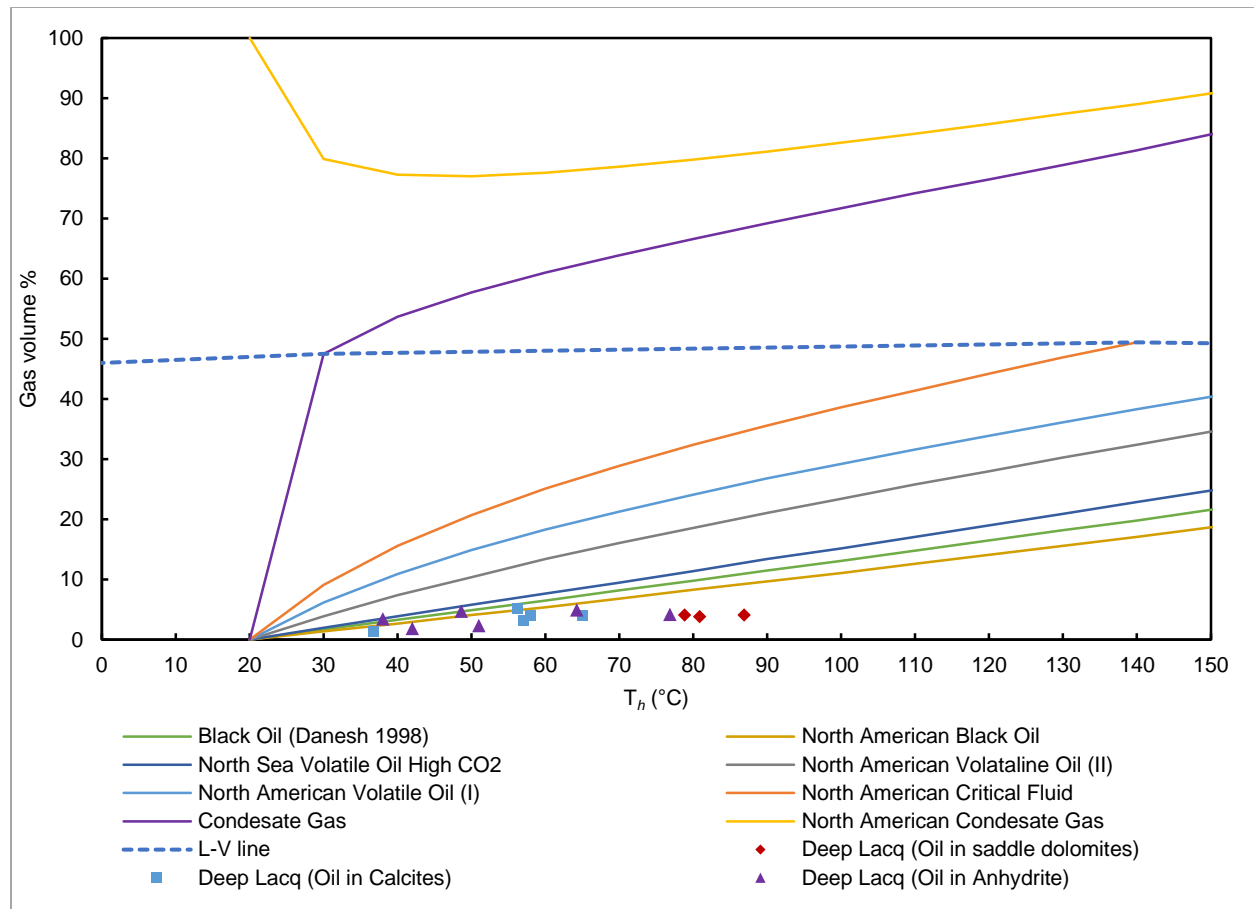


Figure 53. Gas volume % vs. T_h trends for 8 different reference oils. L-V line separates the homogenization to the liquid domain below from the gas domain above. Modified after Bourdet et al.,(2008).

6. Basin modeling

The approach to model the subsidence evolution of Deep Lacq differs from that of the Upper Lacq reservoirs (Chapter 3 part I – section 5). The plot of vitrinites versus depth is illustrated in figure 54. The blue and pink crosses represent the vitrinite maturity values from wells LA-104 and LA-103 respectively (Fig. 54). Green triangles represent equivalent vitrinite maturities, calculated from T_{max} , using the conversion procedure of Jarvie et al. (2001). The difference between the measured vitrinite maturities and those measured from T_{max} is because the latter is a proxy of the temperature at which the maximum release of hydrocarbons from cracking of kerogen occurs during pyrolysis (Killops and Killops, 2013). The measured and calculated vitrinite maturities in figure 54 follow a normal burial trend between the Jounsalles Formation (~1000m) down to the Sainte Suzanne Formation (~3300m). Immediately under the Sainte Suzanne Formation, the vitrinites increase drastically from average values of ~0.7 % R_0 to a maximum of 1.9 % R_0 within a depth

interval of nearly 500m. Several subsidence history scenarios can explain this jump in vitrinite data. For this purpose, we modeled 5 different scenarios with different histories of uplift, fluid circulation and/or basal heat flow values that can result in a best-fit model.

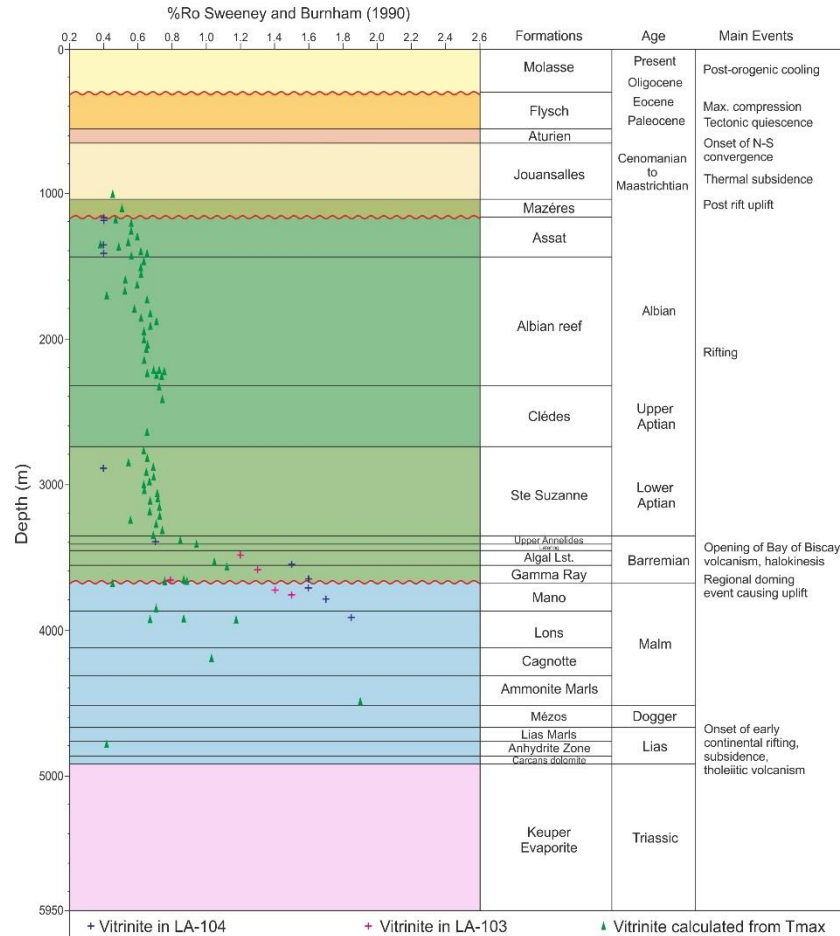


Figure 54. Depth plot of vitrinite data from LA-104, LA-103 and the equivalent vitrinite calculated from Tmax.

Model 1: This model involves an episode of hot hydrothermal fluid circulation in the formations sealed by the Sainte Suzanne Marls during the Aptian rifting phase. The temperatures of the circulating fluids reach a maximum of 250°C assuming similar temperatures to the Chaînons Béarnais (Salardon et al., 2018). Episodes of uplift, exposure and erosion in this model are simulated to remove 1500 m of the Assat Formation during the Albian (base Cenomanian) following the estimations of Le Marrec et al. (1995), and 200m of the Flysch below the Oligocene unconformities in accordance with the shape of the reflectors in figure 8. These values were selected to fit the resulting maturity curve simulated with the Petromod 1D with the vitrinite values. The thermal maturity curve simulated with these conditions is illustrated in figure 55.

Chapter 4 – Part I: Deep Lacq: Results - Basin modeling

The stepwise shift in the vitrinite values at the top of the Assat were caused by the 1500m of erosion while the shift in maturities under the Sainte Suzanne were reached by the heating effect of the 250°C fluids injected during the Aptian. This was done by changing the parameters of the standard igneous intrusion programmed in Petromod 1D. The density of the intrusion was lowered to that of the seawater and the temperature was modified. Basal heat flow was kept at 73 mW/m² during the peak rifting which decreased to 50 mW/m² during the post-rift phase.

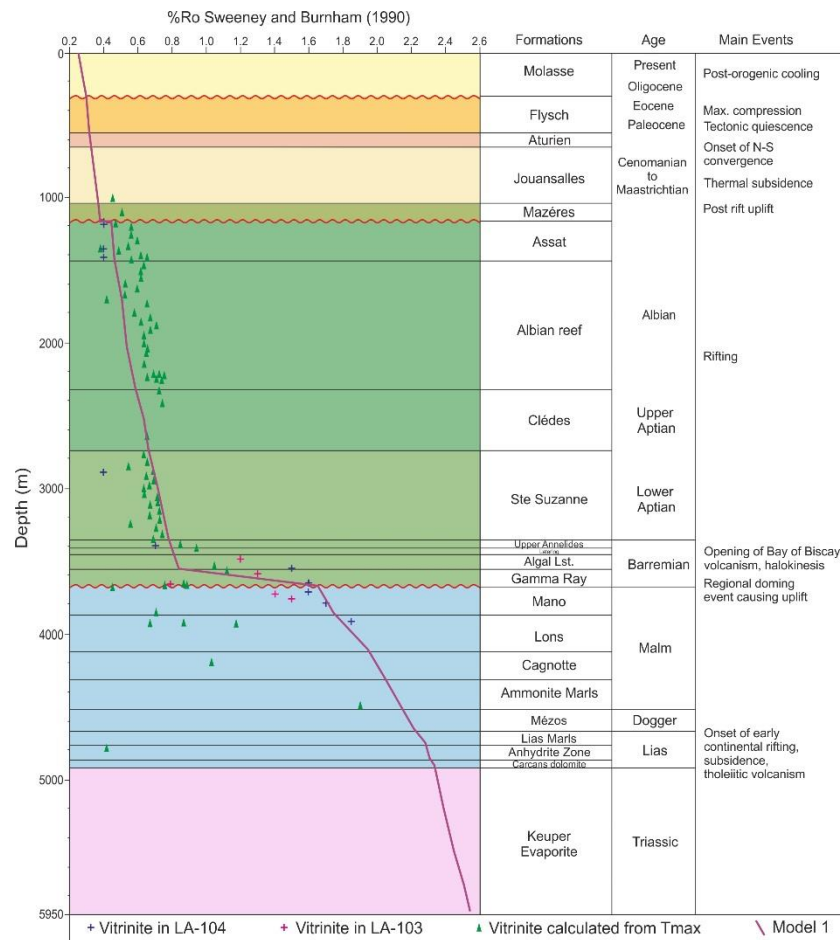


Figure 55. Model 1 of the thermal maturity history.

Model 2: Model 2 also involved an episode of hot fluids circulating during the Aptian. This scenario assumes vertical injection of fluids and not lateral as the case of model 1. These deep fluids have a maximum temperature of 250°C in the Keuper Evaporites and decrease to 150°C in the Sainte Suzanne Formation. Unconformity events were simulated to erode 600m of the Mano Formation during the Neocomian, 600m of the Assat marls at the base Cenomanian and 400m of the Flysch at the base Oligocene. These amounts

Chapter 4 – Part I: Deep Lacq: Results - Basin modeling

of eroded material were selected after several trials and errors to fit the simulated maturity curve with the vitrinite data. The basal heat flow parameters were kept the same as in model 1. The thermal maturity curve of model 2 is drawn in figure 56. The stepwise shift in the vitrinite values at the top of the Assat facies were caused by the 400m of erosion while the gradual shift in the curve under the Sainte Suzanne marls was reached by both the 600m of Neocomian erosion and the evolving fluid temperatures with depth.

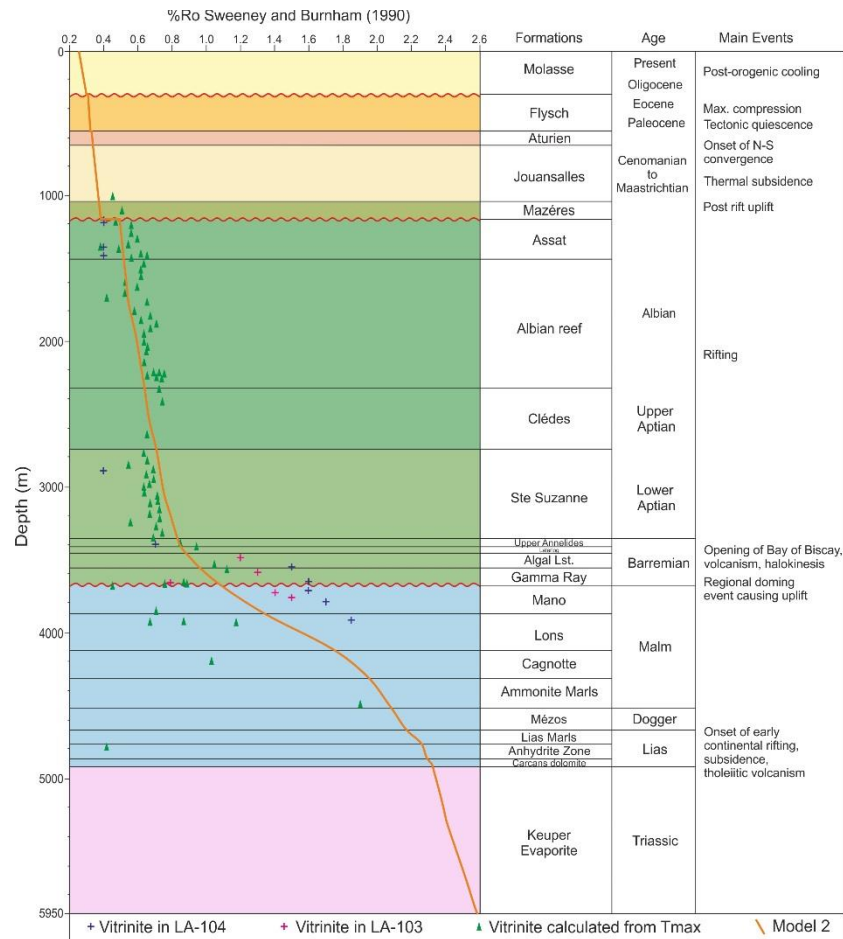


Figure 56. Model 2 of the thermal maturity history.

Model 3: In this model, the shift in the vitrinite maturities under the Sainte Suzanne marls were explained through severe erosional scenarios. No fluids were injected but rather the thickness of eroded material from the Mano Formation reached 500m during the Neocomian. The amount of eroded material is modeled according to the 1250-2000m of eroded Albo-Aptian formations suggested by Le Marrec et al. (1995) in the Aquitaine basin. Additional 2000m were removed from the Assat Formation during the base Cenomanian and 100m of Flysch below the lower Oligocene unconformities. The amounts of eroded material under each

unconformity were selected to test the impact of a severe erosion on the maturity of the vitrinite and the resulting best-fit model. The basal heat flow scenario was also kept unmodified as in models 1 and 2. The simulated thermal maturity is shown in figure 57. After the stepwise shift in simulated maturity at the top of the Assat Formation, the simulated thermal maturity follows a normal burial trend.

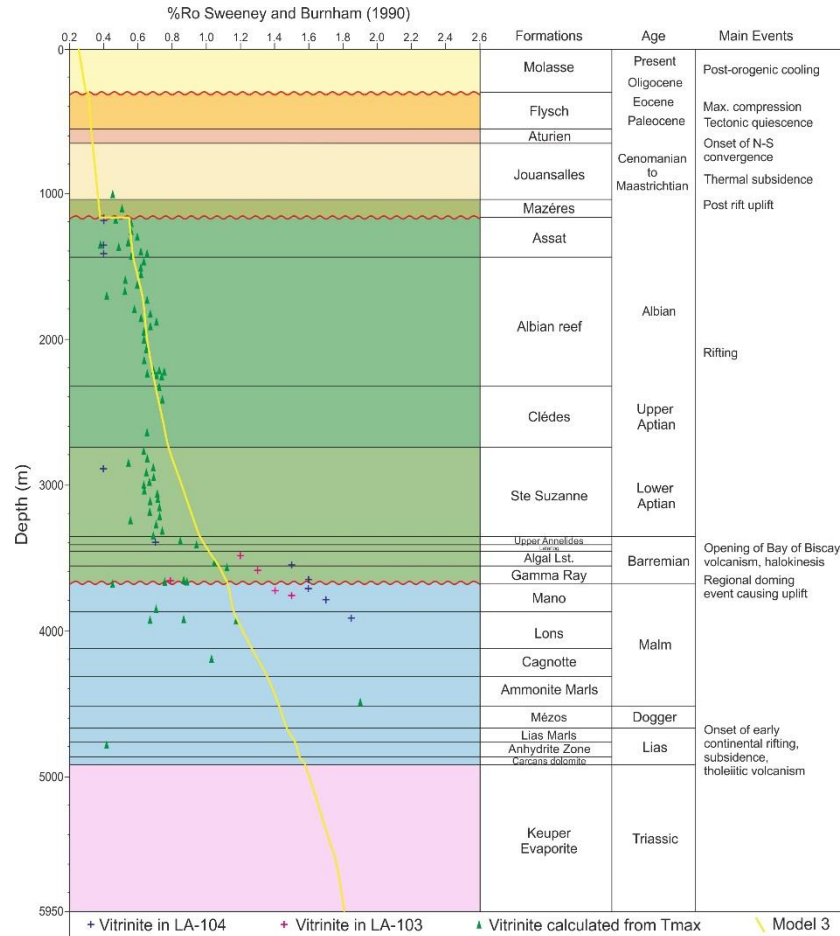


Figure 57. Model 3 of the thermal maturity history.

Model 4: This model was simulated without any injection of fluids. Instead, the high maturities of vitrinites were reached by increasing the basal heat flow during the rifting episodes of the Late Jurassic and Albo-Aptian. The amount of eroded material are lowered to fit with the onlaps and toplaps geometries at the base Cretaceous, base Cenomanian and Base Paleocene unconformities (Fig. 8) with 400m eroded from the top of Flysch formation, 200m from the Assat marls and 50 meters from the Mano Formation (Fig. 58). During the climax of the Aptian rifting, the heat flow reached 130mW/m² (Renard et al., 2019) and decreased gradually to a present day value of 45 mW/m² (Le Marrec et al., 1995). This present-day heat flow of 45

mW/m² is equivalent to a geothermal gradient in Lacq close to 30°C/km. The thermal maturity curve is represented in figure 58. In this model, no sharp steps in the vitrinite maturities are observed. The trend is governed by the high geothermal gradients and the moderate amounts of eroded material.

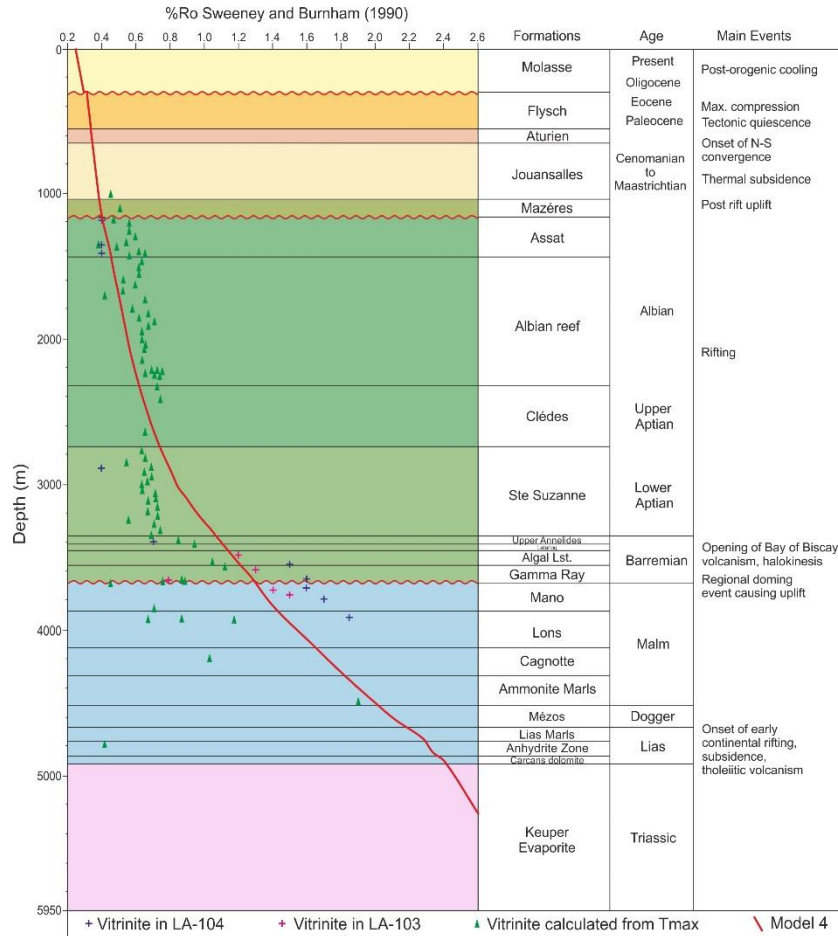


Figure 58. Model 4 of the thermal maturity history.

Model 5: This model assumes the same amounts of eroded material as model 4. However, the geothermal gradient is different. Previous works showed that the thermal peak related to the hyperextension did not cool quickly but took at least 20 to 30 Ma before equilibrating again (Clerc et al., 2015; Salardon et al., 2017; Angrand et al., 2018). This was taken into account in model 5 such that the peak basal heat flow reached 110 mW/m² at 120 Ma and takes 20 Ma to decrease to 85 mW/m². This heat flow value is lower than what Renard et al. (2019) proposed but takes more time to cool down. The present-day geothermal gradient is the same as model 4 and reaches 30°C/km. The resulting thermal model following this scenario is presented in figure 59.

Chapter 4 – Part I: Deep Lacq: Results - Basin modeling

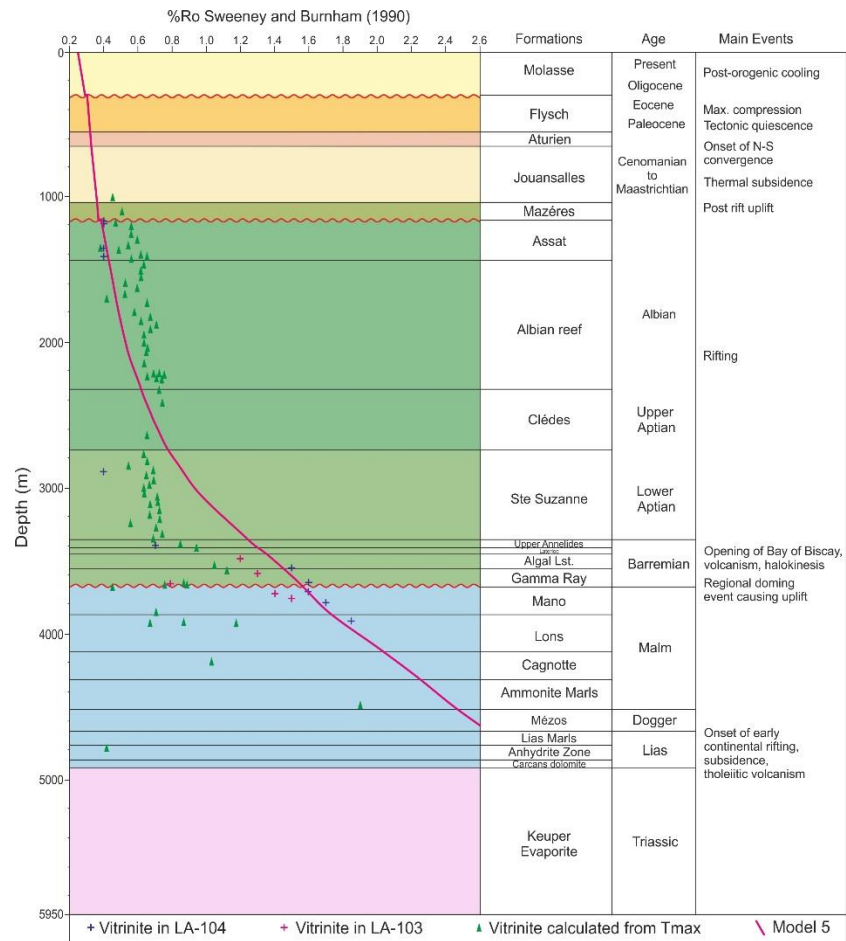


Figure 59. Model 5 of the thermal maturity history.

Chapter 4 – Part II: Deep Lacq: Discussions

1. Basin models

The sharp increase in vitrinite maturities immediately under the Sainte-Suzanne Formation (Fig. 54) was simulated through five different models. Each of these models has its advantages and disadvantages, discussed as follows:

Model 1: To reach the high vitrinite maturities of ~2 %Ro, 1500 m of erosion at the base Cenomanian and circulation of hydrothermal fluids at temperatures of 250°C were simulated as the main events. The karstic horizon at the top of the Mano Formation was considered as a conduit for fluid flow. The temperature of the injected fluids was selected after multiple trial-and-error scenarios in order to have a relatively good fit with the plotted vitrinite data. This model gives a good fit with the vitrinite data and shows a step-wise shift in the thermal maturity between Deep Lacq and Upper Lacq (Fig. 55). However, the 1500m at the base Cenomanian (Le Marrec et al., 1995) is rather extreme which could apply to the succession lying on top of the Grand Rieu Ridge and not the entire basin. In addition, this erosion does not fit neither with the orogenic setting, nor with the seismic cross section that shows nearly parallel onlaps of reflectors above the unconformity (Fig. 8).

Model 2: This model also involves injection of hot fluids, but with less severe erosional events. The fluids were modeled to decrease in temperatures as they move upwards in the stratigraphic column. The resulting thermal maturity model shows a gradual increase of maturities with depth without a sharp shift under the Sainte-Suzanne Formation (Fig. 56). The main disadvantage of this model is the speculation regarding the temperatures of the injected fluids, their mismatch with the recorded temperatures from the fluid inclusions study and the rapid loss of 100°C across a stratigraphic thickness of only ~1500m.

Model 3: In this scenario, the main event influencing the thermal evolution is the extreme erosion of nearly 2000m of Assat marls during the Albian (base Cenomanian unconformity). The accommodation space, and hence the burial depth implied by these 2000m of eroded material would increase the vitrinite maturities. However, this amount does not fit with the seismic cross section that show nearly parallel onlaps at the

crest of the anticline (Fig. 8). Also, such a 2000m of erosion would have provided evidences such as layers of breccia or reworked material, which were not observed in the Albo-Aptian formations in Lacq. In addition, the resulting thermal evolution curve does not fit well with the maturities recorded by the vitrinite (Fig. 57).

Model 4: In this model (Fig. 58), neither fluids were injected into the Deep Lacq reservoirs nor unrealistic amounts of material were eroded during unconformities to reach the vitrinite maturities. In contrast, the basal heat flow was simulated to heat the reservoirs and obtain the observed maturity. The heat flow during the hyperextension reached 130 mW/m^2 and decreased during nearly 6 Ma to reach 80 mW/m^2 and then gradually cooled to 57 mW/m^2 after the Paleogene compression. The 130 mW/m^2 heat flow value follows the scenario modeled by Renard et al. (2019). The advantage of this model is that it doesn't speculate on possible hydrothermal fluid injections and very severe, geologically unrealistic, erosional events. In contrast, the downside is that the drop in the heat flow is rapid and disagrees with the persistence of high post-rift heat flow suggest by Clerc et al. (2015), Salardon et al. (2017) and Angrand et al. (2018).

Model 5: This model (Fig. 59) assumes the same amount of eroded material as model 4 which is in accordance with the shapes of the onlaps in figure 8 and with the overall geologic setting of the area. The basal heat flow was lowered to 100 mW/m^2 , with a geothermal gradient of nearly 95°C/km , during the rift climax but which cooled down to 85 mW/m^2 over a span of 20 Ma (geothermal gradient of 70°C/km). The decrease in the heat flow continued to result in the present-day heat flow of 45 mW/m^2 with an average geothermal gradient of 30°C/km . The present-day geothermal gradient is supported by the modeling of Le Marrec et al. (1995) and also the work of Renard et al. (2019) in the Rousse site, 20 km southwest of the Lacq anticline.

Given all the trials and errors, the geologic constraints, and the data recorded from the fluid inclusion studies, the most realistic scenario, with minimum assumptions and with the best support from published literature data is the one simulated with model 5. However, as seen in figure 59, the sharp shift in vitrinite values in the Barremian formations was not possible to be simulated. Also, the maturity model overlaps well with more mature vitrinites (blue crosses in figure 54). Therefore, this model covers the high maturity range / high temperature range of the vitrinite data and thus, lower geothermal gradients should be

reasonable and should not be discarded. The resulting subsidence history with the evolution of burial temperature is displayed in figure 60.

The subsidence curve begins from the Upper Triassic to present day and includes several episodes of subsidence and uplifts. The Upper Triassic to Jurassic was marked by diffuse early continental rifting (Jammes et al., 2010a). Locally, this was reflected by a slow subsidence that is the combination of the tectonic signature, as well as the sedimentary load of the Keuper Evaporites, Carcans dolomite, Liassic Anhydrite and Liassic Marl formations. These formations were deposited during a slow early rifting phase which then apparently accelerated until the Jurassic – Cretaceous boundary (Fig. 60). The Neocomian (145-130 Ma) was a phase of mantle doming causing regional uplift and erosion, characterized in the North Pyrenean Zone by an unconformity and the deposition of bauxites (Salardon et al., 2017), while in the southern Aquitaine basin a depositional hiatus without sedimentation formed (Le Marrec et al., 1995). The main rifting event during the early Cretaceous was associated with a peak in the basal heat flow reaching 100mW/m^2 (geothermal gradient of 78°C/km). This event was locally associated with an increase in the paleowater depth which allowed the deposition of turbidites of the Sainte-Suzanne formation below the storm wave base at depths of 100m or more (Biteau et al., 2006). After this rifting phase, isostatic rebound caused uplift and erosion at the origin of the base Cenomanian unconformity. It is assumed that no more than 200m were eroded during this uplift. The Cenomanian to Santonian times were marked by cooling and thermal subsidence of the basin. This was also contemporaneous to a gradual increase in the paleobathymetry and sea level transgression (Biteau et al., 2006). The N-S convergence began since the Campanian to Maastrichtian, while the Paleocene was a calm period of tectonic quiescence. The climax of the Pyrenean orogeny is observed in the Eocene with the emergence of the Aquitaine basin and an erosional unconformity with nearly 400 meters removed from the Flysch formation (the base Oligocene unconformity). Since the Oligocene, the basin is gradually subsiding due to the post-orogenic cooling.

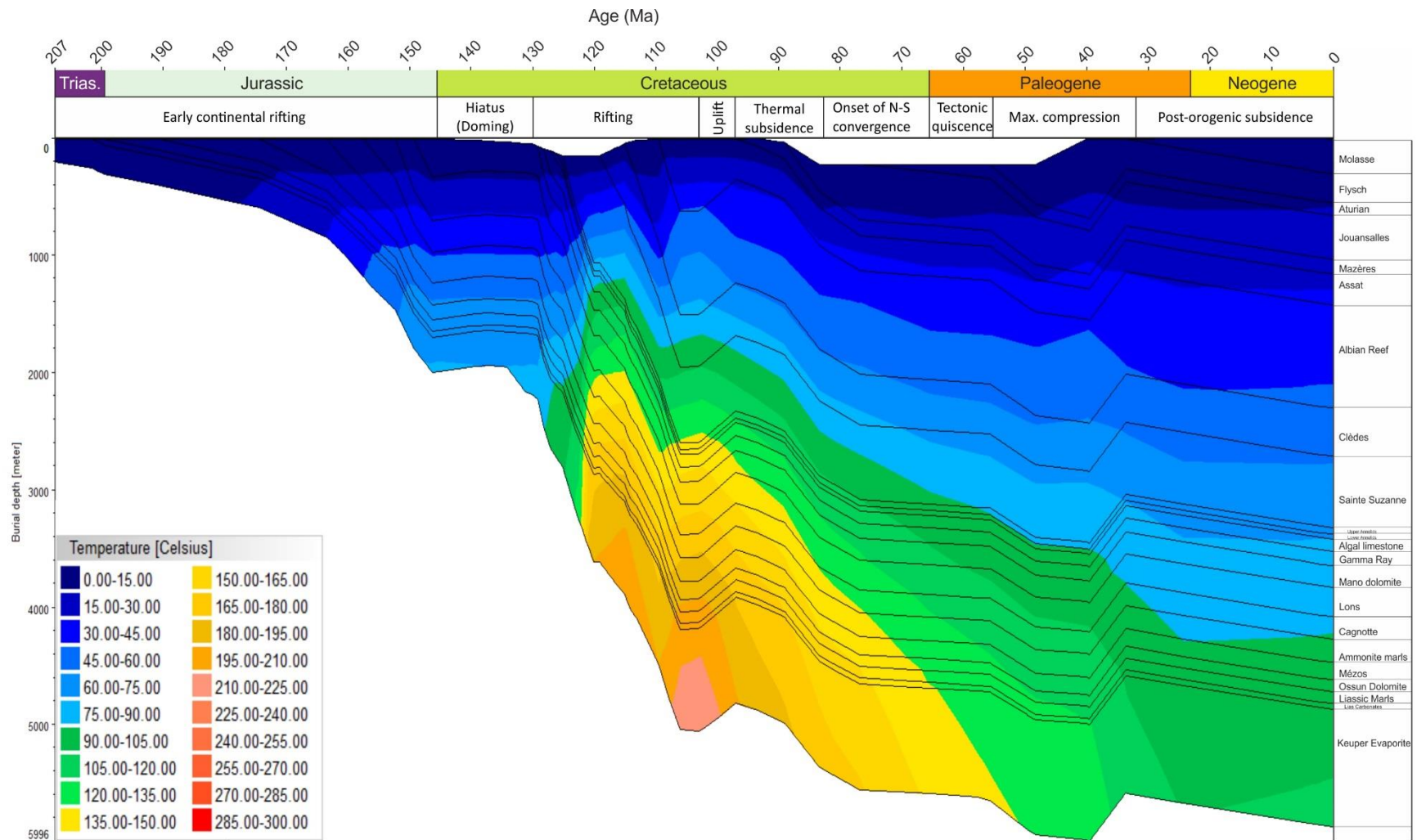


Figure 60. Subsidence history of Lacq showing the main regional geodynamic events and the evolution of burial temperatures. Colored bands follow the temperature chart in °C.

2. H₂S and its effect on phase diagrams

By considering the composition of the aqueous phases listed in table 7, conventional AIT using the equations of state of Duan et al. (2000) cannot be applied because the modeling procedure assumes a system composed of H₂O-NaCl-CH₄ without H₂S. Up to 5.14 mole % of the fluid composition is composed of H₂S, and it would be misleading to ignore this in the computation of the isochores. No published works exist which takes into account the influence of sulfur on the aqueous phase diagrams. To overcome this limitation, the chemistry of the aqueous and oil inclusions were processed at the LRGP (UMR 7274 CNRS-UL Laboratoire Réactions et Génie des Procédés) in Nancy, France with the help of Mme Silvia LASALA, in an attempt to draw more representative isochores and observe the influence of H₂S on the homogenization pressures. Details and explicit data about the thermodynamic model and calculation steps, which follow the GERG-2008 equation of state, were outlined by Kunz and Wagner (2012). However, the GERG-2008 equation of state (Kunz and Wagner, 2012) has a limitation, as it cannot consider ionic species in the chemistry of the solution due to thermodynamic difficulties. Thus, the composition of the aqueous fluids were assumed pure H₂O-H₂S-CH₄ without NaCl. This assumption would overestimate the quantities of CH₄ and H₂S which when translated into an isochore in a P-T plot could give trapping conditions that may not accurately represent the fluid circulation scheme of Deep Lacq. Therefore, conventional AIT modeling to deduce the trapping P-T conditions, using the double-isochore technique (Bourdet et al., 2007), cannot be applied on the diagenetic fluids of Deep Lacq. To understand the influence of H₂S on the phase diagram of an aqueous system composed of H₂S-CH₄-H₂O, two hypothetical fluids were simulated (Fig. 61); fluid (1) is composed of 98% of H₂O, 1.9% of H₂S and 0.1% of CH₄, while fluid (2) consists of 95% of H₂O, 4.5% of H₂S and 0.5% of CH₄. The most important effect related to the increase in H₂S content in the solution is seen in the swelling and expansion of the two-phase region bounded by the isopleth (Fig. 61).

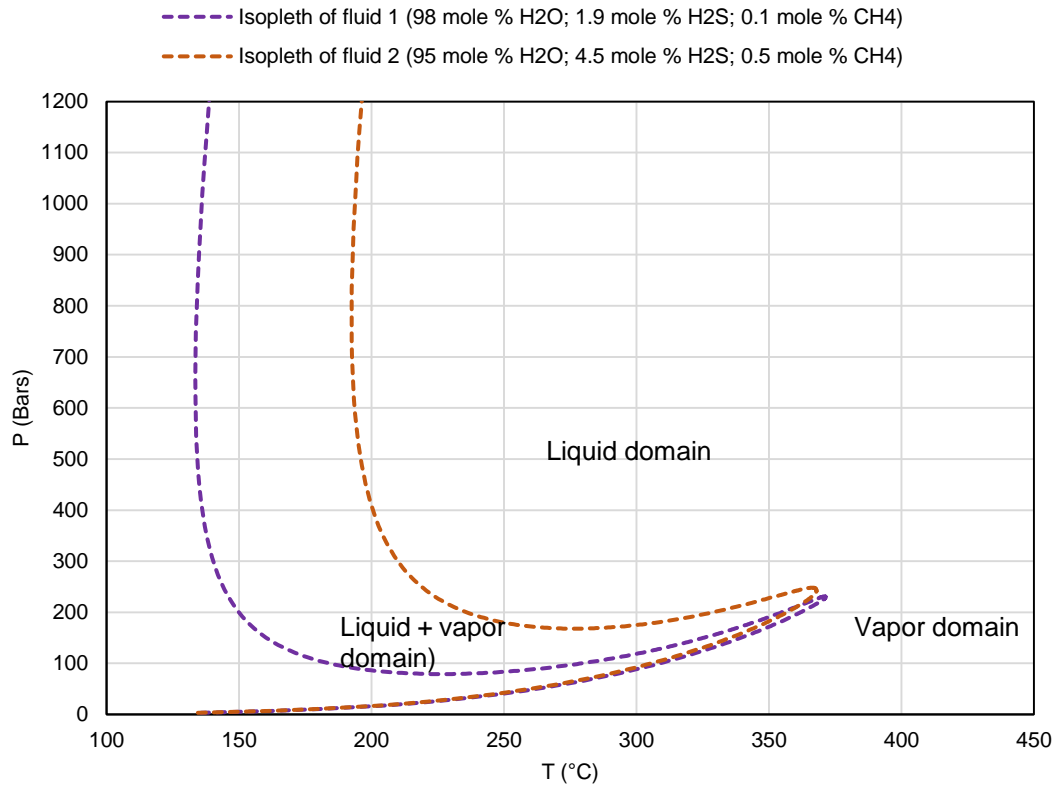


Figure 61. P-T plot of the isopleths of fluid (1) and fluid (2) with different H₂S contents.

If, for example, the two aqueous inclusions homogenize at 200°C, the homogenization pressure of fluid (1) would be 98 bars, while that of fluid (2) would reach 400 bars.

Similarly, to have an example of the influence of H₂S on the phase diagrams of oil, a hypothetical oil inclusion having a T_h of 60°C, a vapor volume of 5% and H₂S concentrations of 0%, 10%, 20%, 30% and 40% was drawn in figure 62. Modeling of this phase diagram is based on the equation of state of Peng and Robinson (1976), integrated into the PIT software (Bourdet et al., 2008). We can observe that as the concentration in H₂S increases, the homogenization pressure and the shape of the isopleth is suppressed and lowered.

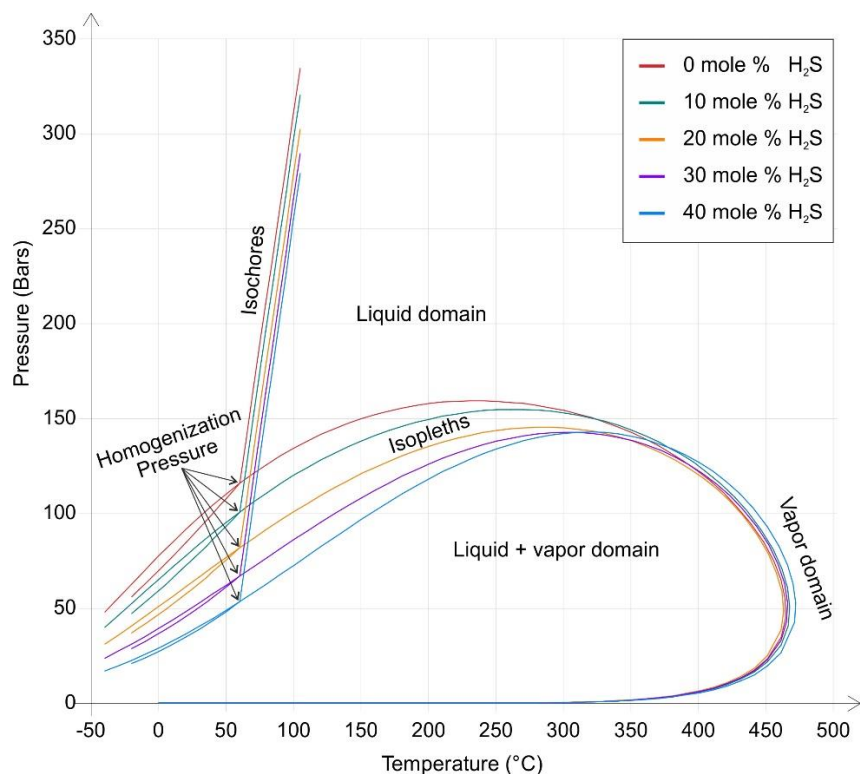


Figure 62. P-T diagram showing depression of homogenization pressures as H₂S concentration increases.

This decrease in homogenization pressure as H₂S increases is opposite to the case of the aqueous inclusions that experienced an elevation of pressures. This different behavior could be related to differences in densities and/or solubility of gases between aqueous and oil fluids.

Consequently, given the current limitations in modeling the phase diagrams of complex fluids composed of H₂O-NaCl-CH₄-H₂S-HS⁻ (table 7), determining the trapping conditions by the intersection of the oil and aqueous inclusion isochores were not possible, due to possible overestimations of the amounts of CH₄ and H₂S which could dramatically overestimate the trapping pressures and hence the timing of fluid entrapment.

3. Ages of the diagenetic fluids

To obtain age constraints on the diagenetic fluids, it is possible to correlate the burial temperatures, determined from the basin modeling through Petromod 1D, to the T_h , considered as the minimum trapping temperature. This is supported by the fact that gases dissolved, detected with Raman spectroscopy, were found in the aqueous inclusions trapped in the saddle dolomites, calcite 3 and anhydrites. The detection of gases is indicative of a high pressure system, thus the difference between the homogenization

temperatures and the trapping temperatures of the fluids should be minimum. With this reason, the homogenization temperatures should be representative of the minimum trapping temperatures. Such an approach would give a minimum age based on the homogenization temperatures. Figure 63 shows the evolution of the burial temperatures of the Mano Dolomite Formation from which the studied Dol. 2 phase was sampled. Aqueous fluid inclusions in Dol. 2 have a T_h range of 132-148°C which coincides with the burial temperatures (dark red box of figure 63) at two minimum age ranges, one during the Apto-Albian rifting between 120 and 110 Ma, the other is between 80-93 Ma. The calcite 3 phase was studied in the Algal and the Lons Limestone Formations whose burial temperatures are plotted in figure 64. Similarly, the blue box represents the range of the homogenization temperatures of the studied fluid inclusions that extends between 100 to 148°C (Fig. 51a). This temperature range intersects the burial temperatures of both formations at points, one during the Aptian rifting between 118 and 122 Ma, the other between 70 to 32 Ma during which the reservoir experienced the onset of N-S compression, tectonic quiescence and the maximum collision phases (Fig. 60). The same approach is applied with the anhydrite phase, such that figure 65 represents the burial temperatures of the Algal Limestone Formation with the purple box representing the T_h of the aqueous inclusions being between 95 to 130°C (Fig. 53a). The intersection with the burial temperatures yield 2 ages, one being at 118-121 Ma (Aptian rifting) while the other extends from the Campanian (73 Ma) to the present day.

An important conclusion with this approach is that all the studied phases circulated from fluids whose minimum temperatures were in thermal equilibrium with the burial temperatures experienced by the host rocks. No evidence of thermal disequilibrium and hydrothermal activity were identified in deep Lacq, in contrast to Upper Lacq, where the saddle dolomites and calcites precipitated from fluids there were at least 30-40°C hotter than the ambient temperatures.

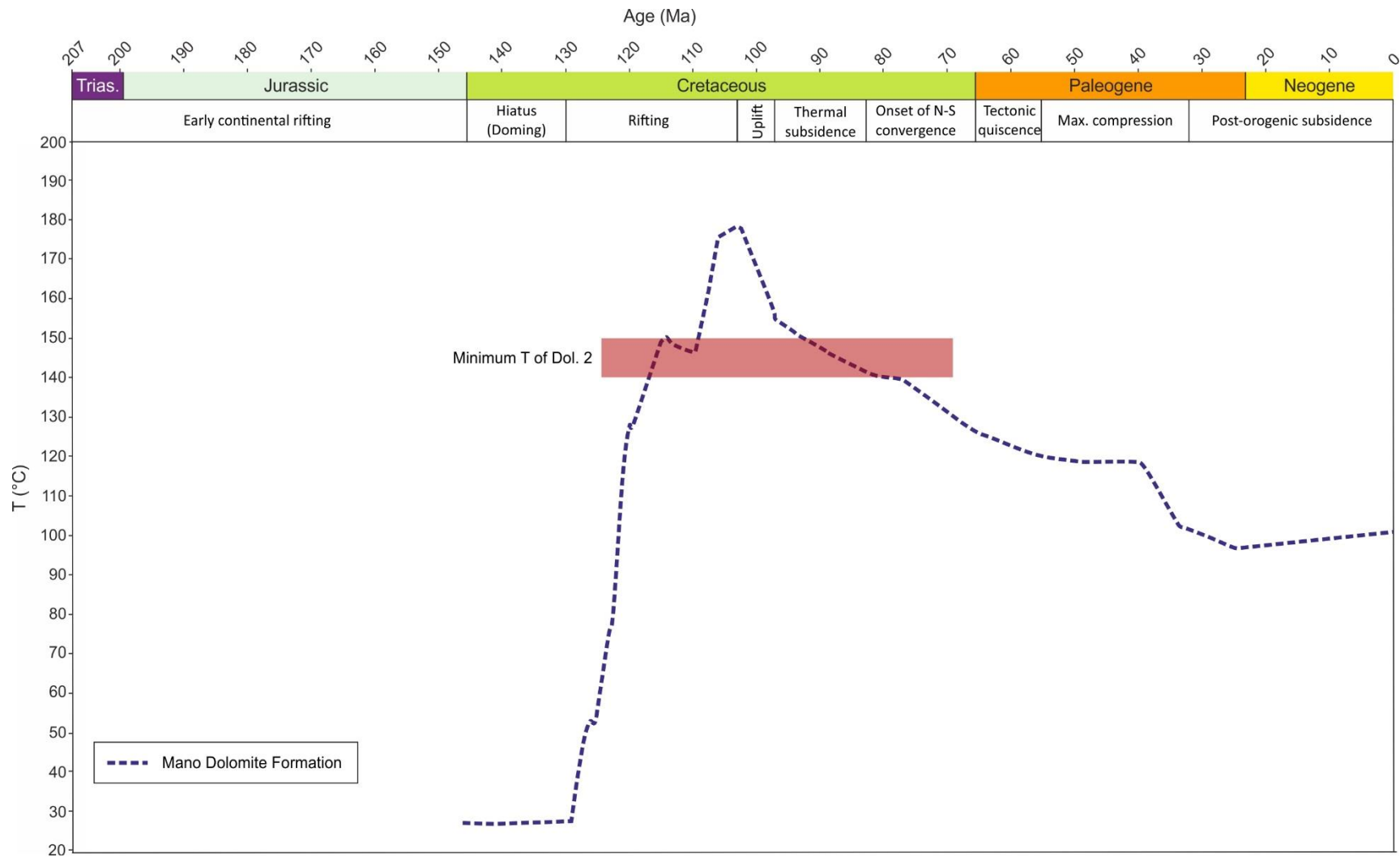


Figure 63. Evolution of the burial temperatures experienced by the Mano Dolomite Formation with the homogenization temperature range of the dol. 2 phase

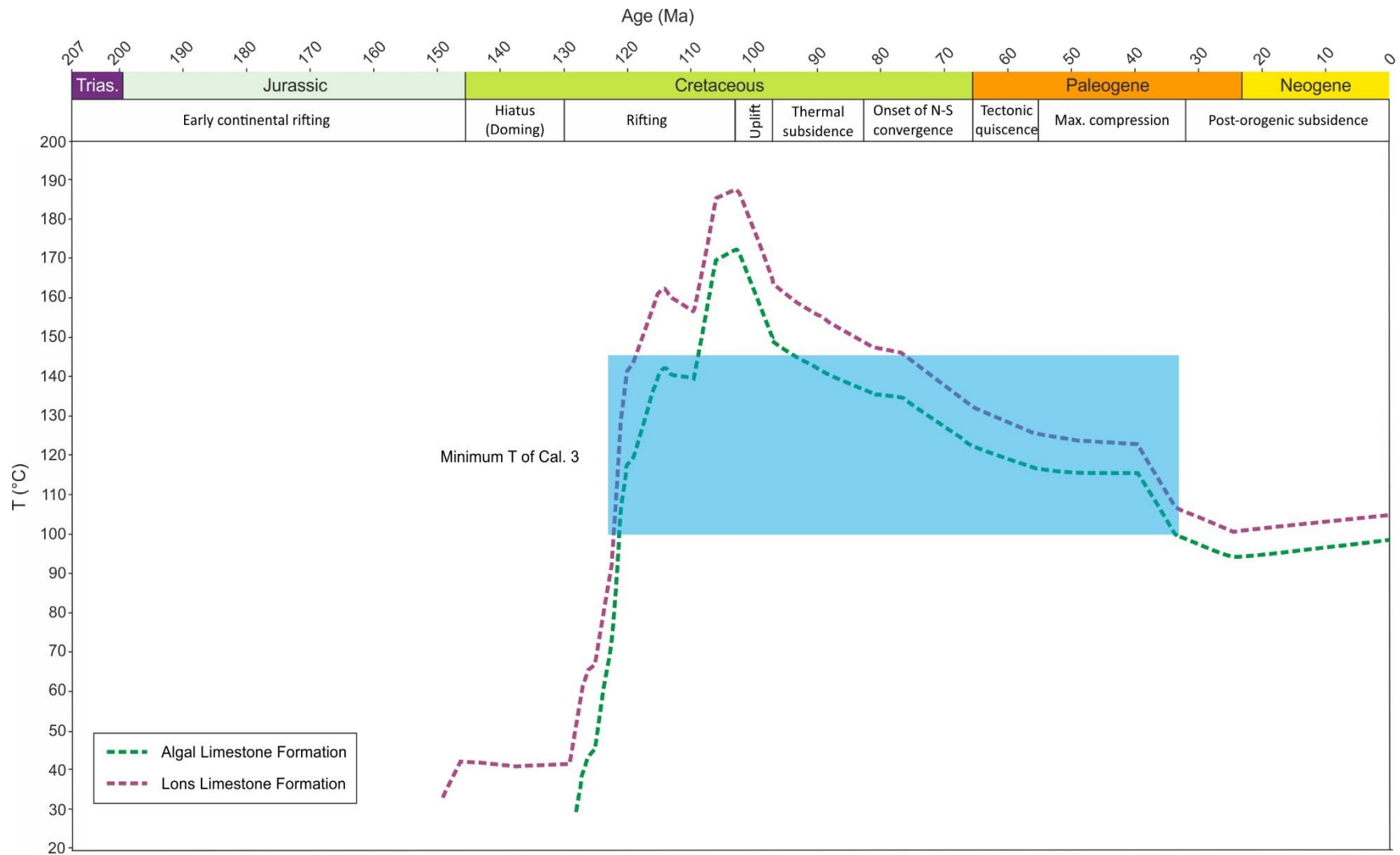


Figure 64. Evolution of the burial temperatures experienced by the Algal and Lons Limestone Formations with the homogenization temperature range of the Cal. 3 phase.



Figure 65. Evolution of the burial temperatures experienced by the Algal Formation with the homogenization temperature range of the Anhydrite phase.

Table 8. Summary of the age ranges estimated from the burial temperatures.

Mineral Phase	Age range 1 (in Ma)	Age range 2 (in Ma)
Saddle dolomite	110-120	80-93
Calcite 3	118-122	70-32
Anhydrite	118-121	73 - 0

These broad ranges can further be reduced and constrained through petrography and geochemistry, discussed in the following section.

4. Timing and sources of diagenetic fluids

Based on petrographic observations, a relative chronology of diagenetic phases and events for Upper Lacq is proposed in figure 66.

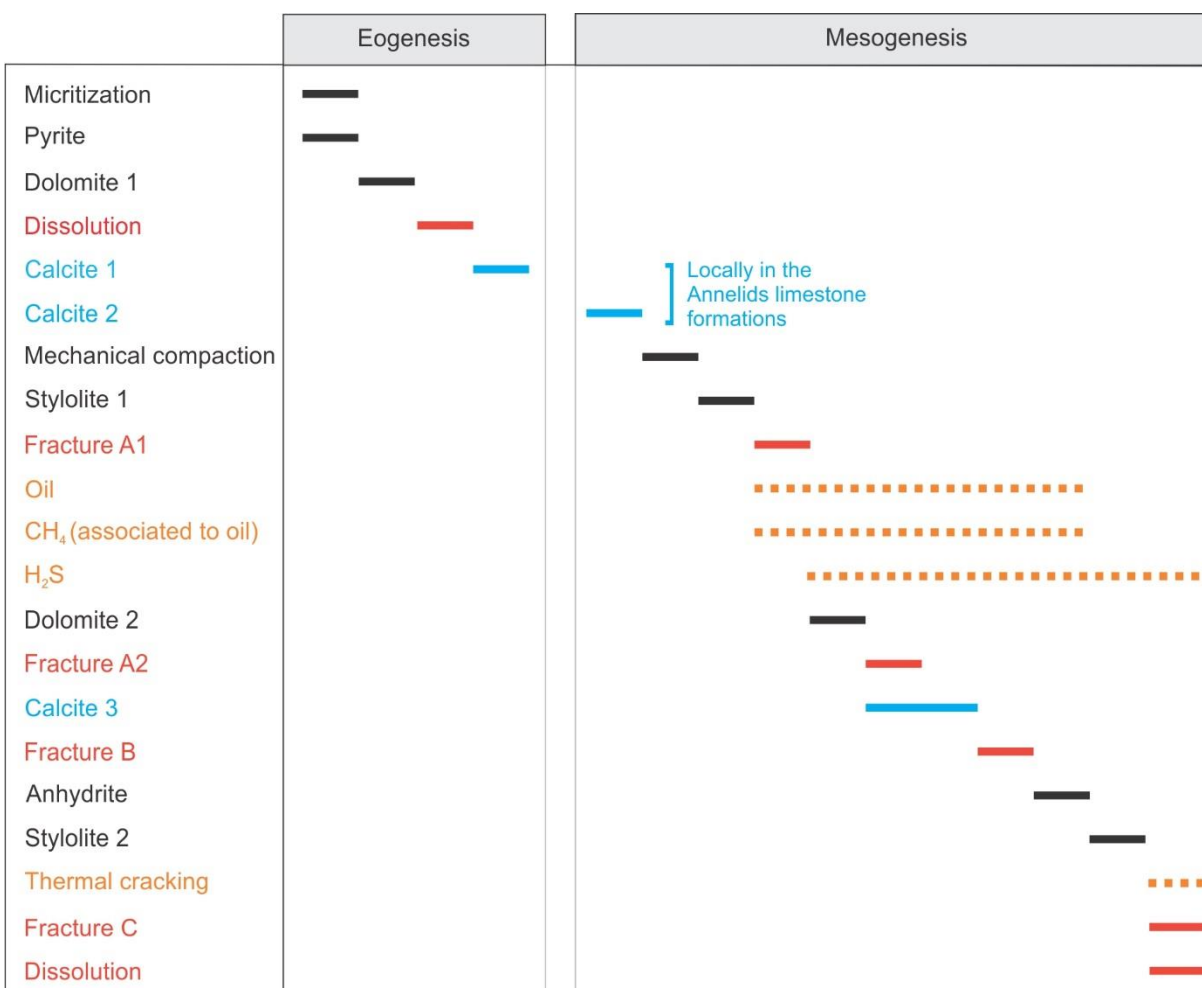


Figure 66. Chronology of petrographic phases observed in Deep Lacq.

The chalky mudstone, bioclastic wackestone to packstone, as well as the pelloidal boundstone with microforaminifera, bivalves, mollusks, sponges, echinoderms and annelids are indicative of a shallow marine depositional environment, in a lagoon to reefal setting. This is also supported by previous paleoenvironment reconstructions of Le Marrec et al. (1995) and Biteau et al. (2006). $\delta^{18}\text{O}$ isotopes of the bulk host rocks (Fig. 40) are depleted relative to the late Jurassic seawater due to recrystallization at higher temperatures, which is evident by the resetting of the orange CCL colors of the micritic host rocks (Figs. 36e and 37b,c,d) to equilibrate with the reducing conditions during burial. Negative $\delta^{13}\text{C}$ values could be due to a possible contribution of carbon from karst-related paleosoils especially that the late Jurassic to Cretaceous boundary was coupled with regional doming and karstification (Le Marrec et al., 1995). Micrite rims and burrows engulfing and penetrating bioclasts (Fig. 36a) are evidence of bacterial activity. This bacterial activity was also responsible for the precipitation of pyrite 1 phase since the framboidal clusters and their rounded to anhedral shapes are typical by-products of bacterial sulphate reduction (BSR) (Machel, 2001). The preferential distribution of framboidal pyrite in shells impacted by micritization is in accordance with BSR, controlled by the local abundance of organic matter. Dolomite 1 has likely precipitated from a marine fluids with a slight contribution of meteoric water source as supported by the $\delta^{18}\text{O}$ and $\delta^{13}\text{C}$ of this phase that range between -1.2 to +1.8‰PDB (Fig. 40). The positive $\delta^{18}\text{O}$ values are interpreted as primary/early low temperature marine dolomite. According to Horita (2014) dolomite in equilibrium with pre-Miocene sea water ($\delta^{18}\text{O} = -1\text{‰}$) at 20°C would have a $\delta^{18}\text{O}$ value of about +2‰. With gradual deepening, the redox conditions under which the fluids percolated varied and fluctuated. This is suggested by the non-luminescent to bright-red luminescent zones under CCL of the dolomite 1 phase (Fig. 36c). The enrichment of $^{87}\text{Sr}/^{86}\text{Sr}$ in Dol. 1 (Fig. 41) above the late Jurassic seawater is a possible indication of large volumes of meteoric fluids that percolated downwards which eventually overcame of the Sr buffering of the host marine limestones (Moore, 2013). At slightly deeper intervals within the eogenetic realm, circulation in the mixing zone, between the phreatic and marine realms, was characterized by episodic mixing between oxidizing meteoric fluids and deeper formational fluids precipitated the dog-tooth calcite 1 phase. Zonations in this phase reflect the fluctuations in the redox states which support precipitation in the phreatic zone rather than a pure marine realm. Transition to mesogenesis was marked by the dominance of the reducing conditions in the calcite 2 phase with diminishing influence of the percolating meteoric fluids. Its equidimensional

morphologies and yellow-orange CCL luminescence (Fig. 36e) are typical of a burial diagenetic environment following the criteria of Tucker and Wright (1990). As the overburden pressure increases, mechanical compaction starts and then evolves to chemical with the development of stylolites 1 (Fig. 37). Since the samples were collected from vertical wells that cut nearly horizontal strata, the orientation of the stylolite planes, being nearly horizontal, allows its classification as bedding-parallel stylolites (BPS). The timing of fluid simulated with the modeling tools indicates that the first saddle dolomites (Dol 2) precipitated during the Aptian. Consequently, between the precipitation of calcite 2 cement, and the precipitation of the saddle dolomites during the Aptian, the Deep Lacq reservoirs did not experience major diagenesis event except compaction and stylolitization.

Oil has likely migrated into in the Deep Lacq reservoir during the precipitation of Dol 2 as suggested by the oil inclusions found in the saddle dolomite crystals. The main source rocks in the Deep Lacq petroleum system are the Annelids and Lons Limestone Formation (Biteau et al., 2006). Source rock maturity modeling indicate that entrance to the oil windows, with vitrinite reflectance of ~0.6% PR_v (oil) has occurred during the Lower Cretaceous on the crest and the NE limb of the Lacq structure (Serjouné, 1995). Such a model agrees with the coeval entrapment of oil and aqueous inclusions in the saddle dolomites and is in accordance with the Aptian timing suggested in figure 63 and table 8. The relative $\delta^{18}\text{O}$ depletion (~-6.2‰PDB) is due to fractionation at elevated temperatures. The presence of H₂S in the aqueous inclusions (Table 7) suggest that TSR was initiated when saddle dolomites precipitated. The fact that saddle dolomites are always identified along fractures (fracture set A, Fig. 37b), support that a fracturing event favored the circulation of parent fluids of Dol 2. The ratio of $^{87}\text{Sr}/^{86}\text{Sr}$ in Dol 2 (Fig. 41), although not statistically enough to make robust arguments (n=1), is however enriched relative to the Late Jurassic seawater. Possible scenarios for Sr enrichment are listed in Travé et al. (2014) and include (1) weathering by meteoric fluids, (2) dissolution of detrital phyllosilicates at high P-T conditions or (3) interaction with marls that have likely experienced smectite to illite transformation. Option (1) is unlikely given that the investigated dolomite phase precipitated during burial with an Aptian seal preventing any inputs of acidic meteoric fluids able to modify the Sr isotopic signatures. Option (2) is possible in the presence of serpentine, talc, micas or chlorite. The absence of these minerals, and hence of a source rich in phyllosilicates in the studied samples and in the Lacq area according to the literature needed to support option (2) disqualify this source. In contrast, the

occurrence of the Ammonite Marls and Liassic Marls Formations few hundreds of meters below the studied samples rather support option (3). The connection and the occurrence of fluid pathways between these marly formations and the Deep Lacq reservoir was accomplished by the fracture set A. Similarly, it is necessary to discuss and compare the possible sources of Mg involved in this dolomitization episode. This is presented as follows:

1. The interstitial connate fluids could have provided the Mg volume required to precipitate the saddle dolomites during burial and compaction (stylolite 1). However, these fluids, being marine in origin, should reflect salinities close to that of seawater. Thus, despite the possible contribution of the connate fluids, the high salinities reaching 8.2-10.2 eq.wt.%NaCl (Fig. 47b) involve the interaction with another salted fluid.
2. The proximity of the Triassic evaporites at the core of the Lacq anticline with the studied samples and the evidence from multiple sulfur isotopes support a possible connection between the Deep Lacq reservoirs and the Triassic diapir. This scenario is mainly supported by the high salinities measured in the fluid inclusions, while uncertainties arise from mass balance considerations by considering the huge thickness of the salt diapir (1000+ meters thick) (Fig. 8) relative to the limited volume of dolomite cements in the fractures.
3. Mg derived from a mantle source involving serpentization reactions could be possible given the depth and age of the reservoir that was impacted by the thermal anomaly during the hyperextension. However, mantle-related fluids would have traces of H₂ or CO₂ in the fluid inclusion. The absence of such evidence based on Raman spectroscopy rules out this Mg source.
4. The underlying Ammonite and Liassic Marls Formations may contain Mg-rich minerals and can serve as another potential source for dolomites. However, more data are needed to validate the presence of Mg-clays in the marls. Mg-clays are rare in sedimentary formations, and when present they are dominantly of two types: Mg-smectites (bedeillite, saponite) or Stevensite/kerolite-Talc clays (Millot, 1970). Both types are usually associated with volcanism and/or hydrothermalism and/or highly alkaline lacustrine settings. This does not fit the Sainte Suzanne marl depositional conditions.
5. Another source could be the dissolution and recrystallization of the early dolomites in the marls as a result of pH lowering during the first stages of organic matter maturation and the associated release of organic acids (Moore, 2013). Such a scenario can justify the elevated $\delta^{18}\text{O}$ values calculated for the

dolomite-forming water of 7.3-9.4 ‰SMOW according to the fractionation curve of Horita (2004). The dissolution of low temperature carbonates in semi-closed conditions is an efficient way to drive the water $\delta^{18}\text{O}$ up to high values and can eventually provide a suitable Mg source.

Petrographic evidences clearly places the calcite 3 after saddle dolomites (Fig. 37b and d). The dull orange to yellow luminescence suggests a precipitation under reducing conditions. The depletion in $\delta^{18}\text{O}$ (-2.8 and -5.63‰PDB) (Fig. 40) is also due to fractionation at elevated temperatures. The difference in $\delta^{18}\text{O}$ between Dol 2 and Cal 3 cements is either due to higher temperature of dolomite precipitation or due to precipitation from a lighter parent fluid source. However, higher temperatures of precipitations are not strongly supported by the FI microthermometry. The $\delta^{13}\text{C}$ signatures of Dol 2 and Cal 3 from the samples collected in this study (Fig. 40) show a trend marked by a decrease in $\delta^{13}\text{C}$. Generally, two processes can generate enriched $\delta^{13}\text{C}$ compared to the host rock; organic fermentation or methanogenesis, which can produce CO_2 having $\delta^{13}\text{C}$ values reaching up to +25‰ (Irwin et al., 1977; Warren, 2000). However, given the relatively high burial temperatures during mesogenesis, bacterial activity at burial depths cannot be supported. Therefore, it is likely that during early diagenesis, early bacterial fermentation and methanogenesis produced isotopically heavy CO_2 which was trapped and later mixed with another pool of CO_2 , buffered by the host rocks, and resulted in broad range of $\delta^{13}\text{C}$ plotted in figure 40. Such a mixing model of CO_2 sources can explain the difference in $\delta^{13}\text{C}$ between the cements of Deep Lacq and other classical examples of TSR-reservoirs. For example, the diagenetic calcites in the Obed reef buildup, Upper Devonian, west-central Alberta, Canada have a $\delta^{13}\text{C}$ signature of -27 ‰PDB (Mountjoy et al., 1999) while the calcites of the Upper Devonian Cairn Formation of the Fairholme carbonate complex, South-West Alberta, Canadian Rockies reach -25.9 ‰PDB (Vandeginste et al., 2009).

Cal 3 cement has a minimum age of nearly 70 Ma or younger (Fig. 64 and Table 8) coeval with the onset of N-S convergence. The Aptian age in figure 64 and table 8 is not possible given the petrographic evidence that clearly places Cal. 3 after Dol. 2 (Fig. 37). Thus, an age older than the dolomites (Aptian) is not envisioned. During the Maastrichtian, as the tectonic regime has shifted from extensional to compressional, the change in stress fields have likely induced a new fracturing event (A2) that reopened fracture set A1 (Fig. 37b) and allowed Ca-rich fluids to circulate. The difference in the homogenization temperatures

recorded in the 2 populations of fluids inclusions trapped in the calcite 3 (Fig. 51) can be explained by the difference in pressure during the fault-valve mechanism (Sibson et al., 1975). This process involves an increase in pressure after cementing and clogging of fractures. When the fracture is reopened, the pressure is reduced, fluids are discharged into the open space and precipitate calcite at a lower pressure (Sibson et al., 1975; Robb, 2005). Therefore, the fluid inclusions with the higher homogenization temperatures are those trapped from fluids of lower pressures. As the pressure increases, the homogenization temperatures are suppressed and the fluids are trapped with the lower temperature population. The high salinities of these fluids (between 9 and 14.3 eq.wt.%NaCl) (Fig. 51b) also support a connection with the Triassic evaporites along fracture set A. The stock of Mg provided by the marly formations was likely already expelled and incorporated in the Dol 2. As a consequence, the new circulation event associated with the reopening of preexisting fractures carried fluids non-enriched in Mg but oversaturated with respect to calcite.

After calcite cementation, new fluids precipitated the massive anhydrites along the fracture set C. $\delta^{34}\text{S}$ measured in this anhydrite phase, with values between 18.97 and 19.12‰V-CDT (Table 6), are enriched relative to the Triassic evaporites having a signature of 12.61 ± 4.65 ‰V-CDT (Crockford et al., 2019). This enrichment of ~6-7‰V-CDT can be a product of one of two possible processes or a mixture of both. The first is related to thermochemical sulphate reduction (TSR). If the Triassic evaporites are considered as the sulphate source for TSR, then the relative enrichment of the studied samples would indicate a closed system for SO_4^{2-} but open for H_2S , such that as TSR proceeded, the residual sulphates became enriched in $\delta^{34}\text{S}$ due to the Rayleigh distillation effect (Misra, 2012). The anhydrites identified in Deep Lacq would then be these residual post-TSR sulphates. Another process that can explain the enrichment of the studied anhydrites relative to the Triassic evaporites could be the mixing of the Triassic source ($\delta^{34}\text{S} = 12.61 \pm 4.65$ ‰V-CDT) (Crockford et al., 2019) with the Barremian Carbonate Associated Sulphates (CAS) that reach values of $\delta^{34}\text{S} = 24.3\text{‰} \pm 4.9$ (Barré et al. in press). Both scenarios are also able to explain the low salinities in the anhydrite relative to the Dol 2 and Cal 3, either by mixing of the Triassic fluids with the Barremian connate fluids or by the dilution of the saline fluids with water generated from TSR (Worden et al., 1996; Jiang et al., 2015). The different morphologies and crystal sizes of the anhydrites (Fig. 38) were possibly controlled by the crystallization space available (Moore, 2013). The minimum age range deduced

from figure 65 and table 8 is not conclusive enough because anhydrite are after Dol 2 and Cal 3, but this anhydrite phase was impacted by stylolite 2 (Fig. 39a). Although the cores were not oriented, the oblique plane of the stylolite relative to the vertical edges of cores, suggest that they correspond to compressional stylolites. Such a compressive event is most likely related to the Eocene Pyrenean compression and allow to constrain an upper age for the anhydrite cement.

The timing of the gas charging and accumulation in commercial quantities in Deep Lacq is post-orogenic. This is supported by the compositions of the aqueous phases at homogenizations temperatures (table 7) which show a nearly constant composition of CH₄ in the studied aqueous inclusions in the Dol 2, Cal 3, and anhydrite cements. This consistency in the average methane content (~ 0.3 mol.%) combined with the absence of gas inclusions in the studied samples suggest that the main episode of gas charging and accumulations in economically valuable quantities must have occurred after the precipitation of the diagenetic cements. Since stylolites 2 are compressional and related to the Pyrenean orogeny, the post-orogenic phase, with the renewal in the thermal subsidence (Angrand et al., 2018) have likely triggered the thermal cracking of oil and the accumulation of gases into the reservoir sealed and trapped by the Sainte Suzanne marls. While the thermal cracking of oil occurred during the post-orogeny, H₂S generation from TSR likely started earlier, at least by the Aptian, as suggested by the relatively higher concentrations of this gas in saddle dolomites and its gradual decrease with time as seen in table 7. The main pulse of H₂S, released from possible deeper TSR-kitchens in the Southern Lacq Basin, occurred during precipitation of the Dol 2, while later calcites and anhydrites trapped residual H₂S as degassing from depth continued. However, as for CH₄, the 32% of H₂S extracted commercially in Lacq (Biteau et al., 2006) suggests a major episode of charging into deep Lacq during the post-orogenic phase. Therefore, to summarize the gas migration into deep Lacq, evidence from the composition of the fluids combined with the fluid inclusion studies indicate that the trace amounts of CH₄ and H₂S were already present in Deep Lacq during burial diagenesis. The main gas accumulation however occurred during the post-orogeny, and after precipitation of Dol. 2, Cal. 3 and the anhydrite cements.

The last diagenetic events experienced by the Deep Lacq reservoirs are fracturing and dissolution. The solution-enhanced fractures that cross-cut most of the previous phases make up the fracture porosity that

is the main reservoir-enhancing property of Deep Lacq. Acidic fluids produced during smectite-to-illite conversion could be the source of this dissolution episode.

A summary of the main geodynamic events and associated diagenetic modifications is compiled in table 9.

Table 9. Summary of the main geodynamic, diagenetic and fluid events in Deep Lacq

Age	Regional geodynamics	Fluid types and sources	Main events	Schematic illustration
Post-Eocene	Post-orogeny	Oil and gas	Thermal cracking of oil Filling of gas in Deep Lacq Migration of oil to Upper Lacq	
Eocene	Pyrenean compression		Tectonic compression Upper age constraint of anhydrite cements	
?	Post-rift thermal subsidence - Onset of N-S convergence	Mixture of a Triassic pool + Barremian formational fluids	New pulse of Triassic fluids Rayleigh distillation of TSR sulphates Production of water from TSR	
		Another pool of Triassic fluids Less Mg from the marly formations	New pulse of Triassic fluids Cementation during fracturing (fault-valve mechanism)	
Aptian	Main rifting event	Mixture of formational, clay-released and Triassic fluids	Entrance to oil window Connexion with pools of deeper Liassic and Triassic fluids via fracture A	
Neocomian Barremian	Regional doming Depositional hiatus	Dominance of reducing formational fluids	Gradual burial and deepening of the reservoirs	
Jurassic to Neocomian	Early continental rifting	Meteoric and formational fluids	Episodic mixing between oxidizing and reducing conditions	
		Evaporated marine and formational fluids	Mg from evaporated seawater Meteoric fluids contribute to oxidizing conditions Reflux dolomitization	

5. Redox conditions

Redox states under which the carbonate phases precipitated is assessed relative to their CCL luminescence and the REE composition. The orange to brown luminescence of the micrite matrix (Fig. 36c-e and Fig. 37b and c) shows that the host rocks were likely affected by later diagenesis under reducing

conditions. Dol 1, interpreted as an early product of hyper-evaporated seawater show CCL zonations alternating between a dark non-luminescent core, a bright red rim and then terminating by a non-luminescent zone (Fig. 36c). The dog-tooth calcite, being a product of the meteoric phreatic zone, also displays non-luminescent to brightly-luminescent zone under CCL (Fig. 36e). Fluctuations between redox states can affect the relative concentrations of Mn^{2+} and Fe^{2+} incorporated into dolomite 1 and calcite 1 crystals. Mn^{2+} and bivalent REE cations are the most important activators of luminescence while Fe^{2+} is the main quencher (Boggs and Krinsley, 2006; Machel, 1985; Price, 1989; Richter et al., 2003). REE patterns in the dolomite 1 and calcite 1 (Fig. 43a) are inconclusive because the concentrations approach the detection limit of the LA-ICPMS. The cross-plot of Pr vs. Ce anomalies (Fig. 43b) show that Dol 1 and Cal1 have mixed signals between the domain of positive La and negative Ce anomalies. This supports fluctuations of redox conditions at depths where the oxidizing conditions became episodic. However, for Cal 1 the Ce negative anomaly is never strongly pronounced suggesting that reducing condition prevailed. Similarly, Cal 2 shows a dull yellow to orange luminescence with slightly pronounced negative Ce anomalies, which indicate a precipitation in a reducing environment. The pattern of saddle dolomites show a relative enrichment in middle REE (Fig. 43a), which suggests possible precipitation under reducing conditions (Haley et al., 2004). The reducing system dominating during mesogenesis are also reflected in the dull orange luminescence of the calcite 2 phase. The REE concentrations in calcite 3 are too low and are not conclusive enough to infer constraints on the redox conditions. However, as in Dol. 2, the occurrence of inclusions containing oil and H_2S are in accordance with a precipitation under reducing conditions for Cal 3.

In summary, oxidizing conditions prevailed during early diagenesis. Upon progressive burial, oxidizing conditions became episodic and gradually diminished as the system shifted to reducing conditions during mesogenesis. Given the present day depth of the deep Lacq reservoirs (>2.7km), it is unlikely that oxidizing conditions have persisted. Hence, the reducing conditions are still dominant in the Deep Lacq reservoirs since burial.

Chapter 4 – Part III: Deep Lacq: Conclusions

An updated diagenetic model of the Jurassic to Barremian Deep Lacq reservoirs is presented and placed in the context of the geodynamic evolution of the basin. The detection of H₂S gases in the studied phases prevented reliable AIT-PIT double-isochore modelling as in the case of Upper Lacq. Instead, interpretations of the petrographic and geochemical data, coupled with the evolution of the burial temperatures of the reservoirs, were used as tools to provide age constraints relative to the geodynamic history of Deep Lacq. The outcome indicates that during the early continental rifting of the Upper Jurassic to Neocomian, the shallow marine conditions permitted bacterial activity revealed by inward micritization on shells and bioclasts with BSR-related framboidal pyrites. Shortly after, Deep Lacq reservoirs experienced mixing zone dolomitization from marine to meteoric fluids in the marine phreatic zone at the origin of early dolomites (Dol. 1). Gradual burial caused a shift from the marine phreatic domain to a mixing zone with fluctuations in reducing conditions represented by the zoned dog-tooth calcite (Cal. 1).

The transition to burial diagenesis during the Neocomian to Barremian was marked by the dominance of reducing conditions and the precipitation of the equidimensional, oval to sub-rounded calcite crystals (Cal. 2) followed by mechanical and chemical compaction. During the Apto-Albian hyperextension, extensional fractures connected Deep Lacq to the underlying Ammonite and Liassic marls, as well as the Triassic salt core, which provided Mg²⁺ and NaCl to precipitate the fracture-related saddle dolomites (Dol. 2) from a saline parent fluid. Mg sourced from the marls is supported by the enrichment of ⁸⁷Sr/⁸⁶Sr relative to the Jurassic seawater. Contemporaneously, the source rock entered the oil window, TSR started, and generated gas and oil which started to migrate, as supported by the presence of oil inclusions and relatively high amounts of H₂S (4.93 mol.%) in the aqueous inclusions. The δ¹³C signature shows a mixed contribution between the enriched residual organic carbon and the carbon buffered by the host rocks. The dolomitizing fluids circulated in thermal equilibrium with the reservoirs, at minimum temperatures of 132-148°C with a mode T_h at 144°C.

Between the Aptian and Maastrichtian, the post-rift thermal subsidence increased the overburden pressures and created new fluid pathways with less contribution of Mg²⁺ provided by the marly formations.

The resulting fluids precipitated a new phase of coarse blocky calcites (Cal.3). These fluids circulated at thermal equilibrium with the host rocks and had salinities that ranged between 9 and 14.3 eq. wt.% NaCl, mostly derived from the Triassic salts. In a similar trend as Dol 2, the $\delta^{13}\text{C}$ signature shows a mixed contribution between the enriched residual organic carbon and the carbon buffered by the host rocks.

The minimum age deduced for the precipitation of anhydrite overlap the ages of the calcites 3. To better constrain this age, additional proxies as clumped isotopes for example, are required and should be investigated in future studies. However, the upper age limit was constrained by the Eocene compression tectonic stylolites that crosscut the anhydrites. This suggests that during the Eocene maximum compression, anhydrites cements were already precipitated in Deep Lacq.

The absence of gas inclusions in the studied phases is indicative that the main pulses of gas accumulation in deep Lacq is post orogenic and not during the precipitation of the diagenetic cements.

Chapter 5: Synthesis

Chapter 5: General conclusions and synthesis

1. Synthetic model of the Upper and Deeper Lacq reservoirs

The coupling of petrographic, geochemical and modeling tools has provided deeper insight to the different processes involved in the diagenesis of the Upper and Deeper Lacq reservoirs. The obtained results were integrated into the regional geodynamic context to document the impact of the rifting and compressional episodes on the types, sources and circulation pathways of the diagenetic fluids.

Between the Jurassic to Early Cretaceous, during the early continental rifting stage, the Jurassic to Barremian reservoirs of Deep Lacq were deposited in a shallow marine to lagoonal setting and witnessed early mixing-zone dolomitization, represented by the early dolomites, as well as bacterial activity with the micritization of the bioclasts and the framboidal pyrites (Fig. 67). Locally, in the Annelids formation, minor amounts of Cal. 1 and Cal. 2 were precipitated, possibly from local pools of fluids.

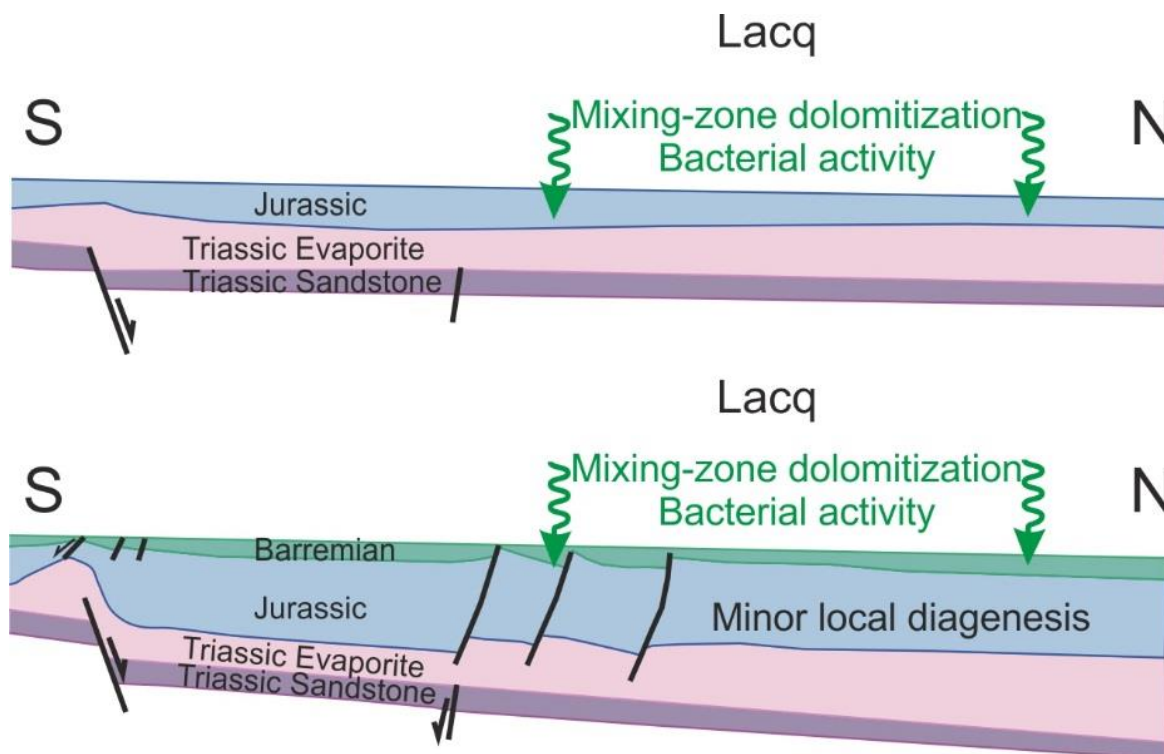


Figure 67. Schematic diagram (not to scale) showing the main diagenetic events during the Jurassic to Early Cretaceous, contemporaneous to the early continental rifting stage. Colored, digitized and modified after Le Marrec (2003) – ENSG course.

The Albo-Aptian hyperextension phase was marked by the high thermal anomalies that allowed the entrance to the oil and gas windows (Fig. 68). With the entrance to the hydrocarbon generation windows, TSR should have also started as witnessed by the dissolved CH_4 and H_2S in the aqueous fluid inclusions trapped in the Aptian saddle dolomites (Table 7). The rift-associated fractures impacted the subsequent circulation of saline Mg-rich fluids. Mg was provided from the Liassic and Ammonite Marls Formation by clay dehydration, while NaCl was derived from the Triassic evaporites. At the same time in Upper Lacq, only the Albian reefs were formed, exposed and partially eroded to form the Base Cenomanian unconformity.

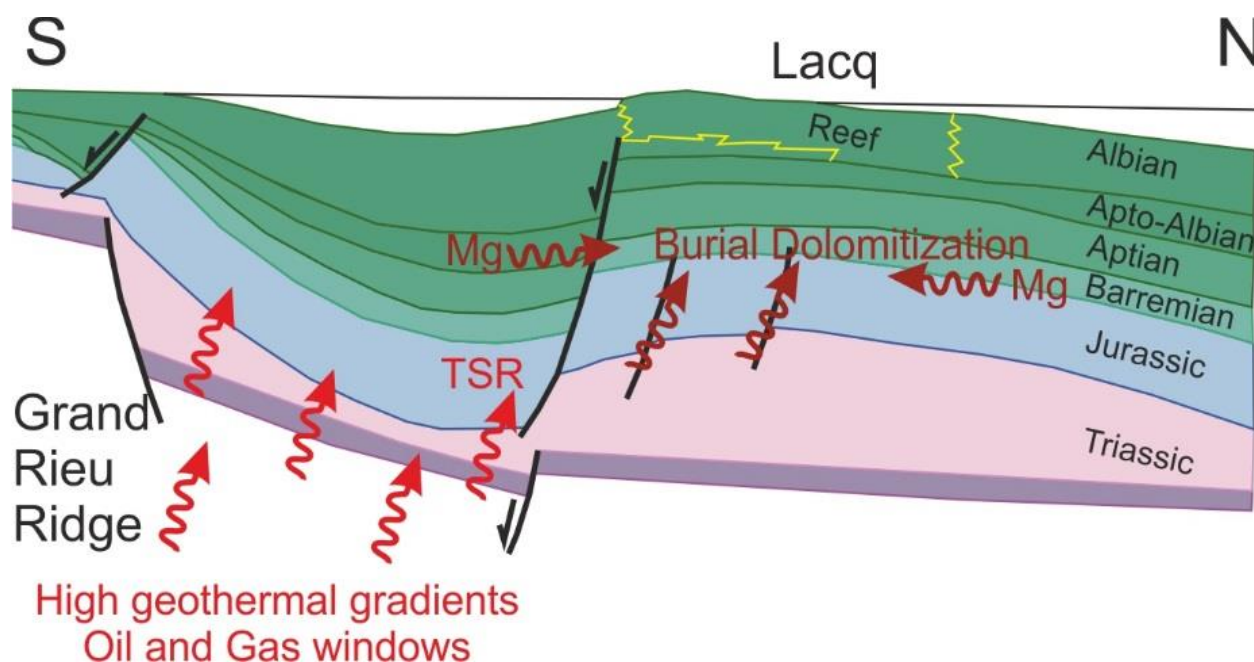


Figure 68. Schematic diagram (not to scale) showing the main diagenetic events during the Apto-Albian hyperextension. Colored, digitized and modified after Le Marrec (2003) – ENSG course.

During the Late Cretaceous, with the onset of the N-S compression between the European and Iberian plates, and after deeper burial and increase of the overburden pressure, new fractures changed the fluid circulation scheme. Mg may have already been used in the precipitation of the saddle dolomites or the new fractures connected Deep Lacq to a pool of Mg-poor and saline fluids that precipitated a new calcite (Fig. 69). Shortly after the precipitation of calcite in Deep Lacq, large volumes of fluids oversaturated with respect to anhydrite circulated and precipitated meter-scale nodules immediately under the Sainte-Suzanne seal. This is likely due to the low permeability of the marls which served as an aquitard under which large volumes

of liquid can accumulate. At the same time, carbonate reservoirs of Upper Lacq were deposited in a shallow marine setting, which were impacted by mixing zone dolomitization and bacterial activity with the early dolomites, framboidal pyrites and micritization of the bioclasts.

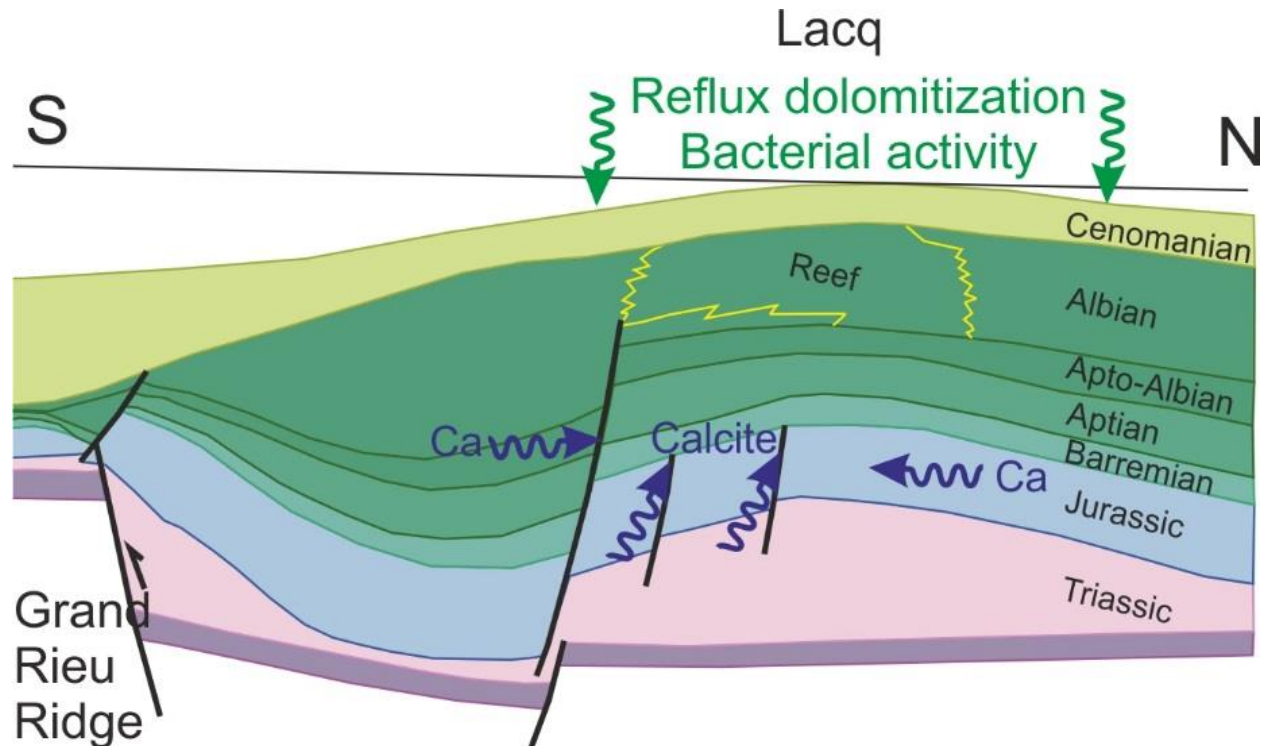


Figure 69. Schematic diagram (not to scale) showing the main diagenetic events during the onset of the N-S compression at the Late Cretaceous. Colored, digitized and modified after Le Marrec (2003) – ENSG course.

During the Eocene Pyrenean convergence, compressional stylolites formed in the Deep Lacq reservoir and cross cut the anhydrite cements, while orogeny-driven hydrothermal fluids migrating laterally along faults and sourced from the Southern Lacq Basin, triggered hydrothermal dolomitization in the Upper Lacq reservoir (Fig. 70).

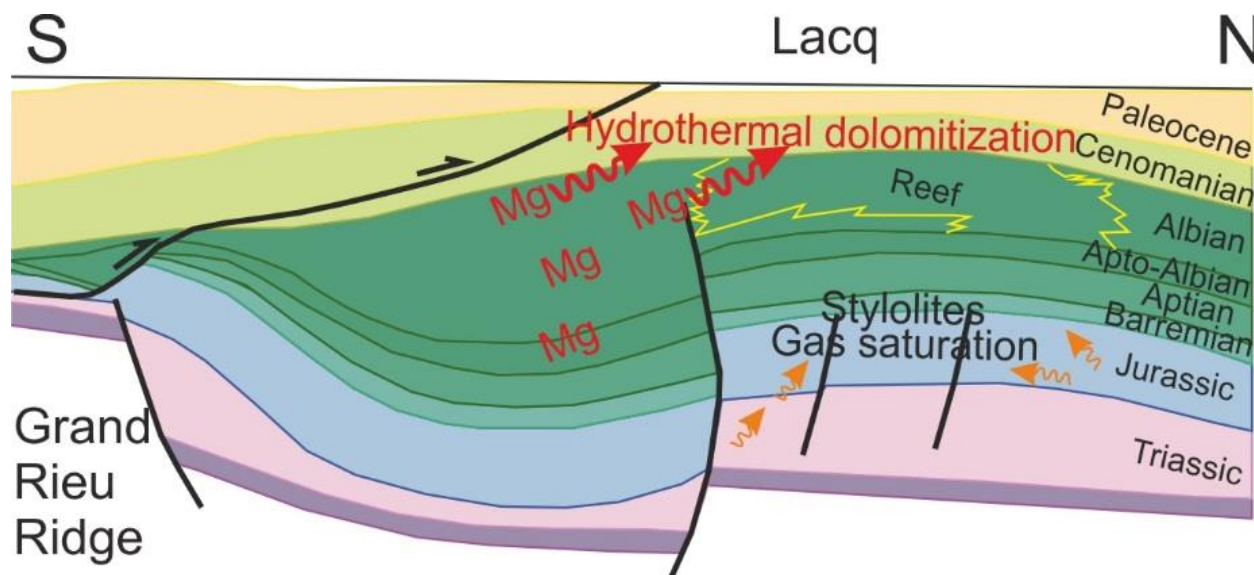


Figure 70. Schematic diagram (not to scale) showing the main diagenetic events during the peak compressional phase of the Eocene. Colored, digitized and modified after Le Marrec (2003) – ENSG course.

These fluids affected only Upper Lacq and did not penetrate through Deep Lacq. This is mainly due to the low permeability of the Sainte-Suzanne Formation and its sealing properties (Biteau et al., 2006) which isolate the diagenetic fluids of Upper Lacq from those of Deep Lacq. The marls, shales, and clays constituting the Sainte-Suzanne Formations are generally characterized by significantly low thermal conductivities, in the range of 0.2-1.0 W/m¹/°C, 2 times lower than the underlying carbonates (Blackwell and Steele, 1989; Clerc et al., 2015). Several fracturing episodes during the Pyrenean convergence connected Upper Lacq to different pools of fluids that precipitated calcite and anhydrite cements. The relative timing of the anhydrite cements, being a late phase in the diagenetic history of both Upper and Deep Lacq reservoir suggest that this phase may have precipitated at the same moment in the two reservoirs. During the peak-orogenic phase, thermal cracking of oil have released commercial amounts of gases which accumulated into Deep Lacq, while heavy oil, possibly through lateral migration, was trapped in Upper Lacq.

A compilation of the main diagenetic events placed in the context of the subsidence history and the main geodynamic events is presented in figure 71.

Chapter 5: General conclusions and synthesis - Synthetic model of the Upper and Deeper Lacq reservoirs

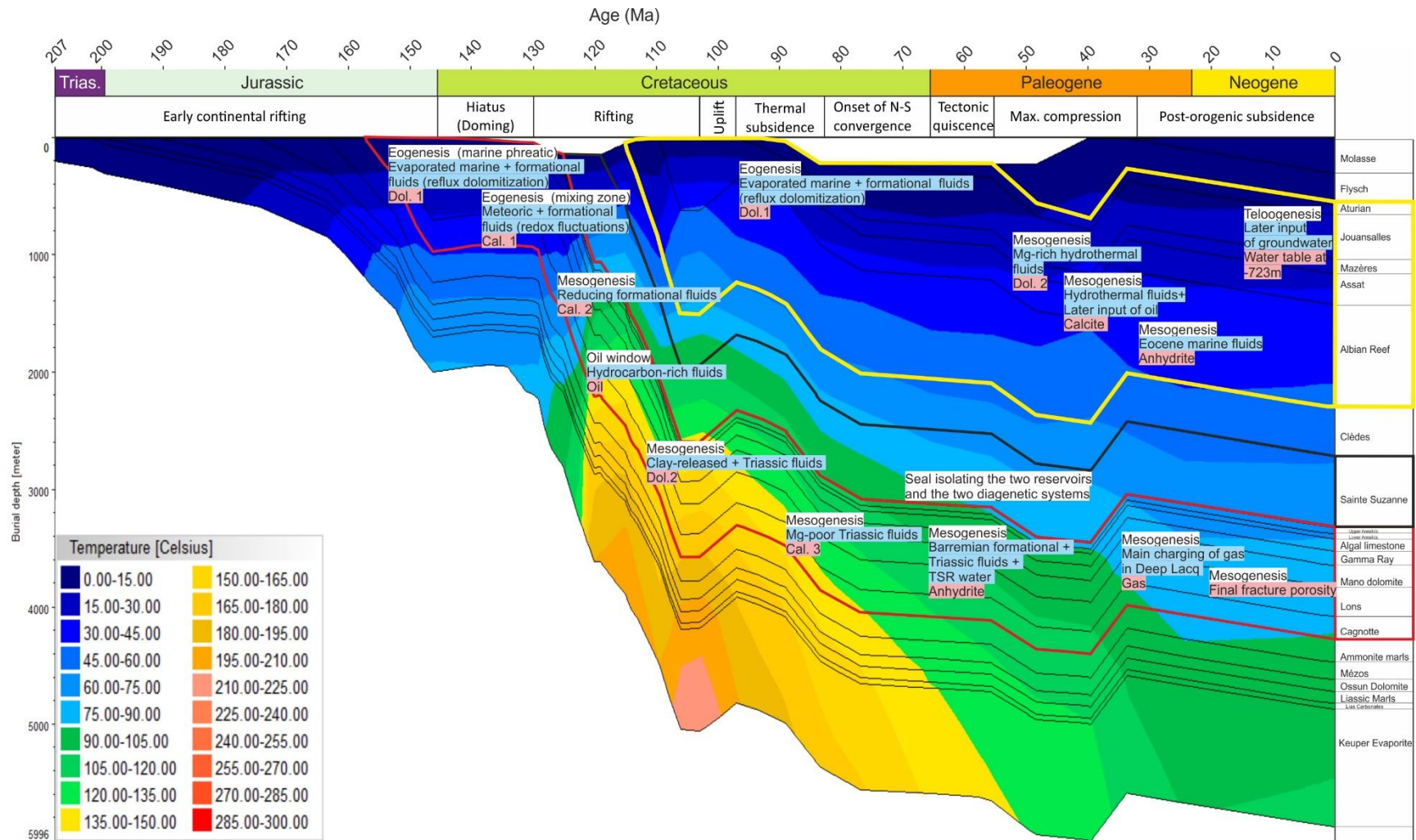


Figure 71. Summary of the main diagenetic realms (white), types of fluids (blue) and their products (pink) relative to the burial history of the reservoirs. The Saint Suzanne marly Formation, being the seal that isolates the two reservoirs, is indicated with the thick black contours. Deep Lacq is represented by the red contours, and Upper Lacq by yellow.

2. Diagenetic fluids between the NPZ and the Aquitaine foreland

To understand and synthesize the geodynamic history and its impact on reservoir diagenesis, the main diagenetic fluids that circulated at similar ages in the Chaînons Béarnais (Salardon et al., 2017) and the Rousse field (Renard et al., 2019) are compared to this study summarized in table 10. The Chaînons Béarnais is located in the North Pyrenean Zone, nearly 40 km south of Lacq, bounded to the North by the North Pyrenean Frontal Thrust (NPFT) and to the south by the North Pyrenean Fault (NPF), the Rousse gas field, a satellite of the Lacq Petroleum System, is located 25 km north of the Chaînons Béarnais (Fig. 1). During the Liassic to Dogger, oxidizing fluids in the Eogenetic realm precipitated an early phase of non-ferroan and non luminescent calcites (Salardon et al., 2017), while in Rousse, the primary dolomites of Mano, whose origin are still debatable (Renard et al., 2019) were formed. In Deep Lacq, eogenesis was marked by mixing-zone dolomitization followed by early zoned calcites during gradual transition towards mesogenesis.

During the Aptian hyperextension, magmatic to mantellic fluids precipitated phases of dolomite and chlorite in fractures within the Jurassic formations in the Chaînons Béarnais, with fluid temperatures reaching up to 350°C and salinities of >25% NaCl (Salardon et al., 2017). At the same time, in Rousse, dolomitizing fluids circulated at temperatures of 147°C to 167°C with low salinities (Renard et al., 2019). Similarly, Deep Lacq experienced saddle dolomite precipitation upon entrance to the oil window. In the Chaînons Béarnais and Rousse however, the proximity of the exhumed mantle bodies in the south and intense fluid-mantle interactions are the source of Mg for the dolomitizing hot fluids. Fluids likely circulated along corridors along the NPFT with a temperature gradient decreasing northward from 350 to 150°C (Renard et al., 2019). The difference in salinities were attributed to the leaching of the Triassic evaporites during the upward migration of the magmatic fluids in the case of the Chaînons Béarnais (Salardon et al., 2017) while a downward migration of meteoric fluids mixed with upward moving serpentization and clay-released low-salinity fluids in Rousse (Renard et al., 2019). In Deep Lacq, the dolomitizing fluids have a temperature range between 140-165°C with salinities higher (8-10 eq. wt.%) than in the Rousse field, but lower than in the Chaînons Béarnais. These dolomitizing fluids are here considered as a mixture of Triassic-sourced fluids with the Mg mainly supplied by the Liassic Marl" and the Ammonite Marls Formation. Mg sources in the Deep Lacq

differ than those in Rousse and Chaînons Béarnais given that there is no evidence of serpentization or mantellic-derived fluids were identified. Similarly, salinities differ from one location to another and depend on the local geology (i.e. presence of unconformity and vertical fluid inputs), proximity to the Triassic salt domes (absent in Rousse) and the exhumed mantle bodies (only in the Chaînons Béarnais).

The fluids that precipitated the post-dolomite calcite in the Chaînons Béarnais circulated at temperatures close to 220°C between the Late Albian to Cenomanian. The salinity of these fluids is lower than the saddle dolomite (15 eq. wt/% NaCl) and were considered as the product of a mixed marine to magmatic fluid source (Salardon et al., 2017). In Rousse, fluids that circulated during the Albian (105 Ma) had temperatures of 145°C with salinities less than that of seawater. The fluid were gas rich sourced from a mixture of the residual dolomitizing fluids and those of meteoric origin that percolated through the base Cenomanian unconformity (Table 10) (Renard et al., 2019). In Deep Lacq, the 2 populations of aqueous inclusions reach an average temperature of 135-140°C, similar to what is recorded in the calcites of Rouse, but the salinities are higher, with 9-14 eq. wt.% NaCl. The fluids here are assumed to be derived from a saline Triassic source and not Mg-enriched by the dehydration of Liassic marls. During the Upper Cretaceous, after the Upper Lacq reservoir was formed, diagenesis was dominated by early reflux dolomitization with Mg sourced evaporated seawater as well as the interstitial formation fluids.

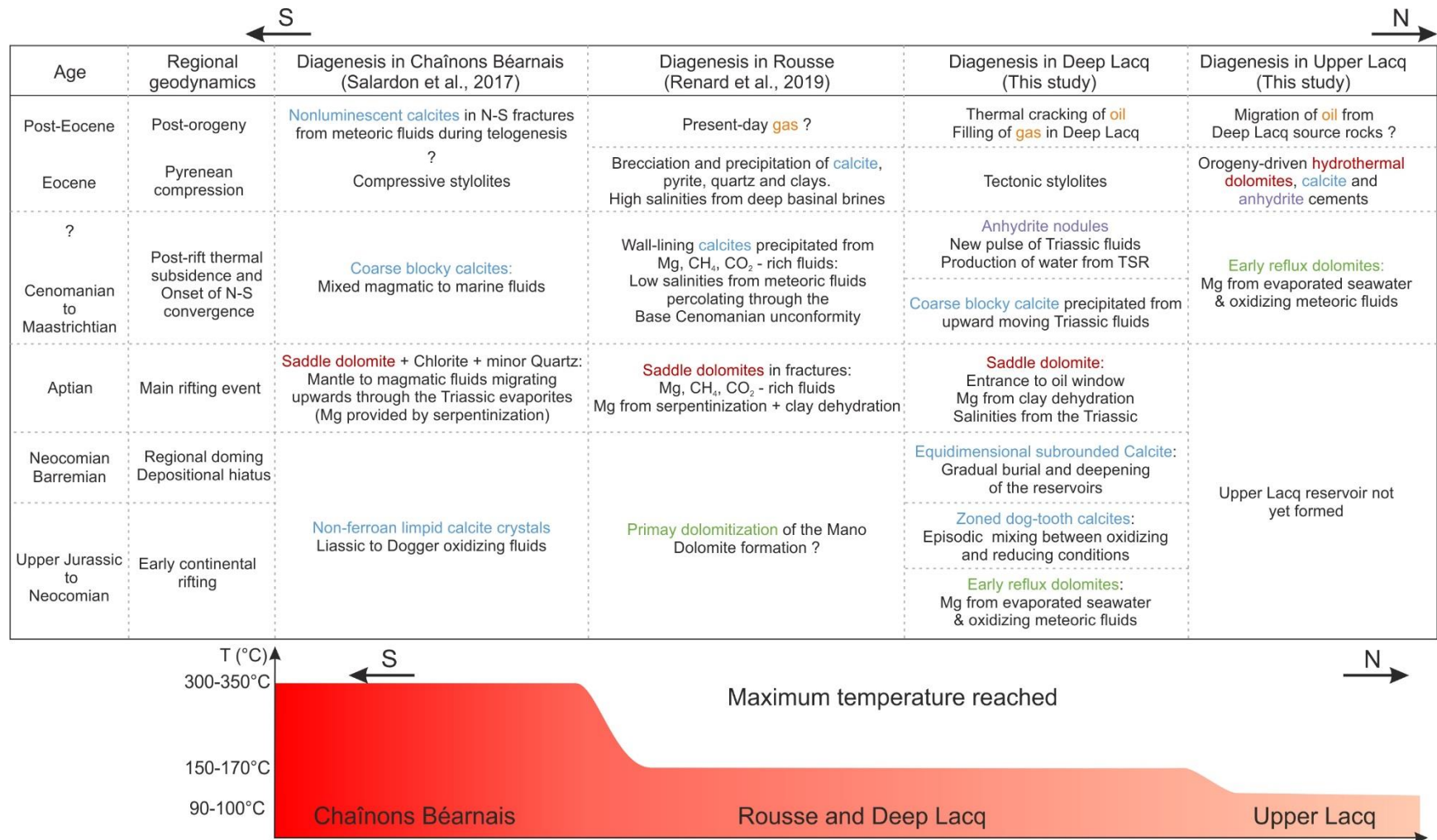
During the Eocene maximum compression, tectonic stylolites developed in the Chaînons Béarnais and Deep Lacq while brecciation and calcite cementation were recorded in Rousse, with high salinities due to upward moving basinal brines. The timing of the telogenetic calcites in the Chaînons Béarnais were not conclusively identified and may also be during the Eocene compression (Salardon et al., 2017). This compression episode was the major event that controlled the diagenesis of Upper Lacq due to the orogeny-driven hydrothermal dolomitization, followed by calcite and anhydrite cementation. The final anhydrites also precipitated, possibly during the same time, in large volumes in Deep Lacq.

Post-orogenic events were similar in Lacq and Rousse and involved the input of hydrocarbons in commercial quantities in the reservoirs. In the Chaînons Béarnais, the proximity of the exhumed mantle domains made the area too hot to be an economically viable petroleum system.

Therefore, it is evident that the overall geodynamic setting, namely the Aptian thermal anomaly had a significant control on temperature of the diagenetic fluids that circulated in the studied area, but the compositions and salinities were more influenced by local geologic settings in the compartmentalized sub-basins, rather than large scale basinal fluid flows.

Chapter 5: General conclusions and synthesis - Diagenetic fluids between the NPZ and the Aquitaine foreland

Table 10. Synthesis of the general diagenetic modifications of Lacq, Rousse and the Chaînons Béarnais



3. Guides for prospection

In general, good reservoir properties are mainly related to the high porosity and permeability that allow economic quantities of hydrocarbons to be trapped and accumulated. These properties however are controlled by diagenetic modifications with possible creation, improvement or blockage of the pore spaces. In the Aquitaine foreland basin, as observed in Lacq, Rousse and other reservoirs, the complex geologic history and the superposition of several fluid flow events have resulted in major diagenetic modifications of the petroleum reservoirs. In the Upper and Deep Lacq reservoirs, fracturing was the main pore-enhancing process, whereas earlier primary porosities or early dolomite-related intercrystalline secondary porosity were mostly blocked by later calcite and/or anhydrite cements. Consequently, primary porosity and early secondary pore spaces were not efficient as the fracturing processes to create spaces for hydrocarbon accumulations. An important prospection step would then involve a detailed structural study to predict the distribution of the fracture networks based on geostatistics (i.e. statistical structural analyses through rose diagrams) (Pointe and Hudson, 1985; Kulatilake et al., 1993) or geomechanics (Olson and Pollard, 1989; Lyakhovsky, 2001; Rives et al., 1992). Another important aspect to consider is the stratigraphic control on the mechanical properties of the reservoir rocks. The differences in mechanical properties of potential reservoir rocks can result in differences in the fracture occurrence, dimensions, sizes, style, and spatial arrangement (Laubach et al., 2009). However, this alone is not sufficient to predict reservoir properties because when mechanical stratigraphy is superimposed by cementation and pore-blocking fluids, the location and sizes of the open fractures and hence fracture porosity will also change. The prospecting efforts should then be focused on prioritizing the analysis of the spatial and temporal distribution of fracture networks as well as the timing and extent of diagenetic fluid circulations.

In the context of the broader geologic setting of the foothills, the thinning of the crust coupled with a high temperature thermal anomaly poses a risk on over-maturing the source rocks and even destroying possible accumulations. This is the case with the very high temperatures that have impacted the petroleum system in the Jurassic of the Chaînons Béarnais where fluids having temperatures $>300^{\circ}\text{C}$ have been documented there (Salardon et al., 2017). Thickened crusts however, together with thrust faults and structural reconfigurations can help in preserving the source rocks to create stocks of oil and gas that can be

redistributed during compression through drains like faults and fractures. Examples of oil and gas being redistributed by orogenic forces include the 18 petroleum systems of Romania that are found in Paleozoic to Cenozoic foreland, stacked, basins in accreted thrust belts and post-tectonic basins (Popescu, 1995). Similarly, the fold-belt area of the Zagros Mountains in SW Iran offer another example of oil and gas accumulations controlled by thickened crusts (Bordenave, 2008).

Perspectives

Chapter 6: Perspectives

This research provides constraints on the diagenesis and timing of fluids influencing the reservoirs of the Lacq Petroleum system. New data about fluid types, sources, chemistries and timings have been provided and thus the need arises to update the database of fluid systems in this inverted hyperextended rift system. A spatial and temporal regional synthesis of the fluid circulation scheme is needed to fully understand the behavior of fluids in similar inverted rift systems. Also, the exact migration mechanism of the hydrocarbons is still poorly documented. The kitchen for TSR generation is still unknown since no evidence of in-situ TSR processes were found in the studied samples. Although many indications point towards the deeper parts of the Aquitaine sub-basins, arguments are not totally conclusive. Another major lack in knowledge are the assumptions and uncertainties in estimating the amount of eroded material from each of the unconformities traversed by the Lacq wells. These may be addressed by running a thermochronology study, if apatite is present in clastic intervals (shales and sands). Such an evaluation would be critical to the thermal reconstruction derived from basin modeling in chapter 4. Also, a detailed analyses of the seismic reflectors geometries (i.e. onlaps, toplaps...) coupled with a basin-scale log-correlation can help quantify the amounts of eroded material. Another uncertainty faced in this PhD is the depth scales of the seismic cross-sections. A velocity model to convert to the TWT(s) scale in depth is of great importance to better visualize the Lacq structure. Restoration of the structural configuration since the Triassic, coupled with 3D seismic stratigraphy modeling, constrained by a grid of borehole data, are very crucial to understand the time-temperature evolution of the source and reservoir rocks across the west Aquitaine basin. This approach would give deeper insight into the timing of entry to the oil and gas windows and help to understand possible TSR kitchens. After identifying the source rocks and their maturation timing, Petromod-2D would be very helpful in identifying the fluid migration pathways at the basin scale.

In Deep Lacq, by calculating the peak area ratios of H_2S and HS^- , the pH of the fluids was calculated to be around 5.0-5.5 for the parent fluids precipitating the saddle dolomites, calcites and anhydrites (table 7). However, for a pure water system, the neutral – equilibrium pH decreases with increasing temperatures and can reach a neutral pH of 5.8 at 160°C (Conway, 1982). To determine the equilibrium pH for the fluids in deep Lacq, which contain NaCl, CH_4 , HS^- , and H_2S , fluid modeling, possibly with PHREEQC®, should

Chapter 6: Perspectives

be done to draw the equilibrium phase diagrams of the studied phases and correlate the stability fields to the P-T conditions of the reservoir. Similarly, the discussion in chapter 4, part II, section 2 highlights the limitations in applying AIT-PIT modeling in complex systems. For this purpose, it is necessary to update the equations of state used to allow the integration of different chemical species to be able to perform accurate and reliable PVT modelling of complex fluids such as $\text{H}_2\text{S}-\text{CH}_4-\text{H}_2\text{O}-\text{NaCl}-\text{H}_2\text{S}-\text{CH}_4$ -oil. This will eventually serve the AIT-PIT modeling approach to determine the trapping P-T conditions of complex fluids.

Also, as presented in chapter 4, it is evident that inverse modeling is unable to provide a unique answer to complex basin models. It is therefore crucial to evaluate the scientific risk associated with the results from such a model. Hantschel and Kauerauf (2009) discussed how the error bars of each data set need to be assessed and raised questions that should be answered to tackle the sensitivities and uncertainties in basin modeling. The questions are summarized as follows:

1. What is the impact of uncertainties in the input data on the outcome of the model? How do the error ranges of the input data reflect on the error bars of the results?
2. What are the important data sets and how do they control the outcome of the model? Which parameters influence which result?

The issues raised with these questions can be formulated into 3 main categories (Hantschel and Kauerauf, 2009) which are:

- (1) Risking: estimation of probabilities, confidence intervals and ranges of errors
- (2) Understanding: correlation between different parameters
- (3) Calibration: calculation of the probability of how good a model fits with the input calibration data.

A common practice for addressing these issues, based on the ranges of uncertainty of input parameters, is to perform a stochastic Monte Carlo Simulation (Thomsen, 1998). This statistical approach is highly recommended to validate and support the arguments used in supporting or discrediting the different vitrinite maturity models simulated in this work.

To highlight more on the risk and limitations in this issue, the work done in chapter 4 regarding the thermal model and the PRv data does not seem to honor the vitrinite measurements in the Sainte Suzanne Marls.

Chapter 6: Perspectives

The misfit between the thermal model and the calculated vitrinites is too high and case pose a limitation in the corresponding burial temperatures and age constraints. For this purpose, it is recommended that the raw data used in the prior works of Le Marrec et al. (1995), Biteau et al. (2006), Salardon et al. (2017), Angrand et al. (2018) and Renard et al. (2019) and run the necessary risk analyses to provide the degree of robustness on the data used as constraints for modeling. For example, infrared spectroscopy should be used to study the preservation state of the macerals and couple this state with the depositional setting and redox conditions of the vitrinites. This step should also be coupled with RockEval data to determine whether the measured and calculated vitrinites (from Tmax) are robust and representative of the thermal regime.

Other important perspectives that are necessary to complete this work and elucidate possible uncertainties should focus on acquiring petrographic, mineralogical and chemical data on clay formations and not only reservoir rocks. It is necessary to gather another temperature and pressure proxies and assess the potential applications of mineral geothermobarometry in diagenesis.

Finally, it is important to note that the Lacq Petroleum System, being a salt-cored anticline with typical carbonate reservoirs sealed by marls and flysch can be regarded as a conventional petroleum system but its petrogenesis is certainly unconventional. The high thermal anomaly during the Albo-Aptian was crucial to enter into the oil and gas windows and trigger the generation of oil and gas. Therefore, the link between oil/gas generation and unusually high thermal anomalies should be regarded as a research priority to understand petrogenesis in rift systems.

List of figures

Figure 1. Simplified map of the main structural domains in the Pyrenean domain (Modified after Biteau et al., 2006).	37
Figure 2. Plate tectonic scenario for the middle Permian (Kroner and Romer, 2013)	38
Figure 3. A: plate kinematic scenario showing the wide transtensional corridor with a dominant strike slip component between the Iberian (IB) and European (EU) plates. B: schematic cross-section showing the formation of multiple flower-structure basins (Jammes et al., 2010a).	39
Figure 4. A: plate kinematic scenario showing the counter-clockwise rotation of IB relative to EU causing orthogonal extension in the western Pyrenees B: asymmetric thinning coupled with regional sagging and deepening of the basins coupled with the thick cover of the Sainte Suzanne marls (Jammes et al., 2010a).	39
Figure 5. Early stage of Pyrenean convergence (Teixell et al., 2016).	40
Figure 6. Protocollision stage expressed by overriding of the Iberian Plate on top of the European plate along the NPFT (Teixell et al., 2016).	41
Figure 7. Simplified geologic map of the SW part of the Aquitaine basin, showing the structural elements and Cretaceous basins surrounding Lacq (modified after Biteau et al., 2006).	42
Figure 8. Interpreted NNE-SSW seismic cross-section through the Lacq structure in the Arzacq basin (See Figure 7 for location). Due to the lack of a reliable velocity model the vertical scale is in two-way time (TWT). For equivalent depth estimations, well LA-104 (red line), reaches a true vertical depth (TVD) of 4346 m.43	
Figure 9. Lithostratigraphic column of the Arzacq and SW Aquitaine Basins including elements of the Lacq petroleum system and a summary of main geodynamic events, which impacted the area since the Triassic.	44
Figure 10. Schematic illustration explaining the distribution of fractures and dolomite bodies in the Upper Lacq's reservoirs (modified after Bouroullec et al., 1986).	47
Figure 11. Sedimentary model to explain distribution of reservoir properties in Upper Lacq modified after Bouroullec et al., 1986).	48

List of figures

Figure 12. A: Senonian isopach map of Lacq reservoir and the location of the LA-415 G1 horizontal well. B: schematic model of the distribution of dolomite bodies based on the observations of LA-415 G1. Modified after (Lambert et al., 2006).....	49
Figure 13. Thin sections from various wells of Lacq kept in the storage facility at CSTJF - Pau	52
Figure 14. Photo of core LA-104 observed and sampled at the storage facility in Boussens.	53
Figure 15. Mass-balance model of equilibrium for Mn and Fe uptake in calcite cement. A: pore space in CaCO_3 sediment incrementally cemented by calcite under successively lower Eh conditions towards point B (Barnaby and Rimstidt, 1989).	55
Figure 16. P-T phase diagram of an oil inclusion. Filled line is the isochore moving from the two-phase domain to the single-phase domain at the T_h . Dashed line is the isopleth that separates the two domains.	65
Figure 17. A: Limestone matrix with micrite and dolomite in PPL. Arrows point to the rounded greenish detrital glauconite pellets. B: CCL photomicrograph showing the dark zoned core of the D1 dolomite (arrows). The red-luminescent overgrowth corresponds to the D2 dolomite. C: Micrite rim (arrow) penetrating a shell fragment in PPL. D: Aggregates of bright yellow framboidal pyrite (arrows) inside in a bivalve shell in PPL. E: Microfracture (arrow) filled by silica in contact with a displaced chert nodule (in PPL). F: Clast of siliceous sponge (in PPL).	70
Figure 18. A: Pyrite 2 crystals engulfing some relics of dolomites (arrow; in PPL). B: CCL Cross-cutting relationships between fractures (between dashed line), partially dissolved and brecciated D1 rhombs (arrows) engulfed by the D2 overgrowths. C: CCL image of a stylolite (yellow line) impacting both brecciated D1 dolomites and saddle dolomites D2. D: Partially dissolved stylolite, in dolomite matrix, filled with pink-stained, blocky calcite (in PPL). Glauconites (arrow) are also displaced and concentrated along the stylolite surface. E: CCL image of fracture walls lined with dull orange to brown blocky calcites. The crystal size increases towards the center of the fracture as indicated by the arrows. F: Same fracture under UV light with oil coatings (arrows) on top of the blocky calcites.	73
Figure 19. A: Tabular anhydrite crystals under plane-polarized light filling inter-dolomite porosity. Brown oil coatings are found on the rims of the dolomite crystals. B: Iron oxides (arrows) on the edges of a pyrite crystal. The colored crystal on the left corner is a tabular anhydrite.....	74

List of figures

Figure 20. A: D2 overgrowth around D1 cores. B: Zoom of the image A showing two-phase aqueous inclusions (arrows) in D2. C: Large crystals of saddle dolomite with their typically curved edges. D: Zoom of the image C with rectangular two-phase aqueous inclusions (arrows). E: Crystal of blocky calcite containing patches of oil and aqueous inclusions. F: Zoom of the image E showing two-phase oil (orange) and aqueous (clear) inclusions.	75
Figure 21. FT-IR spectra of the two types of oil inclusions	76
Figure 22: Frequency histograms of the homogenization temperatures of aqueous and oil inclusions in (A) dolomite and (B) calcite phases.	77
Figure 23. A: Frequency histogram of homogenization temperatures of aqueous and oil inclusions in the blocky calcite of the Albian Reef Formation B: T_h vs. salinity cross-plot of the studied phases.	78
Figure 24. A: $\delta^{18}\text{O}/\delta^{13}\text{C}$ cross plot. Symbol colors refer to specific carbonate phases numbered from '1' to '4'. The colored areas highlight the dispersion of $\delta^{18}\text{O}$ and $\delta^{13}\text{C}$ values recorded for each carbonate phase. Square symbol represents the sample selected for clumped isotope measurements. When not shown, uncertainties are included in the symbol size. The black rectangle represents the expected $\delta^{18}\text{O}$ and $\delta^{13}\text{C}$ values of marine carbonate precipitated in equilibrium with Upper Cretaceous seawater (Steuber, 1999). B: Cross-plot of $\delta^{18}\text{O}$ versus $T(\Delta 47)$. Uncertainties are reported as 1SD of the mean out of one to three replicates. Expected Upper Cretaceous seawater temperature range is reported in the blue shaded area (Steuber, 1999).	80
Figure 25. A: Fractionation curves of O'Neil et al., (1969) to investigate the parent fluids of calcite phases. B; Fractionation curves of Horita et al., (2014) for the parent fluids of dolomite phases. The average signatures of the parent fluids derived from marine and meteoric sources are represented with the blue and green shaded areas respectively.	81
Figure 26. SEM-EDS photomicrograph of a sulphide crystals with the location of spectral measurements and the resulting ratio of Fe and S.	82
Figure 27. PAAS-normalized REE pattern of the micritic host rock, matrix dolomites, saddle dolomite and calcite. Patterns of dolomite and calcite phases show a bulge (relative enrichment) in the middle REE...	83
Figure 28. A: Erroneous phase diagram of oil inclusions in blocky calcites of Upper Lacq using the radii measured from the CSLM fluorescent photomicrographs and with manual selection of the threshold values	

List of figures

without any mathematical processing of the pixels. B: Corrected phase diagram constructed following the protocol described in chapter 2 section 4.5.	84
Figure 29. Gas volume % vs. T_h trends for 8 different reference oils with plotted results for Upper Lacq and Albian reef oils. L-V line separates the homogenization to the liquid domain below from the gas domain above. Modified after Bourdet et al., (2008).....	85
Figure 30. Simulated thermal regime in Petromod constrained by vitrinite reflectance measurements.....	87
Figure 31. Chronology of diagenetic phases and fracturing events observed in Upper Lacq from oldest at the top to youngest at the base. Dashed lines correspond to phases whose exact paragenetic timing cannot be precisely constrained. Asterisks* indicate the phases investigated here in thermometric studies (FI and Δ_{47}).	88
Figure 32. δD vs. $\delta^{18}O$ in ‰ SMOW for the groundwater collected from Upper Lacq plotted against the Global Meteoric Water Line (GMWL). Isotopic values of the present-day rainfall are also added, sourced from IAEA (2018). The slight enrichment of the groundwater in Upper Lacq compared to the GMWL and the present-day rainfall could be the result of mixing with $\delta^{18}O$ – enriched formation fluids or contamination by the host rock.	91
Figure 33. P-T trapping conditions and evolution of fluid pressure gradients simulated with Petromod-1D and PIT-AIT respectively. Numbers in tags are ages in Ma. The pink area represents the calcite temperature estimation deduced from Δ_{47} thermometry (i.e. an isotopic thermometer independent of any pressure effect). The intersection of both isochore types indicates the trapping conditions of inclusions in blocky calcites. The loop in the hydrostatic and lithostatic gradients represent the base Oligocene unconformity at 40-34 Ma. The arrows correspond to the extrapolation of the P-T conditions to the domain between the hydrostatic and lithostatic fluid pressure.	94
Figure 34. Schematic model of the distribution of dolomite bodies based on the observations of the well LA-415 (trajectory shown in dashed red line). The fractures drawn in the scheme were identified on the larger scale NE-SW seismic cross section (Based on Lambert et al., 2006).....	95
Figure 35. Summary diagram of fluid circulation schemes with their main products.....	97
Figure 36. A: PPL image of a shell fragment affected by destructive micritization. The shell is later replaced by other calcite phases. B: reflected light image showing ghosts of bioclasts with local concentrations of	

List of figures

rounded to sub-rounded pyrites. Arrows point to pyrites disseminated into the micritic matrix. C: CCL image of planar rhombic dolomite crystals floating in a micritic matrix and cross-cut by a calcite and anhydrite vein. D: shell mold cemented by calcite and anhydrite cements. This shell was initially dissolved and moldic porosity was filled by younger cement phases. E: CCL image of the zoned “dog-tooth” calcite 1 phase precipitated at the contact with the host rock and covered by the yellow-luminescent calcite 2 phase. F: Broken annelid tubes as evidence of mechanical compaction.	104
Figure 37. A: PPL photomicrograph of stylolite 1 crosscut by fracture set A. B: CCL image of the cross-cutting relationships between fracture A, dolomite 2 and calcite 3 phases. Fragments of host rocks in the fracture are indicators of fracture reopening mechanism. Dolomite 2 is partially replaced by calcite 3 (see the yellow dotted line between Dol. 2 and Cal. 3). C: CCL image of a vuggy pore now filled by Cal. 1 and Cal. 3 calcites. D: CCL image of coarse calcite 3 crystals. Arrows indicate remnants (relics) of Dol. 2 after replacement. Cal. 3 shows heterogeneous shades of yellow to dull orange luminescence.	106
Figure 38. A: Photographs of well LA-101 and LA-104 with massive anhydrites few meters below the Sainte Suzanne Formation. B: CPL image of an anhydrite-filled fracture C in a host micrite matrix in contact with an anhydrite nodule. C: CPL image of an anhydrite with partial replacement of a calcite 3 crystal. D: CPL image of coarse anhydrite crystals with bright 2 nd order birefringence.	107
Figure 39. A: CPL photomicrograph of anhydrite affected by stylolite 2 (arrows). B: PPL image of a fracture A filled by calcite (Cal. 3) crosscut by an open fracture C. C: Anhydrite-infilled fracture B crosscut by fracture C. D: Fracture B crosscut by a fracture C with a solution-enhanced vuggy-porosity.	108
Figure 40. Cross-plot of $\delta^{18}\text{O}$ and $\delta^{13}\text{C}$ isotopes for Deep Lacq. Dashed box represents the Late Jurassic seawater signature (Veizer et al., 1999). Data from TOTAL archives (Pabian-Goyheneche and Anquelle, 1995) are presented as colored circles.	110
Figure 41. Cross plot of $^{87}\text{Sr}/^{86}\text{Sr}$ ration versus $\delta^{13}\text{C}$ values of Dolomite 1, Dolomite 2 and Calcite 3 cement relative to the signature of the Upper Jurassic seawater (Veizer et al., 1999).	111
Figure 42. SEM-EDS photomicrograph of sulphide crystals with the location of spectral measurements and the resulting ratio of Fe and S.	112
Figure 43. PAAS-normalized REE pattern for the studied phase in Deep Lacq. B: Cross-plot of Pr vs. Ce anomalies.	113

List of figures

Figure 44. Coarse dolomite 2 crystal with oil and aqueous inclusions. B: The oil inclusion show a strongly fluorescent blue to white color. Arrows point to small aqueous inclusions in the same growth zone as the oil inclusion.....	114
Figure 45. Fluid inclusion in Cal 3. A: inclusion-rich calcite 3 filling fracture A. B: Oil and aqueous inclusions along growth zones in a coarse calcite 3 crystal. Arrow points to type 1 aqueous inclusion that are slightly deeper in the crystal. A zoomed image is shown in C, which shows co-occurrence of blue fluorescent oil inclusions and type 1 aqueous inclusions. D: Type 2 aqueous inclusions not associated with oil inclusions in the same calcite 3 crystal.	115
Figure 46. Fluid inclusions in anhydrites. A: Photomicrograph under PPL showing brown two-phase oil inclusions surrounded by aqueous two-phase inclusions (arrows). B: UV light showing the strong blue color of oil inclusions.	116
Figure 47. A: Histogram showing homogenization temperatures of aqueous and oil inclusions in the dolomite 2 at a depth of 3707-3715 m in the Mano Dolomite Formation. B: T_h vs. salinity cross-plot of the studied aqueous FIs in Mano Formation.....	117
Figure 48. A: Histogram showing homogenization temperatures of aqueous in the calcite 3 phase at a depth of 3488-3494m in the Lower Annelids formation. B: T_h vs. salinity cross-plot of the studied aqueous FIs.	117
Figure 49. A: Summary histogram showing homogenization temperatures of 2 population of primary aqueous and one population of oil inclusions in the calcite 3 phase at a depth of 3584-3589m in the Algal limestone formation. B: T_h vs. salinity cross-plot of the studied aqueous FIs.....	118
Figure 50. A: Histogram showing homogenization temperatures of aqueous and oil inclusions in the calcite 3 phase at a depth of 4116-4117m in the Lons Limestone Formation. B: T_h vs. salinity cross-plot of the studied aqueous FIs.....	119
Figure 51. A: Summary histogram of the homogenization temperatures recorded in all studied aqueous and oil inclusions in the calcite 3 phase. B: T_h vs. salinity cross-plot of the studied aqueous FIs in Cal. 3 phase.	119

List of figures

Figure 52. A: Histogram showing homogenization temperatures of aqueous and oil inclusions in the anhydrite phase at a depth of 3672-3673m in the Lons limestone formation. B: T_h vs. salinity cross-plot of the studied aqueous FIs.....	120
Figure 53. Gas volume % vs. T_h trends for 8 different reference oils. L-V line separates the homogenization to the liquid domain below from the gas domain above. Modified after Bourdet et al.,(2008).....	122
Figure 54. Depth plot of vitrinite data from LA-104, LA-103 and the equivalent vitrinite calculated from T_{max}	123
Figure 55. Model 1 of the thermal maturity history.	124
Figure 56. Model 2 of the thermal maturity history.	125
Figure 57. Model 3 of the thermal maturity history.	126
Figure 58. Model 4 of the thermal maturity history.	127
Figure 59. Model 5 of the thermal maturity history.	128
Figure 60. Subsidence history of Lacq showing the main regional geodynamic events and the evolution of burial temperatures. Colored bands follow the temperature chart in °C.	132
Figure 61. P-T plot of the isopleths of fluid (1) and fluid (2) with different H_2S contents.	134
Figure 62. P-T diagram showing depression of homogenization pressures as H_2S concentration increases.	135
Figure 63. Evolution of the burial temperatures experienced by the Mano Dolomite Formation with the homogenization temperature range of the dol. 2 phase	137
Figure 64. Evolution of the burial temperatures experienced by the Algal and Lons Limestone Formations with the homogenization temperature range of the Cal. 3 phase.	138
Figure 65. Evolution of the burial temperatures experienced by the Algal Formation with the homogenization temperature range of the Anhydrite phase.	139
Figure 66. Chronology of petrographic phases observed in Deep Lacq.	140
Figure 67. Schematic diagram (not to scale) showing the main diagenetic events during the Jurassic to Early Cretaceous, contemporaneous to the early continental rifting stage. Colored, digitized and modified after Le Marrec (2003) – ENSG course.	153

List of figures

Figure 68. Schematic diagram (not to scale) showing the main diagenetic events during the Apto-Albian hyperextension. Colored, digitized and modified after Le Marrec (2003) – ENSG course.....	154
Figure 69. Schematic diagram (not to scale) showing the main diagenetic events during the onset of the N-S compression at the Late Cretaceous. Colored, digitized and modified after Le Marrec (2003) – ENSG course.....	155
Figure 70. Schematic diagram (not to scale) showing the main diagenetic events during the peak compressional phase of the Eocene. Colored, digitized and modified after Le Marrec (2003) – ENSG course.....	156
Figure 71. Summary of the main diagenetic realms (white), types of fluids (blue) and their products (pink) relative to the burial history of the reservoirs. The Sainte Suzanne marly Formation, being the seal that isolates the two reservoirs, is indicated with the thick black contours. Deep Lacq is represented by the red contours, and Upper Lacq by yellow.	157

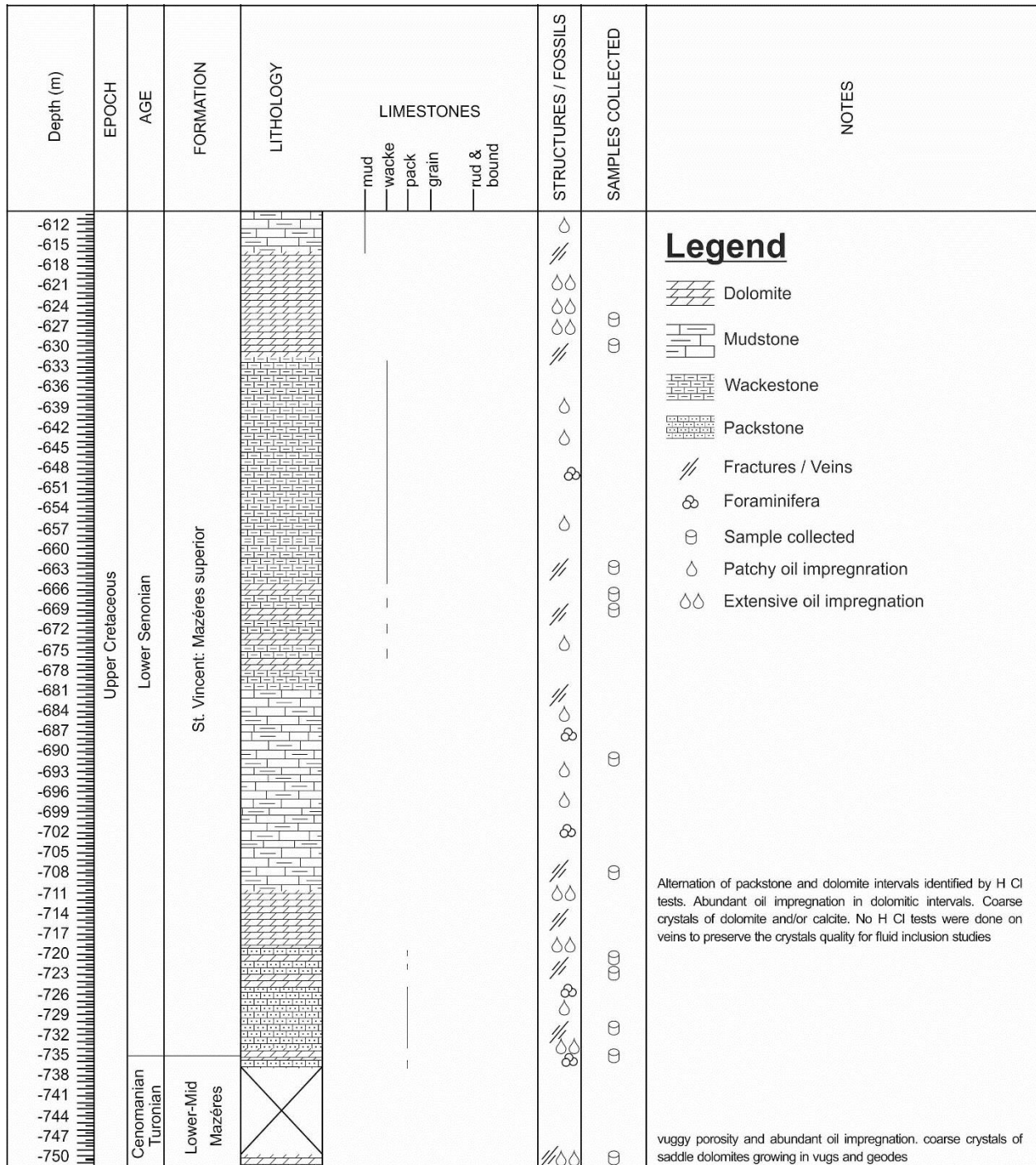
List of tables

Table 1. Summary of main dolomitization models, sources of Mg and hydrological schemes. Compiled from Warren (2000) and Machel (2004).	36
Table 2. Constant coefficients for the H ₂ O-NaCl system obtained by Zhang and Frantz (1987).	64
Table 3. Stable isotope results ($\delta^{18}\text{O}$, $\delta^{13}\text{C}$ and Δ_{47}) of the samples set investigated.....	81
Table 4. U-Pb data acquired through LA-ICPMS on selected phases from Upper Lacq. The obtained results are too low to allow absolute age dating.	83
Table 5. Multiple sulfur isotope signature of CAS from anhydrite-rich samples (this study) and those of the reference Eocene seawater of Crockford et al. (2019) and references therein.	91
Table 6. Multiple sulfur isotope results of Deep Lacq	111
Table 7. Summary of the CH ₄ , H ₂ S and HS ⁻ and pH compositions detected with Raman spectra.	121
Table 8. Summary of the age ranges estimated from the burial temperatures.	140
Table 9. Summary of the main geodynamic, diagenetic and fluid events in Deep Lacq	148
Table 10. Synthesis of the general diagenetic modifications of Lacq, Rousse and the Chaînons Béarnais	161

Appendices

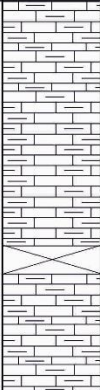


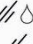
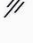




















Appendix 1: Core logs of the studied wells

Well: LA37 / Latitude: 43.411004° - Longitude: -0.634984°

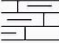







Appendices

Well: LA80 / Latitude: 43.415894° - Longitude: -0.638357°



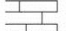

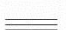


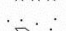
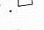
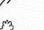






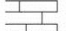

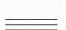


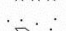
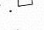
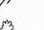






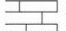

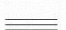


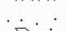
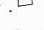
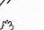






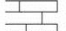

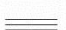


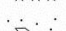
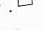
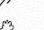






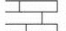

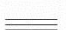


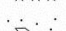
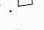
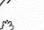






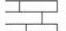

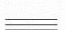


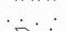
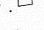
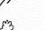






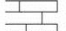

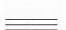


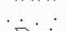
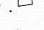
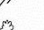






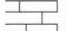

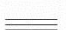


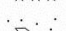
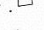
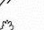






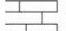

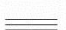


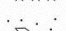
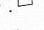
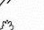






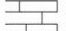

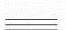


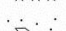
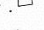
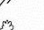






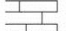

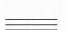


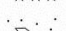
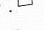
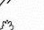






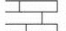

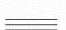


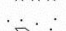
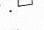
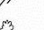






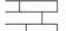

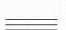


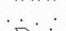
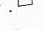
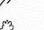






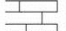

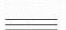


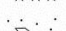
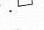
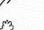






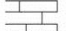

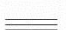


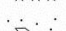
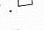
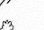






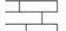

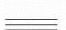


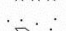
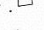
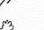






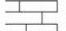

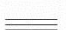


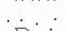
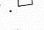
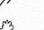






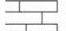

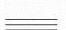


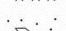
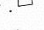
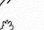






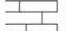

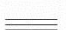


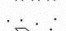
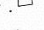
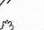






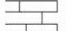

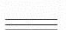


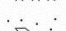
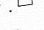
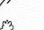




Depth (m)	EPOCH	AGE	FORMATION	LITHOLOGY	LIMESTONES	STRUCTURES / FOSSILS	SAMPLES COLLECTED	NOTES
					mud wacke pack grain rud & bound			
-612 -615 -618 -621 -624 -627 -630 -633 -636 -639	Upper Cretaceous	Lower Senonian	St. Vincent: Mazères superior			        	    	Light grey marly and friable limestone. Abundant glauconite and chert nodules. Nodules are few cm wide. no oil impregnation up to around -625 m. Few BPSs observed 15 cm interval of breccia surrounded by clayey marls at -624m. Fractures, possibly faults as witnessed by slickenlines White marly limestone, tight and heavy weight. Rich in glauconite and compaction seams, minor and limited oil impregnation. Friable glauconite laminae, oblique fault slickenlines Opened fractures with oil impregnation, brown to black HC, minor chert nodules, abundant stylolites breccia and coarse crystals at 647.6-648.6
-645 -648 -651 -654 -657						    	    	

Legend

-  Mudstone
-  Fractures / Veins
-  Foraminifera
-  Sample collected
-  Patchy oil impregnation
-  Extensive oil impregnation

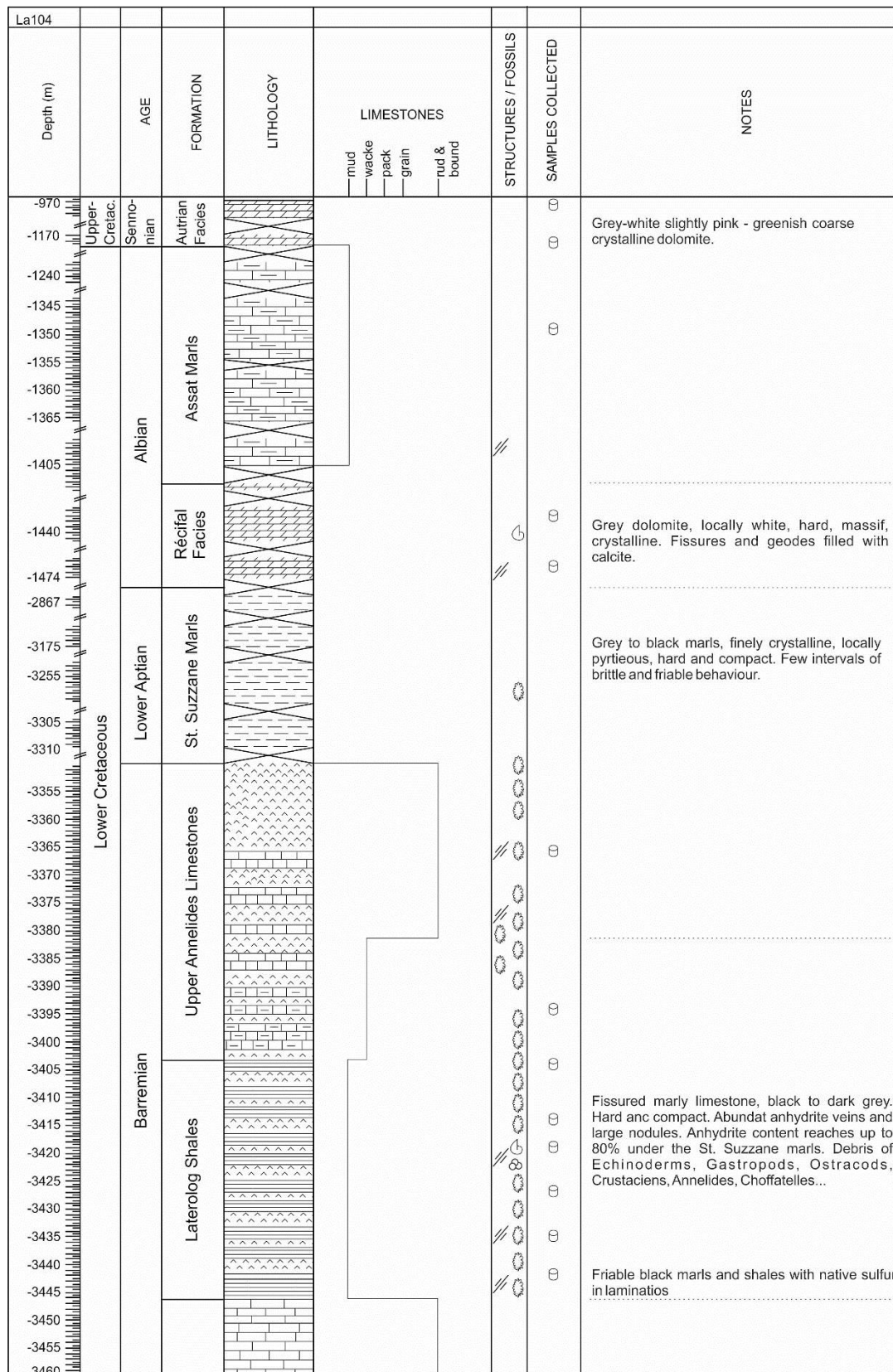
Appendices

Well: LA101/ Latitude: 43.420648° - Longitude: -0.619980°

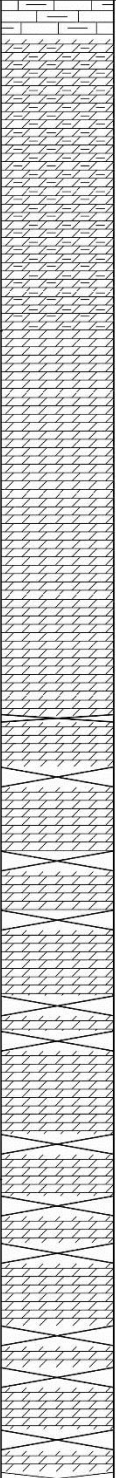


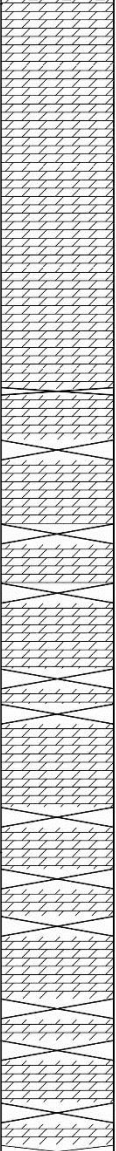


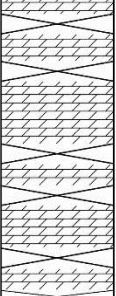


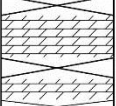


Depth (m)	EPOCH	AGE	FORMATION	LITHOLOGY	LIMESTONES	STRUCTURES / FOSSILS	SAMPLES COLLECTED	NOTES
					<div> <div>mud</div> <div>wacke</div> <div>pack</div> <div>grain</div> <div>rud & bound</div> </div>			
-666			Aturien					Legend  Dolomite  Dolomite with mud / marl intercalations  Limestone  Mudstone  Shale  Marls  Anhydrite  Breccia  Fractures / Veins  Nodules (chicken-wire)  Foraminifera  Shells  Annelides  Sample collected
-2304			Récifal					
-2709			Facies					
-2712			Lower					 Dolomite  Dolomite with mud / marl intercalations  Limestone  Mudstone  Shale  Marls  Anhydrite  Breccia  Fractures / Veins  Nodules (chicken-wire)  Foraminifera  Shells  Annelides  Sample collected
-2931			Clèdes					
-2934								 Dolomite  Dolomite with mud / marl intercalations  Limestone  Mudstone  Shale  Marls  Anhydrite  Breccia  Fractures / Veins  Nodules (chicken-wire)  Foraminifera  Shells  Annelides  Sample collected
-2937								
-3000								 Dolomite  Dolomite with mud / marl intercalations  Limestone  Mudstone  Shale  Marls  Anhydrite  Breccia  Fractures / Veins  Nodules (chicken-wire)  Foraminifera  Shells  Annelides  Sample collected
-3003								
-3084								 Dolomite  Dolomite with mud / marl intercalations  Limestone  Mudstone  Shale  Marls  Anhydrite  Breccia  Fractures / Veins  Nodules (chicken-wire)  Foraminifera  Shells  Annelides  Sample collected
-3168								
-3246								 Dolomite  Dolomite with mud / marl intercalations  Limestone  Mudstone  Shale  Marls  Anhydrite  Breccia  Fractures / Veins  Nodules (chicken-wire)  Foraminifera  Shells  Annelides  Sample collected
-3249								
-3360								 Dolomite  Dolomite with mud / marl intercalations  Limestone  Mudstone  Shale  Marls  Anhydrite  Breccia  Fractures / Veins  Nodules (chicken-wire)  Foraminifera  Shells  Annelides  Sample collected
-3462								
-3561								 Dolomite  Dolomite with mud / marl intercalations  Limestone  Mudstone  Shale  Marls  Anhydrite  Breccia  Fractures / Veins  Nodules (chicken-wire)  Foraminifera  Shells  Annelides  Sample collected
-3570								
-3600								 Dolomite  Dolomite with mud / marl intercalations  Limestone  Mudstone  Shale  Marls  Anhydrite  Breccia  Fractures / Veins  Nodules (chicken-wire)  Foraminifera  Shells  Annelides  Sample collected
-3603								
-3606								 Dolomite  Dolomite with mud / marl intercalations  Limestone  Mudstone  Shale  Marls  Anhydrite  Breccia  Fractures / Veins  Nodules (chicken-wire)  Foraminifera  Shells  Annelides  Sample collected
-3609								
-3612								 Dolomite  Dolomite with mud / marl intercalations  Limestone  Mudstone  Shale  Marls  Anhydrite  Breccia  Fractures / Veins  Nodules (chicken-wire)  Foraminifera  Shells  Annelides  Sample collected
-3615								
-3618								 Dolomite  Dolomite with mud / marl intercalations  Limestone  Mudstone  Shale  Marls  Anhydrite  Breccia  Fractures / Veins  Nodules (chicken-wire)  Foraminifera  Shells  Annelides  Sample collected
-3621								
-3624								 Dolomite  Dolomite with mud / marl intercalations  Limestone  Mudstone  Shale  Marls  Anhydrite  Breccia  Fractures / Veins  Nodules (chicken-wire)  Foraminifera  Shells  Annelides  Sample collected
-3627								
-3630								 Dolomite  Dolomite with mud / marl intercalations  Limestone  Mudstone  Shale  Marls  Anhydrite  Breccia  Fractures / Veins  Nodules (chicken-wire)  Foraminifera  Shells  Annelides  Sample collected
-3633								
-3636								 Dolomite  Dolomite with mud / marl intercalations  Limestone  Mudstone  Shale  Marls  Anhydrite  Breccia  Fractures / Veins  Nodules (chicken-wire)  Foraminifera  Shells  Annelides  Sample collected
-3639								
-3642								 Dolomite  Dolomite with mud / marl intercalations  Limestone  Mudstone  Shale  Marls  Anhydrite  Breccia  Fractures / Veins  Nodules (chicken-wire)  Foraminifera  Shells  Annelides  Sample collected
-3645								
-3648								 Dolomite  Dolomite with mud / marl intercalations  Limestone  Mudstone  Shale  Marls  Anhydrite  Breccia  Fractures / Veins  Nodules (chicken-wire)  Foraminifera  Shells  Annelides  Sample collected
-3651								
-3654								 Dolomite  Dolomite with mud / marl intercalations  Limestone  Mudstone  Shale  Marls  Anhydrite  Breccia  Fractures / Veins  Nodules (chicken-wire)  Foraminifera  Shells  Annelides  Sample collected
-3657								
-3660								 Dolomite  Dolomite with mud / marl intercalations  Limestone  Mudstone  Shale  Marls  Anhydrite  Breccia  Fractures / Veins  Nodules (chicken-wire)  Foraminifera  Shells  Annelides  Sample collected
-3663								
-3666								 Dolomite  Dolomite with mud / marl intercalations  Limestone  Mudstone  Shale  Marls  Anhydrite  Breccia  Fractures / Veins  Nodules (chicken-wire)  Foraminifera  Shells  Annelides  Sample collected
-3669								

Appendices

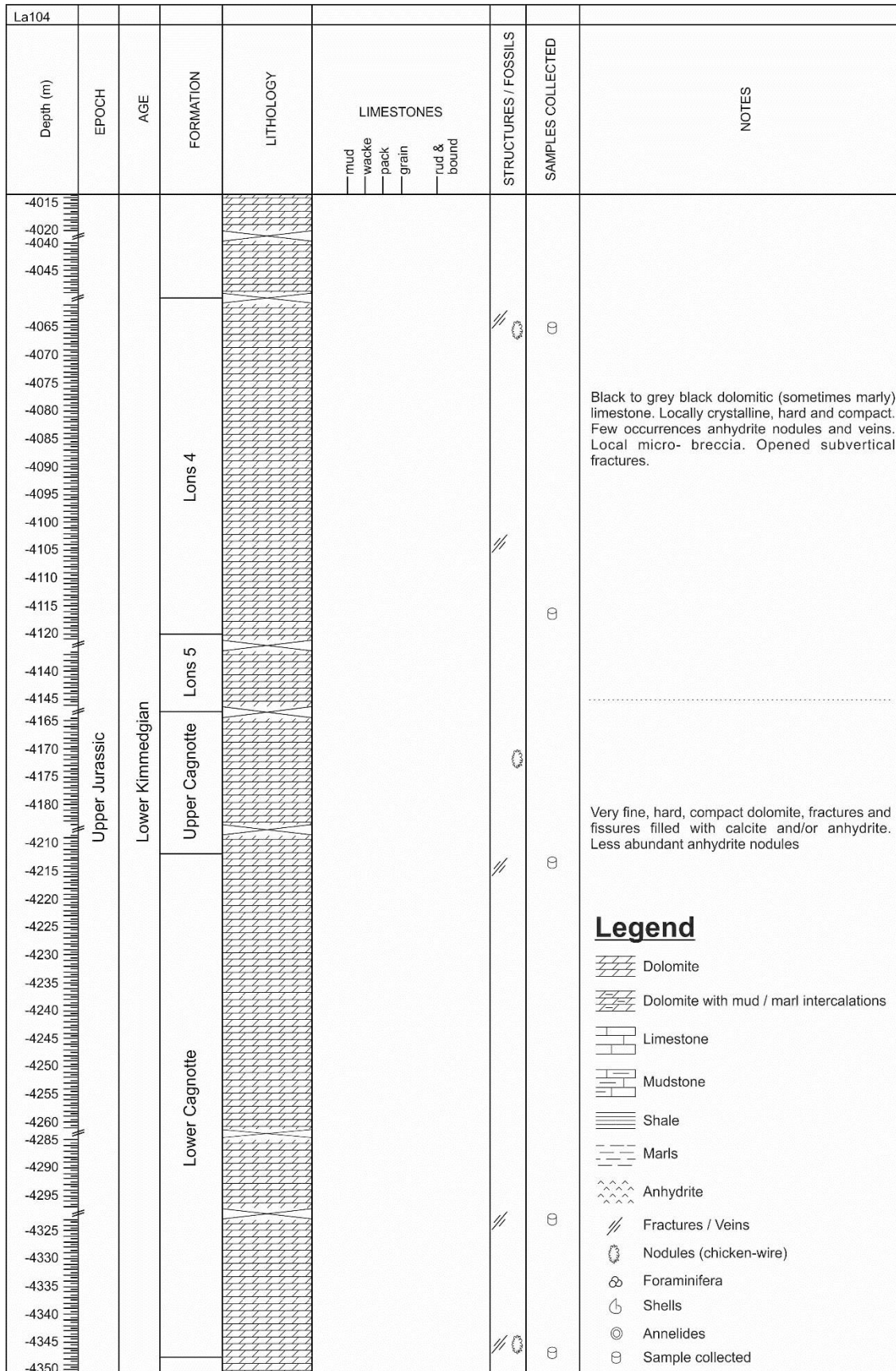
Well: LA104/ Latitude: 43.420421° - Longitude: -0.638811°



Appendices

La104	Depth (m)	EPOCH	AGE	FORMATION	LITHOLOGY	LIMESTONES mud wacke pack grain rud & bound	STRUCTURES / FOSSILS	SAMPLES COLLECTED	NOTES
	-3675 -3680 -3685 -3690 -3695 -3700 -3705 -3710 -3715 -3720	Lower Cretaceous	Berriasian	Gamma Ray					Grey-brown to dark grey dolomite, slightly crystalline, compact with some vuggy pores. Abundant fractures. Several horizons and intercalations of black mud and marls.
	-3725 -3730 -3735 -3740 -3745 -3750 -3755 -3760 -3765 -3770 -3775 -3780 -3795 -3800 -3815 -3820 -3840 -3845 -3859 -3880 -3885 -3890 -3905 -3925 -3940 -3945 -3960 -3985 -4000	Upper Jurassic	Upper Kimmeridgian - Portlandian	Mano Dolomite					Compact and fissured dolomite, locally vuggy. Numerous opened fractures and joints
		Lower Kimmeridgian	Lons 1						Oolitic dolomite - grey to dark brown - traces of anhydrite - small mm-size geodes. Few sub-vertical fractures
			Lons 2						

Appendices



Appendices

Appendix 2: Matlab 2nd derivative algorithms

```
>> syms f(x)
```

```
>> f(x)= 6th degree equation extracted from MS Excel
```

```
>> d1f = diff(f, x) this step calculates the first derivative
```

```
>> d2f = diff(d1f, x) the second derivative is obtained here
```

```
>> d2f == 0 we then solve for  $f''(x)=0$ .
```

At this point, after two derivations, we are with a 4th degree polynomial equation, hence:

```
>> sol = solve(d2f, x, 'MaxDegree', 4) this step solves the 4th degree for  $f(x)=0$ 
```

```
>> vpa(sol) numerical values are displayed here
```


Appendix 3: TVD data used in the Petromod's stratigraphy

Formation name	Top (m)	Base (m)	Present Thickness (m)	Eroded Thickness (m)	Depositional Age (Ma)		Erosion Age (Ma)		Lithology
					from	to	from	to	
Alluvions	0.00	15.00	15.00		2.58	0.00			Conglomerate (typical)
Molasse	15.00	307.00	292.00		34.00	2.58			Conglomerate (typical)
Flysch	307.00	555.00	248.00	400.00	56.00	40.00	40.00	34.00	Limestone (shaly)
Aturien	555.00	663.00	108.00		77.00	56.00			Dolomite (typical)
Jounsalles	663.00	1035.00	372.00		89.00	77.00			Limestone (micrite)
Mazères	1035.00	1160.00	125.00		97.00	89.00			Dolomite (typical)
Assat	1160.00	1424.00	264.00	200.00	109.50	106.00	103.00	97.00	Marl
Albian reef	1424.00	2303.00	879.00		115.00	109.50			Limestone (Waulsortian mound)
Clèdes	2303.00	2714.00	411.00		119.00	114.00			Marl
Brassempouy	2714.00	2738.00	24.00		120.00	121.00			Limestone (ooid grainstone)
Ste-Suzanne	2738.00	3349.00	611.00		125.00	120.00			Marl
Calc. à Annélides sup.	3349.00	3403.00	54.00		126.00	125.00			Dolomite (organic rich)
Latéolog shales	3403.00	3445.00	42.00		127.00	126.00			SHALEcarb
Calc. à Annélides inf	3445.00	3549.00	104.00		128.00	127.00			Limestone (organic rich - typical)
Calc. à Algues	3549.00	3671.00	122.00		129.00	128.00			Limestone (organic rich - typical)
Gamma Ray	3671.00	3721.00	50.00		137.00	139.00			Limestone (Chalk, 75% calcite)
Mano	3721.00	3906.00	185.00	50.00	149.00	146.00	146.00	137.00	Dolomite (typical)
Lons	3906.00	4156.00	250.00		152.00	149.00			Limestone (organic rich - typical)
Cagnotte	4156.00	4346.00	190.00		157.00	152.00			Limestone (micrite)
Ammonite Mars	4346.00	4546.00	200.00		163.00	157.00			Marl
Mézos	4546.00	4696.00	150.00		174.00	163.00			Limestone (micrite)
Liassic marls	4696.00	4796.00	100.00		190.00	174.00			Marl
Liassic Anhydrite zone	4796.00	4896.00	100.00		199.00	190.00			Anhydrite
Carcans Dolomite	4896.00	4946.00	50.00		201.00	199.00			Dolomite (typical)
Keuper Evaporite	4946.00	5946.00	1000.00		230.00	201.00			Salt

Appendix 4: Porosities added as calibrations in Petromod

LA104		LA 101		LA 37	
Depth	Porosity %	Depth	Porosity %	Depth	Porosity %
972	2.70	666	4.10	613	7.00
1171	2.50	667	15.60	615	9.30
1240	1.50	2602	4.00	617	14.40
1346	1.30	2713	2.00	618	16.70
1349	1.50	3087	3.50	620	5.40
1353	1.70	3363	1.80	622	6.20
1365	2.90	3463	1.10	624	19.40
1403	2.90	3562	0.60	626	8.30
1409	4.00	3570	0.60	628	17.40
1441	2.50	3602	0.20	630	10.90
1786	7.80	3614	0.30	632	10.70
2248	6.70	3626	0.90	634	10.50
2602	2.00	3638	7.10	636	4.50
3260	0.40	3639	0.40	638	11.00
3309	0.45	3644	1.10	640	9.00
3353	2.50	3655	6.80	642	8.00
3359	2.00	3667	0.30	644	8.25
3362	3.15	3679	2.40	646	13.00
3368	2.10	3685	0.30	648	12.00
3377	1.30	3696	12.10	650	8.00
3380	1.55	3704	1.10	651	17.00
3389	0.95	3716	1.25	653	8.00
3395	3.55	3728	2.00	654	13.00
3403	4.10			655	17.00
3411	5.00			658	10.00
3420	5.15			660	10.00
3428	2.10			663	8.00
3435	1.95			666	9.00
3441	1.75			668	25.00
3447	3.65			670	11.00
3464	0.35			672	5.00
3476	3.40			689	15.00
3480	0.80			691	9.00
3488	1.35			693	1.00
3494	1.75			696	2.00
3502	1.70			697	3.00
3505	1.50			699	0.20

Appendices

LA104		LA104		LA 37	
Depth	Porosity %	Depth	Porosity %	Depth	Porosity %
3510	7.50	3778	2.00	701	1.20
3513	0.85	3780	5.10	702	1.00
3520	2.40	3783	5.30	703	1.00
3529	2.30	3801	0.85	704	1.00
3538	0.70	3820	7.20	705	2.00
3547	1.20	3845	1.00	706	1.00
3555	5.20	3866	0.40	707	2.00
3563	6.40	3881	3.15	708	1.00
3573	13.95	3890	2.95	709	2.00
3580	3.85	3908	1.15	711	4.00
3584	0.65	3926	1.55	712	2.00
3590	2.90	3947	0.45	713	5.00
3597	5.15	3962	0.70	715	4.00
3615	2.65	3988	1.45	716	1.00
3621	1.60	4001	1.00	717	8.00
3624	2.40	4019	0.65	718	3.00
3626	0.70	4049	0.65	719	5.00
3640	2.75	4070	1.20	720	2.00
3644	1.60	4093	1.15	721	3.00
3647	1.35	4121	1.10	722	4.00
3658	1.90	4146	1.40	723	5.00
3660	1.50	4183	0.60	725	23.00
3671	2.25	4228	0.80	727	5.00
3677	2.45	4261	0.70	729	6.00
3686	1.45	4298	0.80	730	3.00
3691	2.65	4333	0.55	731	14.00
3701	6.15	4352	0.75	735	9.00
3707	3.95				
3715	8.30				
3720	14.35				
3731	8.95				
3738	5.97				
3744	7.55				
3747	3.85				
3748	4.55				
3760	6.00				
3768	7.00				
3771	9.15				
3776	6.30				

Appendix 5: Densities added as calibrations in Petromod

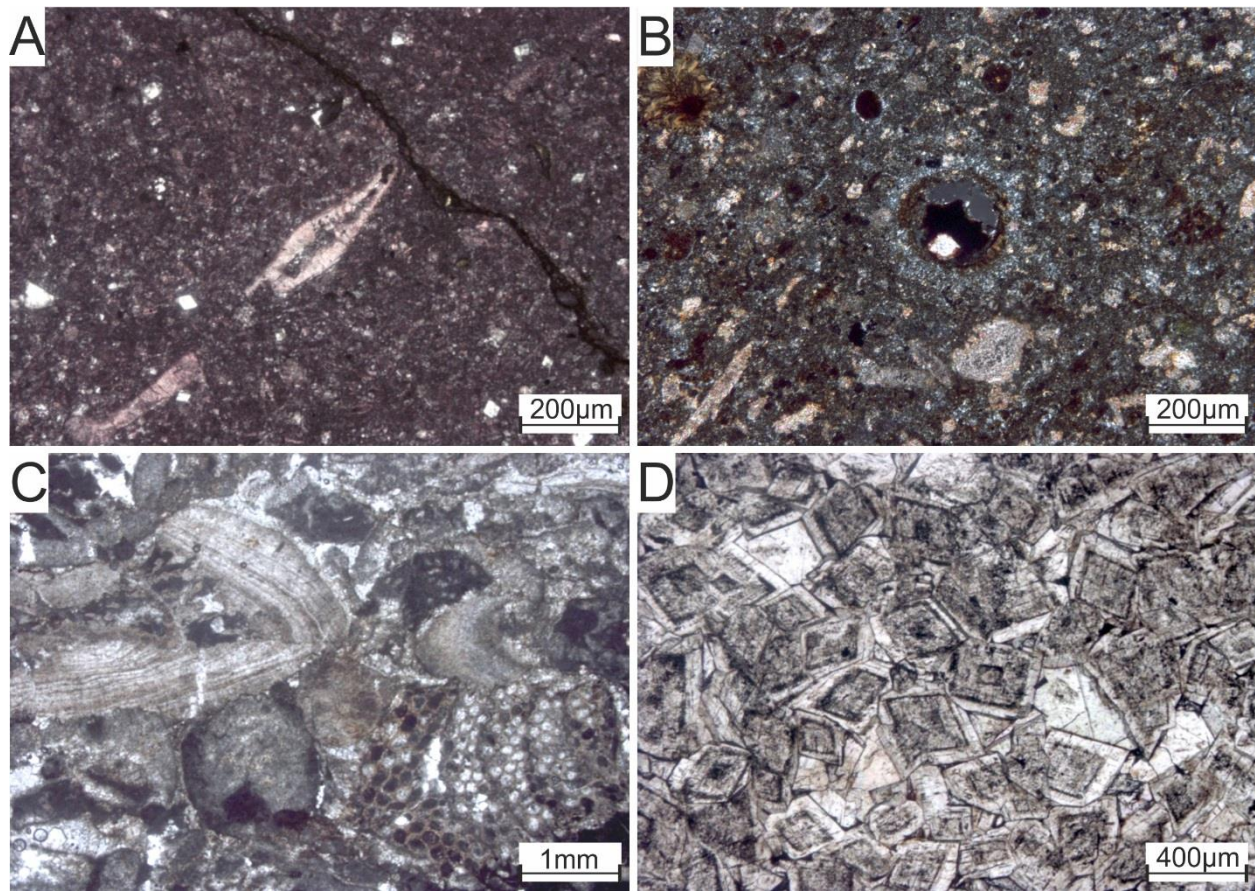
LA104		LA 101		LA 36	
Depth	Density g/cm ³	Depth	Density g/cm ³	Depth	Density g/cm ³
972	2.80	666	2.39	484	2.08
1171	2.52	667	2.34	653	2.21
1240	2.60	2602	2.66	719	2.26
1346	2.50	2713	2.76	735	2.43
1349	2.64	3087	2.60	745	2.26
1409	2.65	3363	2.67	755	2.38
1441	2.80	3463	2.67	770	2.54
1786	2.60	3562	2.70	792	2.64
2248	2.64	3570	2.69	835	2.62
2602	2.30	3602	2.85	850	2.51
3176	2.65	3614	2.64	1053	2.46
3260	2.67	3626	2.72	1095	2.62
3624	2.70	3638	2.80	1111	2.58
3626	2.72	3639	2.78	1188	2.28
3778	2.79	3644	2.77	1199	2.50
3780	2.86	3655	2.80	1241	2.46
3866	2.84	3667	2.79	1480	2.60
3962	2.82	3679	2.67	1600	2.60
4001	2.80	3685	2.79	1762	2.61
		3696	2.56	1885	2.60
		3704	2.69	2090	2.61
		3716	2.70	2200	2.59
		3728	2.82		

Appendix 6: Vitrinite and sterane isomerization data added as calibrations in Petromod

LA104		LA 101	
Depth	Vitrinite reflectance (Ro%)	Depth	Vitrinite reflectance (Ro%)
1170	0.40	3460	1.20
1345	0.40	3559	1.30
1405	0.40	3630	0.79
2865	0.40	3700	1.40
3370	0.70	3726	1.50
3520	1.50		
3618	1.60		
3680	1.60		
3760	1.70		
3881	1.85		

LA104	
Depth	Sterane Isomerization %
1239	0.90
1356	0.80
2866	0.40
3026	0.40
3255	0.80
3350	1.10

Appendix 7: Photomicrographs of the host rocks in Upper Lacq



A: Red/pink stained image of the fossiliferous micrite lithology of the limestones in the Jounsalles formation, Upper Lacq. Viewed under PPL

B: Foraminifera-rich fossiliferous micrite lithology of the limestones in the Mazères formation, Upper Lacq. Viewed under CPL.

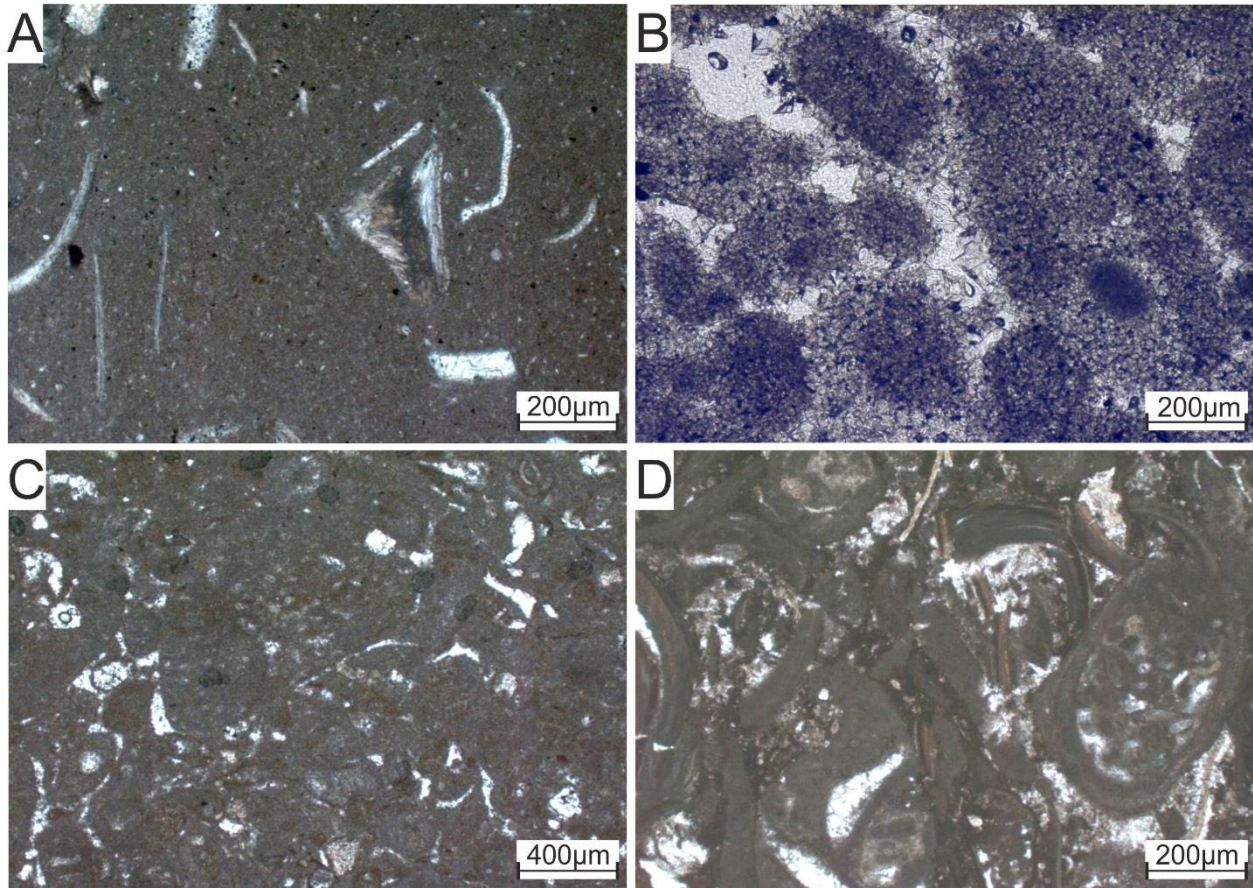
C: Biomicrite facies of the Albian reef, part of the Upper Lacq reservoirs. Viewed under PPL.

D: Fully-dolomitized lithology of Upper Lacq with well-zone sucrosic dolomites whose intercrystalline porosity was later filled by creamy-white anhydrite cements. Viewed under PPL.

Appendix 8: $\delta^{18}\text{O}$ and $\delta^{13}\text{C}$ data of Upper Lacq reservoirs

Sample name	Phase	$\delta^{18}\text{O}$ (‰ PDB)	stdev	$\delta^{13}\text{C}$ (‰ PDB)	stdev
101_665.5-667	Host rock - Marly Limestone	-2,898726496	0,023	1,728735043	0,018
101_665.5-667_H	Host rock - Marly Limestone	-4,352504274	0,021	1,581068376	0,018
104_1400-1403_H	Host rock - Mudstone	-3,059282051	0,011	3,248846154	0,015
104_968.7-971.7	Dolomitized Host Rock	-4,990726496	0,164	3,563290598	0,282
723-725	Dolomitized Host Rock	-5,71665873	0,02	2,90915873	0,016
630_4-632_4-2	Dolomitized Host Rock	-5,767436508	0,009	2,833047619	0,017
630_4-632_4-2	Dolomitized Host Rock	-5,85365873	0,022	2,825380952	0,014
705_45-707-4	Dolomitized Host Rock	-5,19065873	0,025	3,462936508	0,017
705_45-707-2	Dolomitized Host Rock	-6,374992063	0,023	3,063269841	0,021
731-733-2	Dolomitized Host Rock	-7,000992063	0,021	2,488936508	0,015
721-722-1	Dolomitized Host Rock	-5,903880952	0,019	2,581047619	0,022
708-709-1	Dolomitized Host Rock	-5,297325397	0,017	3,20015873	0,02
630_4-632_4-1	Dolomitized Host Rock	-6,328547619	0,015	2,910047619	0,011
626_4-628_4-1	Dolomitized Host Rock	-6,291547619	0,018	2,811492063	0,017
626_4-628_4-1	Dolomitized Host Rock	-6,600325397	0,015	2,87315873	0,014
667_8-669_7-2	Dolomitized Host Rock	-4,890325397	0,021	2,723603175	0,019
667_9-672_3-2	Dolomitized Host Rock	-5,767214286	0,016	2,553825397	0,017
735-737-2	Dolomitized Host Rock	-4,76865873	0,027	3,182936508	0,015
630_4-632_4-1	Dolomitized Host Rock	-5,813325397	0,014	2,860492063	0,012
705_45-707-1	Dolomitized Host Rock	-2,247547619	0,021	3,16415873	0,013
705_45-707-3	Dolomitized Host Rock	-3,030436508	0,021	3,228936508	0,016
691-693-3	Dolomitized Host Rock	-3,532103175	0,022	3,029936508	0,009
708-709-2	Blocky calcite	-10,33954762	0,014	-1,480396825	0,012
691-693-1	Blocky calcite	-10,21021429	0,027	-0,207952381	0,016
101_665.5-667_C	Blocky calcite	-9,146948718	0,019	1,174735043	0,01
691-693-1	Blocky calcite	-10,24521429	0,02	-0,138507937	0,016
669_7-672_3-1	Blocky calcite	-12,37565873	0,031	1,530825397	0,016
667_8-669_7-1	Blocky calcite	-11,14399206	0,013	0,716936508	0,022
735-737-1	Saddle dolomite	-8,207880952	0,024	2,03115873	0,017
731-733-1	Saddle dolomite	-8,234214286	0,01	2,830269841	0,013
708-709-3	Saddle dolomite	-8,685103175	0,021	1,923492063	0,008
691-693-2	Saddle dolomite	-8,916214286	0,021	0,508714286	0,022
663_2-665_7	Saddle dolomite	-9,090547619	0,018	2,417269841	0,01
663_2-665_7	Saddle dolomite	-9,178214286	0,028	2,389603175	0,011

Appendix 9: Photomicrographs of the host rocks in Deep Lacq



A: Fossiliferous micrite lithology of the limestones in the Lons formation of Deep Lacq. Viewed under PPL

B: Pelloidal dolomites lithology of the Mano dolomite formation, Deep Lacq. Viewed under PPL.

C: Biomicrite facies of the Algal limestone formation, Deep Lacq. Viewed under PPL.

D: Packed biomicrite facies of the Annelids limestone formation, Deep Lacq. Viewed under PPL.

Appendix 10: $\delta^{18}\text{O}$ and $\delta^{13}\text{C}$ data of Deep Lacq reservoirs

Sample name	Phase	$\delta^{18}\text{O}$ (‰ PDB)	stdev	$\delta^{13}\text{C}$ (‰ PDB)	stdev
101_3646.7-3647.7	Host rock	-3,22	0,03	-2,41	0,01
101_3697.2-3698.3_H	Host rock	-0,69	0,02	-1,37	0,01
104_3488.10-3494.4_H	Host rock	-2,13	0,02	-1,15	0,01
104_3771.2-3775.7	Host rock	-1,74	0,02	0,04	0,01
104_4136.8-4145.8_M	Host rock	-3,72	0,02	2,29	0,01
104_3584-3589.6_H	Host rock	-2,38	0,02	2,53	0,02
LA 104 3584-4 HR	Host rock	-2,31	0,01	1,54	0,02
LA 104 3584-3 HR	Host rock	-2,60	0,03	1,42	0,02
LA 104 3488-4 HR	Host rock	-2,40	0,02	-0,02	0,01
LA 104 3488-3 HR	Host rock	-2,49	0,02	-0,04	0,01
LA 104 3707-6 SD	Dol. 2	-1,86	0,01	1,52	0,02
LA 104 3707-5 SD	Dol. 2	-6,01	0,01	5,37	0,01
LA 104 3707-4 SD	Dol. 2	-6,06	0,02	5,37	0,01
LA 104 3707-3 SD	Dol. 2	-6,18	0,01	5,44	0,01
104_3488.10-3494.4_C	Calcite 3	-2,90	0,02	1,73	0,02
104_3584-3589.6_C	Calcite 3	-4,35	0,02	1,58	0,02
101_3697.2-3698.3_C	Calcite 3	-3,06	0,01	3,25	0,01
LA 104 3584-2 Cal4	Calcite 3	-5,24	0,02	4,12	0,01
LA 104 3584-1 Cal4	Calcite 3	-5,63	0,02	4,26	0,01
LA 104 3488-2 Cal4	Calcite 3	-4,74	0,03	3,57	0,01
LA 104 3488-1 Cal4	Calcite 3	-5,00	0,02	3,17	0,02

Appendix 11: TOTAL's archives isotopic data (Pabian-Goyheneche and Anquelle, 1995)

Well	Depth	Phase	$\delta^{18}\text{O}$ (‰ PDB)	$\delta^{13}\text{C}$ (‰ PDB)	$^{87}\text{Sr}/^{86}\text{Sr}$
113	3742	Dol. 1	0,9	0,1	
113	3705	Dol. 1	0,3	1,6	
113	3733,2	Dol. 1	1,8	-1,4	
113	3695	Dol. 1	1	1,1	
113	3628,12	Dol. 1	-0,1	0,5	
113	3654,97	Dol. 1	0,4	1,7	
113	3622,65	Dol. 1	0,6	1,3	
113	3677,72	Dol. 1	1,4	1,4	
113	3678,82	Dol. 1	1,3	2,1	0,708113
113	3649,57	Dol. 1	0,4	1,6	
113	3648,62	Dol. 1	0	1,7	
113	3685,52	Dol. 1	1,8	1	
113	3678,22	Dol. 1	1,8	1,2	0,70825
113	3643,72	Dol. 1	-0,2	1,3	0,70777
113	3634,18	Dol. 1	-0,6	0,3	0,70792
104	3766,5	Dol. 2	-8	-5,6	0,707148
113	3462,87	Cal.3	-3,6	2,1	0,707361
113	3469,52	Cal.3	-2,8	1,8	
113	3461,76	Cal.3	-2,8	2	
113	3464,12	Cal.3	-2,9	1,9	
113	3457,32	Cal.3	-3,7	1,8	
113	3456,42	Cal.3	-3,3	1,8	
113	3455,22	Cal.3	-2,5	1,8	0,707489
113	3459,68	Cal.3	-3,3	2	
113	3467,52	Cal.3	-2,6	1,9	
113	3465,72	Cal.3	-2,4	1,9	
113	3450,65	Cal.3	-1,9	1,4	0,70747
113	3476,82	Cal.3	-2,9	1,4	
113	3460,52	Cal.3	-3	2	
113	3454,62	Cal.3	-2,2	1,5	
113	3489,65	Cal.3	-4,2	1,2	
113	3561,65	Cal.3	-4,4	0,4	
113	3472,32	Cal.3	-2,6	1,6	
113	3478,08	Cal.3	-4	1,4	0,707318
103	3697,8	Cal.3	-2,6	-0,8	0,707432
103	3749,3	Cal.3	-2,7	-0,3	0,707303

Well	Depth	Phase	$\delta^{18}\text{O}$ (‰ PDB)	$\delta^{13}\text{C}$ (‰ PDB)	$^{87}\text{Sr}/^{86}\text{Sr}$
103	3614	Cal.3	-5,7	-5,2	0,707397
103	3703,8	Cal.3	-3,1	-2,6	
103	3876,85	Cal.3	-3,6	1,4	
103	3881,2	Cal.3	-3,5	1,3	
103	3862,85	Cal.3	-3	1,1	
102	4165	Cal.3	-5,1	-4,4	
102	4156,5	Cal.3	-3,8	-1	
102	4017	Cal.3	-2,6	0,4	0,707359
102	3992,5	Cal.3	-3,1	0,2	
104	3478	Cal.3	-1,7	-1,2	
104	3480	Cal.3	-2,5	-0,7	0,707549
104	3482,5	Cal.3	-2,8	-1,5	
104	3525,5	Cal.3	-3,1	-0,4	
104	3532,5	Cal.3	-2,8	-0,1	0,707369
104	3539,7	Cal.3	-2,9	0,2	
104	3550,5	Cal.3	-2,9	1,2	0,707278
104	3559,3	Cal.3	-3,8	2,4	
104	3562	Cal.3	-3,8	2,5	0,707441
104	3576	Cal.3	-3,6	1,5	
104	3590,5	Cal.3	-4,4	1,4	0,70735
104	3609	Cal.3	-3,4	1,6	
104	3628,5	Cal.3	-3,5	1,3	
104	3684	Cal.3	-2,9	0	0,707304
104	3671	Cal.3	-3,6	-1,2	
104	3678,5	Cal.3	-5,5	-2,1	0,707235
104	3513,6	Cal.3	-5,9	1,2	
104	3478,46	Cal.3	-6,1	0,9	
104	3477,67	Cal.3	-6,2	1,7	

Appendix 12: U/Pb contents in Deep Lacq

Mineral Phase	Pb (ppm)	Error Range	U (ppm)	Error Range
Micrite host rock	0,502	0,085	2,36	0,12
Micrite host rock	0,198	0,038	2,4	0,14
Micrite host rock	1,41	0,32	2,63	0,11
Micrite host rock	6,6	1,3	5,65	0,61
Micrite host rock	3,77	0,32	3,29	0,25
Micrite host rock	11	1,7	4,72	0,2
Oolitic dolomite grain	0,6	0,13	3,53	0,6
Oolitic dolomite grain	1,19	0,32	5,7	1,5
Oolitic dolomite grain	26	1,9	14,4	3,1
Dol. 1	0,65	0,37	0,45	0,11
Dol. 1	0,43	0,12	0,545	0,071
Dol. 1	1,27	0,27	0,68	0,11
Dol. 1	0,15	0,045	0,661	0,087
Calcite 1	Below detection limit	-	1,39	0,18
Calcite 1	0,36	0,17	0,5	0,15
Calcite 1	0,8	0,15	0,418	0,077
Calcite 2	Below detection limit	-	Below detection limit	-
Calcite 2	Below detection limit	-	1,949	0,099
Calcite 2	Below detection limit	-	1,553	0,086
Dol. 2	1,82	0,24	0,0045	0,003
Dol. 2	0,52	0,23	0,0034	0,0032
Dol. 2	12,7	3,1	2,15	0,78
Dol. 2	3,59	0,92	0,062	0,045
Dol. 2	0,42	0,095	0,027	0,014
Dol. 2	0,07	0,032	0,0039	0,0036
Dol. 2	0,142	0,064	0,0045	0,0042
Dol. 2	0,125	0,046	0,0051	0,0057
Dol. 2	0,091	0,037	0,0062	0,0058
Dol. 2	3,63	0,31	0,0122	0,0089
Dol. 2	Below detection limit	-	Below detection limit	-
Dol. 2	0,143	0,063	0,0035	0,007
Dol. 2	Below detection limit	-	0,013	0,012
Calcite 3	0,062	0,017	0,131	0,02
Calcite 3	0,056	0,018	0,298	0,022
Calcite 3	0,116	0,046	0,39	0,039
Calcite 3	0,054	0,03	0,417	0,08
Calcite 3	Below detection limit	-	0,429	0,086
Calcite 3	Below detection limit	-	0,327	0,059

Mineral Phase	Pb (in ppm)	Error Range	U (in ppm)	Error Range
Calcite 3	Below detection limit	-	0,115	0,039
Calcite 3	Below detection limit	-	0,168	0,04
Calcite 3	Below detection limit	-	0,132	0,029
Calcite 3	0,065	0,041	0,045	0,022
Calcite 3	0,135	0,066	0,017	0,014
Calcite 3	0,101	0,07	0,009	0,012
Calcite 3	Below detection limit	-	0,028	0,014
Calcite 3	0,081	0,054	Below detection limit	-
Calcite 3	0,19	0,1	Below detection limit	-
Calcite 3	Below detection limit	-	Below detection limit	-
Calcite 3	Below detection limit	-	0,124	0,022
Calcite 3	Below detection limit	-	0,196	0,016
Calcite 3	Below detection limit	-	0,064	0,011

References

- Adams, J.E., Rhodes, M.L., 1960. Dolomitization by Seepage Refluxion. *Am. Assoc. Pet. Geol. Bull.* 44, 1912–1920.
- Amierux, P., 1982. La cathodoluminescence methode d'étude sédimentologique des carbonates. *Bull. des Centres Rech. Explor. Elf- Aquitaine* 6, 437–483.
- Amthor, J.E., Mountjoy, E.W., Machel, H.G., 1993. Subsurface dolomites in Upper Devonian Leduc Formation buildups, central part of Rimbey-Meadowbrook reef trend, Alberta, Canada. *Bull. Can. Pet. Geol.* 41, 164–185.
- Angrand, P., Ford, M., Watts, A.B., 2018. Lateral Variations in Foreland Flexure of a Rifted Continental Margin: The Aquitaine Basin (SW France). *Tectonics* 37, 430–449. <https://doi.org/10.1002/2017TC004670>
- Barnaby, R.J., Rimstidt, J.D., 1989. Redox conditions of calcite cementation interpreted from Mn and Fe contents of authigenic calcites. *Geol. Soc. Am. Bull.* 101, 795–804. [https://doi.org/10.1130/0016-7606\(1989\)101<0795:RCOCCI>2.3.CO;2](https://doi.org/10.1130/0016-7606(1989)101<0795:RCOCCI>2.3.CO;2)
- Bathurst, R.G.C., 2007. Boring algae, micrite envelopes and lithification of molluscan biosparites. *Geol. J.* 5, 15–32. <https://doi.org/10.1002/gj.3350050104>
- Bau, M., Dulski, P., 1996. Distribution of yttrium and rare-earth elements in the Penge and Kuruman iron-formations, Transvaal Supergroup, South Africa. *Precambrian Res.* 79, 37–55. [https://doi.org/10.1016/0301-9268\(95\)00087-9](https://doi.org/10.1016/0301-9268(95)00087-9)
- Beziat, D., Joron, J., 1986. Caractéristiques géochimiques et contexte géodynamique des ophites des Pyrénées. 11e Réunion des Sci. la Terre.
- Bilotte, M., Odin, G.S., Vrielynck, B., 2001. Geology and Late Cretaceous palaeogeography of the geological site at Tercis les Bains (Landes , France), in: Odin, G.S. (Ed.), *The Campanian - Maastrichtian Boundary*. Elsevier Science B.V.

- Biteau, J., Le Marrec, A., Le Vot, M., Masset, J.-M., 2006. The Aquitaine Basin. *Pet. Geosci.* 12, 247–273.
<https://doi.org/10.1144/1354-079305-674>
- Blackwell, D.D., Steele, J.L., 1989. Thermal Conductivity of Sedimentary Rocks: Measurement and Significance, in: Naeser, N.D., McCulloh, T.H. (Eds.), *Thermal History of Sedimentary Basins*. Springer New York, New York, NY, pp. 13–36.
- Bodnar, R.J., 1993. Revised equation and table for determining the freezing point depression of H₂O-NaCl solutions. *Geochim. Cosmochim. Acta* 57, 683–684. [https://doi.org/10.1016/0016-7037\(93\)90378-A](https://doi.org/10.1016/0016-7037(93)90378-A)
- Boggs, S., Krinsley, D., 2006. *Application of cathodoluminescence imaging to the study of sedimentary rocks*, 1st ed. Cambridge University Press, Cambridge.
- Boni, M., Parente, G., Bechstädt, T., De Vivo, B., Iannace, A., 2000. Hydrothermal dolomites in SW Sardinia (Italy): evidence for a widespread late-Variscan fluid flow event. *Sediment. Geol.* 131, 181–200.
[https://doi.org/10.1016/S0037-0738\(99\)00131-1](https://doi.org/10.1016/S0037-0738(99)00131-1)
- Bonifacie, M., Calmels, D., Eiler, J.M., Horita, J., Chaduteau, C., Vasconcelos, C., Agrinier, P., Katz, A., Passey, B.H., Ferry, J.M., Bourrand, J.-J., 2017. Calibration of the dolomite clumped isotope thermometer from 25 to 350°C, and implications for a universal calibration for all (Ca, Mg, Fe)CO₃ carbonates. *Geochim. Cosmochim. Acta* 200, 255–279. <https://doi.org/10.1016/j.gca.2016.11.028>
- Bordenave, M.L., 2008. The origin of the Permo-Triassic gas accumulations in the Iranian Zagros Foldbelt and contiguous offshore areas: A Review of the Palaeozoic Petroleum System. *J. Pet. Geol.* 31, 3–42. <https://doi.org/10.1111/j.1747-5457.2008.00405.x>
- Bourdet, J., Eadington, P., 2012. *Fluorescence and Infrared Spectroscopy of oil inclusions*. CSIRO, internal Report EP129625.
- Bourdet, J., Pironon, J., Levresse, G., Tritlla, J., 2008. Petroleum type determination through homogenization temperature and vapour volume fraction measurements in fluid inclusions. *Geofluids* 8, 46–59. <https://doi.org/10.1111/j.1468-8123.2007.00204.x>
- Bourdet, J., Pironon, J., Levresse, G., Tritlla, J., 2007. Combination of fluid inclusion data and basin

- modeling for the reconstruction P,T,X,T conditions in Cretaceous oil carbonate reservoir from Gulf of Mexico. Am. Assoc. Pet. Geol. Hedb. Res. Conf. (The Hague, Netherlands, 5/6-9/2007).
- Bouroullec, J., Leduc, J.P., Chennaux, G., Sanz, M.C., 1986. Etude lithofaciologique de 2 series de Lacq Supérieur, LA.80 et LA.408, TOTAL EP internal report.
- Brand, W.A., Assonov, S.S., Coplen, T.B., 2010. Correction for the ^{17}O interference in $\delta(^{13}\text{C})$ measurements when analyzing CO_2 with stable isotope mass spectrometry. Pure Appl. Chem. 82, 1719–1733. <https://doi.org/10.1351/PAC-REP-09-01-05>
- Brigaud, B., Durllet, C., Deconinck, J., Vincent, B., Thierry, J., Trouiller, A., 2009. The origin and timing of multiphase cementation in carbonates: Impact of regional scale geodynamic events on the Middle Jurassic Limestones diagenesis (Paris Basin, France). Sediment. Geol. 222, 161–180. <https://doi.org/10.1016/j.sedgeo.2009.09.002>
- Butler, G., 1970. Holocene gypsum and anhydrite of the Abu Dhabi sabkha, Trucial Coast: an alternative explanation of origin, in: Rau, J., Dwelling, L. (Eds.), Third Symposium on Salt. Northern Ohio Geological Society, Cleveland, pp. 120–152.
- Canerot, J., Hudec, M.R., Rockenbach, K., 2005. Mesozoic diapirism in the Pyrenean orogen: Salt tectonics on a transform plate boundary. Am. Assoc. Pet. Geol. Bull. 89, 211–229. <https://doi.org/10.1306/09170404007>
- Canerot, J., Lenoble, J.L., Villien, A., 1992. Early Cretaceous Sequence Stratigraphy of the Western Pyrenees, France, in: Mesozoic and Cenozoic Sequence Stratigraphy of European Basins. Dijon, pp. 12–20.
- Canerot, J., Villien, A., Lenoble, J.L., Canérot, J., Villien, A., Lenoble, L., 1990. Sequence stratigraphy and sedimentary unconformities: western Pyrénées (field data) and southern aquitanian basin (subsurface data). Bull. la Société Géologique Fr. 6, 995–1000.
- Carpentier, C., Brigaud, B., Blaise, T., Vincent, B., Durllet, C., Boulvais, P., Pagel, M., Hirsch, C., Yven, B., Lach, P., Cathelineau, M., Boiron, M., Landrein, P., Buschaert, S., 2014. Impact of basin burial and

- exhumation on Jurassic carbonates diagenesis on both sides of a thick clay barrier (Paris Basin, NE France). *Mar. Pet. Geol.* 53, 44–70. <https://doi.org/10.1016/j.marpetgeo.2014.01.011>
- Caumon, M.-C., Dubessy, J., Robert, P., Tarantola, A., 2014. Fused-silica capillary capsules (FSCCs) as reference synthetic aqueous fluid inclusions to determine chlorinity by Raman spectroscopy. *Eur. J. Mineral.* 25, 755–763. <https://doi.org/10.1127/0935-1221/2013/0025-2280>
- Caumon, M.C., Robert, P., Laverret, E., Tarantola, A., Randi, A., Pironon, J., Dubessy, J., Girard, J.P., 2014. Determination of methane content in NaCl-H₂O fluid inclusions by Raman spectroscopy. Calibration and application to the external part of the Central Alps (Switzerland). *Chem. Geol.* 378–379, 52–61. <https://doi.org/10.1016/j.chemgeo.2014.03.016>
- Caumon, M.C., Tarantola, A., Mosser-Ruck, R., 2015. Raman spectra of water in fluid inclusions: I. Effect of host mineral birefringence on salinity measurement. *J. Raman Spectrosc.* 46, 969–976. <https://doi.org/10.1002/jrs.4708>
- Cerepi, A., Barde, J., Labat, N., 2003. High-resolution characterization and integrated study of a reservoir formation: the danian carbonate platform in the Aquitaine Basin (France). *Mar. Pet. Geol.* 20, 1161–1183. <https://doi.org/10.1016/j.marpetgeo.2003.09.005>
- Choquette, P.W., Pray, L., 1970. Geologic nomenclature and classification of porosity in sedimentary carbonates. *Am. Assoc. Pet. Geol. Bull.* 54, 207–250.
- Choukroune, P., Le Pichon, X., Seguret, M., Sibuet, J.-C., 1973. Bay of Biscay and Pyrenees. *Earth Planet. Sci. Lett.* 18, 109–118. [https://doi.org/10.1016/0012-821X\(73\)90041-1](https://doi.org/10.1016/0012-821X(73)90041-1)
- Clerc, C., Lagabrielle, Y., 2014. Thermal control on the modes of crustal thinning leading to mantle exhumation: Insights from the Cretaceous Pyrenean hot paleomargins. *Tectonics* 33, 1340–1359. <https://doi.org/10.1002/2013TC003471>
- Clerc, C., Lahfid, A., Monié, P., Lagabrielle, Y., Chopin, C., Poujol, M., Boulvais, P., Ringenbach, J.-C., Masini, E., de St Blanquat, M., 2015. High-temperature metamorphism during extreme thinning of the continental crust: a reappraisal of the North Pyrenean passive paleomargin. *Solid Earth* 6, 643–668.

<https://doi.org/10.5194/se-6-643-2015>

- Compton, J., 1988. Sediment Composition and Precipitation of Dolomite and Pyrite in the Neogene Monterey and Sisquoc Formations Santa Maria Basin Area California. *Sedimentol. geochemistry dolostones* 43, 53–64.
- Conliffe, J., Azmy, K., Gleeson, S.A., Lavoie, D., 2010. Fluids associated with hydrothermal dolomitization in St. George Group, western Newfoundland, Canada. *Geofluids* 10, 422–437. <https://doi.org/10.1111/j.1468-8123.2010.00295.x>
- Connan, J., Lacrampe-Couloume, G., 1993. The Origin of the Lacq Superieur Heavy Oil Accumulation and of the Giant Lacq Inferieur Gas Field (Aquitaine Basin, SW France), in: Bordenave, M.L. (Ed.), *Applied Petroleum Geochemistry*. Editions Technip, Paris, pp. 464–488.
- Conway, B., 1982. Ionic hydration in chemistry and biophysics, in: Barthel, J., Jaenicke, R. (Eds.), *Studies in Physical and Theoretical Chemistry*. Elsevier, Amsterdam, p. 264.
- Corre, B., Boulvais, P., Boiron, M.C., Lagabrielle, Y., Marasi, L., Clerc, C., 2018. Fluid circulations in response to mantle exhumation at the passive margin setting in the north Pyrenean zone, France. *Mineral. Petrol.* 0, 1–24. <https://doi.org/10.1007/s00710-018-0559-x>
- Corre, B., Lagabrielle, Y., Labaume, P., Fourcade, S., Clerc, C., Ballèvre, M., 2016. Deformation associated with mantle exhumation in a distal, hot passive margin environment: New constraints from the Sarailié Massif (Chaînons Béarnais, North-Pyrenean Zone). *Comptes Rendus Geosci.* 348, 279–289. <https://doi.org/10.1016/j.crte.2015.11.007>
- Crockford, P.W., Kunzmann, M., Bekker, A., Hayles, J., Bao, H., Halverson, G.P., Peng, Y., Bui, T.H., Cox, G.M., Gibson, T.M., Wörndle, S., Rainbird, R., Lepland, A., Swanson-Hysell, N.L., Master, S., Sreenivas, B., Kuznetsov, A., Krupenik, V., Wing, B.A., 2019. Claypool continued: Extending the isotopic record of sedimentary sulfate. *Chem. Geol.* 513, 200–225. <https://doi.org/10.1016/j.chemgeo.2019.02.030>
- Curnelle, R., Dubois, P., 1986. Evolution mesozoïque des grands bassins sédimentaires français; bassins

- de Paris, d'Aquitaine et du Sud-Est. Bull. la Société Géologique Fr. 8, 529–546.
- Curnelle, R., Dubois, P., Seguin, J.C., Whitaker, D., Matthews, D.H., Roberts, D.G., Kent, P., Laughton, A.S., Kholief, M.M., 1982. The Mesozoic-Tertiary Evolution of the Aquitaine Basin [and Discussion]. Philos. Trans. R. Soc. London. Ser. A, Math. Phys. Sci. 305, 63–84.
- Curnelle, R., Dubois, P., Seguin J, C., 1980. Le Bassin d'Aquitaine substratum anté-tertiaire et bordures mesozoïques. in: Itinéraires géologiques. Bull. des centres Rech. Explor. Elf-Aquitaine 3, 47–58.
- Daignières, M., Séguret, M., Specht, M., 1994. The Arzacq-Western Pyrenees ECORS Deep Seismic Profile, in: Hydrocarbon and Petroleum Geology of France. Special Publication of the European Association of Petroleum Geoscientists. Springer Berlin Heidelberg, Berlin, Heidelberg, pp. 199–208. https://doi.org/10.1007/978-3-642-78849-9_15
- Danesh, A., 1998. PVT and phase behaviour of petroleum reservoir fluids, 47th ed. Elsevier.
- Debroas, E.J., Souquet, P., 1976. Sédimentogenèse et position structurale des flyschs crétacés sur le versant nord des Pyrénées centrales. Bull. du Bur. Rech. géologiques minières 1, 305–320.
- Deffeyes, K.S., Lucia, F.J., Weyl, P.K., 1965. Dolomitization of Recent and Plio-Pleistocene Sediments by Marine Evaporite Waters on Bonaire, Netherlands Antilles, in: Pray, L.C., Murray, R.C. (Eds.), Dolomitization and Limestone Diagenesis. SEPM (Society for Sedimentary Geology), Toronto, Canada, pp. 71–88. <https://doi.org/10.2110/pec.65.07.0071>
- Delfaud, J., Gautier, J., 1967. Evolution des milieux de dépôts au passage Jurassique – Crétacé du forage de Lacq 104 (Aquitaine, France, Sud-Ouest). Bull. du Cent. Rech. Pau-SNPA 1, 77–89.
- Delfaud, J., Neurdin, J., Pailhe, P., Thomas, G., 1980. La vallée d'Ossau: traversée des Pyrénées béarnaises. Itinéraires géologiques: Aquitaine, Languedoc, Pyrénées 106–112.
- Dennis, K.J., Affek, H.P., Passey, B.H., Schrag, D.P., Eiler, J.M., 2011. Defining an absolute reference frame for “clumped” isotope studies of CO₂. Geochim. Cosmochim. Acta 75, 7117–7131. <https://doi.org/10.1016/j.gca.2011.09.025>
- Deregnacourt, D., 1981. Contribution à l'étude géologique du Golfe de Gascogne. Université de Paris 6.

- Dickson, J.A.D., 1965. A Modified Staining Technique for Carbonates in Thin Section. *Nature* 205, 587–587. <https://doi.org/10.1038/205587a0>
- Duan, Z., Mao, S., 2006. A thermodynamic model for calculating methane solubility, density and gas phase composition of methane-bearing aqueous fluids from 273 to 523K and from 1 to 2000bar. *Geochim. Cosmochim. Acta* 70, 3369–3386. <https://doi.org/10.1016/j.gca.2006.03.018>
- Duan, Z., Møller, N., Weare, J.H., 2000. Accurate prediction of the thermodynamic properties of fluids in the system H₂O–CO₂–CH₄–N₂ up to 2000 K and 100 kbar from a corresponding states/one fluid equation of state. *Geochim. Cosmochim. Acta* 64, 1069–1075. [https://doi.org/10.1016/S0016-7037\(99\)00368-3](https://doi.org/10.1016/S0016-7037(99)00368-3)
- Dunham, R.J., 1962. Classification of carbonate rocks according to their depositional texture, in: Ham, W.E. (Ed.), *Classification of Carbonate Rocks*. pp. 108–121.
- Esquevin, J., Menedez, R., Sourisse, C., 1987. Dosages Isotopiques S, C, O et H sur les fluides et les carottes d'une serie de puits de la ride Meillon - Pont d'As et de puits de Lacq Superieur. TOTAL EP internal report.
- Farquhar, J., Wu, N., Canfield, D.E., Oduro, H., 2010. Connections between Sulfur Cycle Evolution, Sulfur Isotopes, Sediments, and Base Metal Sulfide Deposits. *Econ. Geol.* 105, 509–533. <https://doi.org/10.2113/gsecongeo.105.3.509>
- Flügel, E., 2004. *Microfacies of Carbonate Rocks*. Springer Berlin Heidelberg, Berlin, Heidelberg. <https://doi.org/10.1007/978-3-662-08726-8>
- Folk, R.L., 1962. Spectral subdivision of limestone types. *AAPG Spec. Publ.* 1, 62–84.
- Ford, M., Hemmer, L., Vacherat, A., Gallagher, K., Christophoul, F., 2016. Retro-wedge foreland basin evolution along the ECORS line, eastern Pyrenees, France. *J. Geol. Soc. London.* 173, 419–437. <https://doi.org/10.1144/jgs2015-129>
- Gasparrini, M., Bechstädt, T., Boni, M., 2006. Massive hydrothermal dolomites in the southwestern Cantabrian Zone (Spain) and their relation to the Late Variscan evolution. *Mar. Pet. Geol.* 23, 543–

568. <https://doi.org/10.1016/j.marpetgeo.2006.05.003>

Girão, A.V., Caputo, G., Ferro, M.C., 2017. Application of Scanning Electron Microscopy–Energy Dispersive X-Ray Spectroscopy (SEM-EDS), in: *Comprehensive Analytical Chemistry*. pp. 153–168. <https://doi.org/10.1016/bs.coac.2016.10.002>

Goldstein, R.H., Reynolds, T.J., 1994. Fluid inclusion microthermometry, in: Goldstein, R.H., Reynolds, T.J. (Eds.), *Systematics of Fluid Inclusions in Diagenetic Minerals*. SEPM (Society for Sedimentary Geology), pp. 87–121. <https://doi.org/10.2110/scn.94.31.0087>

Gregg, J.M., Shelton, K.L., Johnson, A.W., Somerville, I.D., Wright, W.R., 2001. Dolomitization of the Waulsortian Limestone (Lower Carboniferous) in the Irish Midlands. *Sedimentology* 48, 745–766. <https://doi.org/10.1046/j.1365-3091.2001.00397.x>

Grover, G., Read, J.F., 1983. Paleoaquifer and Deep Burial Related Cements Defined by Regional Cathodoluminescent Patterns, Middle Ordovician Carbonates, Virginia. *Am. Assoc. Pet. Geol. Bull.* 67, 1275–1303.

Haile, B.G., Czarniecka, U., Xi, K., Smyrak-Sikora, A., Jahren, J., Braathen, A., Hellevang, H., 2018. Hydrothermally induced diagenesis: Evidence from shallow marine-deltaic sediments, Wilhelmøya, Svalbard. *Geosci. Front.* <https://doi.org/10.1016/j.gsf.2018.02.015>

Haley, B.A., Klinkhammer, G.P., McManus, J., 2004. Rare earth elements in pore waters of marine sediments. *Geochim. Cosmochim. Acta* 68, 1265–1279. <https://doi.org/10.1016/j.gca.2003.09.012>

Hantschel, T., Kauerauf, A., 2009. *Fundamentals of basin and petroleum systems modelin*. Springer Berlin Heidelberg, Berlin Heidelberg.

Hinman, N.W., 1990. Chemical factors influencing the rates and sequences of silica phase transitions: Effects of organic constituents. *Geochim. Cosmochim. Acta* 54, 1563–1574. [https://doi.org/10.1016/0016-7037\(90\)90391-W](https://doi.org/10.1016/0016-7037(90)90391-W)

Hoefs, J., 1996. *Stable Isotope Geochemistry*, 4th ed. ed. Springer Berlin Heidelberg.

Horita, J., 2014. Oxygen and carbon isotope fractionation in the system dolomite–water–CO₂ to elevated

- temperatures. *Geochim. Cosmochim. Acta* 129, 111–124. <https://doi.org/10.1016/j.gca.2013.12.027>
- Houzay, J., Faggionato, J., Despujols, V., 2008. Maturity and source rock potential of the Albo-Aptian series. TOTAL EP internal report.
- Hsu, K.J., 1967. Chemistry of Dolomite Formation, in: Chilingar, G. V., Bissell, H.J., Fairbridge, R.W. (Eds.), *Developments in Sedimentology*. Elsevier B.V, pp. 169–191. [https://doi.org/10.1016/S0070-4571\(08\)71031-8](https://doi.org/10.1016/S0070-4571(08)71031-8)
- Huntington, K.W., Eiler, J.M., Affek, H.P., Guo, W., Bonifacie, M., Yeung, L.Y., Thiagarajan, N., Passey, B., Tripathi, A., Daëron, M., Came, R., 2009. Methods and limitations of “clumped” CO₂ isotope ($\Delta 47$) analysis by gas-source isotope ratio mass spectrometry. *J. Mass Spectrom.* 44, 1318–1329. <https://doi.org/10.1002/jms.1614>
- Huyghe, D., Mouthereau, F., Emmanuel, L., 2012. Oxygen isotopes of marine mollusc shells record Eocene elevation change in the Pyrenees. *Earth Planet. Sci. Lett.* 345–348, 131–141. <https://doi.org/10.1016/j.epsl.2012.06.035>
- IAEA, 2018. IAEA Annual Report 2018.
- Irwin, H., Curtis, C., Coleman, M., 1977. Isotopic evidence for source of diagenetic carbonates formed during burial of organic-rich sediments. *Nature* 269, 209–213. <https://doi.org/10.1038/269209a0>
- Jammes, S., Lavier, L., Manatschal, G., 2010a. Extreme crustal thinning in the Bay of Biscay and the Western Pyrenees: From observations to modeling. *Geochemistry, Geophys. Geosystems* 11. <https://doi.org/10.1029/2010GC003218>
- Jammes, S., Manatschal, G., Lavier, L., 2010b. Interaction between prerift salt and detachment faulting in hyperextended rift systems : The example of the Parentis and Mauléon basins (Bay of Biscay and western Pyrenees). *Am. Assoc. Pet. Geol. Bull.* 94, 957–975. <https://doi.org/10.1306/12090909116>
- Jammes, S., Manatschal, G., Lavier, L., Masini, E., 2009. Tectonosedimentary evolution related to extreme crustal thinning ahead of a propagating ocean: Example of the western Pyrenees. *Tectonics* 28, n/a–n/a. <https://doi.org/10.1029/2008TC002406>

- Jammes, S., Tiberi, C., Manatschal, G., 2010c. 3D architecture of a complex transcurrent rift system: The example of the Bay of Biscay–Western Pyrenees. *Tectonophysics* 489, 210–226. <https://doi.org/10.1016/j.tecto.2010.04.023>
- Jarvie, D.M., Claxton, B.L., Henk, F., Breyer, J.T., 2001. Oil and shale gas from the Barnett Shale, Fort Worth basin, Texas. *Am. Assoc. Pet. Geol. Bull.* 85, A100.
- Jiang, L., Worden, R.H., Cai, C., 2015. Generation of isotopically and compositionally distinct water during thermochemical sulfate reduction (TSR) in carbonate reservoirs: Triassic Feixianguan Formation, Sichuan Basin, China. *Geochim. Cosmochim. Acta* 165, 249–262. <https://doi.org/10.1016/j.gca.2015.05.033>
- Jodry, R.L., 1968. Growth and Dolomitization of Silurian Reefs, St. Clair County, Michigan: ABSTRACT. *Am. Assoc. Pet. Geol. Bull.* 52, 534. <https://doi.org/10.1306/5D25C35B-16C1-11D7-8645000102C1865D>
- Johnston, D.T., Farquhar, J., Wing, B.A., Kaufman, A.J., Canfield, D.E., Habicht, K.S., 2005. Multiple sulfur isotope fractionations in biological systems: A case study with sulfate reducers and sulfur disproportionators. *Am. J. Sci.* 305, 645–660. <https://doi.org/10.2475/ajs.305.6-8.645>
- Jones, G.D., 2000. Analysis of fluid flow constraints in regional-scale reflux dolomitization: constant versus variable-flux hydrogeological models. *Bull. Can. Pet. Geol.* 48, 230–245. <https://doi.org/10.2113/48.3.230>
- Jorgensen, N.O., 1987. Oxygen and carbon isotope compositions of Upper Cretaceous chalk from the Danish sub-basin and the North Sea Central Graben. *Sedimentology* 34, 559–570. <https://doi.org/10.1111/j.1365-3091.1987.tb00786.x>
- Killops, S.D., Killops, V.J., 2013. *Introduction to Organic Geochemistry*, 2nd ed. Blackwell Publishing Ltd.
- Kitayama, Y., Thomassot, E., Galy, A., Golovin, A., Korsakov, A., D'Eyrames, E., Assayag, N., Bouden, N., Ionov, D., 2017. Co-magmatic sulfides and sulfates in the Udachnaya-East pipe (Siberia): A record of the redox state and isotopic composition of sulfur in kimberlites and their mantle sources. *Chem. Geol.*

455, 315–330. <https://doi.org/10.1016/j.chemgeo.2016.10.037>

Koepnick, R.B., 1976. Luminescent zonation of carbonate cements in Upper Cambrian Straight Canyon and Fera Formations of the Dugway Range, Utah. *Nuclide Spectra* 9.

Kouhout, F.A., Henry, H.R., Banks, J.E., 1977. Hydrogeology related to geothermal conditions of the Floridan Plateau, in: Smith, K.L., Griffin, G.M. (Eds.), *The Geothermal Nature of the Floridan Plateau*. Florida Department of Natural Resources Bureau, Florida, pp. 1–34.

Kroner, U., Romer, R.L., 2013. Two plates — Many subduction zones: The Variscan orogeny reconsidered. *Gondwana Res.* 24, 298–329. <https://doi.org/10.1016/j.gr.2013.03.001>

Kulatilake, P.H.S.W., Wathugala, D.N., Stephansson, O., 1993. Joint network modelling with a validation exercise in Stripa mine, Sweden. *Int. J. Rock Mech. Min. Sci. Geomech. Abstr.* 30, 503–526. [https://doi.org/10.1016/0148-9062\(93\)92217-E](https://doi.org/10.1016/0148-9062(93)92217-E)

Kunz, O., Wagner, W., 2012. The GERG-2008 Wide-Range Equation of State for Natural Gases and Other Mixtures: An Expansion of GERG-2004. *J. Chem. Eng. Data* 57, 3032–3091. <https://doi.org/10.1021/jc300655b>

Lagabrielle, Y., Labaume, P., de Saint Blanquat, M., 2010. Mantle exhumation, crustal denudation, and gravity tectonics during Cretaceous rifting in the Pyrenean realm (SW Europe): Insights from the geological setting of the lherzolite bodies. *Tectonics* 29. <https://doi.org/10.1029/2009TC002588>

Lambert, L., Pernin, C., Maza, C., Virgone, A., 2006. Analyse sédimentologique, diagénétique et structurale du drain LA-415.G1. TOTAL EP internal report.

Land, L.S., 1985. The Origin of Massive Dolomite. *J. Geosci. Educ.* 33, 112–125.

Land, L.S., 1973. Contemporaneous Dolomitization of Middle Pleistocene Reefs by Meteoric Water, North Jamaica: ABSTRACT. *Bull. Mar. Sci.* 23, 64–92. <https://doi.org/10.1306/819A3F9A-16C5-11D7-8645000102C1865D>

Laubach, S.E., Olson, J.E., Cross, M.R., 2009. Mechanical and fracture stratigraphy. *Am. Assoc. Pet. Geol. Bull.* 93, 1413–1426. <https://doi.org/10.1306/07270909094>

- Laurent, D., Gaucher, E., Christophe, D., Carpentier, C., Barré, G., Collon, P., Paris, G., Pironon, J., 2019. A Sulfuric Acid Speleogenesis in the northern Pyrenees? Example of the Arbailles karstic region (West Pyrenees, France), in: Conference: EGU 2019. Vienna.
- Le Marrec, A., D'Aboville, O., Delahaye, S., Lagarigue, J., Moen Maurel, L., Dore, M., Lang, J., 1995. Synthèse Géodynamique du Bassin d'Arzacq et de ses bordures. TOTAL EP internal report.
- Li, J., Duan, Z., 2011. A thermodynamic model for the prediction of phase equilibria and speciation in the H₂O-CO₂-NaCl-CaCO₃-CaSO₄ system from 0 to 250°C, 1 to 1000 bar with NaCl concentrations up to halite saturation. *Geochim. Cosmochim. Acta* 75, 4351–4376. <https://doi.org/10.1016/j.gca.2011.05.019>
- López-Horgue, M.A., Iriarte, E., Schröder, S., Fernández-Mendiola, P.A., Caline, B., Corneyllie, H., Frémont, J., Sudrie, M., Zerti, S., 2010. Structurally controlled hydrothermal dolomites in Albian carbonates of the Ason valley, Basque Cantabrian Basin, Northern Spain. *Mar. Pet. Geol.* 27, 1069–1092. <https://doi.org/10.1016/j.marpetgeo.2009.10.015>
- Lyakhovsky, V., 2001. Scaling of fracture length and distributed damage. *Geophys. J. Int.* 144, 114–122. <https://doi.org/10.1046/j.0956-540X.2000.01303.x>
- Machel, H., 2001. Bacterial and thermochemical sulfate reduction in diagenetic settings — old and new insights. *Sediment. Geol.* 140, 143–175. [https://doi.org/10.1016/S0037-0738\(00\)00176-7](https://doi.org/10.1016/S0037-0738(00)00176-7)
- Machel, H.G., 2004. Concepts and models of dolomitization: a critical reappraisal. *Geol. Soc. London, Spec. Publ.* 235, 7–63. <https://doi.org/10.1144/GSL.SP.2004.235.01.02>
- Machel, H.G., 1985. Cathodoluminescence in Calcite and Dolomite and Its Chemical Interpretation. *Geosci. Canada* 12, 139–147.
- Machel, H.G., Anderson, J.H., 1989. Pervasive Subsurface Dolomitization of the Nisku Formation in Central Alberta. *J. Sediment. Res.* 59. <https://doi.org/10.1306/212F90AC-2B24-11D7-8648000102C1865D>
- Machel, H.G., Lonnee, J., 2002. Hydrothermal dolomite—a product of poor definition and imagination. *Sediment. Geol.* 152, 163–171. [https://doi.org/10.1016/S0037-0738\(02\)00259-2](https://doi.org/10.1016/S0037-0738(02)00259-2)

- Mangenot, X., Bonifacie, M., Gasparrini, M., Götz, A., Chaduteau, C., Ader, M., Rouchon, V., 2017. Coupling $\Delta 47$ and fluid inclusion thermometry on carbonate cements to precisely reconstruct the temperature, salinity and $\delta^{18}\text{O}$ of paleo-groundwater in sedimentary basins. *Chem. Geol.* 472, 44–57. <https://doi.org/10.1016/j.chemgeo.2017.10.011>
- Mangenot, X., Gasparrini, M., Rouchon, V., Bonifacie, M., 2018. Basin-scale thermal and fluid flow histories revealed by carbonate clumped isotopes ($\Delta 47$) - Middle Jurassic carbonates of the Paris Basin depocentre. *Sedimentology* 65, 123–150. <https://doi.org/10.1111/sed.12427>
- Masini, E., Manatschal, G., Tugend, J., Mohn, G., Flament, J.-M., 2014. The tectono-sedimentary evolution of a hyper-extended rift basin: the example of the Arzacq–Mauléon rift system (Western Pyrenees, SW France). *Int. J. Earth Sci.* 103, 1569–1596. <https://doi.org/10.1007/s00531-014-1023-8>
- McDermott, J.M., Ono, S., Tivey, M.K., Seewald, J.S., Shanks, W.C., Solow, A.R., 2015. Identification of sulfur sources and isotopic equilibria in submarine hot-springs using multiple sulfur isotopes. *Geochim. Cosmochim. Acta* 160, 169–187. <https://doi.org/10.1016/j.gca.2015.02.016>
- Merino, E., Canals, A., 2011. Self-accelerating dolomite-for-calcite replacement: Self-organized dynamics of burial dolomitization and associated mineralization. *Am. J. Sci.* 311, 573–607. <https://doi.org/10.2475/07.2011.01>
- Meyers, W.J., 1974. Carbonate Cement Stratigraphy of the Lake Valley Formation (Mississippian) Sacramento Mountains, New Mexico. *J. Sediment. Res.* 44, 837–861. <https://doi.org/10.1306/212F6BC2-2B24-11D7-8648000102C1865D>
- Millot, G., 1970. *Geology of Clays, Weathering*. ed. Springer Berlin Heidelberg, Berlin, Heidelberg. <https://doi.org/10.1007/978-3-662-41609-9>
- Minami, H., Hachikubo, A., Yamashita, S., Sakagami, H., Kasashima, R., Konishi, M., Shoji, H., Takahashi, N., Pogodaeva, T., Krylov, A., Khabuev, A., Kazakov, A., De Batist, M., Naudts, L., Chensky, A., Gubin, N., Khlystov, O., 2018. Hydrogen and oxygen isotopic anomalies in pore waters suggesting clay mineral dehydration at gas hydrate-bearing Kedr mud volcano, southern Lake Baikal, Russia. *Geo-Marine Lett.* 38, 403–415. <https://doi.org/10.1007/s00367-018-0542-x>

- Misra, K.C., 2012. Introduction to geochemistry: principles and applications. Wiley - Blackwell, Knoxville, Tennessee.
- Montanez, I.P., Read, J.F., 1992. Fluid-Rock Interaction History During Stabilization of Early Dolomites, Upper Knox Group (Lower Ordovician), U.S. Appalachians. *SEPM J. Sediment. Res.* Vol. 62. <https://doi.org/10.1306/D42679D3-2B26-11D7-8648000102C1865D>
- Montel, F., 1993. Phase equilibria needs for petroleum exploration and production industry. *Fluid Phase Equilib.* 84, 343–367. [https://doi.org/10.1016/0378-3812\(93\)85132-6](https://doi.org/10.1016/0378-3812(93)85132-6)
- Moore, C.H., 2013. Carbonate Reservoirs, Second. ed. Elsevier, Amsterdam.
- Mountjoy, E.W., Green, D., Machel, H.G., Duggan, J., Williams-Jones, A.E., 1999. Devonian matrix dolomites and deep burial carbonate cements: A comparison between the Rimbey-Meadowbrook reef trend and the deep basin of west-central Alberta. *Bull. Can. Pet. Geol.* 47, 487–509.
- Nielsen, P., Swennen, R., Muchez, P., Keppens, E., 1998. Origin of Dinantian zebra dolomites south of the Brabant-Wales Massif, Belgium. *Sedimentology* 45, 727–743. <https://doi.org/10.1046/j.1365-3091.1998.00171.x>
- Norman, M.D., Pearson, N.J., Sharma, A., Griffin, W.L., 1996. Quantitative analysis of trace elements in geological materials by laser ablation ICPMS: instrumental operating conditions and calibration values of NIST glasses. *Geostand. Geoanalytical Res.* 20, 247–261. <https://doi.org/10.1111/j.1751-908X.1996.tb00186.x>
- O'Neil, J.R., Clayton, R.N., Mayeda, T.K., 1969. Oxygen Isotope Fractionation in Divalent Metal Carbonates. *J. Chem. Phys.* 51, 5547–5558. <https://doi.org/10.1063/1.1671982>
- Olson, J., Pollard, D.D., 1989. Inferring paleostresses from natural fracture patterns: A new method. *Geology* 17, 345. [https://doi.org/10.1130/0091-7613\(1989\)017<0345:IPFNFP>2.3.CO;2](https://doi.org/10.1130/0091-7613(1989)017<0345:IPFNFP>2.3.CO;2)
- Ono, S., Wing, B., Johnston, D., Farquhar, J., Rumble, D., 2006. Mass-dependent fractionation of quadruple stable sulfur isotope system as a new tracer of sulfur biogeochemical cycles. *Geochim. Cosmochim. Acta* 70, 2238–2252. <https://doi.org/10.1016/j.gca.2006.01.022>

- Pabian-Goyheneche, C., Anquelle, L., 1995. Lacq Profond: Interprétation structurale du gisement à partir de la sismique 3D Schéma géologique de réservoir TOTAL EP Internal Report. Pau.
- Passey, B.H., Levin, N.E., Cerling, T.E., Brown, F.H., Eiler, J.M., 2010. High-temperature environments of human evolution in East Africa based on bond ordering in paleosol carbonates. *Proc. Natl. Acad. Sci.* 107, 11245–11249. <https://doi.org/10.1073/pnas.1001824107>
- Passey, B.H., Levin, N.E., Cerling, T.E., Brown, F.H., Eiler, J.M., 2010. High-temperature environments of human evolution in East Africa based on bond ordering in paleosol carbonates. *Proc. Natl. Acad. Sci.* <https://doi.org/10.1073/pnas.1001824107>
- Peltzer, E.T., Zhang, X., Walz, P.M., Luna, M., Brewer, P.G., 2016. In situ Raman measurement of HS⁻ and H₂S in sediment pore waters and use of the HS⁻:H₂S ratio as an indicator of pore water pH. *Mar. Chem.* 184, 32–42. <https://doi.org/10.1016/j.marchem.2016.05.006>
- Peng, D.-Y., Robinson, D.B., 1976. A New Two-Constant Equation of State. *Ind. Eng. Chem. Fundam.* 15, 59–64. <https://doi.org/10.1021/i160057a011>
- Perera, P.N., Browder, B., Ben-Amotz, D., 2009. Perturbations of Water by Alkali Halide Ions Measured using Multivariate Raman Curve Resolution. *J. Phys. Chem. B* 113, 1805–1809. <https://doi.org/10.1021/jp808732s>
- Peters, M., Strauss, H., Farquhar, J., Ockert, C., Eickmann, B., Jost, C.L., 2010. Sulfur cycling at the Mid-Atlantic Ridge: A multiple sulfur isotope approach. *Chem. Geol.* 269, 180–196. <https://doi.org/10.1016/j.chemgeo.2009.09.016>
- Pironon, J., Canals, M., Dubessy, J., Walgenwitz, F., Laplace-Builhe, C., 1998. Volumetric reconstruction of individual oil inclusions by confocal scanning laser microscopy. *Eur. J. Mineral.* 10, 1143–1150. <https://doi.org/10.1127/ejm/10/6/1143>
- Pointe, P.R. La, Hudson, J.A., 1985. Characterization and Interpretation of Rock Mass Joint Patterns. *Geol. Soc. Am. Spec. Pap., Geological Society of America Special Papers* 199. <https://doi.org/10.1130/SPE199>

- Popescu, B.M., 1995. Romania's petroleum systems and their remaining potential. *Pet. Geosci.* 1, 337–350. <https://doi.org/10.1144/petgeo.1.4.337>
- Price, G.D., 1989. Cathodoluminescence of Geological Materials. *Mineral. Mag.* 53, 391–391. <https://doi.org/10.1180/minmag.1989.053.371.21>
- Puigdefabregas, C., Souquet, P., 1986. Tectono-Sedimentary Cycles and Depositional Sequences of the Mesozoic and Tertiary from the Pyrenees. *Tectonophysics* 129, 173–203.
- Renard, S., Pironon, J., Sterpenich, J., Carpentier, C., Lescanne, M., Gaucher, E.C., 2019. Diagenesis in Mesozoic carbonate rocks in the North Pyrénées (France) from mineralogy and fluid inclusion analysis: Example of Rousse reservoir and caprock. *Chem. Geol.* 508, 30–46. <https://doi.org/10.1016/j.chemgeo.2018.06.017>
- Richter, D.K., Götze, T., Götze, J., Neuser, R.D., 2003. Progress in application of cathodoluminescence (CL) in sedimentary petrology. *Mineral. Petrol.* 79, 127–166. <https://doi.org/10.1007/s00710-003-0237-4>
- Rives, T., Razack, M., Petit, J.-P., Rawnsley, K.D., 1992. Joint spacing: analogue and numerical simulations. *J. Struct. Geol.* 14, 925–937. [https://doi.org/10.1016/0191-8141\(92\)90024-Q](https://doi.org/10.1016/0191-8141(92)90024-Q)
- Robb, L., 2005. *Introduction to Ore Forming Processes*, 1st ed. Blackwell Publishing Ltd, Oxford, UK.
- Roca, E., Muñoz, J.A., Ferrer, O., Ellouz, N., 2011. The role of the Bay of Biscay Mesozoic extensional structure in the configuration of the Pyrenean orogen: Constraints from the MARCONI deep seismic reflection survey. *Tectonics* 30, n/a-n/a. <https://doi.org/10.1029/2010TC002735>
- Roedder, E., 1984. *Fluid Inclusions*, Volume 12. ed. Mineralogical Society of America, Virginia.
- Rosenbaum, J., Sheppard, S.M., 1986. An isotopic study of siderites, dolomites and ankerites at high temperatures. *Geochim. Cosmochim. Acta* 50, 1147–1150. [https://doi.org/10.1016/0016-7037\(86\)90396-0](https://doi.org/10.1016/0016-7037(86)90396-0)
- Salardon, R., Carpentier, C., Bellahsen, N., Pironon, J., France-Lanord, C., 2017. Interactions between tectonics and fluid circulations in an inverted hyper-extended basin: Example of mesozoic carbonate

- rocks of the western North Pyrenean Zone (Chaînons Béarnais, France). *Mar. Pet. Geol.* 80, 563–586. <https://doi.org/10.1016/j.marpetgeo.2016.11.018>
- Schmidt, C., Seward, T.M., 2017. Raman spectroscopic quantification of sulfur species in aqueous fluids: Ratios of relative molar scattering factors of Raman bands of H₂S, HS⁻, SO₂, HSO₄⁻, SO₄²⁻, S₂O₃²⁻, S₃⁻ and H₂O at ambient conditions and information on changes with pressure. *Chem. Geol.* 467, 64–75. <https://doi.org/10.1016/j.chemgeo.2017.07.022>
- Schrijver, K., Williams-Jones, A.E., Bertrand, R., Chagnon, A., 1996. Genesis and controls of hydrothermal dolomitization in sandstones of the Appalachian thrust belt, Québec, Canada: Implications for associated galena-barite mineralization. *Chem. Geol.* 129, 257–279. [https://doi.org/10.1016/0009-2541\(95\)00146-8](https://doi.org/10.1016/0009-2541(95)00146-8)
- Schuster, R., Stüwe, K., 2008. Permian metamorphic event in the Alps. *Geology* 36, 603. <https://doi.org/10.1130/G24703A.1>
- Serjouné, 1995. Bassin d'Arzacq, Aquitaine simulation de la maturité des roches mères. TOTAL EP internal report.
- Shepherd, T.J., Rankin, A.H., Alderton, D.H.M., 1985. *A Practical Guide to Fluid Inclusion Studies*. Blackie, London.
- Sibley, D.F., Gregg, J.M., 1987. Classification of Dolomite Rock Textures. *SEPM J. Sediment. Res.* Vol. 57. <https://doi.org/10.1306/212F8CBA-2B24-11D7-8648000102C1865D>
- Sibson, R.H., Moore, J.M.M., Rankin, A.H., 1975. Seismic pumping—a hydrothermal fluid transport mechanism. *J. Geol. Soc. London.* 131, 653–659. <https://doi.org/10.1144/gsjgs.131.6.0653>
- Simms, M., 1984. Dolomitization by Groundwater-Flow System in Carbonate Platforms. *Gulf Coast Assoc. Geol. Soc. Trans.* 34, 411–420.
- Swart, P.K., Burns, S.J., Leder, J.J., 1991. Fractionation of the stable isotopes of oxygen and carbon in carbon dioxide during the reaction of calcite with phosphoric acid as a function of temperature and technique. *Chem. Geol. Isot. Geosci. Sect.* 86, 89–96. [https://doi.org/10.1016/0168-9622\(91\)90055-](https://doi.org/10.1016/0168-9622(91)90055-)

- Swennen, R., Vandeginste, V., Ellam, R., 2003. Genesis of zebra dolomites (Cathedral Formation: Canadian Cordillera Fold and Thrust Belt, British Columbia). *J. Geochemical Explor.* 78–79, 571–577. [https://doi.org/10.1016/S0375-6742\(03\)00065-7](https://doi.org/10.1016/S0375-6742(03)00065-7)
- Teixell, A., Labaume, P., Lagabrielle, Y., 2016. The crustal evolution of the west-central Pyrenees revisited: Inferences from a new kinematic scenario. *Comptes Rendus Geosci.* 348, 257–267. <https://doi.org/10.1016/j.crte.2015.10.010>
- Thiéry, R., Pironon, J., Walgenwitz, F., Montel, F., 2002. Individual characterization of petroleum fluid inclusions (composition and P–T trapping conditions) by microthermometry and confocal laser scanning microscopy: inferences from applied thermodynamics of oils. *Mar. Pet. Geol.* 19, 847–859. [https://doi.org/10.1016/S0264-8172\(02\)00110-1](https://doi.org/10.1016/S0264-8172(02)00110-1)
- Thomsen, R.O., 1998. Aspects of applied basin modelling: sensitivity analysis and scientific risk, in: Düppenbecker, S., Illigge, J.E. (Eds.), *Basin Modeling: Practice and Progress*. Geological Society, London, Special Publications, pp. 209–221. <https://doi.org/10.1144/GSL.SP.1998.141.01.13>
- Travé, A., Labaume, P., Vergés, J., 2014. Fluid Systems in Foreland Fold-and-Thrust Belts: An Overview from the Southern Pyrenees, in: Lacombe, O., Roure, F., Lavé, J., Vergés, J. (Eds.), *Thrust Belts and Foreland Basins*, *Frontiers in Earth Sciences*. Springer Berlin Heidelberg, Berlin, Heidelberg, pp. 93–115. https://doi.org/10.1007/978-3-540-69426-7_5
- Tremosa, J., Gailhanou, H., Chiaberge, C., Castilla, R., Gaucher, E., Lassin, A., Gout, C., Fialips, C., Claret, F., 2019. Effects of smectite dehydration and illitisation on overpressures in sedimentary basins: A coupled chemical and thermo-hydro-mechanical modelling approach. *Mar. Pet. Geol.* In press. <https://doi.org/10.1016/j.marpetgeo.2019.08.021>
- Tucker, M., 1995. *Techniques in Sedimentology*. Blackwell Publishing Ltd, Oxford, United Kingdom.
- Tucker, M.E., Wright, V.P., 1990. *Carbonate Sedimentology*, 1st ed. Blackwell Scientific Publications, Oxford London.

- Vacherat, A., Mouthereau, F., Pik, R., Bellahsen, N., Gautheron, C., Berner, M., Daudet, M., Balansa, J., Tibari, B., Pinna Jamme, R., Radal, J., 2016. Rift-to-collision transition recorded by tectonothermal evolution of the northern Pyrenees. *Tectonics* 35, 907–933. <https://doi.org/10.1002/2015TC004016>
- Vacherat, A., Mouthereau, F., Pik, R., Berner, M., Gautheron, C., Masini, E., Le Pourhiet, L., Tibari, B., Lahfid, A., 2014. Thermal imprint of rift-related processes in orogens as recorded in the Pyrenees. *Earth Planet. Sci. Lett.* 408, 296–306. <https://doi.org/10.1016/j.epsl.2014.10.014>
- Vandeginste, V., Swennen, R., Gleeson, S.A., Ellam, R.M., Osadetz, K., Roure, F., 2009. Thermochemical sulphate reduction in the Upper Devonian Cairn Formation of the Fairholme carbonate complex (South-West Alberta, Canadian Rockies): evidence from fluid inclusions and isotopic data. *Sedimentology* 56, 439–460. <https://doi.org/10.1111/j.1365-3091.2008.00978.x>
- Veizer, J., Ala, D., Azmy, K., Bruckschen, P., Buhl, D., Bruhn, F., Carden, G.A.F., Diener, A., Ebner, S., Godderis, Y., Jasper, T., Korte, C., Pawellek, F., Podlaha, O.G., Strauss, H., 1999. $^{87}\text{Sr}/^{86}\text{Sr}$, $\delta^{13}\text{C}$ and $\delta^{18}\text{O}$ evolution of Phanerozoic seawater. *Chem. Geol.* 161, 59–88. [https://doi.org/10.1016/S0009-2541\(99\)00081-9](https://doi.org/10.1016/S0009-2541(99)00081-9)
- Walrafen, G.E., 1962. Raman Spectral Studies of the Effects of Electrolytes on Water. *J. Chem. Phys.* 36, 1035–1042. <https://doi.org/10.1063/1.1732628>
- Warren, J., 2000. Dolomite: occurrence, evolution and economically important associations. *Earth-Science Rev.* 52, 1–81. [https://doi.org/10.1016/S0012-8252\(00\)00022-2](https://doi.org/10.1016/S0012-8252(00)00022-2)
- White, D.E., 1957. Thermal waters of volcanic origin. *Bull. Geol. Soc. Am.* 68, 1637–1658.
- Wilson, A.M., Sanford, W., Whitaker, F., Smart, P., 2001. Spatial patterns of diagenesis during geothermal circulation in carbonate platforms. *Am. J. Sci.* 301, 727–752. <https://doi.org/10.2475/ajs.301.8.727>
- Wilson, E.N., Hardie, L.A., Phillips, O.M., 1990. Dolomitization front geometry, fluid flow patterns, and the origin of massive dolomite; the Triassic Latemar buildup, northern Italy. *Am. J. Sci.* 290, 741–796. <https://doi.org/10.2475/ajs.290.7.741>
- Worden, R.H., Smalley, P.C., Oxtoby, N.H., 1996. The effects of thermochemical sulfate reduction upon

- formation water salinity and oxygen isotopes in carbonate gas reservoirs. *Geochim. Cosmochim. Acta* 60, 3925–3931. [https://doi.org/10.1016/0016-7037\(96\)00216-5](https://doi.org/10.1016/0016-7037(96)00216-5)
- Zengler, D.H., Dunham, J., Ethington, R.L., 1980. Concepts and Models of Dolomitization. SEPM (Society for Sedimentary Geology), Houston, Texas. <https://doi.org/10.2110/pec.80.28>
- Zhabin, A.G., Kremenetskiy, A.A., 1993. The pyrite-pyrrhotite transformation as an ore-concentrating geochemical barrier. *Int. Geol. Rev.* 35, 359–368. <https://doi.org/10.1080/00206819309465534>
- Zhang, Y.-G., Frantz, J.D., 1987. Determination of the homogenization temperatures and densities of supercritical fluids in the system NaClKClCaCl₂H₂O using synthetic fluid inclusions. *Chem. Geol.* 64, 335–350. [https://doi.org/10.1016/0009-2541\(87\)90012-X](https://doi.org/10.1016/0009-2541(87)90012-X)

Résumé

L'évolution géodynamique des bassins exerce un contrôle majeur sur l'évolution des chemins de circulation, de la température, de la pression et de la chimie des fluides diagénétiques. Ceci influence la diagenèse et les propriétés pétrophysiques des réservoirs. Récemment, les modèles géodynamiques des Pyrénées et du bassin sud aquitain ont été revus et mis à jour pour inclure la participation d'une phase de rifting au Crétacé inférieur qui a évolué vers un amincissement crustal extrême couplé à une exhumation du manteau et suivi d'une inversion pendant le Crétacé supérieur et le paléogène. Ce modèle révisé met en évidence l'impact possible des fluides hydrothermaux sur la diagenèse des réservoirs pétroliers dans le sud du bassin aquitain. Ce travail est basé sur l'étude de trois carottes de forage pénétrant dans les réservoirs du Crétacé supérieur (Lacq supérieur) et du Jurassique supérieur au Crétacé inférieur (Lacq inférieur). À l'aide d'une multitude d'outils pétrographiques et géochimiques et d'une modélisation de bassin, nous documentons comment l'hyperextension aptienne a été couplée à la circulation de fluides riches en Mg qui ont partiellement dolomitisé Lacq profond. Le Mg a été fourni à partir des formations riches en argiles présentes en profondeur, tandis que les fortes salinités sont dues à une interaction avec les évaporites du Trias. Différents épisodes de fracturation au cours de la période post-rift, pendant la convergence N-S, ont permis la connexion entre Lacq inférieur et un réservoir de fluides sursaturés vis-à-vis de la calcite. Une troisième phase de circulation de fluides qui s'est terminée pendant la compression Eocène, a précipité des anhydrites massives dans Lacq profond. Dans le même temps, la diagenèse a été marquée par une circulation de fluides hydrothermaux le long des principales failles et fractures au niveau de la crête de l'anticlinal de Lacq. Des dolomies hydrothermales ont été documentées avec des températures environ 40°C plus élevées que celles des roches hôtes environnantes. Différents épisodes de fracturation liés à l'orogénèse pyrénéenne, ont ensuite été responsables de la précipitation de calcite et d'anhydrite. Il apparaît que le chargement en pétrole et en gaz dans Lacq supérieur et Lacq inférieur respectivement, se situe pendant la phase post-orogénique. Par conséquent, il est évident que le cadre géodynamique global et l'évolution géologique des foothills pyrénéens, régis principalement par l'hyperextension Aptienne et la convergence Eocène, ont eu un contrôle significatif sur les types, sources et voies de circulation des fluides diagénétiques, pétroliers et gaziers.

Mots-clefs: Pétrographie; géochimie; diagenèse des carbonates; inclusions fluides; modélisation des bassins

Abstract

The geodynamic evolution of basins exerts a major control on the evolution of the pathways, temperature, pressure and chemistry of circulating fluids. This in turn influences the diagenesis and petrophysical properties of petroleum reservoirs. Recently, geodynamic models of the Pyrenees and the south Aquitaine basin were revisited and updated to include the involvement of an Early Cretaceous rifting phase that evolved to extreme crustal thinning coupled with mantle exhumation, followed by an inversion and convergence during the Late Cretaceous and the Paleogene. This revised model highlights the possible impact of hydrothermal fluids on the diagenesis of petroleum reservoirs in the southern Aquitaine Basin. This work is based on the study of three drill cores penetrating the Upper Cretaceous (Upper Lacq) reservoirs and the Upper Jurassic to Early Cretaceous (Deep Lacq) reservoirs. Using a multitude of petrographic, geochemical and modeling tools, we document how the Aptian hyperextension was coupled with the circulation of Mg-rich fluids that partially dolomitized Deep Lacq. Mg was provided from the clay-rich formations at depths while salinities were the result of fluid interaction with the Triassic evaporites. Different fracturing episodes during the post-rift stage, when the N-S convergence started, connected Deep Lacq with a pool of fluids oversaturated with respect to calcites. A third fluid pulse, linked to the Eocene compression, precipitated massive anhydrites in Deep Lacq. At the same time in Upper Lacq, diagenesis was marked by orogeny-driven hydrothermal fluid circulations along the major faults and fractures on the crest of Lacq anticline. Hydrothermal dolomites were documented with temperatures nearly 40°C higher than the surrounding host rocks. Different fracturing episodes, related to the Pyrenean orogeny, were later responsible for calcite and anhydrite cementation. The oil and gas infilling of Upper and Deep Lacq respectively are assumed to be post-orogenic. Therefore, it is evident that the overall geodynamic setting and the geologic evolution of the Pyrenean foothills, governed mainly by the Aptian hyperextension and the Eocene convergence, had a significant control on the types, sources and circulation pathways of the diagenetic fluids.

Keywords: Petrography; geochemistry; carbonate diagenesis; fluid inclusions; basin modeling